



MINISTÉRIO DA CIÊNCIA, TECNOLOGIA, INOVAÇÕES E COMUNICAÇÕES  
**INSTITUTO NACIONAL DE PESQUISAS ESPACIAIS**

sid.inpe.br/mtc-m21b/2017/02.16.21.15-TDI

**EVOLUTION OF THE ELECTRON DENSITY,  
TEMPERATURE DISTRIBUTION IN THE SOLAR  
CORONA DURING SOLAR CYCLES 23 AND 24**

Jenny Marcela Rodríguez Gómez

Doctorate Thesis of the Graduate  
Course in Space Geophysics,  
guided by Drs. Luis Eduardo  
Antunes Vieira, and Alisson Dal  
Lago, approved in March 16, 2017.

URL of the original document:

<http://urlib.net/8JMKD3MGP3W34P/3NCJQLB>

INPE  
São José dos Campos  
2017

**PUBLISHED BY:**

Instituto Nacional de Pesquisas Espaciais - INPE

Gabinete do Diretor (GB)

Serviço de Informação e Documentação (SID)

Caixa Postal 515 - CEP 12.245-970

São José dos Campos - SP - Brasil

Tel.:(012) 3208-6923/6921

Fax: (012) 3208-6919

E-mail: pubtc@inpe.br

**COMMISSION OF BOARD OF PUBLISHING AND PRESERVATION  
OF INPE INTELLECTUAL PRODUCTION (DE/DIR-544):****Chairperson:**

Maria do Carmo de Andrade Nono - Conselho de Pós-Graduação (CPG)

**Members:**

Dr. Plínio Carlos Alvalá - Centro de Ciência do Sistema Terrestre (CST)

Dr. André de Castro Milone - Coordenação de Ciências Espaciais e Atmosféricas (CEA)

Dra. Carina de Barros Melo - Coordenação de Laboratórios Associados (CTE)

Dr. Evandro Marconi Rocco - Coordenação de Engenharia e Tecnologia Espacial (ETE)

Dr. Hermann Johann Heinrich Kux - Coordenação de Observação da Terra (OBT)

Dr. Marley Cavalcante de Lima Moscati - Centro de Previsão de Tempo e Estudos Climáticos (CPT)

Silvia Castro Marcelino - Serviço de Informação e Documentação (SID) **DIGITAL**

**LIBRARY:**

Dr. Gerald Jean Francis Banon

Clayton Martins Pereira - Serviço de Informação e Documentação (SID)

**DOCUMENT REVIEW:**

Simone Angélica Del Duca Barbedo - Serviço de Informação e Documentação (SID)

Yolanda Ribeiro da Silva Souza - Serviço de Informação e Documentação (SID)

**ELECTRONIC EDITING:**

Marcelo de Castro Pazos - Serviço de Informação e Documentação (SID)

André Luis Dias Fernandes - Serviço de Informação e Documentação (SID)



MINISTÉRIO DA CIÊNCIA, TECNOLOGIA, INOVAÇÕES E COMUNICAÇÕES  
**INSTITUTO NACIONAL DE PESQUISAS ESPACIAIS**

sid.inpe.br/mtc-m21b/2017/02.16.21.15-TDI

**EVOLUTION OF THE ELECTRON DENSITY,  
TEMPERATURE DISTRIBUTION IN THE SOLAR  
CORONA DURING SOLAR CYCLES 23 AND 24**

Jenny Marcela Rodríguez Gómez

Doctorate Thesis of the Graduate  
Course in Space Geophysics,  
guided by Drs. Luis Eduardo  
Antunes Vieira, and Alisson Dal  
Lago, approved in March 16, 2017.

URL of the original document:

<<http://urlib.net/8JMKD3MGP3W34P/3NCJQLB>>

INPE  
São José dos Campos  
2017

Cataloging in Publication Data

---

Rodríguez Gómez, Jenny Marcela.

R618e Evolution of the electron density, temperature distribution in the solar corona during solar cycles 23 and 24 / Jenny Marcela Rodríguez Gómez. – São José dos Campos : INPE, 2017.  
xxx + 158 p. ; (sid.inpe.br/mtc-m21b/2017/02.16.21.15-TDI)

Thesis (Doctorate in Space Geophysics) – Instituto Nacional de Pesquisas Espaciais, São José dos Campos, 2017.

Guiding : Drs. Luis Eduardo Antunes Vieira, and Alisson Dal Lago.

1. Magnetic flux. 2. Irradiance. 3. Electron density.  
4. Temperature. 5. Photosphere. I.Title.

CDU 52-337:523.947

---



Esta obra foi licenciada sob uma Licença [Creative Commons Atribuição-NãoComercial 3.0 Não Adaptada](https://creativecommons.org/licenses/by-nc/3.0/).

This work is licensed under a [Creative Commons Attribution-NonCommercial 3.0 Unported License](https://creativecommons.org/licenses/by-nc/3.0/).

Aluno (a): **Jenny Marcela Rodríguez Gómez**

Título: "EVOLUTION OF THE ELECTRON DENSITY, TEMPERATURE DISTRIBUTION IN THE SOLAR CORONA DURING SOLAR CYCLES 23 AND 24".

Aprovado (a) pela Banca Examinadora em cumprimento ao requisito exigido para obtenção do Título de **Doutor(a)** em **Geofísica Espacial/Ciências do Ambiente Solar-Terrestre**

Dr. Polinaya Muralikrishna



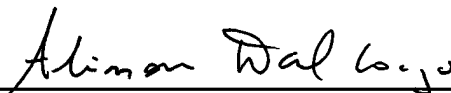
Presidente / INPE / São José dos Campos - SP

Dr. Luis Eduardo Antunes Vieira



Orientador(a) / INPE / São José dos Campos - SP

Dr. Alisson Dal Lago



Orientador(a) / INPE / São José dos Campos - SP

Dr. Joaquim Eduardo Rezende Costa



Membro da Banca / INPE / São José dos Campos - SP

Dr. Caius Lucius Selhorst



Convidado(a) / UNICSUL / São Paulo - SP

Dra. Judit Palacios Hernández



Convidado(a) / UAH / Espanha - ES

**Este trabalho foi aprovado por:**

maioria simples

unanimidade

São José dos Campos, 16 de Março de 2017



*To my parents José Campo and Maria Gladys: my sister,  
Lady and my brother, Jaminton for the unconditional support.*



## ACKNOWLEDGEMENTS

I would like to express my sincere gratitude to my advisors Dr. Luis Eduardo Antunes Vieira and Dr. Alisson Dal Lago for their full support, guidance and comprehension in my thesis work. I would like to thank Dr. Judith Palacios, for her support and collaboration during the last years.

My thanks to the National Institute for Space Research (INPE) for the opportunity to do my PhD in Space Geophysics. I am very grateful to the CAPES and CNPq for the financial support.

To all my friends and colleagues, thank you for your understanding and encouragement in this way.

*Muchas gracias!!*



## ABSTRACT

The present thesis aims at the study of the plasma parameters in the solar corona, using a flux transport model, force free-field extrapolations, a model of emission and optimization algorithm. The physical model is based on the assumption that the variation of the irradiance and plasma parameters is due to the evolution of the solar magnetic field. The goal is to reconstruct electron density and temperature distributions in the solar corona and the emission in four different wavelengths during the last two solar cycles (large scale) and also the emission, electron density and temperature profiles from Active Region NOAA 11855 (small scale). The relation between photospheric dynamics, emission, and plasma parameters in different time scales are reviewed. These characteristics are important in the Astrophysical and Geophysical fields, because they can help to understand physical phenomena such as coronal heating and eruptive events.

Keywords:

Magnetic flux. Irradiance. Electron density. Temperature. Photosphere. Chromosphere. Transition region. Corona.



# EVOLUÇÃO DAS DISTRIBUIÇÕES DE DENSIDADE ELETRÔNICA, TEMPERATURA NA COROA SOLAR NOS CICLOS SOLARES 23 E 24

## RESUMO

Esta tese tem como objetivo principal o estudo dos parâmetros de plasma na coroa solar, usando um modelo de transporte de fluxo, extrapolações de campo livre de forças, um modelo de emissão e um algoritmo de otimização. O modelo está baseado na ideia que as variações da irradiância e os parâmetros de plasma estão relacionados com a evolução do campo magnético solar. O objetivo é reconstruir as distribuições de densidade e temperatura na coroa solar e a emissão em quatro comprimentos de onda diferentes durante os dois últimos ciclos solares e também a emissão, perfis de densidade eletrônica e temperatura usando a região ativa NOAA 11855. A relação entre a dinâmica, emissão e parâmetros de plasma em diferentes escalas de tempo são revisadas. Estas características são importantes em astrofísica e geofísica, porque podem ajudar a entender fenômenos físicos como o aquecimento coronal e eventos eruptivos.

Palavras-chave: Campo magnético. Irradiância espectral. Densidade eletrônica. Temperatura. Fotosfera. Cromosfera. Região de transição. Corona.



## LIST OF FIGURES

	<u>Page</u>
1.1 The solar structure. Courtesy of The International Solar-Terrestrial Physics Program and NASA. . . . .	3
1.2 A Magnetic Butterfly Diagram constructed from longitudinally and radial magnetic field obtained from Kitt Peak and SOHO (HATHAWAY, 2015). . . . .	8
1.3 The Babcock-Leighton mechanism. . . . .	10
1.4 Image of solar granulation in the G-continuum, image from the Swedish 1m Solar Telescope and Institute of Theoretical Astrophysics, Stockholm. . . . .	12
1.5 Internal rotation profile of the Sun inferred from helioseismology. . . . .	14
1.6 Flux transport model ingredients. . . . .	16
1.7 Contribution function from CHIANTI atomic database 8.0, using ionization equilibrium from MAZZOTTA et al. (1998) and coronal abundances from MEYER (1985), in different wavelengths at $17.1nm$ , $19.3nm$ , $21.1nm$ and $33.5nm$ . . . . .	23
1.8 Electron density and temperature model of the chromosphere (Fontenla et al. 1990; Model FAL-C) and lower corona (Gabriel 1976) . . . . .	25
1.9 Coronagraph images from Large Angle Spectrometric Coronagraph (LASCO) Aug.17 (2016) (a) LASCO C2 image and (b) LASCO C3 image. . . . .	27
1.10 Time and wavelength of available SSI measurements . . . . .	34
2.1 The solar spectral irradiance from SORCE and TIMED observations, from Apr. 22 (2004) to Jul. 23 (2010) A) shows the average solar spectral irradiance inferred from SORCE and TIMED. B) shows the altitude absorption in the Earth's atmosphere. . . . .	38
2.2 Schematic description of the COronal DEnsity and Temperature (CODET) model. . . . .	39
2.3 Schematic magneto-static magnetic flux tube model, $B_E$ is magnetic field outside and $B_o$ is magnetic field inside, $P_E$ external pressure and $P_o$ inside pressure. . . . .	39
2.4 $Bf$ condition for the magnetic field with $bf_0 = 20$ , $\tau_{bf} = 1.2$ and $R_{sun} = 1.0 - 2.5$ . . . . .	42
2.5 Schematic description of optimization algorithm, where dotted lines describe the input parameters. . . . .	45

2.6	Source surface model. Photospheric magnetic field in Region 1. Loops appear in Region 2. Solar wind extends into the interplanetary space. . . . .	48
2.7	Wavelength $17.1nm$ . First column: Solar Spectral Irradiance from observational data (green line) and modelled (blue line). Second column: average temperature profiles in all layers for each model. Third column: average density profiles in all layers according to the model. . . . .	51
2.8	Wavelength $19.3nm$ . First column: Solar Spectral Irradiance from observational data (green line) and modelled (blue line) 1. Second column: average temperature profiles in all layers for each model. Third column: average density profiles in all layers according to the model. . . . .	53
2.9	Wavelength $33.5nm$ . First column: Solar Spectral Irradiance from observational data (green line) and modelled (blue line). Second column: average temperature profiles in all layers for each model. Third column: average density profiles in all layers according to the model. . . . .	55
2.10	Wavelength $21.1nm$ . First column: Solar Spectral Irradiance from observational data (green line) and modelled (blue line). Second column: average temperature profiles in all layers for each model. Third column: average density profiles in all layers according to the model. . . . .	57
2.11	Fit $17.1nm$ , $19.3nm$ and $21.1nm$ using the model 1. Upper panel: Solar Spectral Irradiance from observational data (green line) and modelled (blue line), left panel: $17.1nm$ , middle panel: $19.3nm$ and right panel: $21.1nm$ . Lower panel: average temperature profiles in all layers (left panel) and average density profiles in all layers (right panel). . . . .	58
2.12	Fit $17.1nm$ , $19.3nm$ and $21.1nm$ using the model 2. Upper panel: Solar Spectral Irradiance from observational data (green line) and modelled (blue line), left panel: $17.1nm$ , middle panel: $19.3nm$ and right panel: $21.1nm$ . Lower panel: average temperature profiles in all layers (left panel) and average density profiles in all layers (right panel). . . . .	59
2.13	Fit $17.1nm$ , $19.3nm$ and $21.1nm$ using the model 3. Upper panel: Solar Spectral Irradiance from observational data (green line) and modelled (blue line), left panel: $17.1nm$ , middle panel: $19.3nm$ and right panel: $21.1nm$ . Lower panel: average temperature profiles in all layers (left panel) and average density profiles in all layers (right panel). . . . .	60
2.14	Fit $17.1nm$ , $19.3nm$ and $33.5nm$ using the model 1. Upper panel: Solar Spectral Irradiance from observational data (green line) and modelled (blue line), left panel: $17.1nm$ , middle panel: $19.3nm$ and right panel: $33.5nm$ . Lower panel: average temperature profiles in all layers (left panel) and average density profiles in all layers (right panel). . . . .	61

2.15	Fit 17.1nm, 19.3nm and 33.5nm using the model 2. Upper panel: Solar Spectral Irradiance from observational data (green line) and modelled (blue line), left panel: 17.1nm, middle panel: 19.3nm and right panel: 33.5nm. Lower panel: average temperature profiles in all layers (left panel) and average density profiles in all layers (right panel). . . . .	62
2.16	Fit 17.1nm, 19.3nm and 33.5nm using the model 3. Upper panel: Solar Spectral Irradiance from observational data (green line) and modelled (blue line), left panel: 17.1nm, middle panel: 19.3nm and right panel: 33.5nm. Lower panel: average temperature profiles in all layers (left panel) and average density profiles in all layers (right panel). . . . .	63
2.17	Fit 17.1nm and 19.3nm using the model 1. Upper panel: Solar Spectral Irradiance from observational data (green line) and modelled (blue line), left panel: 17.1nm and right panel: 19.3nm. Lower panel: average temperature profiles in all layers (left panel) and average density profiles in all layers (right panel). . . . .	64
2.18	Fit 21.1nm and 33.5nm using the model 1. Upper panel: Solar Spectral Irradiance from observational data (green line) and modelled (blue line), left panel: 21.1nm and right panel: 33.5nm. Lower panel: average temperature profiles in all layers (left panel) and average density profiles in all layers (right panel). . . . .	65
2.19	Fit 21.1nm and 33.5nm using the model 2. Upper panel: Solar Spectral Irradiance from observational data (green line) and modelled (blue line), left panel: 21.1nm and right panel: 33.5nm. Lower panel: average temperature profiles in all layers (left panel) and average density profiles in all layers (right panel). . . . .	66
2.20	Fit 21.1nm and 33.5nm using the model 3. Upper panel: Solar Spectral Irradiance from observational data (green line) and modelled (blue line), left panel: 21.1nm and right panel: 33.5nm. Lower panel: average temperature profiles in all layers (left panel) and average density profiles in all layers (right panel). . . . .	67
2.21	Fit 21.1nm and 33.5nm using the model 4. Upper panel: Solar Spectral Irradiance from observational data (green line) and modelled (blue line), left panel: 21.1nm and right panel: 33.5nm. Lower panel: average temperature profiles in all layers (left panel) and average density profiles in all layers (right panel). . . . .	68

2.22	Fit 19.3nm and 21.1nm using the model 1. Upper panel: Solar Spectral Irradiance from observational data (green line) and modelled (blue line), left panel: 19.3nm and right panel: 21.1nm. Lower panel: average temperature profiles in all layers (left panel) and average density profiles in all layers (right panel). . . . .	69
2.23	Fit 19.3nm and 21.1nm using the model 2. Upper panel: Solar Spectral Irradiance from observational data (green line) and modelled (blue line), left panel: 19.3nm and right panel: 21.1nm. Lower panel: average temperature profiles in all layers (left panel) and average density profiles in all layers (right panel). . . . .	70
2.24	Solar Spectral Irradiance (SSI) using 17.1nm model 5 (green line) and Solar Spectral Irradiance (SSI) from TIMED/SEE (blue line) during the solar cycle 23 and 24. Upper panel: SSI at 17.1nm, middle panels: SSI at 19.3nm and 21.1nm, lower panel: SSI at 33.5nm. . . . .	72
2.25	Scatter plot using the parameters from 17.1nm model 5 and Chi-squared test ( $\chi^2$ ) in each case. Upper panel: scatter plot of 17.1nm, middle panels: scatter plot of 19.3nm and 21.1nm, lower panel: scatter plot of 33.5nm. . . . .	73
2.26	Solar Spectral Irradiance (SSI) using 17.1nm model 5 (green line) and Solar Spectral Irradiance (SSI) from TIMED/SEE (blue line) from Jan. 01 (2012) to Jan. 01 (2014). Upper panel: SSI at 17.1nm, lower panel: SSI at 19.5nm. . . . .	74
2.27	Comparison between the observed uncertainty from TIMED/SEE (dotted green line) and difference between observational and modelled data using the parameters from 17.1nm model 5 (blue line). Upper panel: analysis at 17.1nm, middle panels: analysis at 19.3nm and difference between observed and modelled data at 21.1nm, lower panel: analysis at 33.5nm. . . . .	75
2.28	Solar Spectral Irradiance (SSI) using 19.3nm model 5 (green line) and Solar Spectral Irradiance (SSI) from TIMED/SEE (blue line) during the solar cycle 23 and 24. Upper panel: SSI at 17.1nm, middle panels: SSI at 19.3nm and 21.1nm, lower panel: SSI at 33.5nm. . . . .	76
2.29	Scatter plot using the parameters from 19.3nm model 5 and Chi-squared test ( $\chi^2$ ) in each case. Upper panel: scatter plot of 17.1nm, middle panels: scatter plot of 19.3nm and 21.1nm, lower panel: scatter plot of 33.5nm. . . . .	77
2.30	Solar Spectral Irradiance (SSI) using the parameters from 19.3nm model 5 (green line) and Solar Spectral Irradiance (SSI) from TIMED/SEE (blue line) from Jan. 01 (2012) to Jan. 01 (2014). Upper panel: SSI at 19.3nm, middle panels: SSI at 21.1nm, lower panel: SSI at 33.5nm. . . . .	78

2.31	Comparison between the observed uncertainty from TIMED/SEE (dotted green line) and difference between observational and modelled data using the parameters from 19.3nm model 5 (blue line). Upper panel: analysis at 17.1nm, middle panels: analysis at 19.3nm and difference between observed and modelled data at 21.1nm, lower panel: analysis at 33.5nm. . . . .	79
2.32	Solar Spectral Irradiance (SSI) using the parameters from 33.5nm model 2 (green line) and Solar Spectral Irradiance (SSI) from TIMED/SEE (blue line) during the solar cycle 23 and 24. Upper panel: SSI at 17.1nm, middle panels: SSI at 19.3nm and 21.1nm, lower panel: SSI at 33.5nm. . . . .	80
2.33	Scatter plot using the parameters from 33.5nm model 2 and Chi-squared test ( $\chi^2$ ) in each case. Upper panel: scatter plot of 17.1nm, middle panels: scatter plot of 19.3nm and 21.1nm, lower panel: scatter plot of 33.5nm. . . . .	81
2.34	Solar Spectral Irradiance (SSI) using the parameters from 33.5nm model 2 (green line) and Solar Spectral Irradiance (SSI) from TIMED/SEE (blue line) from Jan. 01 (2010) to Dec. 01 (2010). Upper panel: SSI at 21.1nm, lower panel: SSI at 33.5nm. . . . .	82
2.35	Comparison between the observed uncertainty from TIMED/SEE (dotted green line) and difference between observational and modelled data using the parameters from 33.5nm model 2 (blue line). Upper panel: analysis at 17.1nm, middle panels: analysis at 19.3nm and difference between observed and modelled data at 21.1nm, lower panel: analysis at 33.5nm. . . . .	83
2.36	Solar Spectral Irradiance (SSI) using the parameters from 21.1nm model 1 (green line) and Solar Spectral Irradiance (SSI) from TIMED/SEE (blue line) during the solar cycle 23 and 24. Upper panel: SSI at 17.1nm, middle panels: SSI at 19.3nm and 21.1nm, lower panel: SSI at 33.5nm. . . . .	84
2.37	Scatter plot using the parameters from 21.1nm model 1 and Chi-squared test ( $\chi^2$ ) in each case. Upper panel: scatter plot of 17.1nm, middle panels: scatter plot of 19.3nm and 21.1nm, lower panel: scatter plot of 33.5nm. . . . .	85
2.38	Solar Spectral Irradiance (SSI) using the parameters from 21.1nm model 1 (green line) and Solar Spectral Irradiance (SSI) from TIMED/SEE (blue line) from Jan. 01 (2010) to Dec. 31 (2010). . . . .	86

2.39	Comparison between the observed uncertainty from TIMED/SEE (dotted green line) and difference between observational and modelled data using the parameters from 21.1nm model 1 (blue line). Upper panel: analysis at 17.1nm, middle panels: analysis at 19.3nm and difference between observed and modelled data at 21.1nm, lower panel: analysis at 33.5nm. . . . .	87
2.40	Solar Spectral Irradiance (SSI) using the parameters from 21.1nm model 3 (green line) and Solar Spectral Irradiance (SSI) from TIMED/SEE (blue line) during the solar cycle 23 and 24. Upper panel: SSI at 17.1nm, middle panels: SSI at 19.3nm and 21.1nm, lower panel: SSI at 33.5nm. . . . .	88
2.41	Scatter plot using the parameters from 21.1nm model 3 and Chi-squared test ( $\chi^2$ ) in each case. Upper panel: scatter plot of 17.1nm, middle panels: scatter plot of 19.3nm and 21.1nm, lower panel: scatter plot of 33.5nm. . . . .	89
2.42	Comparison between the observed uncertainty from TIMED/SEE (dotted green line) and difference between observational and modelled data using the parameters from 21.1nm model 3 (blue line). Upper panel: analysis at 17.1nm, middle panels: analysis at 19.3nm and difference between observed and modelled data at 21.1nm, lower panel: analysis at 33.5nm. . . . .	90
2.43	Solar Spectral Irradiance (SSI) using the parameters from 17.1nm, 19.3nm and 21.1nm model 2 (green line) and Solar spectral Irradiance (SSI) from TIMED/SEE (blue line) during the solar cycle 23 and 24. Upper panel: SSI at 17.1nm, middle panels: SSI at 19.3nm and 21.1nm, lower panel: SSI at 33.5nm. . . . .	91
2.44	Scatter plot using the parameters from 17.1nm, 19.3nm and 21.1nm model 2 and Chi-squared test ( $\chi^2$ ) in each case. Upper panel: scatter plot of 17.1nm, middle panels: scatter plot of 19.3nm and 21.1nm, lower panel: scatter plot of 33.5nm. . . . .	92
2.45	Solar Spectral Irradiance (SSI) using the parameters from 17.1nm, 19.3nm and 21.1nm model 2 (green line) and Solar spectral Irradiance (SSI) from TIMED/SEE (blue line) from Jan. 01 (2004) to Dec. 31 (2004). Upper panel: SSI at 17.1nm, middle panels: SSI at 19.3nm and 21.1nm, lower panel: SSI at 33.5nm. . . . .	93

2.46	Comparison between the observed uncertainty from TIMED/SEE (dotted green line) and difference between observational and modelled data using the parameters from 17.1nm, 19.3nm and 21.1nm model 2 (blue line). Upper panel: analysis at 17.1nm, middle panels: analysis at 19.3nm and difference between observed and modelled data at 21.1nm, lower panel: analysis at 33.5nm. . . . .	94
2.47	Solar Spectral Irradiance (SSI) using the parameters from 17.1nm and 19.3nm model 2 (green line) and Solar Spectral Irradiance (SSI) from TIMED/SEE (blue line) during the solar cycle 23 and 24. Upper panel: SSI at 17.1nm, middle panels: SSI at 19.3nm and 21.1nm, lower panel: SSI at 33.5nm. . . . .	95
2.48	Scatter plot using the parameters from 17.1nm and 19.3nm model 2 and Chi-squared test ( $\chi^2$ ) in each case. Upper panel: scatter plot of 17.1nm, middle panels: scatter plot of 19.3nm and 21.1nm, lower panel: scatter plot of 33.5nm. . . . .	96
2.49	Solar Spectral Irradiance (SSI) using the parameters from 17.1nm and 19.3nm model 2 (green line) and Solar Spectral Irradiance (SSI) from TIMED/SEE (blue line) from Jan. 01 (2004) to Dec. 31 (2004). Upper panel: SSI at 17.1nm, lower panel: SSI at 19.3nm. . . . .	97
2.50	Comparison between the observed uncertainty from TIMED/SEE (dotted green line) and difference between observational and modelled data using the parameters from 17.1nm and 19.3nm model 2 (blue line). Upper panel: analysis at 17.1nm, middle panels: analysis at 19.3nm and difference between observed and modelled data at 21.1nm, lower panel: analysis at 33.5nm. . . . .	98
2.51	Solar Spectral Irradiance (SSI) using the parameters from 21.1nm and 33.5nm model 3 (green line) and Solar Spectral Irradiance (SSI) from TIMED/SEE (blue line) during the solar cycle 23 and 24. Upper panel: SSI at 17.1nm, middle panels: SSI at 19.3nm and 21.1nm, lower panel: SSI at 33.5nm. . . . .	99
2.52	Scatter plot using the parameters from 21.1nm and 33.5nm model 3 and Chi-squared test ( $\chi^2$ ) in each case. Upper panel: scatter plot of 17.1nm, middle panels: scatter plot of 19.3nm and 21.1nm, lower panel: scatter plot of 33.5nm. . . . .	100
2.53	Solar Spectral Irradiance (SSI) using the parameters from 21.1nm and 33.5nm model 3 (green line) and Solar Spectral Irradiance (SSI) from TIMED/SEE (blue line) from Jan. 01 to Dec. 31 (2010). Upper panel: SSI at 21.1nm, lower panel: SSI at 33.5nm. . . . .	101

2.54	Comparison between the observed uncertainty from TIMED/SEE (dotted green line) and difference between observational and modelled data using the parameters from 21.1nm and 33.5nm model 3 (blue line). Upper panel: analysis at 17.1nm, middle panels: analysis at 19.3nm and difference between observed and modelled data at 21.1nm, lower panel: analysis at 33.5nm. . . . .	102
2.55	Solar Spectral Irradiance (SSI) using the parameters from 19.3nm and 21.1nm model 1 (green line) and Solar Spectral Irradiance (SSI) from TIMED/SEE (blue line) during the solar cycle 23 and 24. Upper panel: SSI at 17.1nm, middle panels: SSI at 19.3nm and 21.1nm, lower panel: SSI at 33.5nm. . . . .	103
2.56	Scatter plot using the parameters from 19.3nm and 21.1nm model 1 and Chi-squared test ( $\chi^2$ ) in each case. Upper panel: scatter plot of 17.1nm, middle panels: scatter plot of 19.3nm and 21.1nm, lower panel: scatter plot of 33.5nm. . . . .	104
2.57	Solar Spectral Irradiance (SSI) using the parameters from 19.3nm and 21.1nm model 1 (green line) and Solar Spectral Irradiance (SSI) from TIMED/SEE (blue line) from Jan. 01 to Dec. 31 (2007). Upper panel: SSI at 19.3nm, middle panels: SSI at 21.1nm, lower panel: SSI at 33.5nm.	105
2.58	Comparison between the observed uncertainty from TIMED/SEE (dotted green line) and difference between observational and modelled data using the parameters from 19.3nm and 21.1nm model 1 (blue line). Upper panel: analysis at 17.1nm, middle panels: analysis at 19.3nm and difference between observed and modelled data at 21.1nm, lower panel: analysis at 33.5nm. . . . .	106
3.1	Average temperature (upper panel) and density (lower panel) profiles using the parameters from the model 1, through different layers (Rsun=1.000, 1.016, 1.032, 1.049, 1.067, 1.165, 1.282), during the solar cycle 23 and 24. . . . .	112
3.2	Evolution of plasma parameters during the solar cycle 23 and 24, using the model 1. Upper left panel: mean temperature per day (red line). Upper right panel: moving average temperature with time period of 90 days. Lower left panel: mean density per day (red line). Lower right panel: moving average density with the time period of 90 days. . . . .	113
3.3	Average temperature (upper panel) and density (lower panel) profiles using the parameters from the model 2, in different layers (Rsun=1.000, 1.016, 1.032, 1.049, 1.067, 1.165, 1.282), during the solar cycle 23 and 24.	114

3.4	Evolution of plasma parameters during the solar cycle 23 and 24, using the model 2. Upper left panel: mean temperature per day (red line). Upper right panel: moving average temperature with time period of 90 days. Lower left panel: mean density per day (red line). Lower right panel: moving average density with the time period of 90 days. . . . .	115
3.5	Average temperature (upper panel) and density (lower panel) profiles using the parameters from the model 3, in different layers ( $R_{sun}=1.000, 1.016, 1.032, 1.049, 1.067, 1.165, 1.282$ ), during the solar cycle 23 and 24.	116
3.6	Evolution of plasma parameters during the solar cycle 23 and 24, using the model 3. Upper left panel: mean temperature per day (red line). Upper right panel: moving average temperature with time period of 90 days. Lower left panel: mean density per day (red line). Lower right panel: moving average density with the time period of 90 days. . . . .	117
3.7	Comparison between temperature, density and magnitude of magnetic field in different layers first row $R_{sun} = 1.00$ , second row $R_{sun} = 1.02$ , third row $R_{sun} = 1.05$ , fourth row $R_{sun} = 1.10$ and the last row $R_{sun} = 1.16$ , using the model 1, Oct. 01 (1999). First column: temperature maps (log temperature T(K)), second column: density maps (log density $N(cm^{-3})$ ) and last column: magnetic field maps (log magnetic field B(G)). . . . .	119
3.8	Comparison between temperature, density and magnitude of magnetic field in different layers first row $R_{sun} = 1.00$ , second row $R_{sun} = 1.02$ , third row $R_{sun} = 1.05$ , fourth row $R_{sun} = 1.10$ and the last row $R_{sun} = 1.16$ , using the model 1, Oct. 01 (2014). First column: temperature maps (log temperature T(K)), second column: density maps (log density $N(cm^{-3})$ ) and last column: magnetic field maps (log magnetic field B(G)). . . . .	120
3.9	Comparison between temperature, density and magnitude of magnetic field in different layers first row $R_{sun} = 1.00$ , second row $R_{sun} = 1.02$ , third row $R_{sun} = 1.05$ , fourth row $R_{sun} = 1.10$ and the last row $R_{sun} = 1.16$ , using the model 1, Oct. 01 (2016). First column: temperature maps (log temperature T(K)), second column: density maps (log density $N(cm^{-3})$ ) and last column: magnetic field maps (log magnetic field B(G)). . . . .	121

3.10	Comparison between temperature, density and magnitude of magnetic field in different layers first row $R_{sun} = 1.00$ , second row $R_{sun} = 1.02$ , third row $R_{sun} = 1.05$ , fourth row $R_{sun} = 1.10$ and the last row $R_{sun} = 1.16$ , using the model 2, Oct. 01 (1999). First column: temperature maps (log temperature T(K)), second column: density maps (log density $N(cm^{-3})$ ) and last column: magnetic field maps (log magnetic field B(G)). . . . .	122
3.11	Comparison between temperature, density and magnitude of magnetic field in different layers first row $R_{sun} = 1.00$ , second row $R_{sun} = 1.02$ , third row $R_{sun} = 1.05$ , fourth row $R_{sun} = 1.10$ and the last row $R_{sun} = 1.16$ , using the model 2, Oct. 01 (2014). First column: temperature maps (log temperature T(K)), second column: density maps (log density $N(cm^{-3})$ ) and last column: magnetic field maps (log magnetic field B(G)). . . . .	123
3.12	Comparison between temperature, density and magnitude of magnetic field in different layers first row $R_{sun} = 1.00$ , second row $R_{sun} = 1.02$ , third row $R_{sun} = 1.05$ , fourth row $R_{sun} = 1.10$ and the last row $R_{sun} = 1.16$ , using the model 2, Oct. 01 (2016). First column: temperature maps (log temperature T(K)), second column: density maps (log density $N(cm^{-3})$ ) and last column: magnetic field maps (log magnetic field B(G)). . . . .	124
3.13	Intensity map at $17.1nm$ from model 1, Oct. 01 (2014) . . . . .	125
3.14	Intensity map at $19.3nm$ from model 1, Oct. 01 (2014) . . . . .	126
3.15	Intensity map at $21.1nm$ from model 1, Oct. 01 (2014) . . . . .	127
3.16	Intensity map at $33.5nm$ from model 1, Oct. 01 (2014) . . . . .	128
3.17	Intensity map at $17.1nm$ from model 2, Oct. 01 (2014) . . . . .	129
3.18	Intensity map at $19.3nm$ from model 2, Oct. 01 (2014) . . . . .	130
3.19	Intensity map at $21.1nm$ from model 2, Oct. 01 (2014) . . . . .	131
3.20	Intensity map at $33.5nm$ from model 2, Oct. 01 (2014) . . . . .	132
3.21	Evolution of the plasma $\beta$ parameter during the solar cycle 23 and 24. Using the moving average $\beta$ values with the time period of 90 days. Upper panel: Model 1 parameters through all layers. Lower panel: Model 2 parameters through all layers. . . . .	133
3.22	Plasma $\beta$ variation with the height through the solar atmosphere. Two days were chosen Jul.01 (1996) (blue line) and Jul. 01 (2016) (red line). . . . .	134
4.1	Evolution of the emergence flux region in HMI/SDO photospheric magnetic field. North is bottom. . . . .	137

4.2	Evolution of the Active Region NOAA11855 (SHARPS/HMI), from Sept. 29 to Oct. 06 (2013). First row: Sept. 29 18:00UT, Sept. 30 18:00UT, Oct. 01 00:00UT, Oct. 02 12:00UT. Second row: Oct. 03 12:00UT, Oct. 04 18:00UT, Oct. 05 18:00UT and Oct. 06 18:00UT. North is up. . . . .	138
4.3	Schematic description of the density and temperature model in ARs. . .	139
4.4	Images at $30.4nm$ from AIA/SDO (left panel) and composite images using photospheric magnetic field from HMI/SDO for the same region with blue contours marks (right panels). . . . .	140
4.5	Images at $17.1nm$ from AIA/SDO (left panel) and composite images using photospheric magnetic field from HMI/SDO for the same region with blue contours marks (right panel). . . . .	141
4.6	Emission in the NOAA 11855 using the parameters from selected models (chapter 3). Integrated intensity from the AIA/SDO (blue line), emission from the CODET model (green line). Upper panels: Emission at $17.1nm$ and $30.4nm$ using the parameters of the model 1. Lower panels: Emission at $17.1nm$ and $30.4nm$ using the parameters of the model 2. . . . .	142



## LIST OF TABLES

	<u>Page</u>
1.1 Historical review of solar dynamo theory . . . . .	8
1.2 Typical density values $N$ in the solar atmosphere. . . . .	27
1.3 Some density models using observational data and analytical expressions	28
1.4 Typical temperature values $T$ in the solar corona. . . . .	29
1.5 Typical temperature in some specific wavelengths . . . . .	29
1.6 Temperature from some methods and using observational data . . . . .	31
1.7 The HMI instrument characteristics. . . . .	33
2.1 Model fit at $17.1nm$ , the value parameters ( $\gamma$ , $\alpha$ , $N_o$ , $T_o$ and $B_{sat}$ ) for each model and information about the optimization algorithm (Population size and generations). . . . .	50
2.2 Model fit at $19.3nm$ describes the value parameters ( $\gamma$ , $\alpha$ , $N_o$ , $T_o$ and $B_{sat}$ ) for each model and information about the optimization algorithm (Population size and generations). . . . .	52
2.3 Model fit at $33.5nm$ describes the value parameters ( $\gamma$ , $\alpha$ , $N_o$ , $T_o$ and $B_{sat}$ ) for each model and information about the optimization algorithm (Population size and generations). . . . .	54
2.4 Model fit at $21.1nm$ describes the value parameters ( $\gamma$ , $\alpha$ , $N_o$ , $T_o$ and $B_{sat}$ ) for each model and information about the optimization algorithm (Population size and generations). . . . .	56
2.5 Model fit between $17.1nm$ , $19.3nm$ and $21.1nm$ describes the value parameters ( $\gamma$ , $\alpha$ , $N_o$ , $T_o$ and $B_{sat}$ ) for each model and information about the optimization algorithm (Population size and generations). . . . .	58
2.6 Model fit between $17.1nm$ , $19.3nm$ and $33.5nm$ describes the value parameters ( $\gamma$ , $\alpha$ , $N_o$ , $T_o$ and $B_{sat}$ ) for each model and information about the optimization algorithm (Population size and generations). . . . .	60
2.7 Model fit between $17.1nm$ and $19.3nm$ describes the value parameters ( $\gamma$ , $\alpha$ , $N_o$ , $T_o$ and $B_{sat}$ ) for each model and information about the optimization algorithm (Population size and generations). . . . .	63
2.8 Model fit between $21.1nm$ and $33.5nm$ describes the value parameters ( $\gamma$ , $\alpha$ , $N_o$ , $T_o$ and $B_{sat}$ ) for each model and information about the optimization algorithm (Population size and generations). . . . .	64

2.9	Model fit between 19.3nm and 21.1nm describes the value parameters ( $\gamma$ , $\alpha$ , $N_o$ , $T_o$ and $B_{sat}$ ) for each model and information about the optimization algorithm (Population size and generations). . . . .	68
2.10	Results the best fit in different cases, from Table 2.1 to 2.2 (cells with cyan color). . . . .	70
3.1	New numbering of the models in this chapter and the corresponding model described in the previous chapter. . . . .	110
3.2	Parameters ( $\gamma$ , $\alpha$ , $N_o$ , $T_o$ and $B_{sat}$ ) for each selected model. . . . .	110
3.3	Minimum temperature values (MK) in each layer (Rsun=1.000, 1.016, 1.032, 1.049, 1.067, 1.165, 1.282) during the solar cycle 23 and 24, using the selected models. . . . .	111
3.4	Maximun density values ( $cm^{-3}$ ) in each layer (Rsun=1.000, 1.016, 1.032, 1.049, 1.067, 1.165, 1.282) during the solar cycle 23 and 24, using the selected models. . . . .	111

## LIST OF SYMBOLS

$R_{sun}$	– Solar radius
$AU$	– Astronomical unit
$\mathbf{J}$	– Current density
$\mathbf{B}$	– Vectorial magnetic field
$B$	– Magnitude of the magnetic field
$B_r, B_\theta$ and $B_\phi$	– Spherical component of the magnetic field
$N$	– Density profile
$N_o$	– Background density
$T$	– Temperature profile
$T_o$	– Background temperature
$B_{sat}$	– Saturation coefficient of the magnetic field
$\gamma$	– Exponent for the variation in density profile
$\alpha$	– Exponent for the variation in temperature profile
$I_o$	– Intensity in each pixel
$I$	– Integrated intensity over the solar disc at 1AU
$G(\lambda, T)$	– Contribution function
$d\lambda$	– Spectral resolution
$\chi^2$	– Chi-squared test
$\beta$	– Plasma parameter
$k_B$	– Boltzman constant
$Bf$	– Condition for the magnetic field



# CONTENTS

	<u>Page</u>
<b>1 INTRODUCTION</b> . . . . .	<b>1</b>
1.1 The Sun . . . . .	3
1.1.1 Solar structure . . . . .	3
1.1.2 Solar cycle . . . . .	7
1.1.3 Solar dynamo . . . . .	8
1.2 The flux transport . . . . .	12
1.2.1 Solar flux flows . . . . .	12
1.2.2 Flux-transport solar dynamo . . . . .	14
1.2.3 Surface flux transport models . . . . .	15
1.3 Radiative process in the solar corona . . . . .	18
1.3.1 Atomic processes in the solar corona . . . . .	19
1.3.2 Chemical composition in the solar corona . . . . .	20
1.4 Electron density and temperature in the solar corona . . . . .	25
1.4.1 Electron density distribution in the corona . . . . .	26
1.4.2 Temperature in the solar corona . . . . .	28
1.5 Solar data . . . . .	31
1.5.1 Photospheric magnetic field . . . . .	32
1.5.2 Solar Spectral Irradiance (SSI) . . . . .	34
<b>2 THE SOLAR MODEL PLASMA PARAMETERS</b> . . . . .	<b>37</b>
2.1 Approach . . . . .	38
2.1.1 Genetic algorithms . . . . .	43
2.1.2 Magnetic field extrapolations . . . . .	46
2.2 Model fit . . . . .	48
2.3 Analysis of the results . . . . .	70
2.4 Summary . . . . .	107
<b>3 ELECTRON DENSITY AND TEMPERATURE PROFILES DURING THE SOLAR CYCLE 23 AND 24</b> . . . . .	<b>109</b>
3.1 Electron density and temperature profiles through the solar corona . . .	110
3.2 Temperature and Density maps . . . . .	118
3.3 Intensity maps . . . . .	124
3.4 Plasma $\beta$ parameter in solar corona . . . . .	132

3.5	Summary . . . . .	134
<b>4</b>	<b>EVOLUTION AND EMISSION OF THE ACTIVE REGION</b>	
	<b>NOAA 11855 . . . . .</b>	<b>137</b>
4.1	Evolution of the Active region NOAA 11855 . . . . .	138
4.1.1	Emission . . . . .	138
4.2	Summary . . . . .	142
<b>5</b>	<b>CONCLUSIONS . . . . .</b>	<b>143</b>
	<b>REFERENCES . . . . .</b>	<b>147</b>

# 1 INTRODUCTION

## Contents

---

1.1	The Sun . . . . .	<b>3</b>
1.1.1	Solar structure . . . . .	3
1.1.2	Solar cycle . . . . .	7
1.1.3	Solar dynamo . . . . .	8
1.2	The flux transport . . . . .	<b>12</b>
1.2.1	Solar flux flows . . . . .	12
1.2.2	Flux-transport solar dynamo . . . . .	14
1.2.3	Surface flux transport models . . . . .	15
1.3	Radiative process in the solar corona . . . . .	<b>18</b>
1.3.1	Atomic processes in the solar corona . . . . .	19
1.3.2	Chemical composition in the solar corona . . . . .	20
1.4	Electron density and temperature in the solar corona . . . . .	<b>25</b>
1.4.1	Electron density distribution in the corona . . . . .	26
1.4.2	Temperature in the solar corona . . . . .	28
1.5	Solar data . . . . .	<b>31</b>
1.5.1	Photospheric magnetic field . . . . .	32
1.5.2	Solar Spectral Irradiance (SSI) . . . . .	34

---

The magnetic field constitutes a natural link between the Sun and the Earth. The Sun plays an important role in Earth's life; and in essence, it is the astrophysical laboratory to study plasmas. In this scenario it is important to describe the interaction between the solar atmosphere and the solar magnetic field and their relationship with the plasma parameters. The magnetic field is created in the solar interior by the solar dynamo action and it is related to physical processes in the solar atmosphere.

The problem of high temperatures in solar corona has been of interest and it is still a fundamental problem in astrophysics. The study of plasma parameters such as electron density and temperature can contribute to understanding this problem. Some coronal features can be characterised using parameters such as the temperature and density. However, the measurement of these parameters is not trivial in the solar corona because the plasma is optically thin and the information received is integrated over all the plasma column along the line of sight mixing information from

different wavelengths and the characteristics of the solar corona. For this reason, it is important to build models that can be used to study this behavior and check whether or not the results are related to characteristics of the solar cycle and if they are changing in different time scales.

The variation of the density and temperature profiles over the solar cycle are important and gives clues for the solar corona dynamics. The descriptions of the density and temperature profiles of the Active Regions can be used to probe the relationship between the photosphere, chromosphere, transition region and solar corona. In this context, we have decided to build a physics-based model that relies on the assumption that the density, temperature and emission variations are due to the evolution of the structure of the solar magnetic field. The COronal DENsity and Temperature (CODET) model allows us to investigate some important aspects such as variations of density and temperature through the solar corona, in different heights and time scales. These variations are examined in large and small scale.

The important relationship between solar activity and Earth's atmosphere is related to how the solar activity cycle modulates the temperature and density of the Earth's thermosphere. Specifically UV and EUV irradiance produce changes in different altitudes. EUV photons are absorbed in the Earth's thermosphere, the atmospheric region between  $\sim 90$  and  $\sim 500$  km, creating the ionosphere within it, and causing its temperature to increase with altitude, reaching  $\sim 600$  K at  $\sim 400$  km (at solar minimum) and as high as  $\sim 1500$  K (at solar maximum) (SOLOMON *et al.*, 2010).

When the Sun is active, EUV emissions can change in lower time scales. This phenomenon heat the upper Earth's atmosphere. Also, it creates a layer of ions that alters the radio communications and GPS navigation. Bringing knowledge on how the emission changes over the last solar cycles and their relationship with the solar magnetic field is one of the goals of this thesis.

The main body of this thesis comprises the review of some concepts about the structure of the Sun and the basic physical processes (sections 2, 3, 4 and 5) and solar data (section 6). In chapter 2, we present a description of our model. In chapter 3, we present the long-term evolution of electron density and temperature in different layers through the solar corona, Solar Spectral Irradiance (SSI) during the last solar cycles. In chapter 4, we present the short-term evolution of the emission, electron density and temperature distributions in the Active Region NOAA 11855. Finally, an outlook of future work based on the results presented is provided in chapter 5.

## 1.1 The Sun

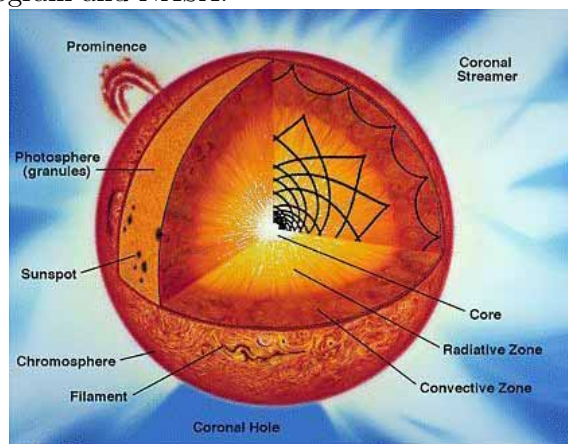
The Sun shows magnetic activity in different temporal and spatial scales. The humanity has been curious about some phenomena such as sunspots and at the general representation of the magnetic field. The sun is the closest star with spectral type G2V. It is 1.4 million kilometers in diameter and angular size against our sky, on average 32 arc minutes. It consists of hydrogen (90%) and helium (10%).

The Sun rotates in  $\approx 27$  days. This rotation was detected by observing sunspots. It has differential rotation, the equator rotating faster than the poles; the tool for knowing the velocity profile into the solar interior is the Helioseismology. The distance between the Sun and the Earth is  $1.4959787 \times 10^{11}\text{m}$ ; this value corresponds to one astronomical unit (AU). In this chapter, a brief description of solar structure, solar cycle and the solar magnetic field will be given.

### 1.1.1 Solar structure

In general the Sun is considered as stratified body composed of a core, radiative zone, convective zone, photosphere, chromosphere, transition region and corona (Figure 1.1.1).

Figure 1.1 - The solar structure. Courtesy of The International Solar-Terrestrial Physics Program and NASA.



SOURCE: NASA (2000)

The energy radiated by the Sun, specifically electromagnetic radiation (becoming an important part of this thesis) originates in the core. The Sun's core high pressure and

temperature compose the scenario to produce nuclear energy; fusion of hydrogen in helium through Proton-Proton cycle, which releases neutrinos (weakly interacting) and gamma photons (repeatedly scattered in the dense plasma). The energy flux radiated, comprising corpuscular and electromagnetic radiation, originates in the thermonuclear core (MITALAS; SILLS, 1992; STIX, 2000).

The Sun's radiative zone located directly above the core is characterized by the energy transport through radiation. The photons interact with the plasma present and these are absorbed and re-radiate.

In the convection zone energy is transported through the passage of plasma from deep in the zone to the upper layer. In this scenario hydrogen is ionized and with the effect of the opacity (plasma absorbing radiation and heating up) with depth. The movement of the fluid, ascending/descending until top/bottom of the convective zone, produces the convection cell pattern visible on the solar surface. In fact, the convection pattern shows that the radial gradient of temperature is larger than the adiabatic temperature gradient, described through the Schwarzschild criterion (ZIRIN, 1988):

$$\left| \frac{dT}{dr} \right| > \left| \left( \frac{dT}{dr} \right)_{ad} \right| \quad (1.1)$$

Where  $\frac{dT}{dr}$  is the radial gradient of temperature and  $\left(\frac{dT}{dr}\right)_{ad}$  correspond to the adiabatic temperature gradient. The heat from below can no longer be transmitted towards the surface by radiation alone, that heat is then transported by material motion.

The solar atmosphere is composed of several layers, such as the photosphere, the chromosphere and the corona. It is frequently characterized by using spherical shells, where the density is a function of the distance from the surface. In general the spherical structure is the result of the gravitational stratification (WIEGELMANN et al., 2014; ASCHWANDEN, 2005).

## Photosphere

The photosphere is the layer that emits the radiative energy flux. The solar photosphere is the visible solar surface, in general temperature decreases from  $\sim 6000K$  at the bottom of the photosphere to about  $\sim 4000K$  (SOLANKI, 2001). Here it is revealed a granular pattern (ascending warmer gas in the center of the granules and

descending cooler gas in the intergranular lanes).

Sunspots are areas of strong magnetic field; they are darker, due to the suppression of convection by magnetic field. Sunspots have lifetimes from days to three months and sizes between 5 – 50 Mm. It can be divided in two parts: umbra (dark) and penumbra (brighter). Frequently these features shows to an equatorial belt between  $\pm 35$  degrees latitude. The sunspots are often preceded accompanied by "faculae" (bright areas with intense magnetic fields) (100 – 500G) or "plage" at chromospheric levels (SOLANKI, 2003; SOLANKI, 2001).

In general the magnetic field can be measured using the Zeeman effect (the spectral lines split into many components) by polarization, where the strength of the magnetic field is proportional to the separation between lines (ZEEMAN; WINAWER, 1910).

## Chromosphere

The chromosphere is dominated by waves in the internetwork regions, specifically acoustics waves (with a period of three minutes). The magnetic flux concentrations at the photosphere coincide with the bright network at chromospheric levels.

The photospheric magnetic field is radially oriented, but the chromospheric field expands in all directions forming a **magnetic canopy**. The magnetic canopy is a layer of magnetic field located in the low chromosphere, this field is of the order of 0.001T. In general it is related to excess heating inside magnetic elements (WIEGELMANN *et al.*, 2014; STEINER, 2000). The chromospheric magnetic field can be directly measured using the infrared lines or indirectly using models and magnetic field measurements in the lower atmosphere.

## Transition Region

The transition region is a layer that separates the corona and chromosphere. This region shows a particular behaviour with a steep temperature gradient (FONTENLA *et al.*, 1993). The transition region is dominated by ions of CIV, OIV and Si IV; these ions emit in the UV. These emissions are accessible from space (Solar Maximum Mission, the Solar and Heliospheric Observatory and the Transition Region and Coronal Explorer (TRACE)) because these lines are absorbed by the Earth's atmosphere.

## Corona

The solar corona has a high temperature ( $\approx 1 \times 10^6 \text{K}$ ), but this characteristic cannot be explained by the radiative transfer from the other layers of the Sun. Different mechanisms have been proposed for explaining this phenomenon, magnetohydrodynamic waves, reconnection of magnetic field lines and nanoflares; but the coronal heating is still under debate.

The corona observed during eclipses show some components: K-corona formed with polarized continuum emission from the photospheric light of free electrons; L-corona, that contains spectral line emission from highly ionized atoms; F-corona presents absorption lines of the photospheric Fraunhofer spectrum; and T-corona caused by the thermal emission of the interplanetary dust (STIX, 2000; ASCHWANDEN, 2005).

Also, due to its dynamical activity, the solar corona subdivides as follows: (1) **active regions** with strong magnetic fields, usually these regions show closed field lines. The plasma heating in the chromosphere upflows into coronal loops, which are hotter and denser than the background corona, producing bright emission in soft X-rays and extreme ultraviolet (EUV) wavelengths; (2) **quiet sun regions** show a widely dynamics processes in different scales from nanoflares to explosive events and transequatorial loops; (3) **coronal hole regions** (CHs) are dominated by open magnetic field lines. CHs show reduced density, most of the time appear much darker than the quiet sun (GOLUB; PASACHOFF, 2009).

The coronal magnetic field can be measured using the infrared lines from the ground or from space with coronagraphs. The Fe XIII 10750Å line has been used to measure the Stokes vector in the corona, but it is not an easy task. Therefore, it is necessary to use magnetic field extrapolations from the photospheric magnetic field (more details in section 2.1.2).

The solar corona shows different configurations of magnetic field, open and closed field lines. The open magnetic field lines carry plasma into the heliosphere while the closed field lines show confined chromospheric plasma. Along the open field structures, plasma is transported outwards, allowing charged particles to escape from the solar atmosphere. During the solar activity minimum, open magnetic flux is concentrated around the poles, causing depleted regions which emit less than their surrounding temperatures above 1MK and consequently appear dark in coronal images (CHs).

Closed coronal loops connect regions with opposite magnetic polarity. Frequent connecting with neighboring ARs and/or the quiet sun surrounding and several loops are often found in magnetically complex ARs which can be related to eruptive processes such as flares or CMEs. During the solar maximum strongly emitting (bright) loop systems occupy a considerably large volume within the corona, they may be associated with eruptive phenomena (WIEGELMANN et al., 2014).

Instabilities in the coronal magnetic field cause eruptions in different scales (solar flares, jets, CMEs) and they affect the space weather. The solar coronal heating is observed in the soft X-ray (SXR) and EUV bands and it plays a critical role in controlling the thermodynamics and chemistry of the Earth's upper atmosphere (AIRAPETIAN; ALLRED, 2015; SOLANKI et al., 2013; KRESTZSCHMAR et al., 2004; MEIER, 1991).

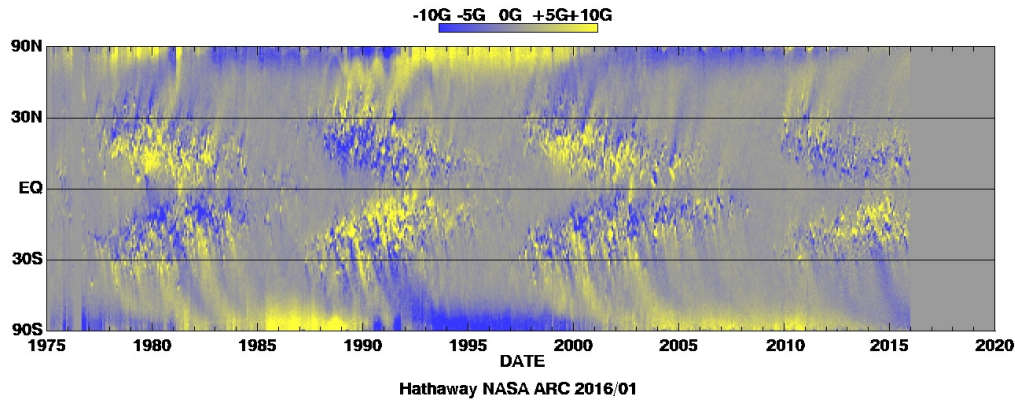
### 1.1.2 Solar cycle

Sunspots were the first features to be observed on the Sun. In general the sunspots are formed when magnetic field lines emerge through the photosphere. The observations of sunspots have revealed several characteristics such as: the Sun rotates over  $\approx 27$  days (Carrington Rotation), sunspots usually appear in groups or active regions; these active regions follow Joy's Law, which describes that sunspot groups have a tilt that change with latitude; this law provides observational evidence of the alpha effect in the solar dynamo. The Hale polarity law describes that sunspot groups have opposite polarity from north to south and these polarity changes from cycle to cycle.

Systematic observations of solar magnetic field over solar disc; specifically, synoptic maps were used to average magnetograms over each solar rotation and produce the "Magnetic Butterfly Diagram" as shown in Figure 1.2. This diagram exemplifies Hale's Polarity law, Joy's law and transport of magnetic field elements.

The sunspot and active regions numbers vary with an eleven year cycle. The sunspots tend to appear in the belt at  $\pm 35^\circ$  in latitude. At the beginning of the cycle the sunspots appear at high latitudes, while the cycle progresses the sunspots reach lower latitudes. In general the minimum of the cycle is defined when the number of sunspots over solar surface is minimum. The average cycle lasts around 11 years since it comprises the sunspot count number from minimum to minimum. In general the amplitudes of the sunspot cycle vary widely. Also, the Sun shows periods of inactivity

Figure 1.2 - A Magnetic Butterfly Diagram constructed from longitudinally and radial magnetic field obtained from Kitt Peak and SOHO (HATHAWAY, 2015).



SOURCE: HATHAWAY (2015)

like the Maunder Minimum and periods of high activity.

### 1.1.3 Solar dynamo

The generation of the solar magnetic field is associated with the magnetic dynamo, which operates into the Sun. It is believed that it operates in a region called tachocline or interface layer between the radiative zone and the convection zone. The magnetic solar dynamo can generate large-scale and small-scale magnetic field. The observation of sunspots and the discovery of solar cycle was a motivation for some scientists to search for models able to explain these phenomena (Table 1.1).

Table 1.1 - Historical review of solar dynamo theory

George Hale (1843)	Magnetic toroidal flux
Sir Joseph Larmor (1919)	Inductive action of moving fluid
E.N. Parker (1955)	Twist and helicity
Babcock and Leighton (1960)	Transformation toroidal in poloidal $\mathbf{B}$ and vice versa

SOURCE: Author

In general a model of solar dynamo must explain:

- Sunspots cycle (11-year period)
- Butterfly diagram (equator-ward drift and reversal of the polar magnetic fields)
- Hale’s polarity law
- Joy’s law

The Sun’s magnetic fields are related to differential rotation generating poloidal magnetic field from the toroidal magnetic field with the help of differential rotation. This is frequently called  $\alpha$ -effect. The generation of toroidal magnetic field from poloidal magnetic field is called the  $\Omega$ -effect.

### Solar dynamo theory

To approach the dynamo theory it is necessary to use Maxwell’s equations to obtain the magnetic field evolution. This is known as the induction equation in magneto-hydrodynamics:

$$\frac{\partial \mathbf{B}}{\partial t} = \underbrace{\nabla \times (\mathbf{U} \times \mathbf{B})}_{\text{Inductive term}} - \underbrace{\nabla \times (\eta \nabla \times \mathbf{B})}_{\text{Resistive term}} \quad (1.2)$$

Where  $\eta = \frac{1}{\mu_0 \sigma}$  is the magnetic diffusivity,  $\sigma$  is the electric conductivity,  $\mathbf{U}$  is the velocity field and the magnetic field  $\mathbf{B}$ .

The Magnetic Reynolds number  $R_m$  corresponds the ratio between the inductive and resistive term (Equation 1.2). In astrophysical plasmas  $R_m \gg 1$

$$R_m = \frac{\nabla \times (\mathbf{U} \times \mathbf{B})}{\nabla \times (\eta \nabla \times \mathbf{B})} \quad (1.3)$$

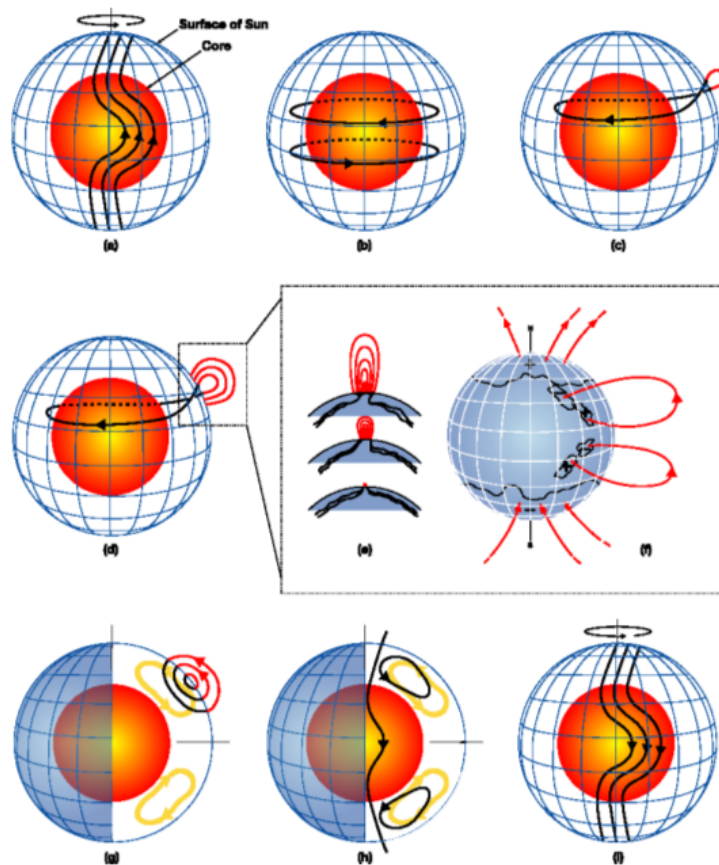
Some models of solar dynamo used a weak initial seed field, that grows exponentially in time, saturates after reaching some level of strength, as turbulent models (KÄPYLÄ et al., 2010; KÄPYLÄ et al., 2008; KÄPYLÄ et al., 2004), models that describe solar differential rotation (GUERRERO et al., 2013; GUERRERO; KÄPYLÄ, 2011),  $\alpha$ -effect, bipolar magnetic structures (WARNECKE et al., 2013), flux transport dynamo (DIKPATI; CHARBONNEAU, 1999) and dynamo models of the solar cycle in CHARBONNEAU (2010) and references therein.

## The Babcock-Leighton mechanism

The Babcock-Leighton mechanism was first developed in 1960, this mechanism considers bipolar magnetic regions. These regions are the photospheric manifestation of a toroidal field emerging as a loop. Babcock demonstrated empirically from observation that the bipolar magnetic regions decay and they show drift to higher latitudes.

The Babcock-Leighton mechanism operates on larger scales, the twist related to Coriolis force acting on the flow leads to magnetic flux tube buoyancy.

Figure 1.3 - The Babcock-Leighton mechanism.



(a) The Babcock-Leighton mechanism

SOURCE: DIKPATI and GILMAN (2009)

The Figure 1.3 shows the schematic processes from Babcock-Leighton mechanism and the relationship with the solar flux transport dynamo processes. Shearing of poloidal field by differential rotation (a), toroidal field is produced by this shear-

ing and differential rotation (b), when the toroidal field is strong enough, buoyant loops rise to the surface, twisting due to rotational influence (c). The sunspots are formed from these loops and flux emerges (d-e) and spread in latitude and longitude (f) generating open and closed magnetic field lines. Meridional flow carries surface magnetic flux poleward, causing polar fields to reverse (g) some of this flux is then transported downward to the bottom and towards the equator (h) and the cycle begins again. The reversed poloidal flux is then sheared again by the differential rotation to produce the new toroidal field opposite in sign.

The following section describes a flux-transport mechanism at the solar photosphere based on the Babcock-Leighton mechanism and the main concepts of the solar dynamo.

## 1.2 The flux transport

Solar photosphere shows a complex dynamics, transport phenomena, formation of active regions and evolution. The magnetic flux transport is very important to explain solar cycle and how the solar dynamo operates.

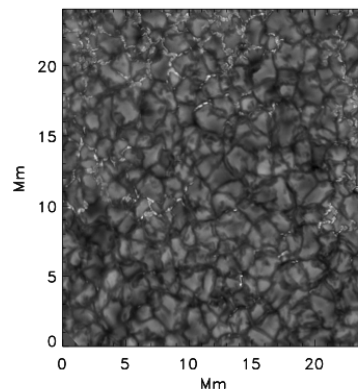
### 1.2.1 Solar flux flows

Motions of magnetic flux on the solar surface are characterized by different mechanisms such as supergranular flows, differential rotation and meridional flows. A brief description about these important concepts will be presented.

#### Supergranulation

In general, the convection is related to a large temperature gradient in the Sun's convection zone. [NORDLUND et al. \(2009\)](#) describe the granulation pattern as a feature associated with heat transport by convection, on horizontal scales of the order of a thousand kilometers, or one megameter (Mm). The granules are the dominant feature of solar surface convection (Figure 1.4). Frequently it is modelled in radiative MHD simulations, with characteristics width  $\sim 1\text{Mm}$ , lifetime  $\sim 10\text{min}$  and generation of acoustic waves.

Figure 1.4 - Image of solar granulation in the G-continuum, image from the Swedish 1m Solar Telescope and Institute of Theoretical Astrophysics, Stockholm.



SOURCE: [NORDLUND et al. \(2009\)](#)

The supergranular flows are caused by convection in the sun, acting on multiple scales. Supergranules are cellular flow pattern, with lifetime  $\sim 1\text{day}$ , width  $\sim 30\text{Mm}$ , they drive the surface shear. It was first observed by Hart (1956) and studied in more

detail later using observations and numerical hydro-and MHD-simulations (RIEUTORD; RINCON, 2010; RIEUTORD et al., 2002; NOVEMBER; SIMON, 1988; LEIGHTON, 1964). Mesogranules have intermediate size between the granules and supergranules with typical sizes of  $\sim 10\text{Mm}$  and lifetimes of hours. It was first detected by NOVEMBER et al. (1981). Giant cells appear in numerical simulations (MIESCH et al., 2008), their existence is suggested by observations (SOHO/MDI) but it has not been possible to characterize (NORDLUND et al. (2009) and references therein).

### Differential rotation

Differential rotation is a feature of the Sun, because it is not a solid body and it rotates at different rates depending on latitude and depth. It is characterized by helioseismology. The surface differential rotation is an important ingredient of flux transport, although it is known that it is rapidly changing in each solar cycle.

In 1850's Richard C. Carrington tracked the motions of sunspots on the sun, in order to create a standard reference. Carrington calculated the average synodic rotation rate of the sun. A full rotation is known as a **Carrington Rotation (CR)**.

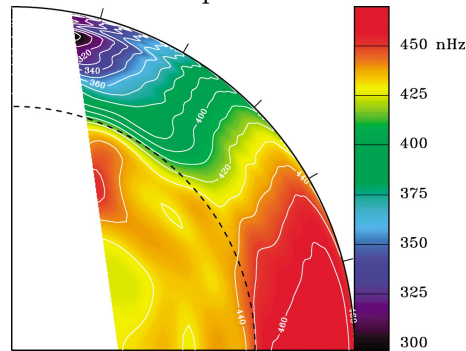
By observing the rotation rate of the sunspots, some expressions can be obtained to characterize the rotation rate. HOWARD and LABONTE (1980) measured the rotation rate using Doppler images (these measurements can be made at all latitudes), they characterized the rotation rate for each Carrington Rotation

$$\Omega(\theta) = A + B \sin^2(\theta) + C \sin^4(\theta) \quad (1.4)$$

Where  $\Omega(\theta)$  is the rotation rate,  $A, B, C$  are coefficients and  $\theta$  is latitude. They calculate the average rotation rate and subtracted this from the rotation rate measurement for each rotation and they found an oscillation pattern "torsional oscillations". In general, the torsional oscillations can describe zones starting at high latitudes and drifting towards the equator at around 22 years.

The differential rotation is important near the solar surface, because magnetic elements can be transported and can add features for magnetic flux transport. The rotation rate is faster at the equator and slower at the poles and the fluid flows from the equator to the poles at the surface (Figure 1.5).

Figure 1.5 - Internal rotation profile of the Sun inferred from helioseismology.



SOURCE: UCAR (2017)

### Meridional flows

Meridional flows from the equator towards the north and south poles have been observed on the solar surface. The poleward flow can transport the magnetic remnants of sunspots generated at low latitudes and, therefore, contributes to the cyclic polar field reversal (DWIVEDI; PARKER, 2003).

The velocities obtained with different methods are representative of the flows at different depths. In general, solar flux flow measurements can characterise the apparent motion of sunspots and granulation or in general the magnetic features (KOMM et al., 1993). It is used Doppler measurements to calculate the shift of photospheric spectral lines and obtain the velocity along the line of sight (HATHAWAY, 1996). Also, helioseismology is used to measure the rotation of global oscillation modes or difference in travel times for acoustic waves giving horizontal flows as a function of latitude, longitude and depth (BASU; ANTIA, 2010).

#### 1.2.2 Flux-transport solar dynamo

A large scale solar dynamo model was built by Parker (1955). There it was described the generation of magnetic field by a fluid with a velocity and conductivity. In general, flux transport dynamos are called  $\alpha - \Omega$  dynamos with meridional circulation. Flux-transport dynamos have three processes:

- Production of toroidal magnetic fields with help of the differential rotation ( $\Omega$ -effect)
- Regeneration of poloidal fields ( $\alpha$ -effect)
- Transport of magnetic flux by meridional circulation

The Figure 1.3 shows solar flux-transport dynamo processes. The Babcock-Leighton mechanism (section 1.1.3) is the clue to understand flux-transport dynamo solution.

### 1.2.3 Surface flux transport models

The aim of magnetic flux transport models is to simulate how the flux is transported to the solar surface. It is considered the contribution due to flows and velocities on large scales to correspond to the differential rotation and meridional flows. On smaller scales, the contribution is believed to be related to convective processes on granular and supergranular scales.

It is important to have the knowledge of the solar magnetic field in different scales with high resolution observations. It can be achieved by characterizing the evolution of the magnetic field. In general the magnetic flux transport is characterized by large-scale axisymmetric flows (differential rotation and meridional flows), smaller scale non-axisymmetric flows (granules, supergranules, flows in active regions) and diffusion of the radial component of the magnetic field.

#### Standard model

The standard model of magnetic flux transport is obtained from the radial component of the magnetic induction equation under some assumptions:  $v_r = 0$  and  $\frac{\partial v}{\partial r} = 0$  (alternatively, the magnetic flux transport equation may be obtained through spatially averaging the radial component of the induction equation (McCLOUGHAN; DURRANT, 2002; DeVORE et al., 1984)). These assumptions can be related with the radial component on a spherical shell having a fixed radius; and the time evolution of the radial field component is decoupled from the horizontal field components.

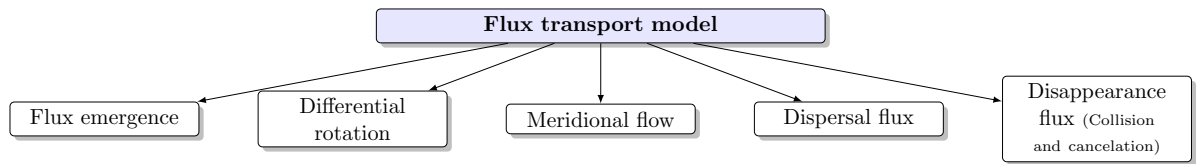
The evolution of radial magnetic field  $B_r$  at the solar surface  $R_{sun} = 1.00$

$$\frac{\partial B_r}{\partial t} = \frac{1}{\sin\theta} \frac{\partial}{\partial \theta} \left( \sin\theta \left( -u(\theta)B_r + D \frac{\partial B_r}{\partial \theta} \right) \right) - \Omega(\theta) \frac{\partial B_r}{\partial \phi} + \frac{D}{\sin^2\theta} \frac{\partial^2 B_r}{\partial \phi^2} + S(\theta, \phi, t) \quad (1.5)$$

where  $\Omega(\theta)$  is the surface flows of differential rotation,  $u(\theta)$  is the meridional flow,  $D$  is the isotropic diffusion coefficient in general representing the supergranular diffusion,  $S(\theta, \phi, t)$  is a source term to represent the emergence of new magnetic flux (JIANG et al., 2014; MACKAY; YEATES, 2012).

The differential rotation is related to sheared magnetic fields in an east-west direction. In general the strongest shear occurs at mid-latitudes and produces bands

Figure 1.6 - Flux transport model ingredients.



SOURCE: Author

of alternating positive and negative polarity. On the other hand, the supergranular diffusion represents the effect of the large-scale magnetic field of the convective motions of supergranules. The meridional flows represent an observed weak flow of magnetic flux from the equator to the poles in each hemisphere. The magnetic flux emergence represents a contribution to the radial magnetic field from the emergence of new magnetic bipoles.

The evolution of the photospheric magnetic field is commonly used as the boundary condition for extrapolating the coronal and heliospheric magnetic fields and the surface evolution gives us insight into the dynamo process. In particular, it plays an essential role in the Babcock-Leighton model of the solar dynamo. Describing this evolution is the aim of the surface flux transport model (JIANG et al., 2014).

The following section describes the magnetic flux transport model of SCHRIJVER (2001). This model is used for modelling coronal electron density and temperature profiles from the photospheric magnetic field.

### Magnetic flux transport from SCHRIJVER (2001)

The large scale solar magnetic field is successfully modelled using the surface diffusion model for the evolution of magnetic flux over the solar surface.

Schrijver formulated numerical recipes for flux transport based on solar observations (Figure 1.6). The diffusion model is used in all scales, also the flux injection is described by a combination of random processes, capturing the properties of emerging flux. He described three important ingredients for the simulations of the magnetic field:

- The flux emergence from the interior

- The flux dispersal over the surface
- The disappearance of flux in the photosphere

After the flux in a bipolar region has fully emerged, the region decays and the flux disperses across the surface. The flux dispersal in the photosphere is frequently modelled as a passive random walk diffusion, involving supergranulation, meridional flow and differential rotation.

Schrijver modified the standard model (section 1.2.3) to include the small and ephemeral regions to estimate the flux outside the plages and the interaction of individual concentrations, including fragmentation and the collision of flux concentrations as well as the flux disappearance from the photosphere in cancellation collisions.

Source function for bipolar regions is approximated by the sum of two power laws:

$$n(S, A)dSdt = \left( a_o A S^{-p} + a_1 A^\alpha S^{-p-1} \right) dS dt \quad (1.6)$$

where  $A$  is the flux injection parameter (different levels of activity),  $S$  correspond to the number density per hemisphere, per day, per square degree in area. At the cycle maximum the coefficients  $a_o = 8$  and  $p = 1.9$  are determined by a fit to the area distribution for emerging active regions,  $a_1$  is set to  $8 \text{ deg}^{-2} \text{ day}^{-1} \text{ hemisphere}^{-1}$ , through a power-law scaling with the flux emergence parameter  $A$  with a power law index  $\alpha = \frac{1}{3}$ .

Differential rotation ( $\Omega(\theta)$ ) and meridional flow ( $M(\theta)$ ) are described:

$$M(\theta) = m[12.9 \sin(2\theta) + 1.4 \sin(4\theta)] \quad [m \text{ s}^{-1}] \quad (1.7)$$

$$\Omega(\theta) = d[\Omega_o - 1.95 \sin^2(\theta) - 2.17 \sin^4(\theta)] \quad [deg \text{ day}^{-1}] \quad (1.8)$$

where  $d$  and  $m$  are adjusted from the model of SCHRIJVER (2001), Table 1 and  $\theta$  is latitude.

The dispersal of flux  $\Delta r$  and magnetoconvective coupling are described following:

$$\Delta r = C(|\Phi|)\sqrt{4D(|\varphi|)\Delta t} \quad (1.9)$$

at each step all flux concentrations are moved in a random direction on a sphere, with a step length that is determined by characteristic flux dispersal coefficient  $D$  and the time step  $\Delta t$ ,  $\Phi$  is the flux contained in the concentration and  $\varphi$  is the average flux density in the neighborhood of the concentration. The flux dispersal coefficient  $D(|\varphi|)$  depends on the local average flux density  $|\varphi|$  (all fluxes in Mx). The function  $C(|\Phi|)$  is the magnetoconvective coupling. The relationship between velocity and flux dispersal is parametrized as an exponential function:

$$C(|\Phi|) = 1.7 \exp\left(\frac{-|\Phi|}{3 \times 10^{19}}\right) \quad (1.10)$$

The relation between flux density ( $\phi$ ) from the photosphere and flux from outer radiative chromospheric diagnostic can be expressed as:

$$F_i = a_i |\phi|^{b_i} \quad (1.11)$$

where  $F_i$  corresponds to flux density, for a chromospheric diagnostic  $b_i \approx 0.6$ . The flux densities are computed by weighting the expected intensities  $I_i(|\phi|)$  from small areas, and in general they exclude sunspots because the atmospheric emission are considered weak over sunspots.

In general the flux transport model from [SCHRIJVER \(2001\)](#) describes the dynamics of the solar photosphere, given a source function for bipolar regions, differential rotation, meridional flow, dispersal flux, and specified dynamics of flux concentration (collision and fragmentation). This model will be applied to estimate electron density and temperature profiles in the solar corona from the solar cycle 23 to solar cycle 24.

### 1.3 Radiative process in the solar corona

The solar spectrum is a continuous spectrum. It behaves as a black body with a temperature of 5800K; due to the photosphere, the plasma is dominated by collisions, then it behaves approximately like a blackbody emitter. The blackbody spectrum appears from the wavelength dependence of the opacity and the temperature gradient; then the radiation formed in different heights is related to different wavelengths and consequently different temperatures.

The solar atmosphere is composed of light elements such as hydrogen and helium, which are completely ionized. Heavier elements are present too but they are partially

ionized, depending on the temperature.

Some processes by which coronal electrons are accelerated and emit radiation, such as the acceleration by the electromagnetic field of photospheric radiation (scatter radiation), interaction between electrons, protons and ions (free-free emission) and electron capture (free-bound emission), are described in details in the next section.

### 1.3.1 Atomic processes in the solar corona

Some atomic processes that contribute to the continuum and line emission are described as follows:

- **The induced absorption** is a type of bound-bound transition, which produces absorption lines in solar corona (optical wavelengths and UV), in which a photon can excite an electron in an atom to a higher energy state.
- **Thompson scattering** is an important process in the solar corona, where photons are scattered off by electrons of the coronal plasma and produce the white-light corona (visible during solar eclipses). This process do not depend on the wavelength and the usual name is K-corona. The first method used to measure the electron density in the solar corona was the Thompson scattering, whose rate in general is proportional to the electron density.
- **Free-free emission** also called Bremsstrahlung, essentially occurs when a free electron of the coronal plasma is elastically scattered off by an ion and escapes as a free electron. Then, a photon is emitted, according to the principle of energy conservation, because the energy of the emitted photon is only positive when the electron loses energy. The free emission from the chromosphere and corona is related to the emission in microwaves, soft X-rays and hard X-rays during flares.

Hot plasmas, such as the coronal gas or in the laboratory such as Tokamak machine radiate energy, especially if they contain a fraction of heavy elements. The EUV spectra also contain emission lines of highly ionized metals that carry information about the solar chromosphere, transition region and corona. EUV emission is produced by free-free emission, by scattering off ions with lower temperatures from FeIX to FeXV. The solar corona is fully ionized. Then, the electrons and ions move freely, interacting with each other.

Then, continuum radiation is formed by free-free and bound-free processes. The spectral lines are formed by bound-bound process, and different heights depending of abundance of the species (YEO, 2014). In the following sections it is described the emission measurements of the solar corona and its chemical composition, which are important concepts for this thesis.

### 1.3.2 Chemical composition in the solar corona

In general spectroscopic diagnostics in the solar plasma need to know the intensity  $I(\lambda_{ij})$  of an optically thin spectral line of wavelength  $\lambda_{ij}$  as:

$$I(\lambda_{ij}) = \frac{h\nu_{ij}}{4\pi} \int N_j A_{ij} dh_1 \quad (1.12)$$

where  $i, j$  are lower and upper levels,  $A_{ij}$  is the spontaneous transition probability,  $N_j$  is the number density of the upper level  $j$  of the emitting ion and  $h_1$  is the line of sight through the emitting plasma and  $dh_1$  is line of sight differential.

The number density  $N_j(X^{+m})$  is usually obtained using the hydrogen abundance relative to the electron density  $\frac{N(H)}{N_e}$ , the abundance of element  $X$  relative to hydrogen  $\frac{N(X)}{N(H)}$ , the fraction of element  $X$  at ionization stage  $+m$ ,  $\frac{N(X^{+m})}{N(X)}$  and the fraction of atoms of element  $X$  at ionization stage  $+m$  in a level  $j$ ,  $\frac{N_j(X^{+m})}{N(X^{+m})}$ . The number density in each level  $j$  can be expressed as:

$$N_j(X^{+m}) = \frac{N_j(X^{+m})}{N(X^{+m})} \frac{N(X^{+m})}{N(X)} \frac{N(X)}{N(H)} \frac{N(H)}{N_e} N_e \quad (1.13)$$

The term  $\frac{N(X^{+m})}{N(X)}$  is related to the fraction of element  $X$  which is  $m$ -times ionized, in the ionization stage  $X^{+m}$ . The ionization equilibrium for a volume of plasma at some temperature  $T$ , in solar corona a low density, high temperature plasma, occurs by collision with free electrons. When the ionization equilibrium is calculated and it is possible to obtain curves of the fractional abundances.

The abundances of elements of the corona determine the opacity of the atmosphere and characterize the heating process. It has played an important role in atomic physics equations for the coronal emission lines.

The chemical composition of the Sun has been measured more accurately in the photosphere, where the line emission is brightest, while measurements of elemental abundances in the corona are much less sensitive, due to the corona being many orders of magnitude weaker. The chemical composition in the photosphere and the

corona are largely similar for most of the elements, and are also consistent with the cosmic abundances, as they have been measured from chemical analyses of meteorites and by comparison of the white light scattered by the corona during eclipses with the brightness of the optical emission lines.

The strength of the emission of a spectral line of a given element in the corona depends directly on the abundance of that element in the emitting region (GOLUB; PASACHOFF, 2009). Hydrogen and Helium are the principal chemical elements in the corona, but extending abundance measurements to the other elements, it is evident, such as the abundance is a function of the first ionization potential (FIP). The FIP effect can be related to the transport process of chromospheric plasma upward into coronal structures. These effects show the enhancement or depletion, respectively, in coronal abundance with respect to photospheric values of elements with FIP below 10eV (LAMING, 2015); this is an important question in solar physics.

The choice of abundances is complicated by the apparent increase of low first ionization potential elements between the photosphere and the corona. Coronal temperatures are contributing to the irradiance or emission lines from low-FIP elements (Fe, Si and Mg), the transition regions and chromosphere contribute to the solar EUV irradiance from high-FIP elements (C, N, O, H, He and Ne) (WARREN et al., 1998).

The important characteristic of the corona is the high temperature and consequently the state of extreme ionization. The ionization equilibrium is the common method used to calculate the relative line strengths in the coronal plasma. The ionization equilibrium in the corona is an equilibrium between collisional ionization and radiative and dielectronic recombinations. The ionization equilibrium defines the number of bound-bound transition in a plasma expressed by the Saha equation:

$$\frac{N_k}{N_o} = \frac{2}{n_e} \frac{(2\pi m_e k_B T)^{3/2}}{h^3} \frac{g'_k}{g_o} \exp\left(-\frac{\epsilon_k}{k_B T}\right) \quad (1.14)$$

This equation is an expression that relates the ionization state of an element to the temperature and density, the population ratio is  $\frac{N_k}{N_o}$  for a ionization state  $k$ ,  $n_e$  is the electron density. Also, it is possible to generalize two different states  $k$  and  $k + 1$  in the corona

$$\frac{N_{k+1}}{N_k} = \frac{2}{n_e} \frac{(2\pi m_e k_B T)^{3/2}}{h^3} \frac{g_{k+1}}{g_k} \exp\left(-\frac{\epsilon_{k+1} - \epsilon_k}{k_B T}\right) \quad (1.15)$$

where  $n_e$  is the free electron number density,  $h$  is the Planck constant, the statistical weight of an ion in the upper ionization state is  $g_{k+1}$  and the statistical weight of an ion in the lower ionization state is  $g_k$ . The energies of two states  $\epsilon_{k+1}$  and  $\epsilon_k$ ;  $k_B$  is the Boltzman constant.

Some models of the ionization equilibrium are available in CHIANTI atomic database 8.0 released, sept, 2015<sup>1</sup>, this database consist of atomic data to calculate the spectra from astrophysical plasmas.

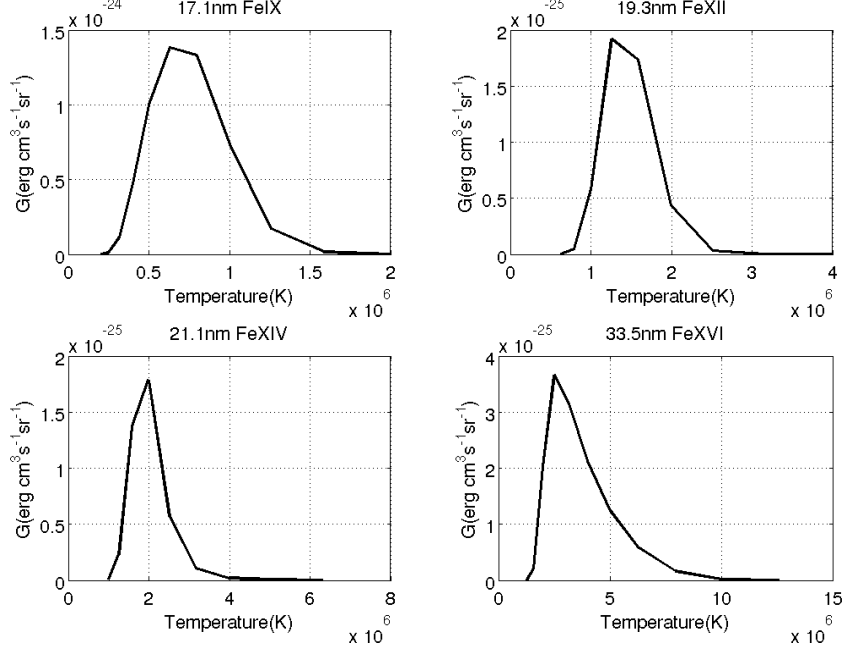
The ionization equilibrium has been taken from the tabulated values in the published literature such as Arnaud and Raymod (1992), Arnaud and Rothenflug (1985) and MAZZOTTA et al. (1998). It consist in collecting ionization and radiative, dielectronic recombination rates using data from space observatories.

Some models are available to compute the solar standard composition such as Grevesse and Sauval (1998), Schmelz et al.(2012) and MEYER (1985). They consist of a solar mixture of metals, based on photospheric abundances, convection zone helium abundance. Also, these models considered the solar corona such as an optical thin layer and this way are free of the problem of radiation transfer. The solar wind and spectroscopic data were considered and specifically forbidden lines of highly excited atoms in the visible wavelengths and first ionization potential were used, because the hydrogen is completely ionized at high coronal temperatures.

---

<sup>1</sup><http://www.chiantidatabase.org/>

Figure 1.7 - Contribution function from CHIANTI atomic database 8.0, using ionization equilibrium from MAZZOTTA et al. (1998) and coronal abundances from MEYER (1985), in different wavelengths at 17.1nm, 19.3nm, 21.1nm and 33.5nm.



SOURCE: Author

The ionization equilibrium from MAZZOTTA et al. (1998) and coronal abundances from MEYER (1985) are important ingredients to build the solar spectrum and modelling the electron density and temperature through the solar corona.

The emission measure analysis, for a specific spectral line, considering transition, coronal abundance and ionization equilibrium can describe the intensity at a distance  $R$  from the Sun:

$$I(\lambda_{ij}) = \frac{1}{4\pi R^2} A_X \int G(T, \lambda_{ij}) N_e^2 dV \quad [\text{erg cm}^{-2} \text{s}^{-1} \text{sr}^{-1}] \quad (1.16)$$

where  $G(T, \lambda_{ij})$  [ $\text{erg} \cdot \text{cm}^3 \text{s}^{-1} \text{sr}^{-1}$ ] is called the Contribution function and contains all of the relevant atomic physical parameters such as ionization equilibrium and coronal abundances. Also, this function is strongly peaks in temperature (Figure 1.7) (GOLUB; PASACHOFF, 2009). It is possible to calculate the Contribution function from CHIANTI atomic database 8.0 and using ionization equilibrium and coronal

abundances and using the specific wavelength. The Figure 1.7 shows the contribution functions from using ionization equilibrium from MAZZOTTA et al. (1998) and coronal abundances from MEYER (1985) at different wavelengths.  $A_X$  corresponds to the abundance relative to the hydrogen.

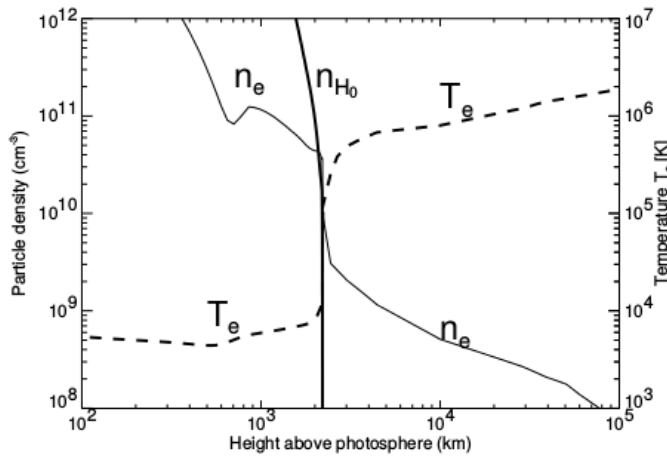
The term  $N_e^2 dV$  is generally defined such as Differential Emission Measure (DEM), correspond to the measure of the emitting material as a function of temperature in the coronal plasma, in principle DEM can be derived from the integral equation 1.16.

In the following section, I will give a description of the electron density and temperature in the solar corona and a brief description about some models.

## 1.4 Electron density and temperature in the solar corona

The electron density and temperature profiles can yield important information about the dynamics and the characteristics of the solar corona and their variations in different time scales. The problem of high temperatures in solar corona has been of interest and it is still a fundamental problem in astrophysics. The Sun's photosphere is at a temperature of  $\sim 5,800\text{K}$ . However, the transition region shows a sharp rise in temperature ( $> 10^6\text{K}$ ). The transition region is the boundary where the density is about of several orders of magnitude if compared to the coronal values (Figure 1.8).

Figure 1.8 - Electron density and temperature model of the chromosphere (Fontenla et al. 1990; Model FAL-C) and lower corona (Gabriel 1976)



SOURCE: ASCHWANDEN (2005)

Also, another problem is the observational diagnostic because the computation is based on the distribution of matter along the line of sight. It is important to build models to describe the density and temperature distributions in the solar corona in large and small scale and obtain physical information of the solar atmosphere during the solar cycle and their relation with the heliosphere and the Earth's atmosphere. In this chapter, I will give a brief description of the electron density and temperature distributions and some techniques and models to quantify these parameters.

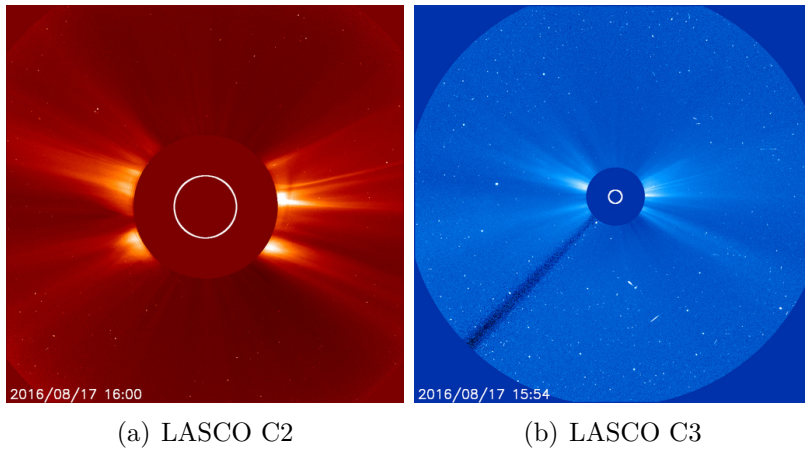
### 1.4.1 Electron density distribution in the corona

The density distribution in the corona is very complicated and it is described in qualitative terms. The distribution is inferred as a function of height at minimum and maximum of solar cycle, and compared to the poles and to the equator. The coronal electron density can be measured from ground-based (white-light and using frequency of radio bursts) and space-borne (EUV and soft X-rays data using the emission measure) observations.

Measurements of polarized continuum intensity during solar eclipses and white-light (due to Thompson scattering, Section 1.3.1) images of the corona have been used in determining the electron density in the solar corona. In general, the coronal densities can be determined from eclipse data using different intensities of the continuum in the K-corona (NEWKIRK JR., 1961), electron density distributions in equatorial and polar regions, streamers and coronal holes (KOUTCHMY et al., 1991) (Table 1.2) and employing spectrographic observations from different coronagraph of several coronal regions in different wavelengths and frequently using an intensity ratio of Fe lines (HABBAL et al., 2010; SINGH et al., 2002; HAYES et al., 2001; GUHATHAKURTA et al., 1992).

Coronagraph images can be employed to measure the electron density distributions and they can help to characterize some events such as Coronal Mass Ejections (CMEs), helmet streamers and polar plumes. The Large Angle Spectrometric Coronagraph (LASCO) take images of the solar corona by blocking the light coming from the solar disc, creating an artificial eclipse. The LASCO C2 image shows the inner solar corona up to  $8.4 \times 10^6$ km and C3 have a large field of view, 32 solar radii (Figure 1.9).

Figure 1.9 - Coronagraph images from Large Angle Spectrometric Coronagraph (LASCO) Aug.17 (2016) (a) LASCO C2 image and (b) LASCO C3 image.



SOURCE: SOHO - Solar and Heliospheric Observatory (2017)

Table 1.2 - Typical density values  $N$  in the solar atmosphere.

Open field regions Coronal Holes [ $cm^{-3}$ ]	Close field quiet-sun corona [ $cm^{-3}$ ]	Coronal streamers [ $cm^{-3}$ ]	Active Regions ARs [ $cm^{-3}$ ]	Upper corona [ $cm^{-3}$ ]
$0.5 - 1.0 \times 10^8$	$1.0 - 2.0 \times 10^8$	$3.0 - 5.0 \times 10^8$	$2 \times 10^8 - 2 \times 10^9$	$10^6 - 10^7$

SOURCE: ASCHWANDEN (2005)

Problems with the electron density measurements can be attributed to the presence of Fraunhofer lines, and the decrease of polarization with the radial distance (ALLEN, 1947). In the following section, a brief review of density distribution models will be presented.

### Density models

Density models were developed using observational data from eclipses and empirical laws relating with the coronal brightness and height. The first method to measure the electron density in the solar corona was the Thompson scattering (section 1.3.1). The Table 1.3 shows the historical models used to determine the density distribution and main expressions used to calculate density in the solar corona.

Table 1.3 - Some density models using observational data and analytical expressions

Model	Description
Saito (1950)	F corona is constant in solar cycle (an acceptable description to zodiacal-light observations) <sup>2</sup> ( $N(r) = 10^8 \left[ \frac{1.93}{r^2} + \frac{1.47}{r^{16}} \right]$ ).
Van de Hulst (1950)	It was the first to perform a global corona reconstruction using eclipse images and confirming N decrease from sunspot maximum to minimum, where $J$ is the mean source function ( $N = 9.6 \times 10^5 J$ ).
Pottasch (1960)	Model of corona for the equatorial sunspot minimum and incorporated eclipse observations, from the chromosphere to $R_{sun} = 10$
Ingham (1961)	Model for the sunspot minimum, equatorial corona for $r > R_{sun} = 6$ ( $N = \frac{6.75 \times 10^6}{r^3}$ ).
Newkirk (1961)	Explain the variation in polarization in coronal enhancements, it is considered density enhancement in the active regions as Gaussian function (where $N_Q = N_o \times 10^{4.32/r}$ , $N_o = 4.2 \times 10^4$ and $\beta$ is the distance from the axis of ARs) ( $N = N_Q [1 + C \exp(-\beta^2/2\sigma^2)]$ ).

SOURCE: BILLINGS (1966)

The density profiles in the solar atmosphere specifically above the photosphere, in the transition region shows an increase boundary where the density increase, but at the coronal region the density profiles decrease. Chromospheric density models were based on the abundances and EUV lines, radiative transfer (VERNAZZA et al., 1981) and diffusion (FONTENLA et al., 2011). These profiles show regions that are consistent with the eclipse measurements at low altitude above the limb ( $\sim 100$ Mm or  $\sim R_{sun} = 1.15$ ) (GUHATHAKURTA et al., 1992; HABBAL et al., 2010).

### 1.4.2 Temperature in the solar corona

The electron temperature is commonly derived from the intensity ratios of collisionally excited spectral lines observed in EUV generally limited to the distance. The electron temperature maps can also be obtained; and they can be related to bulges of streamers, open magnetic structures and the solar wind. Some typical values of temperature at different regions are described in Table 1.4.

<sup>2</sup>Corresponding to diffuse white glow seen in the night sky, appear in the vicinity of the Sun along the ecliptic, and it is caused by scattered sunlight.

Table 1.4 - Typical temperature values  $T$  in the solar corona.

Open field regions Coronal Holes (CHs) [K]	Close field quiet-sun corona [MK]	Active regions ARs [MK]	Strong Flares [MK]
$10^5$	$\approx 1$ to 2	up to 2 to 6	10 to 20

SOURCE: (WIEGELMANN et al., 2014; ASCHWANDEN, 2005)

The coronal loops can help to describe temperature in the solar corona as follows: Cool loops are generally detected in EUV lines at temperatures  $1 \times 10^5 - 1 \times 10^6$  K. Warm loops are observed by EUV imagers SDO/AIA, SOHO/EIT and TRACE (Table 1.5) as confined plasma with temperatures 1 – 1.5MK. Hot loops are typically observed in X-ray band, UV and EUV lines (FeXVI) and EUV 33.5nm with temperatures 2MK. Cool plasma at temperature  $T < 0.5$ MK might contribute considerably to the emission, especially at the loop footpoints and it can be related with upflows observed in the 17.1nm band of millions degrees plasma (REALE, 2014; TRIPATHI et al., 2008).

Table 1.5 - Typical temperature in some specific wavelengths

Wavelength (nm)	Temperature (K)	Characteristics
17.1	$1 \times 10^6$	Quiet corona and upper transition region
19.3	$1.25 \times 10^6$	Corona and hot flare plasma
21.1	$2.6 \times 10^6$	Active regions of the corona
33.5	$2.8 \times 10^6$	Active regions of the corona

SOURCE: The South Florida Amateur Astronomers Association and the Fox Observatory at Markham Park (2003-2017)

A brief review of methods and models to quantify the coronal temperatures will be presented.

### Temperature methods and models

The coronal temperatures can be measured using different methods such as the degree of ionization, line profiles or from density distributions and space measurements.

The Table 1.6 shows the main ideas and expressions frequently used to determine the temperature in the solar corona.

The temperature by degree of ionization  $\frac{N_{XIV}}{N_X}$ , is computed using two different coronal lines with different states of ionization usually Fe XIV 5303Å (green line) and Fe X 6374Å (red line) in works such as Schwartz (1959), Billing and Lehman (1962) and Firor and Zirin (1962). The radio wavelength method of measuring coronal temperature, considers the fact that the apparent temperature of the Sun increase with the wavelength and related it to an increase in the contribution to the emission from the solar corona. In general this method uses Planck function of coronal and chromospheric temperature, and the optical depth (GOLUB; PASACHOFF, 2009; MACRIS, 1971; BILLINGS, 1966).

The Temperature can be inferred from density distributions assuming that the corona is in hydrostatic equilibrium or using an idea of Parker (1960) considered the non-hydrostatic equilibrium, considered the corona is expanding and accelerated, and T is known from a density distribution. The scale-height method (shm), is based on electron density profiles inferred from white light measurements of the corona during solar eclipses (GOLUB; PASACHOFF, 2009; MACRIS, 1971; BILLINGS, 1966).

In the early 70's the space probe Skylab with an X-ray telescope was studying some characteristics of the solar corona such as temperature and density, in specific elements such as coronal holes and coronal bright points. The SOHO and TRACE satellites obtaining observations of the Sun's corona, provide images in different wavelengths and using data from coronagraphs.

Table 1.6 - Temperature from some methods and using observational data

Method	Description
Ionization degree	Use the rate between two lines, the main assumption is the ratio emission ( $\frac{I_{\lambda 5303}}{I_{\lambda 6374}}$ ) is constant along the line-of-sight ( $\frac{I_{\lambda 5303}}{I_{\lambda 6374}} = 2.4 \frac{N_{XIV}}{N_X} e^{-\frac{4.63 \times 10^3}{T}}$ ).
Line profiles	It is considered the kinetic temperature, atomic parameters and Doppler half-width ( $T = \frac{m_j c^2 (\Delta \lambda_D)^2}{2k}$ ).
Radio temperature	This technique considers transfer equation with parameters such as optical depth ( $\tau_c$ ), and Planck function of corona $T_c$ and chromospheric $T_{ch}$ temperature ( $I_{Em} = B(T_c)(1 - e^{-\tau_c}) + B(T_{ch})e^{-\tau_c}$ ).
Density distributions	Hydrostatic equilibrium is considered or a hydrodynamic description <sup>3</sup> , variations are made using some simplifications. $T_1$ is the acceleration of the gravity at the solar surface and $(1/x)$ a spatial interval, ( $\frac{T_1}{T} = \frac{d}{d(1/x)} \ln N + \frac{d}{d(1/x)} \ln T$ ).
Space-Probe	Provides images and using coronagraphs is possible to know the kinetic temperature using DEM method and studying coronal loops.

SOURCE: BILLINGS (1966)

Recently more models of the temperature in the solar atmosphere have been developed using many features in the solar photosphere. Temperature profiles in the solar atmosphere from FONTENLA et al. (2014), FONTENLA et al. (2011), calculated for different solar features: dark quiet sun inter-network, quiet sun inter-network, quiet sun network lane, enhanced network, plage, facula and hot facula.

## 1.5 Solar data

Solar space missions began around 1960 with the purpose of understanding the origin of dynamics phenomena of the Sun. To achieve this goal, observations were carried out in several wavelengths, such as ultra-violet (UV) and extreme ultra-violet (EUV) imaging, together with X-ray and gamma-ray spectroscopy. In the subsequent decades, important missions were launched and provided information about the temperature and density of the hot plasma, and about the motions of the plasma along the line of sight; they also explored events involving magnetic

<sup>3</sup>The hydrodynamic equation  $\frac{1}{T} \frac{dT}{dr} = -\frac{1}{N} \frac{dN}{dr} - \frac{\mu}{kT} (g + v \frac{dv}{dr})$ , where  $\mu$  is the mean particle mass,  $v$  is the rate of radial expansion of the corona.

reconnection.

The increasing resolution achieved in the instruments described above, stimulates the use of techniques and models to obtain a description of the EUV emission for better description of phenomena present in the solar corona and their relation with space weather.

### 1.5.1 Photospheric magnetic field

The longitudinal (or line-of-sight) magnetic field is measured using the Zeeman-Doppler shift of a photospheric line. Some missions search for magnetic field changes in the photosphere such as the HINODE mission with the Solar Optical Telescope (SOT), the Solar and Heliospheric Observatory (SOHO) with the instrument Michelson Doppler Imager (MDI) and the Solar Dynamics Observatory (SDO) with the instrument Helioseismic and Magnetic Imager (HMI). In this thesis we use the SOHO/MDI and SDO/HMI data, as an inner boundary to extrapolate coronal magnetic field (PFSS/SSW).

#### The Solar Dynamics Observatory (SDO)

The Solar Dynamics Observatory (SDO) was designed to study several aspects of the Sun: the internal structure of the sun; features present in the solar atmosphere such as the quiet sun, the solar wind, active regions, bright points; the origin of the solar wind, flares, CMEs, the solar cycle; the total solar irradiance; and attempt to understand the complex interactions between the Sun and the Earth.

SDO has scientific instruments such as the Atmospheric Imaging Assembly (**AIA**), the EUV Variability Experiment (**EVE**) and the Helioseismic and Magnetic Imager (**HMI**) (PESNELL et al., 2012; SCHERRER et al., 2012; WOODS et al., 2012).

#### The Helioseismic and Magnetic Imager (HMI)

The Helioseismic and Magnetic Imager (HMI) observes the full solar disc at FeI at 6173Å (Table 1.7). HMI is a successor of the Michelson Doppler Imager (MDI) aboard the Solar and Heliospheric Observatory (SOHO).

HMI obtains filtergrams in various positions at the 6173Å spectral line and a set of polarizations. The basic observables are full-disc Doppler velocity, a continuum brightness proxy, line-of-sight magnetic field, and vector magnetic field. HMI pro-

vides temporal resolution to Doppler velocity and longitudinal magnetogram 45-second cadence; and vectorial magnetogram 90-second cadence. The basic vector magnetic field quantity is an array of 24 filtergrams (six wavelengths, four Stokes parameters) averaged over 12 minutes (SCHERRER et al., 2012).

The Helioseismic and Magnetic Imager has as scientific goals, the study of tachocline, meridional circulation, differential rotation, active regions, sunspots and flux emergence, convection zone dynamics and solar dynamo. Frequently these data are used in coronal magnetic field extrapolations. The vector magnetic field is derived from

Table 1.7 - The HMI instrument characteristics.

Primary diameter	14cm
Effective focal length	4.125 m
Pixel size/Resolution	0.5 arcsec
CCD detector	4096 × 4096 pixels
Wide spectral band	76mÅ

full-disc filtergrams collected in a 135-second cadence. The observations are obtained in polarized light at several wavelengths across a spectral line <sup>4</sup>. Additionally, SDO/HMI provides products for Space Weather: vector field in HMI Active Region Patches (HARPS) and tracked Space-weather HMI Active Region Patches (SHARPS), for the study of specific active regions ARs.

### Magnetograms and synoptic Maps

The line-of-sight magnetic field is computed from the difference of the wavelengths observed in two circular polarizations. The line-of-sight mode with the cadence of 45s uses twelve filtergrams combined in each circular polarization and wavelength<sup>5</sup>.

The magnetic synoptic map is a proxy of the entire surface distribution of the photospheric magnetic field. The synoptic map of the solar magnetic field is assembled from individual magnetograms observed over the course of a solar rotation  $\pm 27$  days. The Carrington Synoptic maps were constructed over a Carrington Rotation and it is assumed that the photospheric magnetic field is stable over one solar rotation and rotating rigidly. In general the magnetograms are remapped, converting magnetic field from the circular disc plan into cylindrical surface in heliographic coordinates

<sup>4</sup>[http://jsoc.stanford.edu/HMI/Vector\\_products.html](http://jsoc.stanford.edu/HMI/Vector_products.html)

<sup>5</sup><http://jsoc.stanford.edu/jsocwiki/MagneticField>

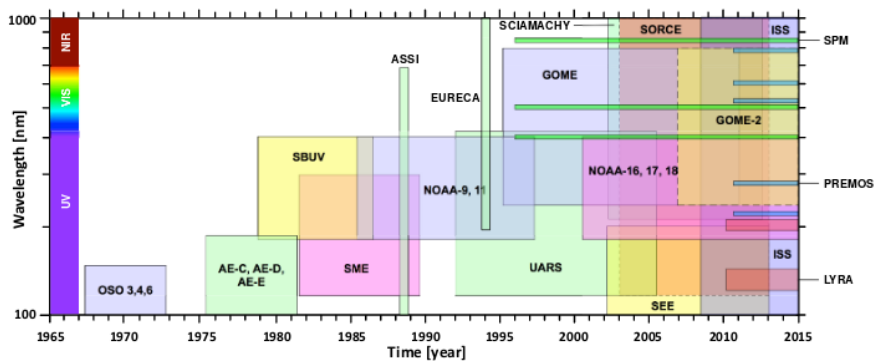
(latitude ( $\theta$ ) and longitude ( $\phi$ ))(WORDEN and HARVEY (2000) and references therein).

Synoptic maps from HMI are computed from line-of-sight magnetograms, assembled by the combining the 20 best observations nearest to central meridian at each longitude. Synoptic maps are provided as line-of-sight and inferred radial field<sup>6</sup>.

### 1.5.2 Solar Spectral Irradiance (SSI)

Solar irradiance can be defined as the radiation generated by the Sun and received by the Earth (1 UA). This radiation covers a widely range of wavelengths, frequently named Solar Spectral Irradiance (SSI). The Total Solar Irradiance (TSI) is composed of spectral solar irradiance. Satellite observations were made since the 1960s. However, there are many gaps in the observations, because the SSI instruments show degradation of their detectors and have a limited lifetime. The Figure 1.10 shows the satellite observations from 1962 to 2015, in EUV, UV, VIS and NIR wavelengths.

Figure 1.10 - Time and wavelength of available SSI measurements



SOURCE: ERMOLLI et al. (2013)

The Solar Spectral Irradiance data (TIMED/SEE) were used in this thesis are described in the following section.

### TIMED/SEE

TIMED mission has as scientific objective to understand the energetics in the mesosphere, lower thermosphere and ionosphere. The daily measurement of the full-disc

<sup>6</sup><http://jsoc.stanford.edu/jsocwiki/MagneticField>

solar ultraviolet irradiance by the Solar EUV Experiment (SEE) are registered. The SEE instrument was developed at the Laboratory for Atmospheric and Space Physics (LASP) at the University of Colorado <sup>7</sup>. SEE is accurate to determine the solar irradiance and variability during the TIMED mission. The wavelength range includes the soft x-ray (XUV) from 0.1 to 30nm, the extreme ultraviolet (EUV) from 0 to 120nm, and the far ultraviolet (FUV) from 120 to 200nm.

These SSI data from TIMED/SEE are of interest in this thesis to compare the SSI from the CODET model at specific wavelengths 17.1, 19.3, 21.1 and 33.5nm. The important concepts such as Solar Spectral Irradiance (SSI) physical origin, variation and their relation with photospheric magnetic field, the evolution of magnetic elements and the relation to plasma parameters such as density and temperature in the solar corona are part of the scope of this thesis.

---

<sup>7</sup><http://lasp.colorado.edu/home/see/overview/>



## 2 THE SOLAR MODEL PLASMA PARAMETERS

### Contents

---

2.1	Approach . . . . .	<b>38</b>
2.1.1	Genetic algorithms . . . . .	43
2.1.2	Magnetic field extrapolations . . . . .	46
2.2	Model fit . . . . .	<b>48</b>
2.3	Analysis of the results . . . . .	<b>70</b>
2.4	Summary . . . . .	<b>107</b>

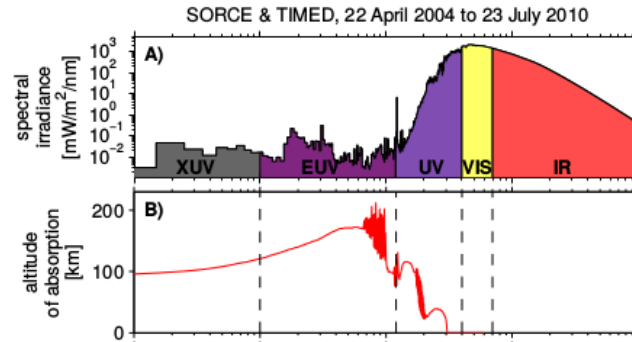
---

The solar spectral irradiance (SSI) influences the Earth’s atmosphere for each wavelength in different altitudes. Its variability is important for EUV and UV absorption and the relationship with the chemistry and dynamics of Earth’s atmosphere (Figure 2.1).

Some SSI space experiments have observed different bands of the spectrum (section 1.10). Solar irradiance measurements from different experiments are interrupted and show discrepancies between measurements due to degradation. Time series of solar irradiance over different time scales are important to understand the influence over the Earth’s atmosphere and climate. Then, it is necessary to use models that are capable to build reliable simulations of SSI. Considerable progress has been achieved in modelling total and spectral solar irradiance. In general, it has been assumed that the variations in irradiance are strongly related to changes in the photospheric magnetic field.

The proxy models use proxies of solar magnetic field features using sunspot areas, photometric sunspot index (PSI), MgII index and lines, CaII and F10.7. These proxies are combined with regression to obtain changes in total solar irradiance. Other models have been developed using different features of the solar atmosphere and radiative transfer codes. In general, these codes compute synthetic stellar spectra using opacity databases to modelling stellar atmospheres, i.e. the Solar Radiation Physical Modelling (SRPM) (FONTENLA et al., 2011). The Spectral And Total Irradiance REconstructions (SATIRE) (VIEIRA et al., 2011; VIEIRA; SOLANKI, 2010; KRIVOVA et al., 2003; FLIGGE et al., 2000; UNRUH et al., 1999), has some ingredients: the surface area covered with magnetic features in the solar photosphere and their evolution in time; the brightness of these magnetic features as a function of the position in the solar disc at each wavelength.

Figure 2.1 - The solar spectral irradiance from SORCE and TIMED observations, from Apr. 22 (2004) to Jul. 23 (2010) A) shows the average solar spectral irradiance inferred from SORCE and TIMED. B) shows the altitude absorption in the Earth's atmosphere.



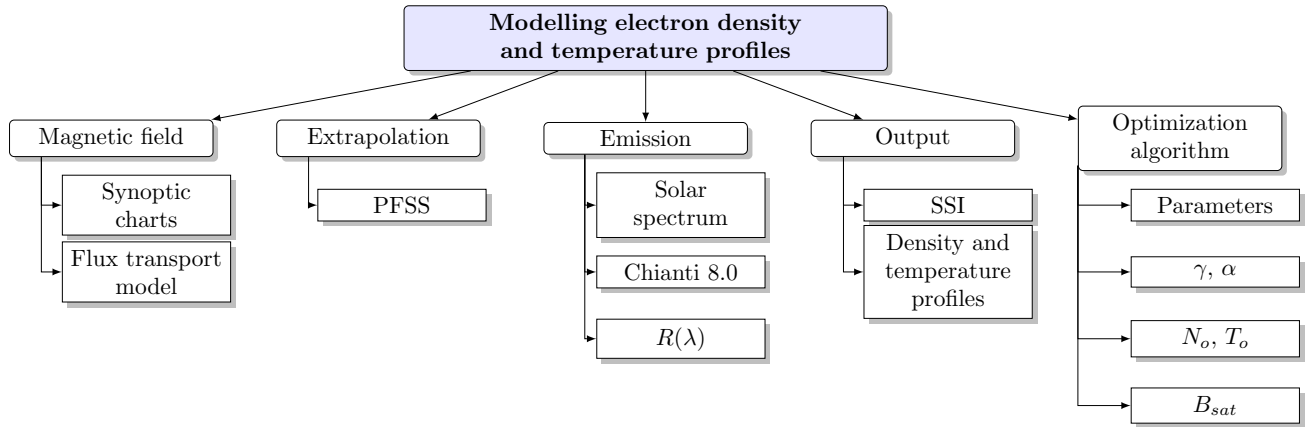
SOURCE: ERMOLLI et al. (2013)

Following the ideas outlined above, the COronal DENsity and Temperature (CODET) model developed based on the evolution of the photospheric magnetic field, will be presented. In this chapter, the COronal DENsity and Temperature (CODET) model will first be described, and some different tools for modelling electron density and temperature in the solar corona. One of these tools is the genetic algorithm Pikaia. In the next section, a review of some concepts about the magnetic field extrapolations will be presented. In the last sections, the fit model using four wavelengths and the selected models it will be discussed.

## 2.1 Approach

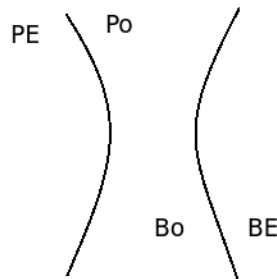
The COronal DENsity and Temperature (CODET) model is a physical model based on the assumption that the variation of the irradiance and plasma parameters is due to the evolution of the solar magnetic field. The CODET model uses the magnetic field from MDI/SOHO and HMI/SDO, a flux transport model, magnetic field extrapolation, an emission model and the optimization algorithm Pikaia (Figure 2.2). The CODET model has as output the solar Spectral Irradiance from the photospheric magnetic field evolution. An emission model was considered (section 2.1) using CHIANTI atomic database 8.0 (section 1.3.2).

Figure 2.2 - Schematic description of the COronal DEnsity and Temperature (CODET) model.



SOURCE: Author

Figure 2.3 - Schematic magneto-static magnetic flux tube model, BE is magnetic field outside and Bo is magnetic field inside, PE external pressure and Po inside pressure.



SOURCE: Author

The magnetic field lines can be described assuming that they behave like vertical fluxtubes; this is possible considering the MHD equations in the case of static equilibrium and constant flows, From MHD momentum equation:

$$0 = -\nabla p - \rho \mathbf{g} + \mathbf{J} \times \mathbf{B} \quad (2.1)$$

Considering that the horizontal pressure balance, using the current density  $\mathbf{J} = \left(\frac{1}{4\pi}\right) (\nabla \times \mathbf{B})$  from Maxwell's equation:

$$-\nabla p - \frac{1}{4\pi} \mathbf{B} \times (\nabla \times \mathbf{B}) = 0 \quad (2.2)$$

Using vector identities

$$\underbrace{-\nabla \left( p + \frac{B^2}{8\pi} \right)}_{\text{The gradient of total pressure}} + \underbrace{\frac{1}{4\pi} (\mathbf{B} \cdot \nabla) \mathbf{B}}_{\text{The magnetic tension}} = 0 \quad (2.3)$$

The gradient of total pressure is the sum of thermal and magnetic pressure. The vertical flux tubes are assumed not to be curved and thus have no magnetic tension (neglected the second term). For the horizontal pressure balance the total pressure is constant:

$$-\nabla \left( p + \frac{B^2}{8\pi} \right) = 0 \quad (2.4)$$

The magneto-static model contains a strong magnetic field ( $B_0$ ) inside and the field outside can be neglected ( $B_E = 0$ ).

The ratio in terms of equation 2.4 is called the plasma- $\beta$  parameter

$$\beta = \frac{p}{\frac{B^2}{8\pi}} \quad (2.5)$$

where  $p = 2n_e k_B T$  is the thermal pressure,  $n_e$  is the electron density,  $k_B$  is the Boltzman constant,  $T$  is the temperature and  $B$  is the magnetic field. In the solar corona the plasma- $\beta$  parameter is much lower than unity, that means the magnetic pressure dominates over thermal pressure.

From the equation 2.4 it is possible to obtain the relationship between density, temperature and magnetic field. It is considered the thin flux tube model, a pressure balance is assumed between the tube and the ambient. In this case  $\beta \ll 1$  (in solar corona)

$$\frac{B^2 \beta}{8\pi} = 2N k_B T$$

$$N = \frac{B^2 \beta}{2(8\pi k_B T)}$$

$$N \propto \frac{B^\gamma}{cts} \quad (2.6)$$

$$T = \frac{B^2 \beta}{2(8\pi k_B N)}$$

$$T \propto \frac{B^\alpha}{cts} \quad (2.7)$$

where  $\gamma$  and  $\alpha$  are parameters of the model,  $cts$  correspond to a constant value. Considering the magnetic field  $B$

$$B = \sqrt{(B_r^2 + B_\phi^2 + B_\theta^2)} \quad (2.8)$$

where  $B_r$ ,  $B_\phi$  and  $B_\theta$  are magnetic field components from linear force free extrapolation (i.e Potential field source surface (PFSS/SSW<sup>1</sup>) was used to extrapolate the line-of-sight surface magnetic field from the photosphere  $R_{sun} = 1.0$  up to the corona  $R_{sun} = 2.5$ ). The magnetic field  $B$  is measured in  $[G]$  units. Additionally, it was used the function  $Bf$ ,  $bf_0$  and  $\tau bf$  are constant values; it allows to define regions with strong or weak photospheric magnetic field.

$$Bf = bf_0 \times e^{-\left(\frac{R_{sun}}{\tau bf}\right)^2} \quad [G] \quad (2.9)$$

From the equations 2.6, 2.7 and 2.9, it is possible to build some expressions to electron density and temperature profiles, using a referenced magnetic field  $B_{sat}$

Density profile:

$$N = N_o \left(\frac{B}{B_{sat}}\right)^\gamma \quad [cm^{-3}] \quad (2.10)$$

using the following conditions it is possible to define the temperature profile:

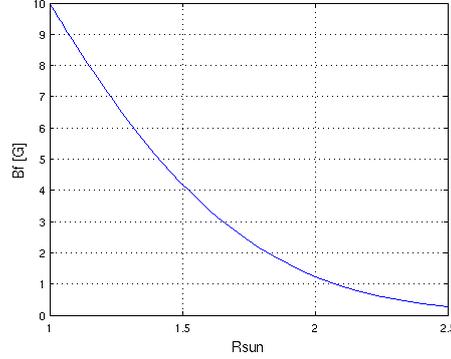
if  $B < Bf$

$$T = T_o \quad [K] \quad (2.11)$$

---

<sup>1</sup>solarsoft [www.lmsal.com/solarsoft](http://www.lmsal.com/solarsoft)

Figure 2.4 -  $Bf$  condition for the magnetic field with  $bf_0 = 20$ ,  $\tau_{bf} = 1.2$  and  $R_{sun} = 1.0 - 2.5$ .



SOURCE: Author

If  $B > Bf$

$$T = T_o \left( \frac{B}{B_{sat}} \right)^\alpha \quad [K] \quad (2.12)$$

Where  $\gamma$  and  $\alpha$  are power law indices,  $\left( \frac{B}{B_{sat}} \right)$  is the filling factor related to the amount of flux in each pixel,  $B_{sat}$  is a constant value of the magnetic field,  $N_o$  and  $T_o$  are background density and temperature. The temperature  $T$  and electron density  $N$  are measured in  $[K]$  and  $[cm^{-3}]$  respectively.

### Emission measure formalism

Different models were employed to describe the emission measurement in different wavelengths. In this section, some characteristics of emission measure formalism used in the CODET model will be described (WARREN, 2006; WARREN et al., 1998; VERNAZZA et al., 1981) .

Assuming that the emission lines are optically thin, it is possible to measure only the integrated emission along a given line of sight, but it is necessary to consider the ionization and recombination coefficients. This emission line depends on the atomic transitions and the conditions of the solar atmosphere, the specific intensity can be described by:

$$I_o = \int \int R(\lambda) G(\lambda, T) d\lambda N^2 ds \quad (2.13)$$

where  $G(\lambda, T)$  [ $erg\ cm^3\ s^{-1}\ sr^{-1}$ ] is the contribution function from The CHIANTI atomic database,  $d\lambda$  [ $nm$ ] is the differential element in wavelength,  $N$  [ $cm^{-3}$ ] is the electron density,  $ds$  [ $cm$ ] is the differential distance along the line-of-sight and  $R(\lambda)$  is the instrumental response.

The contribution function was used to construct the solar spectra for a specific wavelength, abundance and ionization equilibrium (this function describes physical parameters of the electronic transitions).

The instrumental response depends on wavelength and temperature; it constitutes an important characteristic of the instruments. Typically investigations have been carried out using the value of emission measure and variations of density throughout the corona (RAFTERY, 2012).

$$I_o = \int \int \underbrace{G(\lambda, T)}_{[erg\ cm^3\ s^{-1}\ sr^{-1}]} \underbrace{d\lambda}_{[nm]} \underbrace{N^2 ds}_{[cm^{-5}]}$$

$$I_o = [erg\ cm^{-2}\ s^{-1}\ sr^{-1}\ nm]$$

$$I = \frac{I_o}{D^2} \quad [W/m^2/nm] \quad (2.14)$$

$I$  is the full-disc intensity measured at Earth from an emission line, where  $D = 1AU = 1.4960 \times 10^{11}m$ .

Some tools are necessary for modelling the electron density and temperature as force free extrapolations specially potential field extrapolations and optimization algorithm (Pikaia) (Figure 2.1), and they will be described in the following sections.

### 2.1.1 Genetic algorithms

The genetic algorithms are adaptive methods, generally used in optimization problems. The genetic algorithms are based on natural selection, combining the survivor of the best individual or variable in the optimization problem. To achieve the solution to the problem is part of an initial set of individuals or population randomly generated.

The development of genetic algorithms is due largely to John Holland, a researcher

at the University of Michigan. A late 1960's he developed a technique that imitates the natural selection. The Genetic algorithms consists of populations of encoded solutions similar to the chromosomes, each of these chromosomes will be associated with an adjustment value or goodness-of-fit, which quantifies its validity as a solution to the problem. Based on this value it will bring together more or less opportunities for reproduction (GESTAL et al., 2010) and references therein.

The genetic algorithms are based on inheritance, mutation, selection and crossover or recombination. Frequently used the biological terminology: **Gene** correspond to a single encoding of part of the solution space, **Chromosome** is a string of genes that represents a solution, **Population** is the number of chromosomes available to test and the **goodness-of-fit** determines the environment within which the solutions "live".

The best solutions get a higher chance to become parents for next generation solutions. Usually the genetic algorithms employ the Roulette Wheel Algorithm: it consists of assigning each individual a part of the wheel and the possible selections are based on their goodness-of-fit value (DAVIS, 1998).

Next, it will be described the specific genetic algorithm, Pikaia Algorithm. This algorithm is used to optimize the free parameters in the model to electron density and temperature in the solar corona.

### **Pikaia Algorithm**

The Pikaia algorithm is a method for optimization based on genetic algorithm developed by CHARBONNEAU (1995). In general a population of individuals is chosen at random range, then they are surveyed to determine their goodness-of-fit. A new generation of individuals is generated and their characteristics are passed on to the next generation. Pikaia uses a stochastic selection, using the Roulette Wheel Algorithm based on the idea of better solutions get a greater chance to become parents for next generation solutions (CHARBONNEAU, 1995).

In order to implement Pikaia Algorithm, we use BELUGA that is a MATLAB optimization package and is freely available from Medical School at University of Michigan in the virtual physiological Rat Project<sup>2</sup>. Beluga finds in a local minimum  $x$  of an objective function (our model) an initial population of candidate solutions. The free parameters are defined following:

---

<sup>2</sup><http://virtualrat.org/software/beluga>

$$parameter = parameter_{min} + (parameter_{max} - parameter_{min}) \times par(n) \quad (2.15)$$

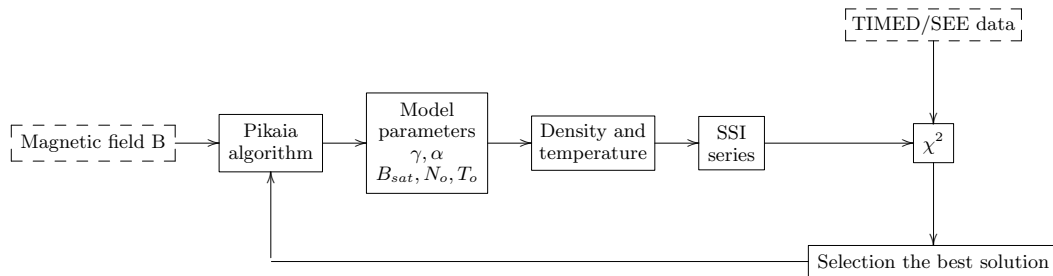
where  $parameter$  is the free parameter that will be optimized by Pikaia algorithm,  $parameter_{max}$  and  $parameter_{min}$  are the lower and upper limits of  $parameter$ ,  $par(n)$  be situated at the interval  $[0, 1]$ ,  $n$  is the number of free parameters.

It is calculated a goodness-of-fit  $\chi^2$  between the observed and modelling data, in general  $\chi^2 \lesssim 1$  indicates an acceptable fit. The goodness-of-fit is the key point between the Pikaia algorithm and the model of plasma parameters.

The optimization of the model's free parameters is done using the genetic algorithm Pikaia. This approach was successful applied in Reconstructions of solar irradiance in VIEIRA et al. (2011), VIEIRA and SOLANKI (2010), KRIVOVA et al. (2010), stellar structure modelling METCALFE and CHARBONNEAU (2003), empirical modelling of the solar corona GIBSON and CHARBONNEAU (1998), Doppler shifts of solar ultraviolet emission lines PETER and JUDGE (1999) and modelling solar microwave emissions Pinto (2015).

The parameters of the CODET model ( $\gamma$ ,  $\alpha$ ,  $B_{sat}$ ,  $T_o$  and  $N_o$ ) are characterized using maximum and minimum values and making variations between those limits using the equation 2.15 in Pikaia genetic algorithm.

Figure 2.5 - Schematic description of optimization algorithm, where dotted lines describe the input parameters.



SOURCE: Author

### 2.1.2 Magnetic field extrapolations

Magnetic field extrapolation is an important tool to study the three-dimensional solar coronal magnetic field, which is difficult to measure directly, because the coronal magnetic field is weaker than that of the photosphere. In general extrapolation of the solar magnetic field models give static representations of the solar corona at an instant. Three models are used frequently for force free-field extrapolation: potential field, linear force-free field and nonlinear force-free field model. In this chapter, it will be described briefly force free fields and potential field extrapolations, which are of interest in this work.

From the equation 2.2 for strong magnetic fields and a very small plasma- $\beta$  parameter in the solar corona, its gradient can be neglected. Thus equation 2.2 reduces to

$$\mathbf{B} \times (\nabla \times \mathbf{B}) = 0 \quad (2.16)$$

A magnetic field satisfying equation 2.16 is called force-free. This implies that the curl of the magnetic field and the current density is in the direction of the magnetic field

$$(\nabla \times \mathbf{B}) = \alpha \mathbf{B} \quad (2.17)$$

where  $\alpha$  is a scalar function of space, but  $\alpha$  do not vary along a magnetic field line because of

$$\nabla \cdot (\alpha \mathbf{B}) = \mathbf{B} \cdot \nabla \alpha = 0 \quad (2.18)$$

A second class of solutions of equation 2.16 are potential fields.

#### Potential field

The potential field describes the current free plasma

$$\nabla \times \mathbf{B} = 0 \quad (2.19)$$

then, the magnetic field can be represented by a scalar potential

$$\mathbf{B} = -\nabla \phi \quad (2.20)$$

then the potential magnetic field satisfies the Laplace equation

$$\nabla^2 \phi = 0 \quad (2.21)$$

A magnetic potential field  $\phi$  is equivalent to a "current-free" field,  $\mathbf{j} = 0$ . This approximation is often applied in the lower solar corona and solar chromosphere.

Magnetic field modelling uses the longitudinal photospheric magnetic field components as boundary condition for force-free magnetic field extrapolation. This is possible since the solar corona is almost force-free, because the magnetic pressure is several orders of magnitude higher than the plasma pressure (WIEGELMANN et al., 2014).

### Potential field source surface extrapolation

The Potential-Field Source Surface (PFSS) model extrapolates the line-of-sight surface magnetic field through the corona. Using the main idea of Source Surface Model developed by SCHATTEEN et al. (1969), this model describes interplanetary and coronal magnetic fields. There are three different regions: Region 1: the photosphere, where the magnetic field is governed by the plasma motion. Region 2: where the magnetic energy density is greater than the plasma energy density and controls the configuration, in this region, it is possible to use the force-free condition (current free) and the magnetic field can be derived from a potential. Region 3: the transverse magnetic fields are transported by the radially flowing plasma. The source surface is the region where currents in the corona cancel the transverse magnetic field.

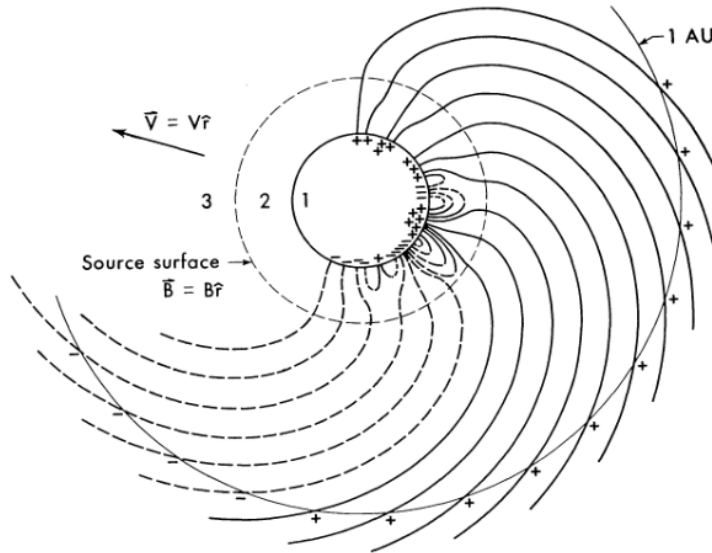
The field in the Region 2 or solar corona region of interest is calculated from potential theory. Then, the problem consists of finding the scalar potential  $\phi$ , in spherical geometry. The usual solution method involves spherical harmonics. The Laplace's equation is solved within volume above the photosphere in terms of a spherical harmonic expansion, the coefficients of which are derived from Carrington maps of the photospheric magnetic field (maps assembled over an entire solar rotation from magnetograms on the Earth's surface or on board a spacecraft in orbit around the L1 Lagrange point). It is assumed that there are no temporal variations within the  $\pm 27$  days taken to build up the synoptic map, that there are no currents in the corona and it is used a small heliospheric distance ( $2.5R_{sun}$ ) to allow unique solutions.

It is commonly used the potential-field source surface (PFSS) (the software is freely available for installation via solar software (SSW<sup>3</sup>)) algorithm developed by Marc de Rosa (SCHRIJVER; De ROSA, 2003). PFSS has been very successful in the study of a wide range of solar and heliospheric phenomena such as coronal structure as seen during eclipses, modelling of Earth-impacting coronal mass ejections (CMEs), coro-

---

<sup>3</sup>Solarsoft [www.lmsal.com/solarsoft](http://www.lmsal.com/solarsoft)

Figure 2.6 - Source surface model. Photospheric magnetic field in Region 1. Loops appear in Region 2. Solar wind extends into the interplanetary space.



(a) Source Surface Model

SOURCE: Courtesy. [SCHATTEN et al. \(1969\)](#)

nal null points and CME release, interplanetary magnetic fields, heliospheric current sheet structure, waves in the corona, solar wind acceleration, stellar coronal fields, coronal hole and fast solar wind stream evolution, solar wind speed prediction, solar wind density structure, pseudostreamers (see [LOCKWOOD \(2013\)](#) and references therein).

The potential field source surface (PFSS) model can be used as an input surface-flux transport model of photospheric magnetism developed by [SCHRIJVER \(2001\)](#) and described in the chapter 1.2. This model advects surface flux across the surface, generating by differential rotation, meridional flow, convective profiles, fragmentation.

## 2.2 Model fit

The optimization algorithm was applied to fit different wavelengths  $17.1nm$ ,  $19.3nm$ ,  $33.5nm$  and  $21.1nm$ . Each wavelength was individually fitted and the wavelengths were fitted simultaneously. The definition of the limits of the density and temperature in each model were used information from Table 1.5, Table 1.4 and Table 1.2. Also, the description of the radiative processes in the solar corona (section 1.3), and the contribution functions in each wavelength (Figure 1.7).

Several cases were explored to search the best fit between the observational data and data from the model. The  $\chi^2$  function was defined after several tests such as:

$$\chi^2 = \frac{(I_{model} - I_{obs})^2}{|I_{obs}|} \quad (2.22)$$

where  $I_{model}$  is the intensity from our model and  $I_{obs}$  correspond to the intensity from observations (TIMED/SEE). In this case, it was chosen a period of ten days during the solar cycle 23 and 24 (Feb. 01 (2003), Oct. 01 (2003), Oct. 01 (2004), Oct. 01 (2005), Oct.01 (2007) Oct. 01 (2008), Oct. 01 (2009), Oct. 01 (2011), Oct. 01 (2014), Oct. 01 (2016) at 12 : 00UT). The average temperature and density profiles in all layers (from  $R_{sun} = 1.0$  to  $R_{sun} = 2.5$  solar radii) were obtained in each model.

The model fit was made using different wavelengths, ie. using individual wavelength to fit (Model fit at  $17.1nm$ , model fit at  $19.3nm$ , model fit at  $33.5nm$  and model fit at  $21.1nm$ ). Using three wavelengths simultaneously to fit (Model fit at  $17.1nm$ ,  $19.3nm$  and  $21.1nm$ , model fit at  $17.1nm$ ,  $19.3nm$  and  $33.5nm$ ) and using two wavelengths simultaneously to fit (Model fit at  $17.1nm-19.3nm$ , model fit  $21.1nm-33.5nm$  and model fit  $19.3nm-21.1nm$ ).

The characteristics evaluated in each case were:

- 1) Goodness-of-fit between Solar Spectral Irradiance from observational and modelled data.
- 2) Electron density and temperature profiles according to observational and model descriptions in section 1.4.

Then, the best models are highlighted with cells in cyan color.

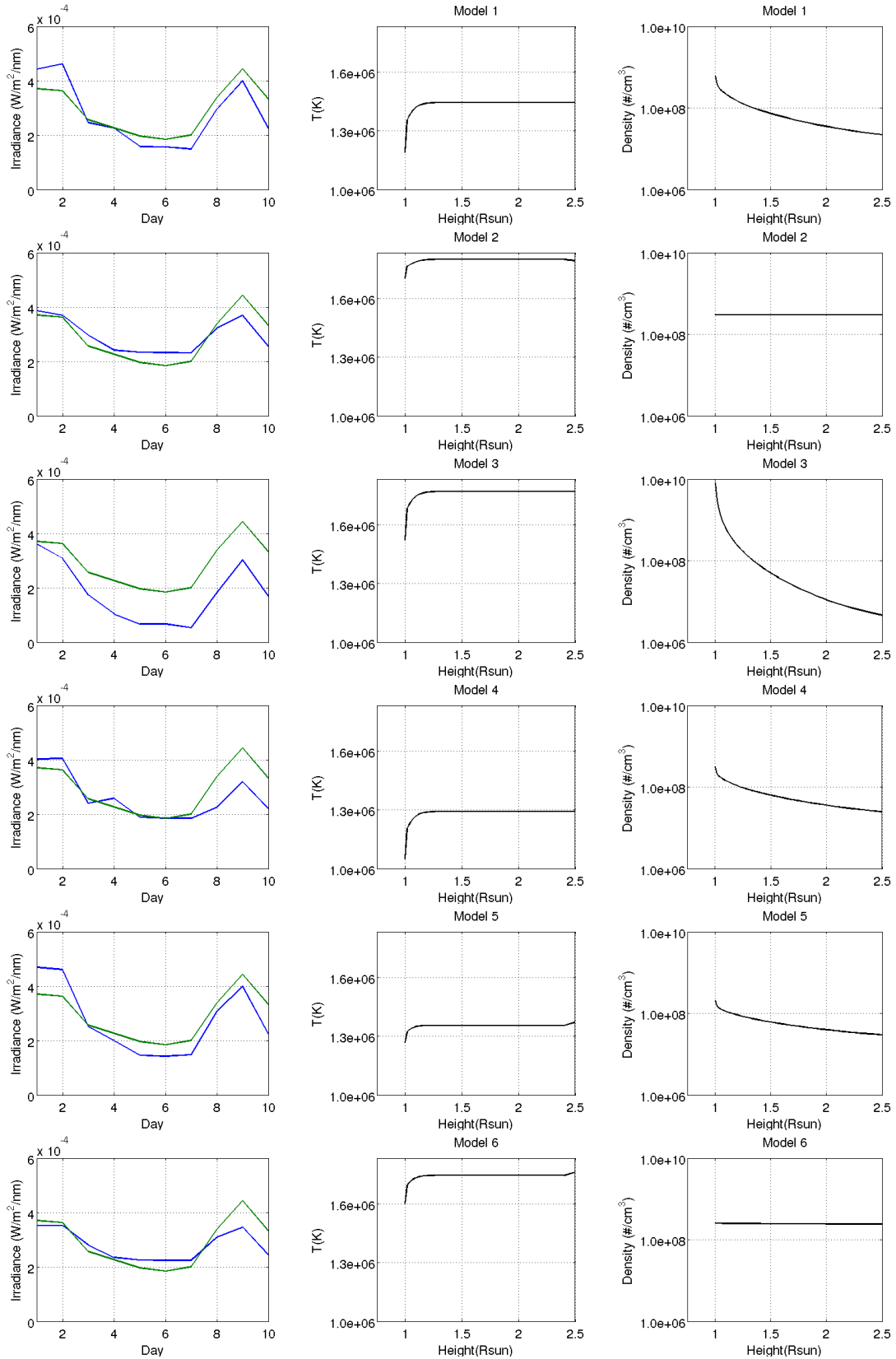
## Model fit at 17.1nm

Table 2.1 - Model fit at 17.1nm, the value parameters ( $\gamma$ ,  $\alpha$ ,  $N_o$ ,  $T_o$  and  $B_{sat}$ ) for each model and information about the optimization algorithm (Population size and generations).

Parameter	Model 1	Model 2	Model 3	Model 4	Model 5	Model 6
$\gamma$	0.7472	$-4.0 \times 10^{-4}$	1.5334	0.5757	0.4374	0.0135
$\alpha$	-1.9894	0.5551	-1.5841	-3.7059	-0.3872	-0.4851
$N_o$	$1.48098 \times 10^8$	$2.99306 \times 10^8$	$2.80077 \times 10^8$	$2.90865 \times 10^8$	$1.95252 \times 10^8$	$2.54122 \times 10^8$
$T_o$	$1.40610 \times 10^6$	$1.85024 \times 10^6$	$1.80730 \times 10^6$	$1.25050 \times 10^6$	$1.31470 \times 10^6$	$1.77480 \times 10^6$
$B_{sat}$	1.0	54.3337	1.3495	5.3857	5.2744	2.7964
$\chi^2$	$1.1034 \times 10^{-4}$	$6.3902 \times 10^{-5}$	$5.6289 \times 10^{-4}$	$1.2418 \times 10^{-4}$	$1.3421 \times 10^{-4}$	$6.6841 \times 10^{-5}$
Population size	8	8	8	8	8	8
Generations	25	20	25	25	25	25

SOURCE: Author

Figure 2.7 - Wavelength  $17.1\text{nm}$ . First column: Solar Spectral Irradiance from observational data (green line) and modelled (blue line). Second column: average temperature profiles in all layers for each model. Third column: average density profiles in all layers according to the model.



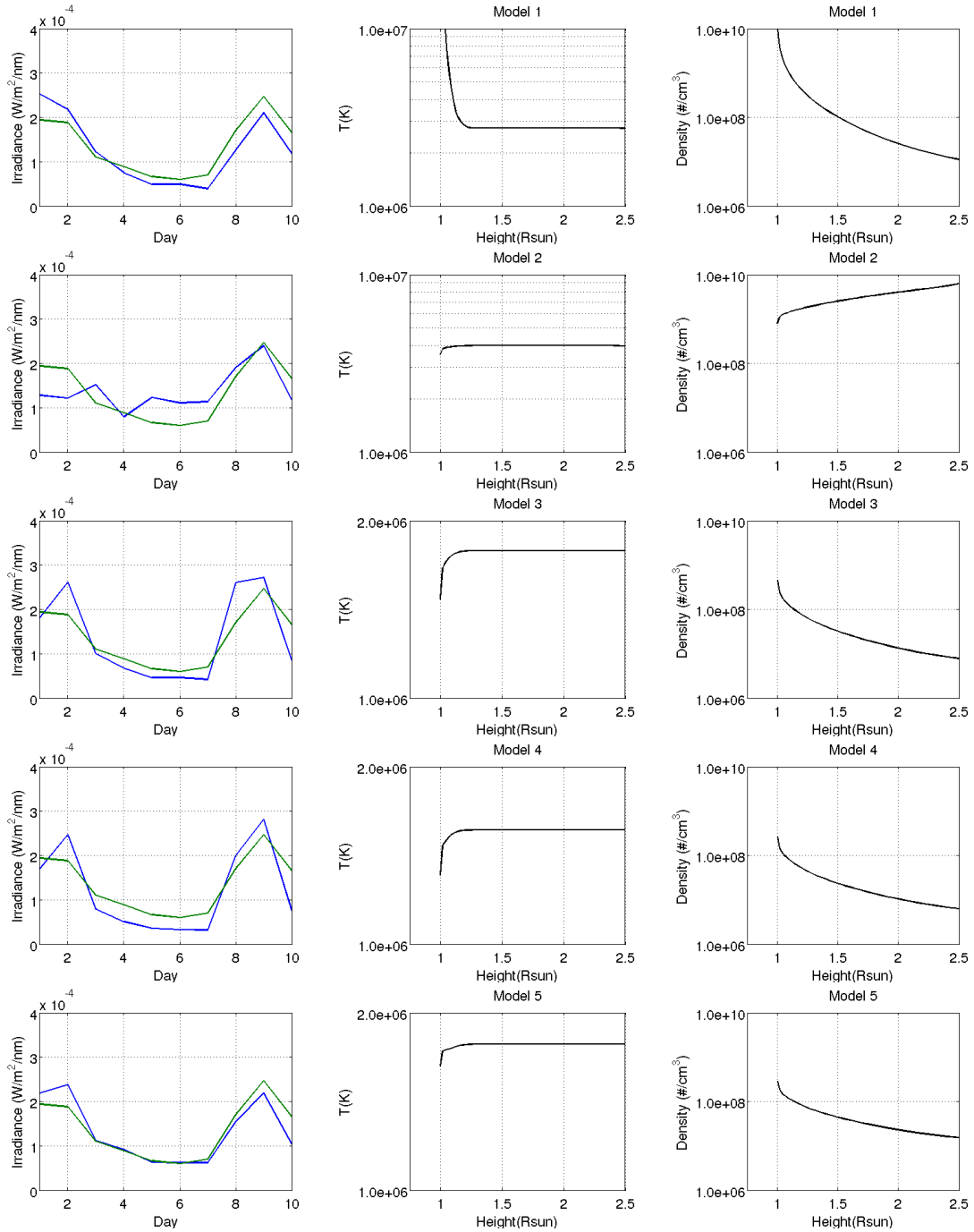
## Model fit at 19.3nm

Table 2.2 - Model fit at 19.3nm describes the value parameters ( $\gamma$ ,  $\alpha$ ,  $N_o$ ,  $T_o$  and  $B_{sat}$ ) for each model and information about the optimization algorithm (Population size and generations).

Parameter	Model 1	Model 2	Model 3	Model 4	Model 5
$\gamma$	1.4156	-0.4544	0.8980	0.8336	0.6644
$\alpha$	1.3104	0.3135	-2.5552	-5.3066	-5.0187
$N_o$	$3.36978 \times 10^8$	$1.02890 \times 10^8$	$2.21990 \times 10^8$	$2.57370 \times 10^8$	$0.99929 \times 10^8$
$T_o$	$2.75727 \times 10^6$	$3.97460 \times 10^6$	$1.77820 \times 10^6$	$1.56180 \times 10^6$	$1.76760 \times 10^6$
$B_{sat}$	1.0	358.8880	3.3961	6.9472	1.3042
$\chi^2$	$1.400 \times 10^{-4}$	$1.9587 \times 10^{-4}$	$1.4534 \times 10^{-4}$	$1.5316 \times 10^{-4}$	$4.4817 \times 10^{-5}$
Population size	8	8	8	8	8
Generations	25	25	25	25	25

SOURCE: Author

Figure 2.8 - Wavelength  $19.3nm$ . First column: Solar Spectral Irradiance from observational data (green line) and modelled (blue line) 1. Second column: average temperature profiles in all layers for each model. Third column: average density profiles in all layers according to the model.



SOURCE: Author

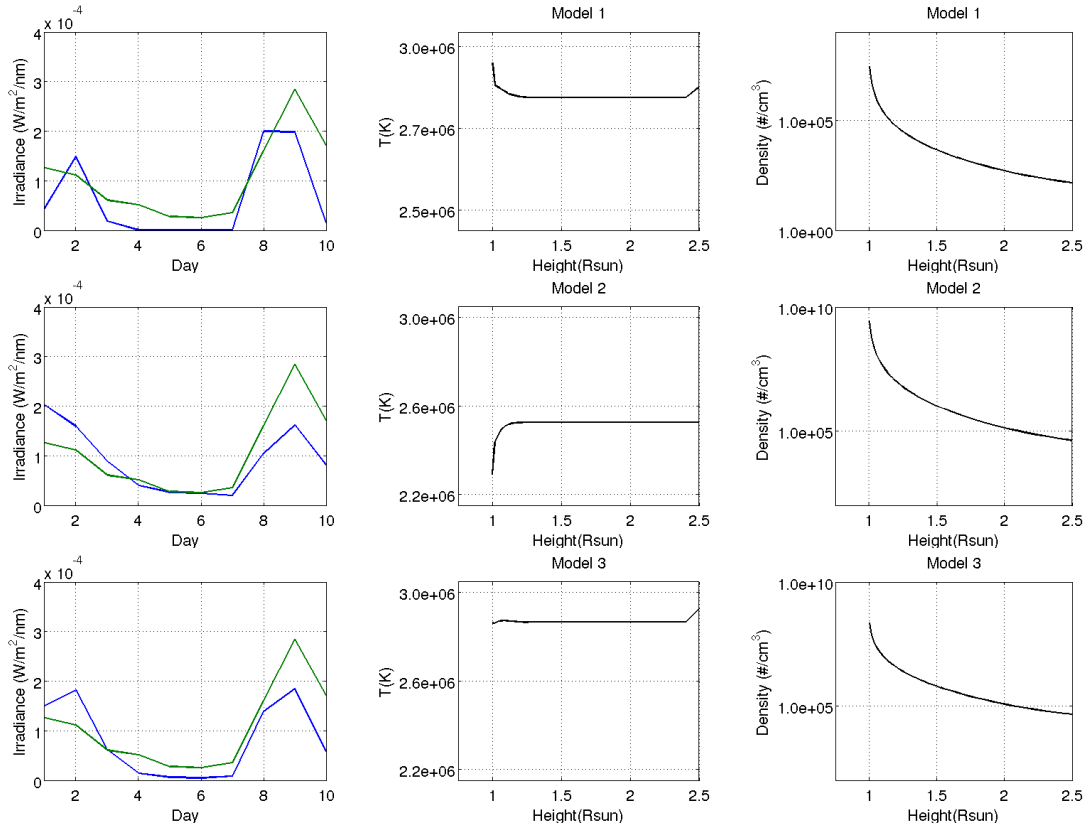
### Model fit at 33.5nm

Table 2.3 - Model fit at 33.5nm describes the value parameters ( $\gamma$ ,  $\alpha$ ,  $N_o$ ,  $T_o$  and  $B_{sat}$ ) for each model and information about the optimization algorithm (Population size and generations).

Parameter	Model 1	Model 2	Model 3
$\gamma$	2.2246	2.0832	1.7010
$\alpha$	-0.2142	-0.6846	-0.3727
$N_o$	$1.17644 \times 10^8$	$3.02850 \times 10^8$	$3.13314 \times 10^8$
$T_o$	$2.78697 \times 10^6$	$2.50432 \times 10^6$	$2.81650 \times 10^6$
$B_{sat}$	46.5553	7.1978	17.2888
$\chi^2$	$4.1044 \times 10^{-4}$	$2.0824 \times 10^{-4}$	$2.4480 \times 10^{-4}$
Population size	8	8	8
Generations	20	20	20

SOURCE: Author

Figure 2.9 - Wavelength  $33.5\text{nm}$ . First column: Solar Spectral Irradiance from observational data (green line) and modelled (blue line). Second column: average temperature profiles in all layers for each model. Third column: average density profiles in all layers according to the model.



SOURCE: Author

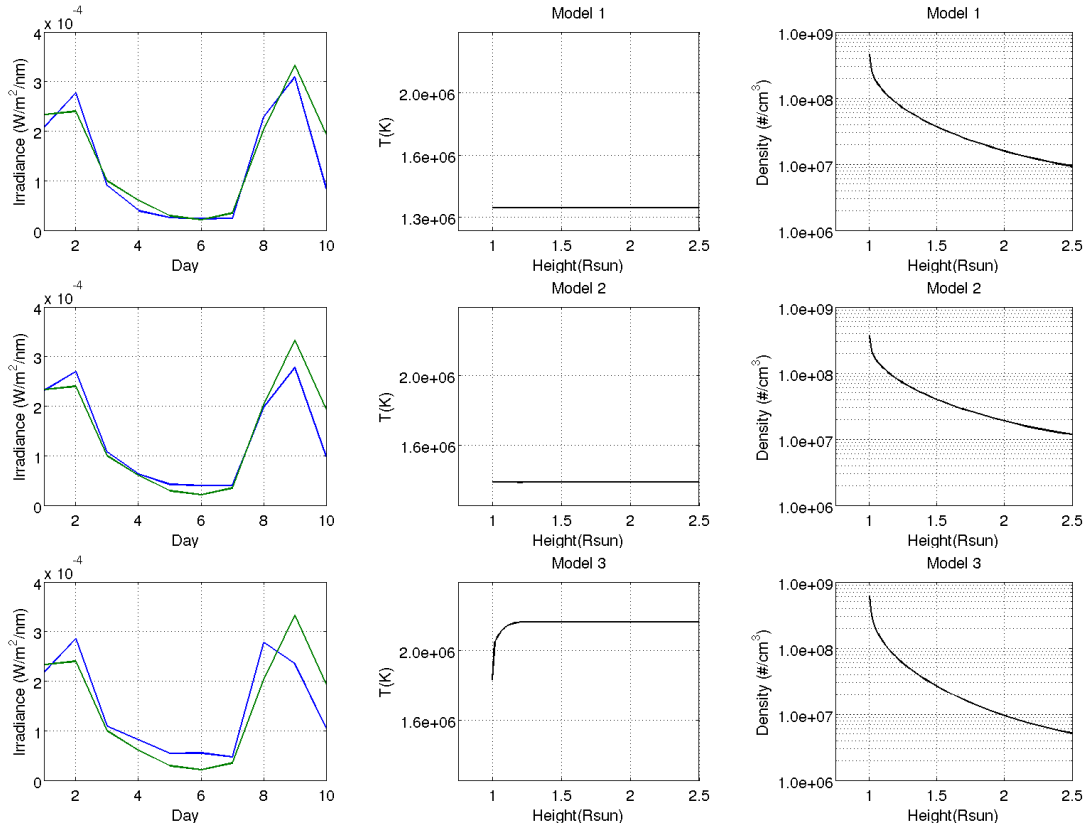
### Model fit at 21.1nm

Table 2.4 - Model fit at 21.1nm describes the value parameters ( $\gamma$ ,  $\alpha$ ,  $N_o$ ,  $T_o$  and  $B_{sat}$ ) for each model and information about the optimization algorithm (Population size and generations).

Parameter	Model 1	Model 2	Model 3
$\gamma$	0.8666	0.7686	1.0444
$\alpha$	-6.9272	-13.3588	-1.9642
$N_o$	$0.82701 \times 10^8$	$2.0237 \times 10^8$	$1.4123 \times 10^8$
$T_o$	$1.30511 \times 10^6$	$1.40365 \times 10^6$	$2.19235 \times 10^6$
$B_{sat}$	1.0	3.1951	2.0134
$\chi^2$	$8.8001 \times 10^{-5}$	$8.3366 \times 10^{-5}$	$1.9379 \times 10^{-4}$
Population size	8	8	8
Generation	25	25	25

SOURCE: Author

Figure 2.10 - Wavelength  $21.1nm$ . First column: Solar Spectral Irradiance from observational data (green line) and modelled (blue line). Second column: average temperature profiles in all layers for each model. Third column: average density profiles in all layers according to the model.



SOURCE: Author

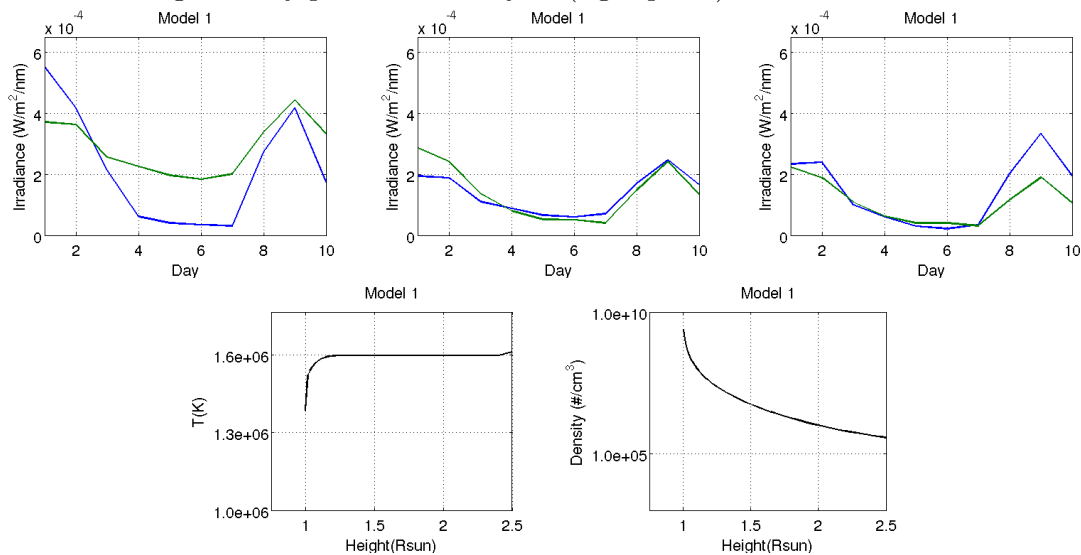
## Model fit between 17.1nm, 19.3nm and 21.1nm

Table 2.5 - Model fit between 17.1nm, 19.3nm and 21.1nm describes the value parameters ( $\gamma$ ,  $\alpha$ ,  $N_o$ ,  $T_o$  and  $B_{sat}$ ) for each model and information about the optimization algorithm (Population size and generations).

Parameter	Model 1	Model 2	Model 3
$\gamma$	1.7430	1.2582	0.7536
$\alpha$	-0.7073	-1.4938	-5.1794
$N_o$	$0.30735 \times 10^8$	$2.95592 \times 10^8$	$2.6561 \times 10^8$
$T_o$	$1.58185 \times 10^6$	$1.66501 \times 10^6$	$1.20522 \times 10^6$
$B_{sat}$	1.2040	4.1752	6.2176
$\chi^2$	$9.6643 \times 10^{-4}$	0.0010	0.0016
Population size	8	8	8
Generation	25	50	25

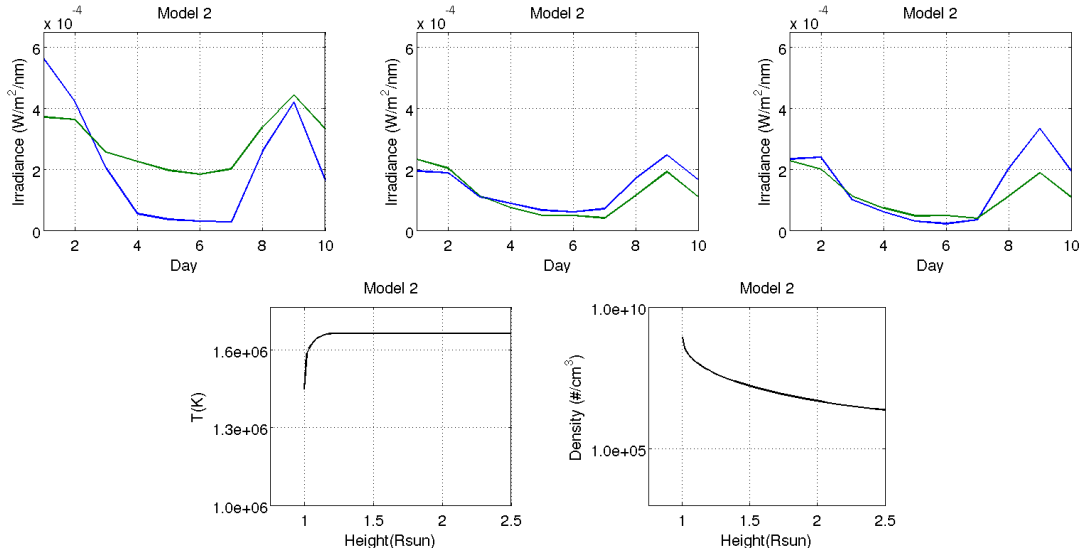
SOURCE: Author

Figure 2.11 - Fit 17.1nm, 19.3nm and 21.1nm using the model 1. Upper panel: Solar Spectral Irradiance from observational data (green line) and modelled (blue line), left panel: 17.1nm, middle panel: 19.3nm and right panel: 21.1nm. Lower panel: average temperature profiles in all layers (left panel) and average density profiles in all layers (right panel).



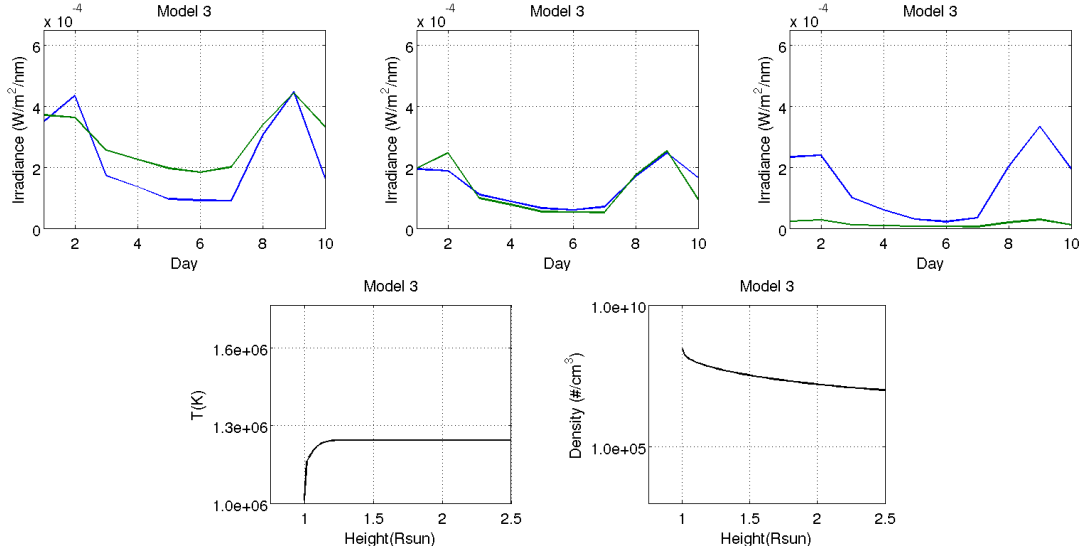
SOURCE: Author

Figure 2.12 - Fit 17.1nm, 19.3nm and 21.1nm using the model 2. Upper panel: Solar Spectral Irradiance from observational data (green line) and modelled (blue line), left panel: 17.1nm, middle panel: 19.3nm and right panel: 21.1nm. Lower panel: average temperature profiles in all layers (left panel) and average density profiles in all layers (right panel).



SOURCE: Author

Figure 2.13 - Fit 17.1nm, 19.3nm and 21.1nm using the model 3. Upper panel: Solar Spectral Irradiance from observational data (green line) and modelled (blue line), left panel: 17.1nm, middle panel: 19.3nm and right panel: 21.1nm. Lower panel: average temperature profiles in all layers (left panel) and average density profiles in all layers (right panel).



SOURCE: Author

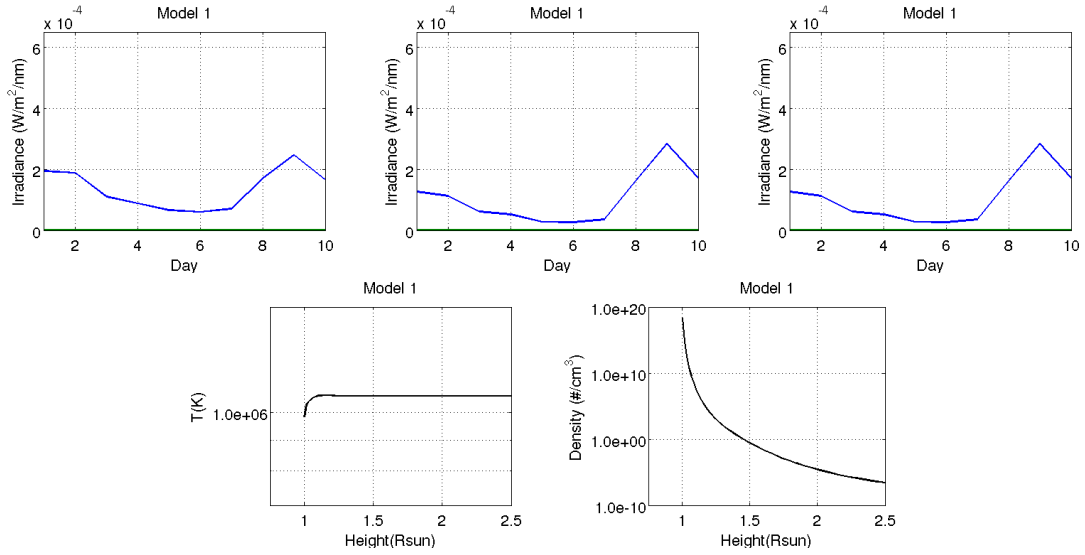
### Model fit between 17.1nm, 19.3nm and 33.5nm

Table 2.6 - Model fit between 17.1nm, 19.3nm and 33.5nm describes the value parameters ( $\gamma$ ,  $\alpha$ ,  $N_o$ ,  $T_o$  and  $B_{sat}$ ) for each model and information about the optimization algorithm (Population size and generations).

Parameter	Model 1	Model 2	Model 3
$\gamma$	7.7360	1.3520	6.2500
$\alpha$	-2.4014	-11.0860	-3.1780
$N_o$	$0.653610 \times 10^8$	$0.81804 \times 10^8$	$2.1538 \times 10^8$
$T_o$	$1.06517 \times 10^6$	$1.77445 \times 10^6$	$2.03185 \times 10^6$
$B_{sat}$	11.5644	10.1973	42.7970
$\chi^2$	0.0035	0.0039	0.0034
Population size	8	8	8
Generation	25	25	25

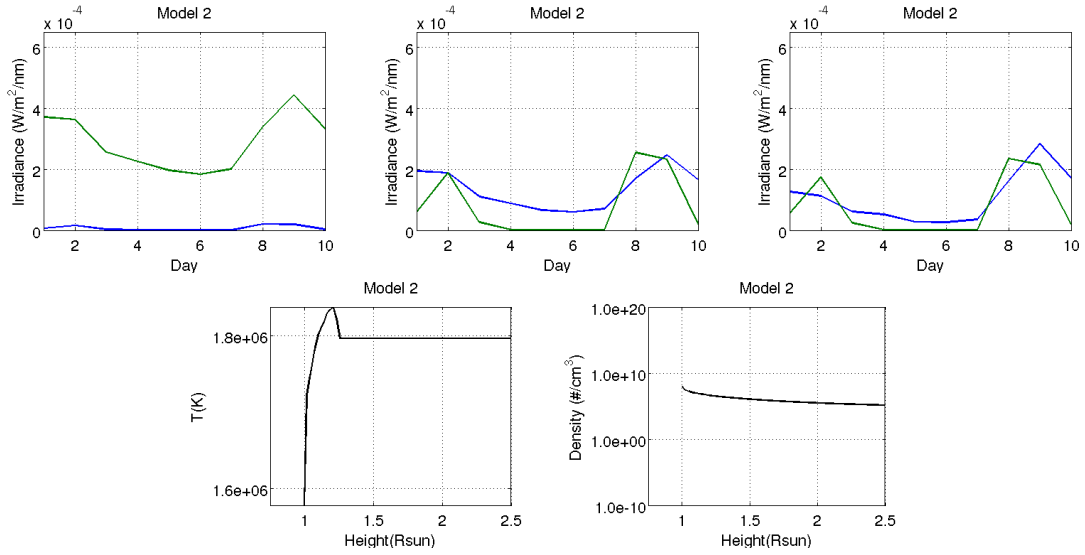
SOURCE: Author

Figure 2.14 - Fit  $17.1nm$ ,  $19.3nm$  and  $33.5nm$  using the model 1. Upper panel: Solar Spectral Irradiance from observational data (green line) and modelled (blue line), left panel:  $17.1nm$ , middle panel:  $19.3nm$  and right panel:  $33.5nm$ . Lower panel: average temperature profiles in all layers (left panel) and average density profiles in all layers (right panel).



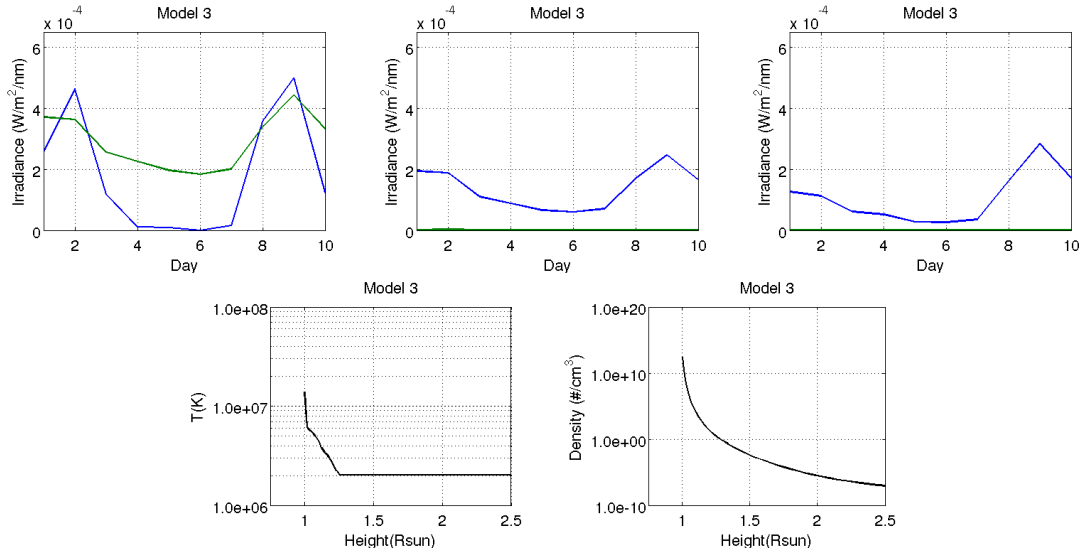
SOURCE: Author

Figure 2.15 - Fit  $17.1nm$ ,  $19.3nm$  and  $33.5nm$  using the model 2. Upper panel: Solar Spectral Irradiance from observational data (green line) and modelled (blue line), left panel:  $17.1nm$ , middle panel:  $19.3nm$  and right panel:  $33.5nm$ . Lower panel: average temperature profiles in all layers (left panel) and average density profiles in all layers (right panel).



SOURCE: Author

Figure 2.16 - Fit 17.1nm, 19.3nm and 33.5nm using the model 3. Upper panel: Solar Spectral Irradiance from observational data (green line) and modelled (blue line), left panel: 17.1nm, middle panel: 19.3nm and right panel: 33.5nm. Lower panel: average temperature profiles in all layers (left panel) and average density profiles in all layers (right panel).



SOURCE: Author

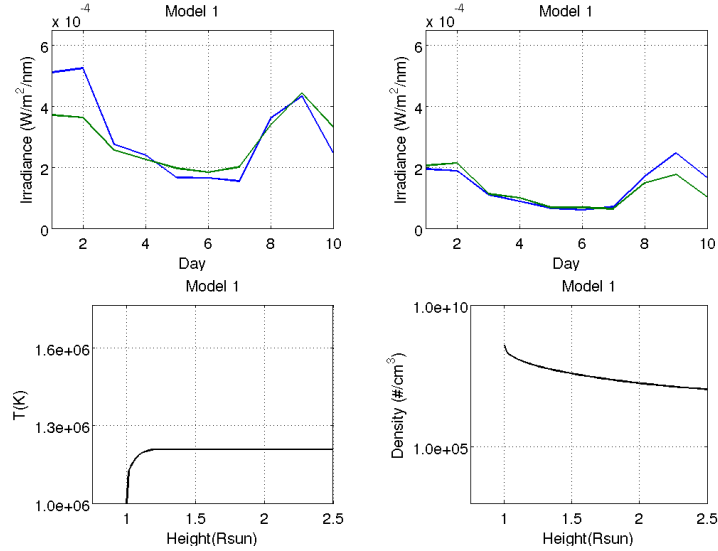
### Model fit between 17.1nm and 19.3nm

Table 2.7 - Model fit between 17.1nm and 19.3nm describes the value parameters ( $\gamma$ ,  $\alpha$ ,  $N_o$ ,  $T_o$  and  $B_{sat}$ ) for each model and information about the optimization algorithm (Population size and generations).

Parameter	Model 1
$\gamma$	0.8022
$\alpha$	-2.4173
$N_o$	$2.98405 \times 10^8$
$T_o$	$1.17340 \times 10^6$
$B_{sat}$	5.1352
$\chi^2$	$2.2233 \times 10^{-4}$
Population size	8
Generation	25

SOURCE: Author

Figure 2.17 - Fit 17.1nm and 19.3nm using the model 1. Upper panel: Solar Spectral Irradiance from observational data (green line) and modelled (blue line), left panel: 17.1nm and right panel: 19.3nm. Lower panel: average temperature profiles in all layers (left panel) and average density profiles in all layers (right panel).



SOURCE: Author

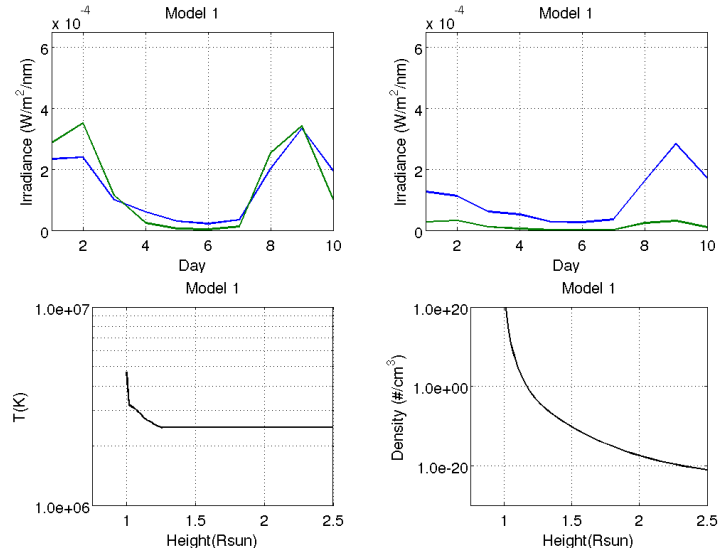
### Model fit between 21.1nm and 33.5nm

Table 2.8 - Model fit between 21.1nm and 33.5nm describes the value parameters ( $\gamma$ ,  $\alpha$ ,  $N_o$ ,  $T_o$  and  $B_{sat}$ ) for each model and information about the optimization algorithm (Population size and generations).

Parameter	Model 1	Model 2	Model 3	Model 4
$\gamma$	13.4862	13.0270	1.2950	9.7760
$\alpha$	-2.3835	-1.2211	-0.2593	-1.9309
$N_o$	$0.31416 \times 10^8$	$0.37156 \times 10^8$	$1.81883 \times 10^8$	$1.05178 \times 10^8$
$T_o$	$2.46520 \times 10^6$	$2.27255 \times 10^6$	$2.42702 \times 10^6$	$2.56040 \times 10^6$
$B_{sat}$	31.2330	101.5899	5.6944	7.1224
$\chi^2$	$9.8928 \times 10^{-4}$	0.0014	$5.1410 \times 10^{-4}$	$4.9274 \times 10^{-4}$
Population size	8	8	8	8
Generation	25	25	25	25

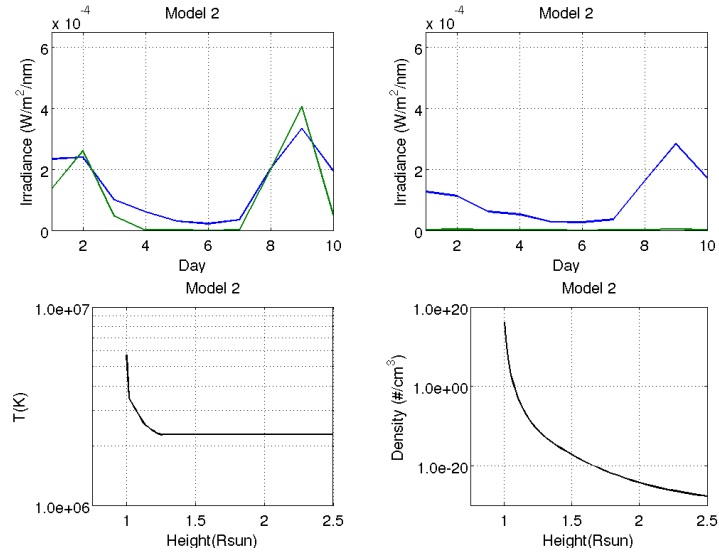
SOURCE: Author

Figure 2.18 - Fit 21.1nm and 33.5nm using the model 1. Upper panel: Solar Spectral Irradiance from observational data (green line) and modelled (blue line), left panel: 21.1nm and right panel: 33.5nm. Lower panel: average temperature profiles in all layers (left panel) and average density profiles in all layers (right panel).



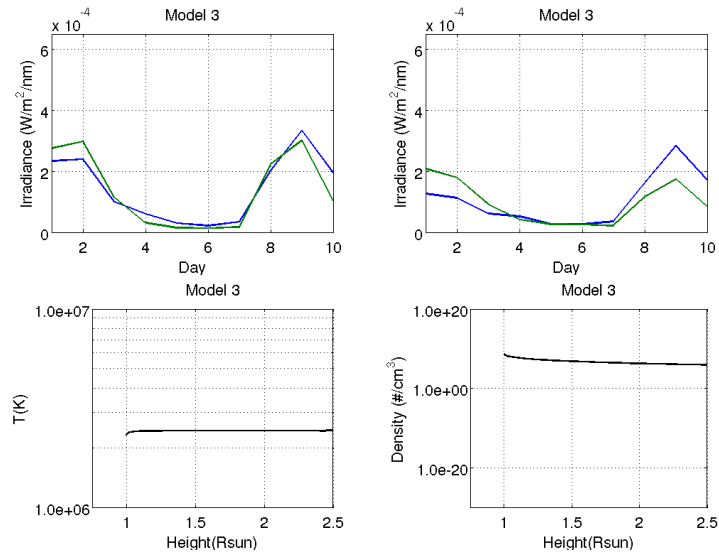
SOURCE: Author

Figure 2.19 - Fit 21.1nm and 33.5nm using the model 2. Upper panel: Solar Spectral Irradiance from observational data (green line) and modelled (blue line), left panel: 21.1nm and right panel: 33.5nm. Lower panel: average temperature profiles in all layers (left panel) and average density profiles in all layers (right panel).



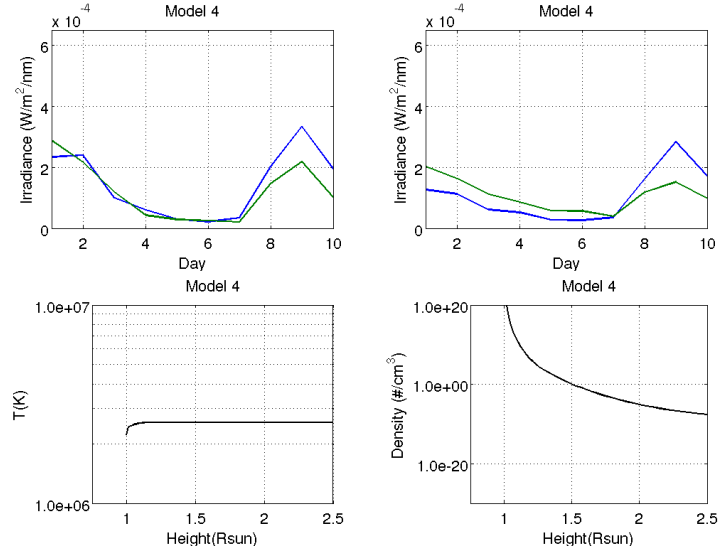
SOURCE: Author

Figure 2.20 - Fit 21.1nm and 33.5nm using the model 3. Upper panel: Solar Spectral Irradiance from observational data (green line) and modelled (blue line), left panel: 21.1nm and right panel: 33.5nm. Lower panel: average temperature profiles in all layers (left panel) and average density profiles in all layers (right panel).



SOURCE: Author

Figure 2.21 - Fit 21.1nm and 33.5nm using the model 4. Upper panel: Solar Spectral Irradiance from observational data (green line) and modelled (blue line), left panel: 21.1nm and right panel: 33.5nm. Lower panel: average temperature profiles in all layers (left panel) and average density profiles in all layers (right panel).



SOURCE: Author

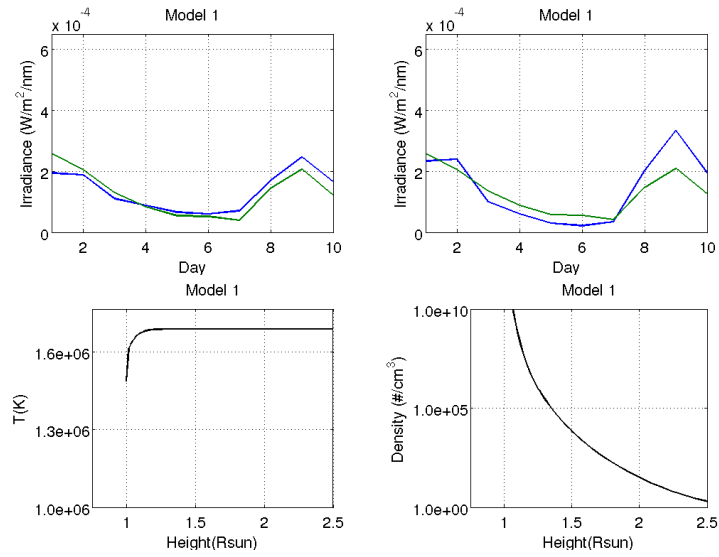
### Model fit between 19.3nm and 21.1nm

Table 2.9 - Model fit between 19.3nm and 21.1nm describes the value parameters ( $\gamma$ ,  $\alpha$ ,  $N_o$ ,  $T_o$  and  $B_{sat}$ ) for each model and information about the optimization algorithm (Population size and generations).

Parameter	Model 1	Model 2
$\gamma$	4.8864	2.0768
$\alpha$	-1.7328	-1.4224
$N_o$	$2.42667 \times 10^8$	$1.35367 \times 10^8$
$T_o$	$1.69435 \times 10^6$	$1.83920 \times 10^6$
$B_{sat}$	5.9766	3.3393
$\chi^2$	$2.7090 \times 10^{-4}$	$5.6040 \times 10^{-4}$
Population size	8	8
Generation	50	25

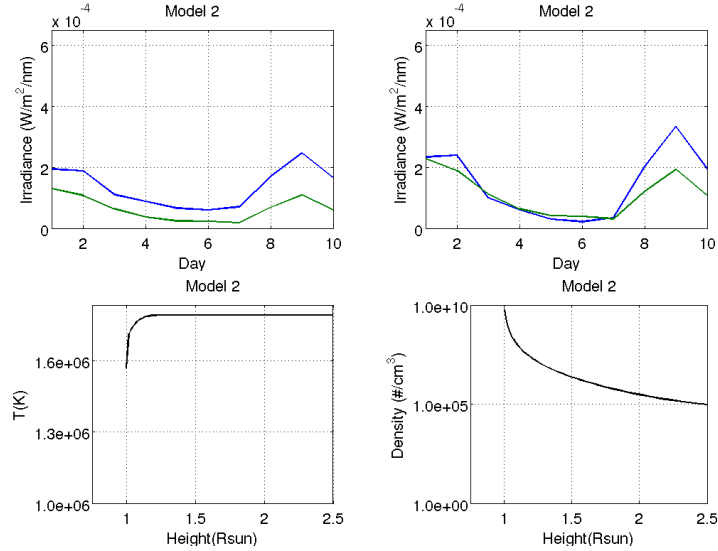
SOURCE: Author

Figure 2.22 - Fit 19.3nm and 21.1nm using the model 1. Upper panel: Solar Spectral Irradiance from observational data (green line) and modelled (blue line), left panel: 19.3nm and right panel: 21.1nm. Lower panel: average temperature profiles in all layers (left panel) and average density profiles in all layers (right panel).



SOURCE: Author

Figure 2.23 - Fit  $19.3nm$  and  $21.1nm$  using the model 2. Upper panel: Solar Spectral Irradiance from observational data (green line) and modelled (blue line), left panel:  $19.3nm$  and right panel:  $21.1nm$ . Lower panel: average temperature profiles in all layers (left panel) and average density profiles in all layers (right panel).



SOURCE: Author

### 2.3 Analysis of the results

In this section some fits using the Pikaia optimization algorithm were explored. The best fit in different cases is shown in the Table 2.10:

Table 2.10 - Results the best fit in different cases, from Table 2.1 to 2.2 (cells with cyan color).

Fit	Model
$17.1nm$	5
$19.3nm$	5
$33.5nm$	2
$21.1nm$	1 and 3
$17.1nm$ , $19.3nm$ and $21.1nm$	2
$17.1nm$ and $19.3nm$	1
$21.1nm$ and $33.5$	3
$19.3nm$ and $21.1$	1

SOURCE: Author

Using one wavelength the fit is in agreement with the characteristics presented previously. When it tries to fit three wavelengths simultaneously it is only possible to fit two of them (in the case of  $17.1nm$ ,  $19.3nm$  and  $21.1nm$ ) or none of them (in the case  $17.1nm$ ,  $19.3nm$  and  $33.5nm$ ). But when the fit is made from two wavelengths simultaneously it is possible to fit and find the best solution (case  $17.1nm$  -  $19.3nm$ ,  $21.1nm$ - $33.5nm$  and  $19.3nm$ - $21.1nm$ ) using ten random points over the last two solar cycles.

The Solar Spectral Irradiance (SSI) was extended over the solar cycle 23 and 24. Four wavelengths  $17.1nm$ ,  $19.3nm$ ,  $21.1nm$  and  $33.5nm$  were used for this purpose. The parameters of the each model are shown in Table 2.10. The scatter plots were obtained in each case and the chi-squared test ( $\chi^2$ ) was calculated. Comparison between the observed uncertainty from TIMED/SEE and the difference between observational and modelled data were analyzed. The uncertainty at  $21.1nm$  is not available. Then, only the difference between observed and modelled data is shown for this wavelength.

Small interval was plot using as reference the best results from the chi-squared test in each case. Next, the behaviour will be described using the selected models in different intervals.

Using  $17.1nm$  model 5 it is possible to follow the Solar Spectral Irradiance (SSI) at  $17.1nm$  and  $19.3nm$  (Figure 2.24) during the solar cycle 23 and 24. The scatter plot (Figure 2.25) and the chi-squared test endorses this result.

Figure 2.24 - Solar Spectral Irradiance (SSI) using 17.1nm model 5 (green line) and Solar Spectral Irradiance (SSI) from TIMED/SEE (blue line) during the solar cycle 23 and 24. Upper panel: SSI at 17.1nm, middle panels: SSI at 19.3nm and 21.1nm, lower panel: SSI at 33.5nm.

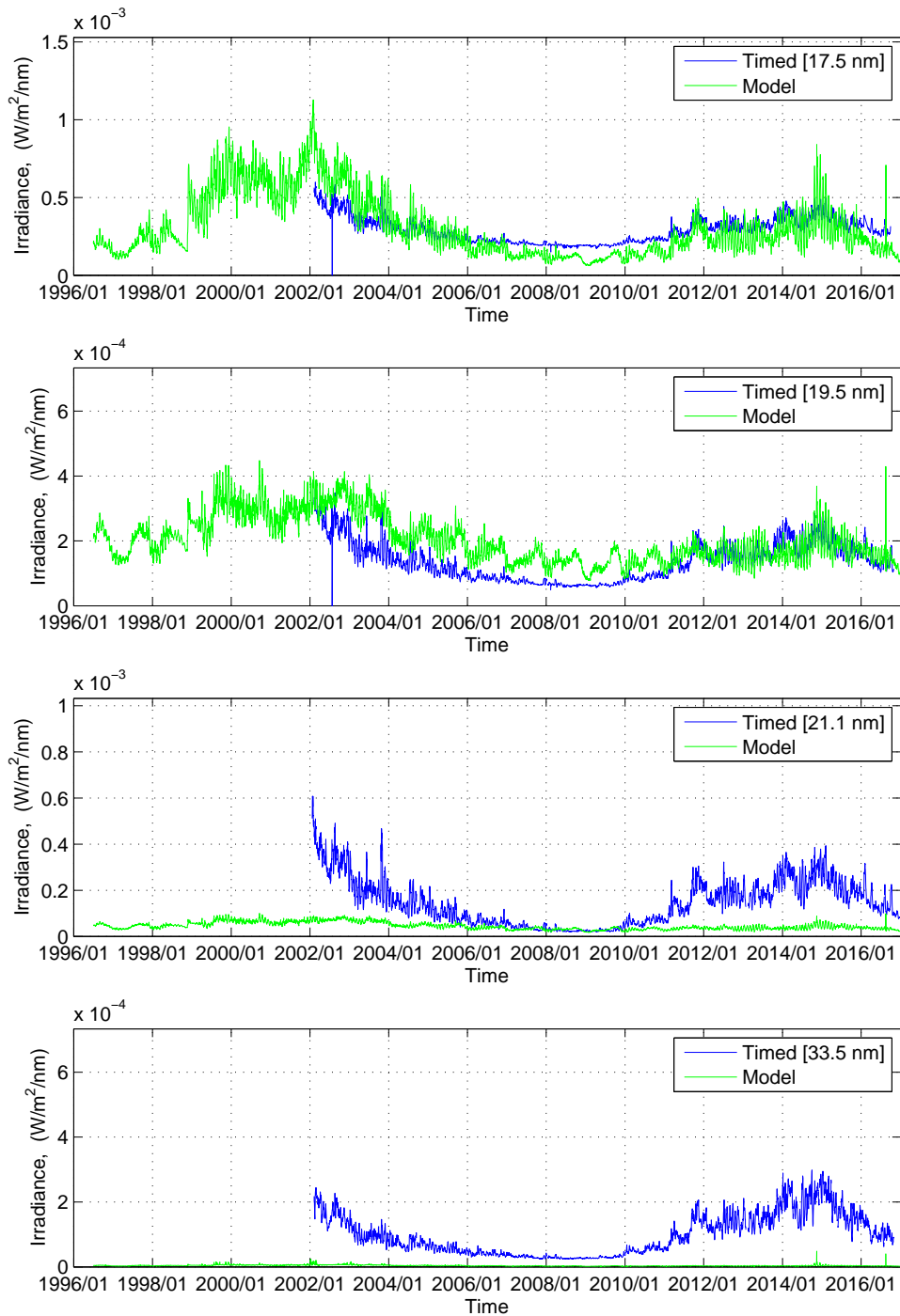
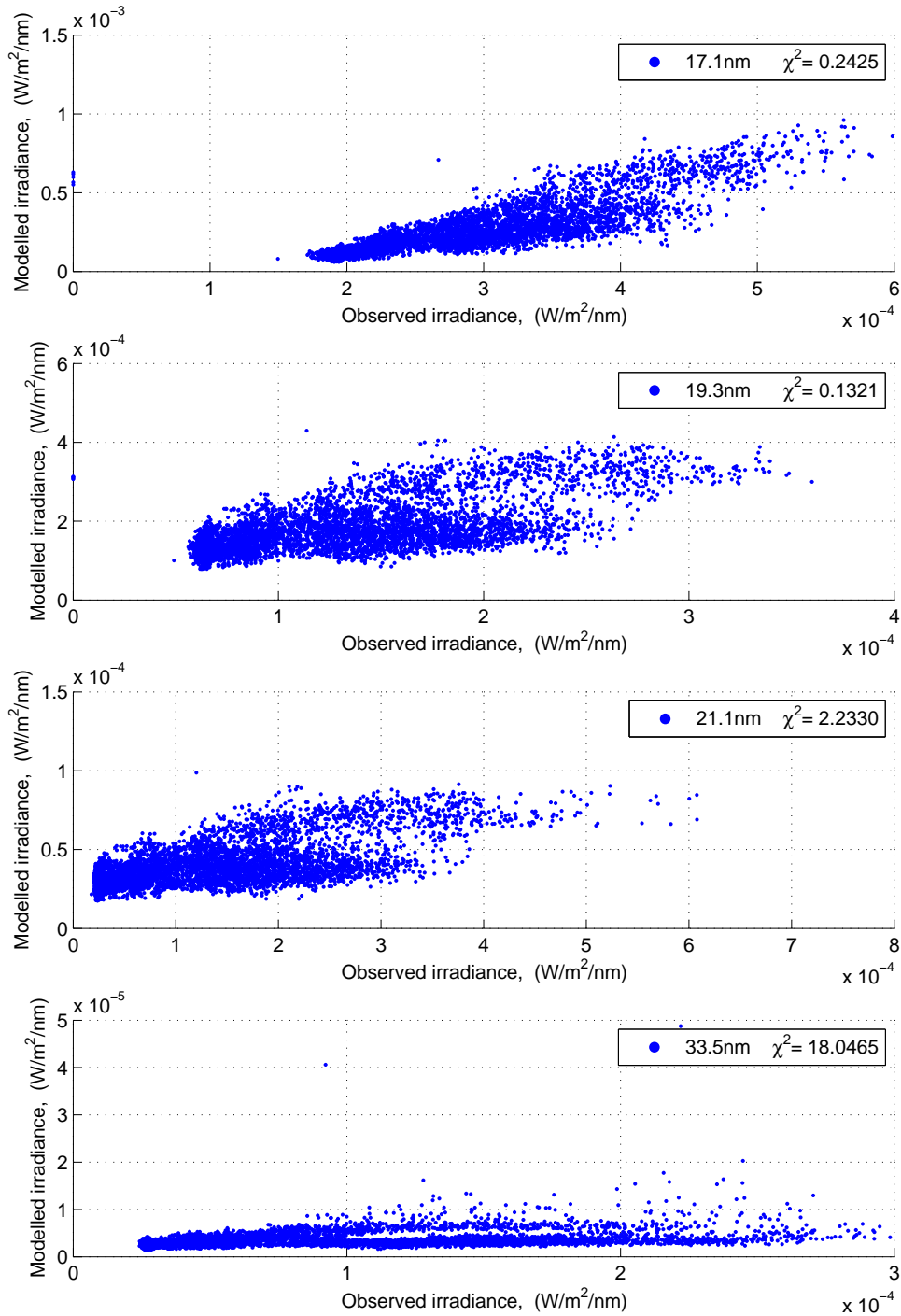
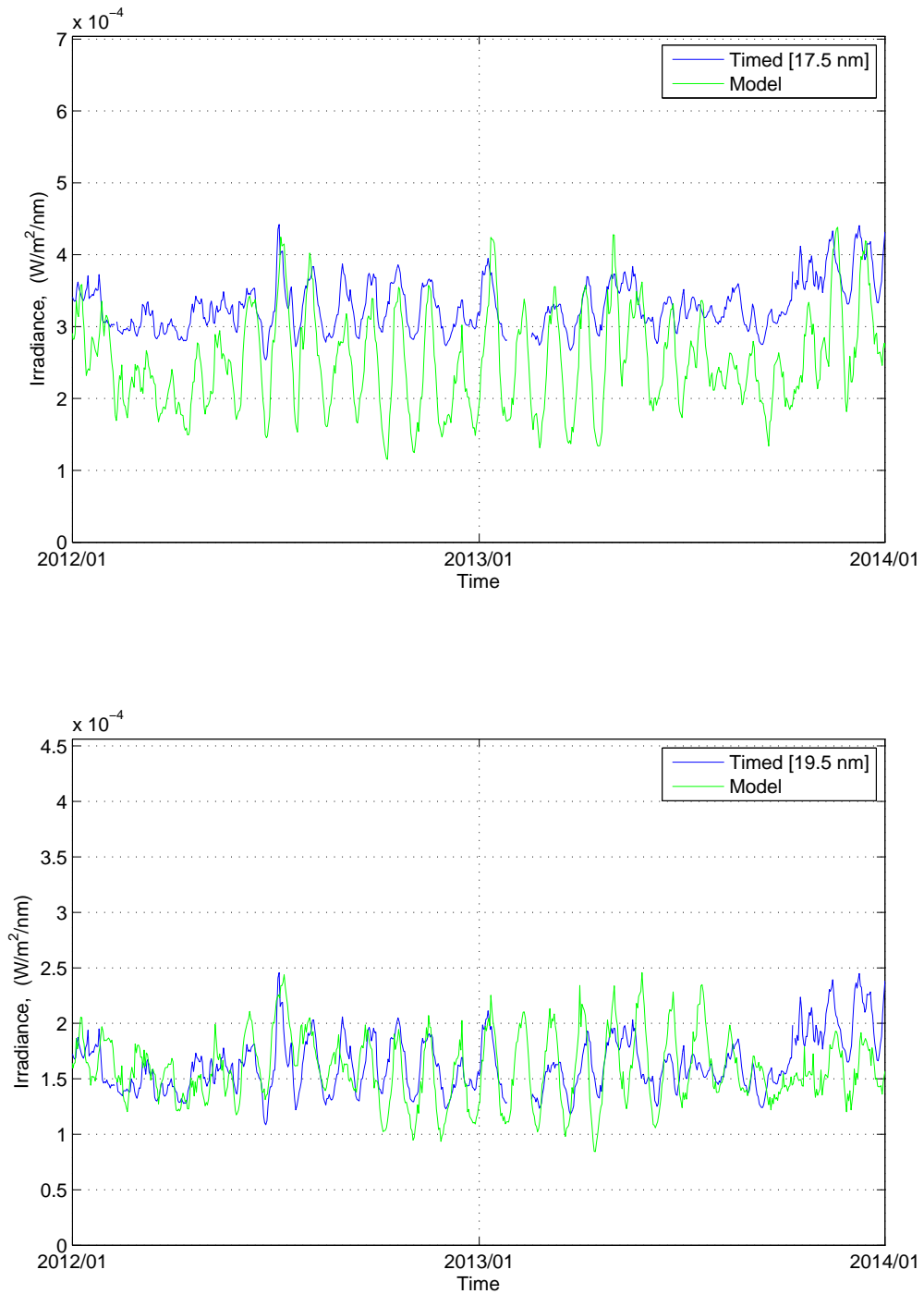


Figure 2.25 - Scatter plot using the parameters from 17.1nm model 5 and Chi-squared test ( $\chi^2$ ) in each case. Upper panel: scatter plot of 17.1nm, middle panels: scatter plot of 19.3nm and 21.1nm, lower panel: scatter plot of 33.5nm.



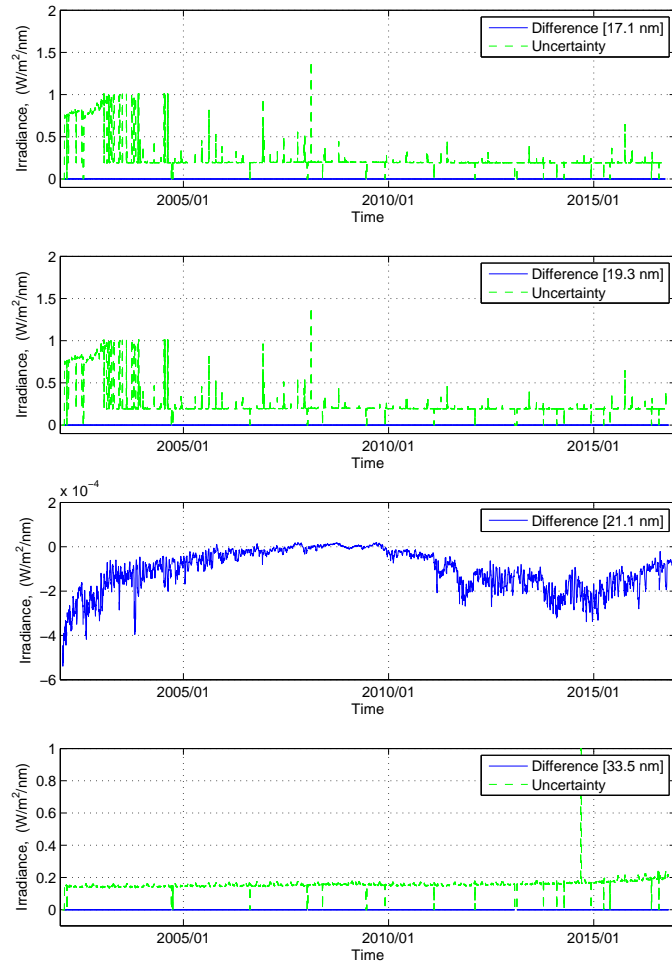
SOURCE: Author

Figure 2.26 - Solar Spectral Irradiance (SSI) using 17.1nm model 5 (green line) and Solar Spectral Irradiance (SSI) from TIMED/SEE (blue line) from Jan. 01 (2012) to Jan. 01 (2014). Upper panel: SSI at 17.1nm, lower panel: SSI at 19.5nm.



SOURCE: Author

Figure 2.27 - Comparison between the observed uncertainty from TIMED/SEE (dotted green line) and difference between observational and modelled data using the parameters from 17.1nm model 5 (blue line). Upper panel: analysis at 17.1nm, middle panels: analysis at 19.3nm and difference between observed and modelled data at 21.1nm, lower panel: analysis at 33.5nm.



SOURCE: Author

On the other hand, using 19.3nm model 5 it is possible to reproduce the Solar Spectral Irradiance (SSI) at 19.3nm, 21.1nm and 33.5nm (Figure 2.28) during the solar cycle 23 and 24. The scatter plot (Figure 2.29) and the chi-squared test to confirm this result.

Figure 2.28 - Solar Spectral Irradiance (SSI) using 19.3nm model 5 (green line) and Solar Spectral Irradiance (SSI) from TIMED/SEE (blue line) during the solar cycle 23 and 24. Upper panel: SSI at 17.1nm, middle panels: SSI at 19.3nm and 21.1nm, lower panel: SSI at 33.5nm.

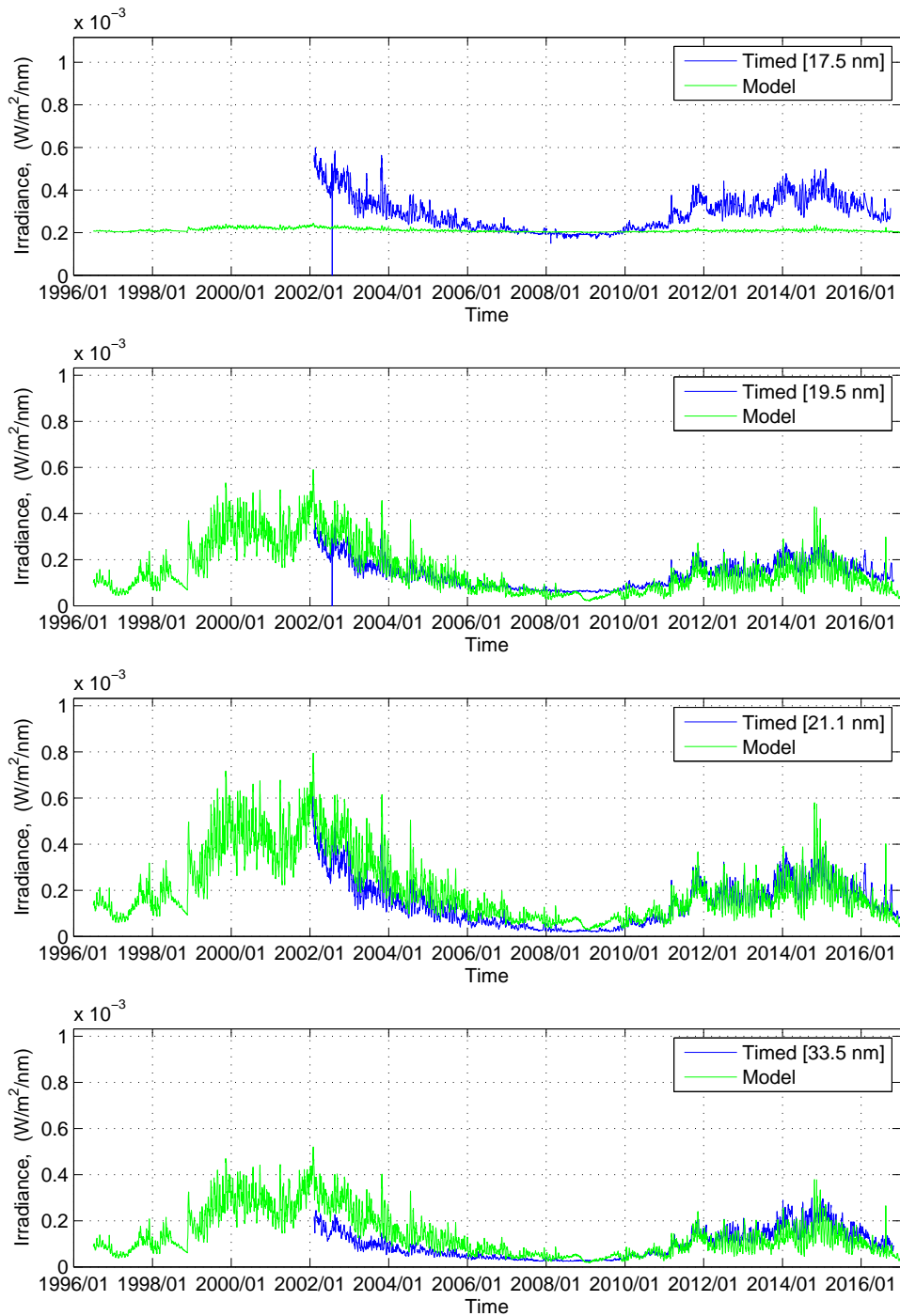
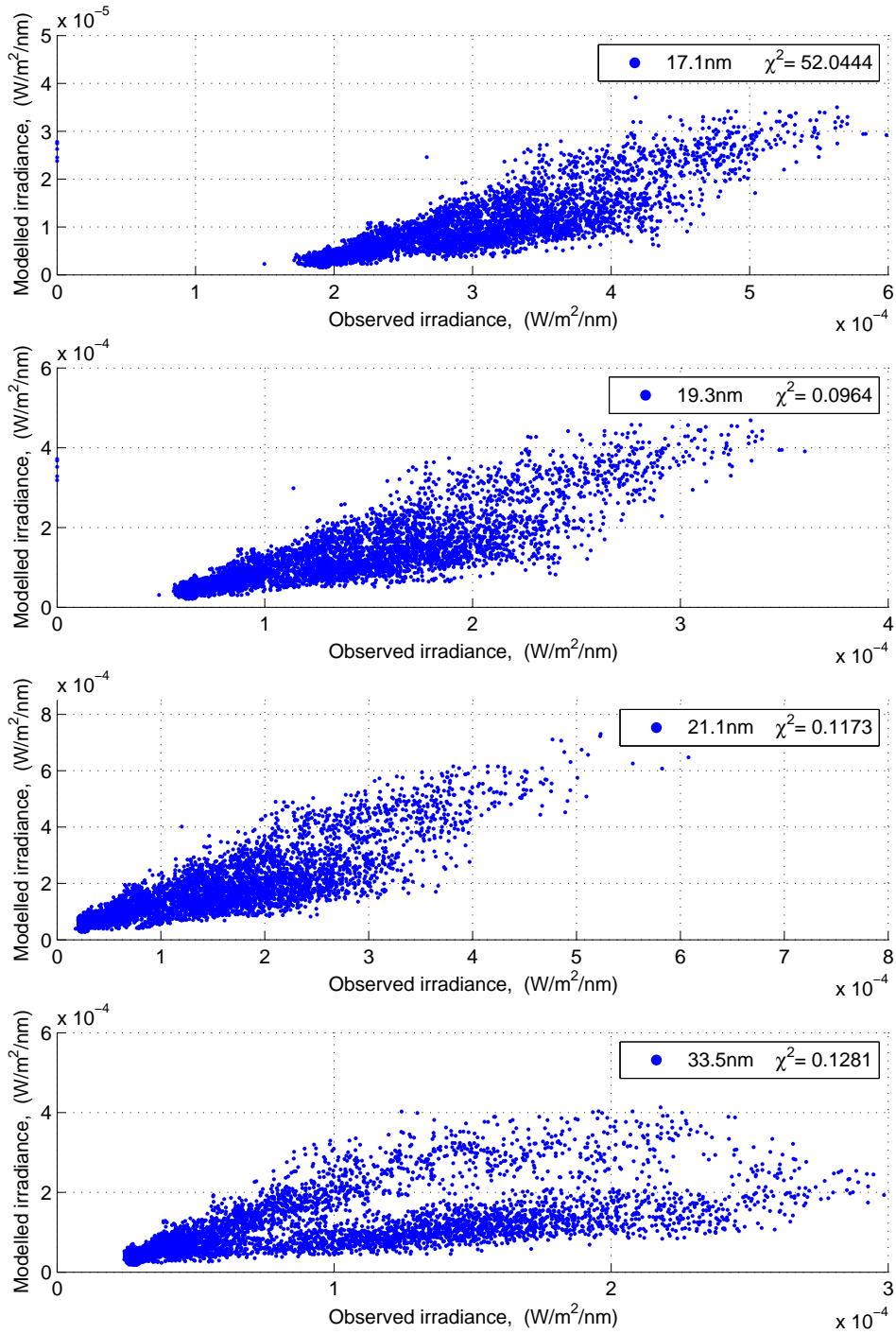


Figure 2.29 - Scatter plot using the parameters from 19.3nm model 5 and Chi-squared test ( $\chi^2$ ) in each case. Upper panel: scatter plot of 17.1nm, middle panels: scatter plot of 19.3nm and 21.1nm, lower panel: scatter plot of 33.5nm.



SOURCE: Author

Figure 2.30 - Solar Spectral Irradiance (SSI) using the parameters from 19.3nm model 5 (green line) and Solar Spectral Irradiance (SSI) from TIMED/SEE (blue line) from Jan. 01 (2012) to Jan. 01 (2014). Upper panel: SSI at 19.3nm, middle panels: SSI at 21.1nm, lower panel: SSI at 33.5nm.

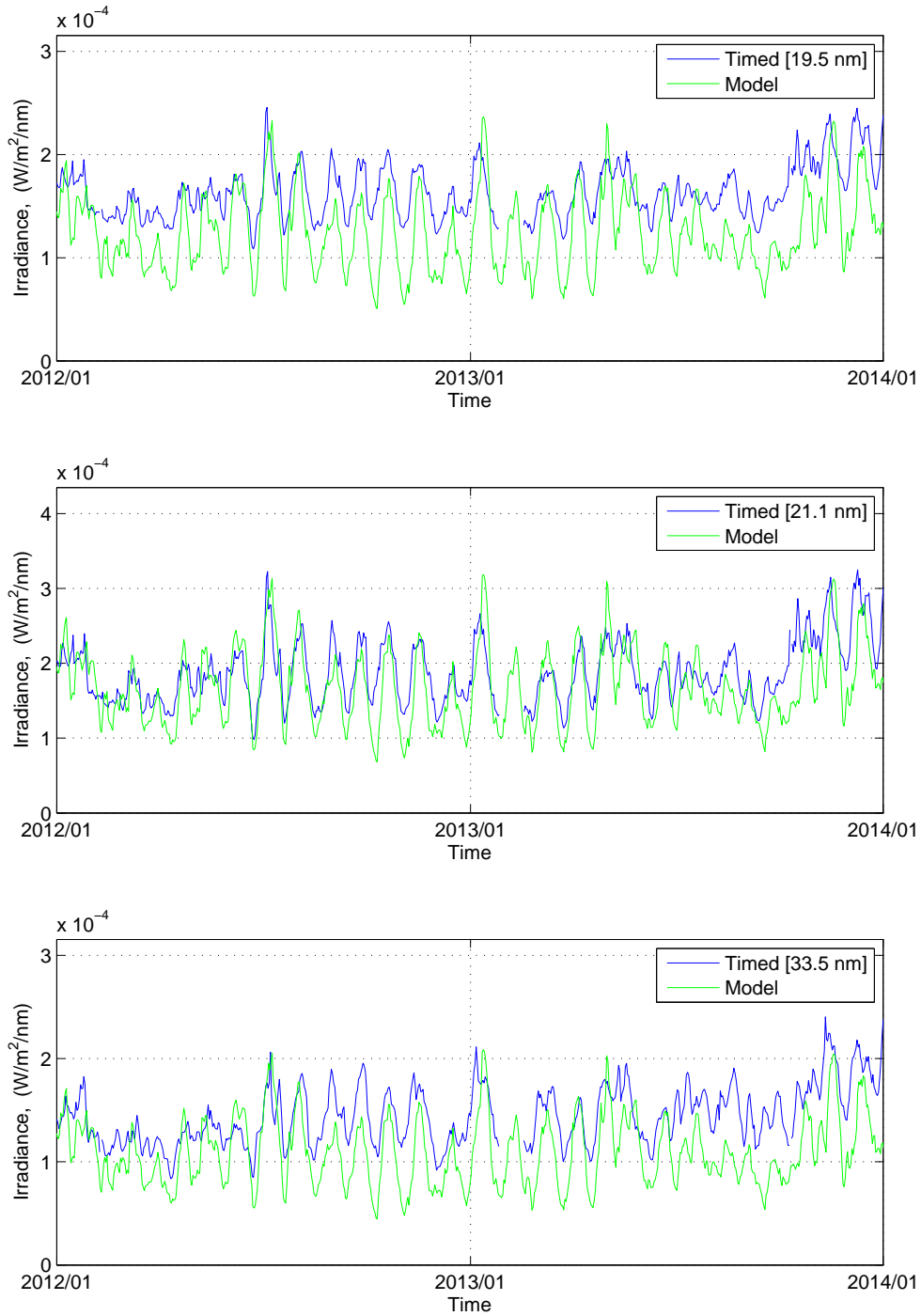
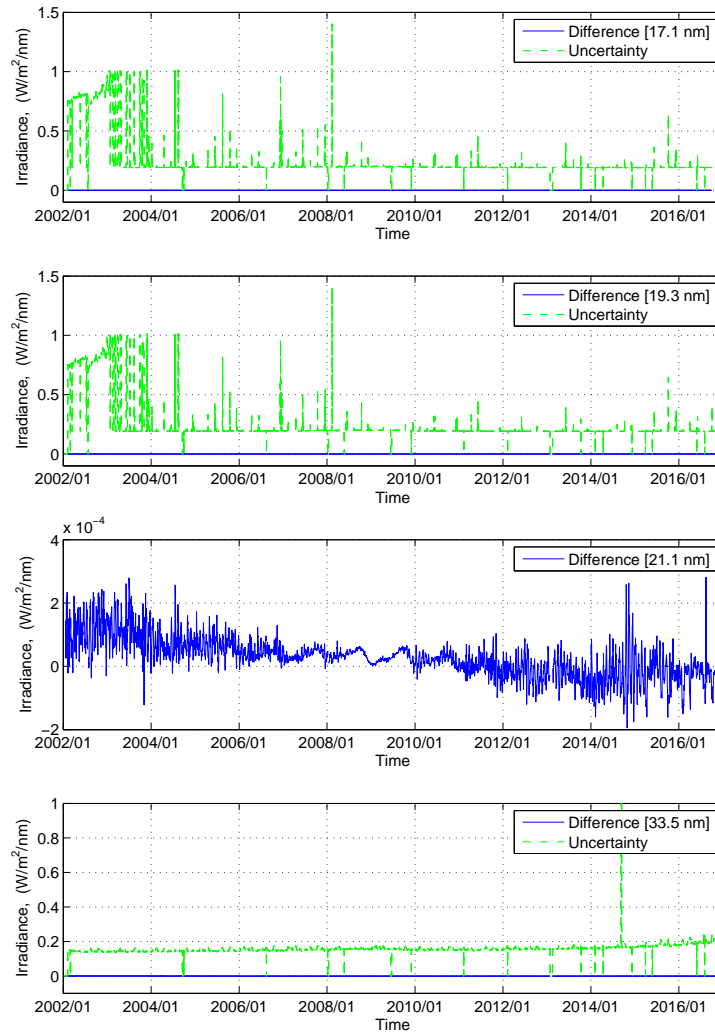


Figure 2.31 - Comparison between the observed uncertainty from TIMED/SEE (dotted green line) and difference between observational and modelled data using the parameters from 19.3nm model 5 (blue line). Upper panel: analysis at 17.1nm, middle panels: analysis at 19.3nm and difference between observed and modelled data at 21.1nm, lower panel: analysis at 33.5nm.



SOURCE: Author

Moreover, using 33.5nm model 2 it is possible to follow the Solar Spectral Irradiance (SSI) at 21.1nm and 33.5nm (Figure 2.32) during the solar cycle 23 and 24. The scatter plot (Figure 2.33) and the chi-squared test show the best goodness-of-fit.

Figure 2.32 - Solar Spectral Irradiance (SSI) using the parameters from 33.5nm model 2 (green line) and Solar Spectral Irradiance (SSI) from TIMED/SEE (blue line) during the solar cycle 23 and 24. Upper panel: SSI at 17.1nm, middle panels: SSI at 19.3nm and 21.1nm, lower panel: SSI at 33.5nm.

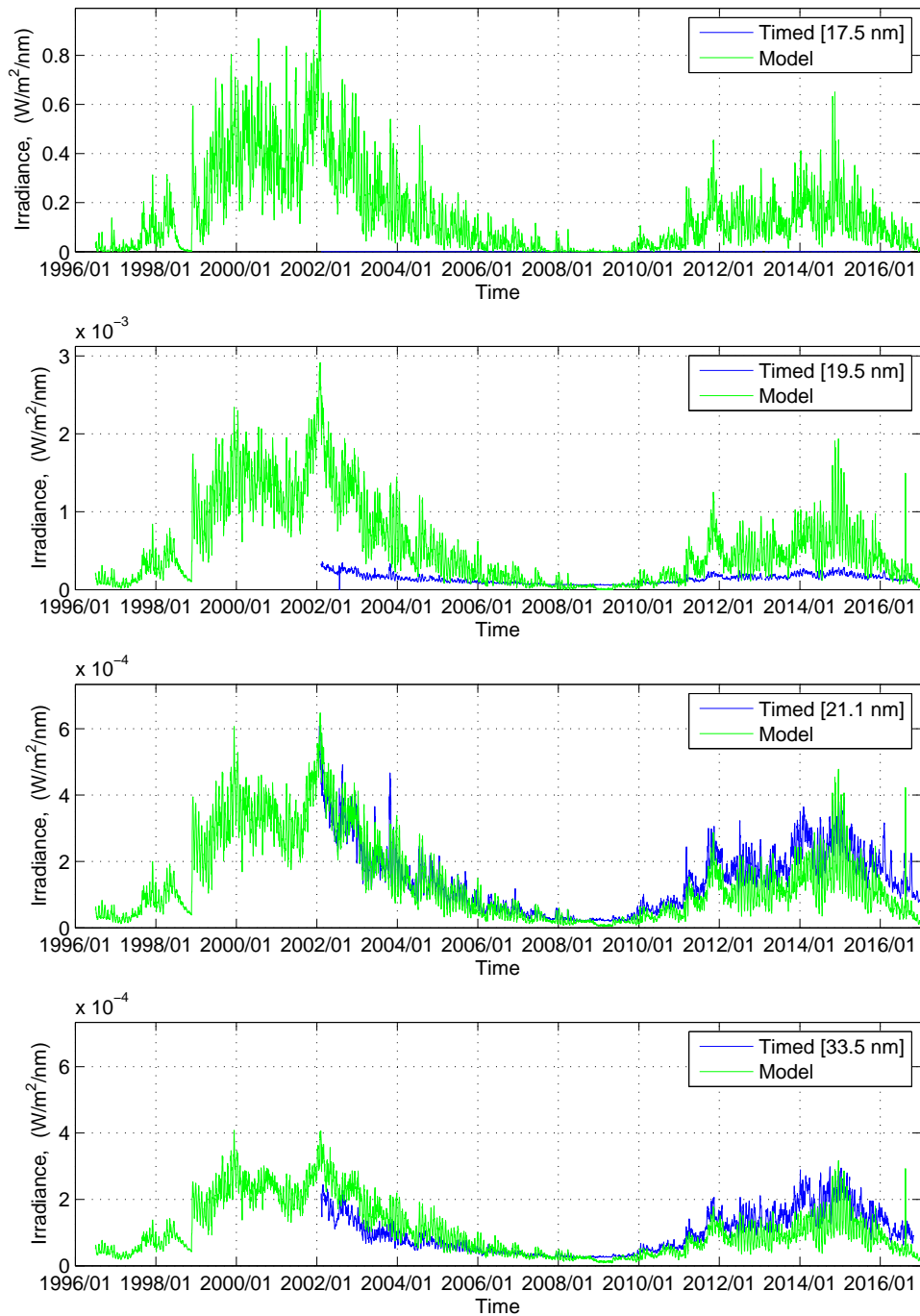
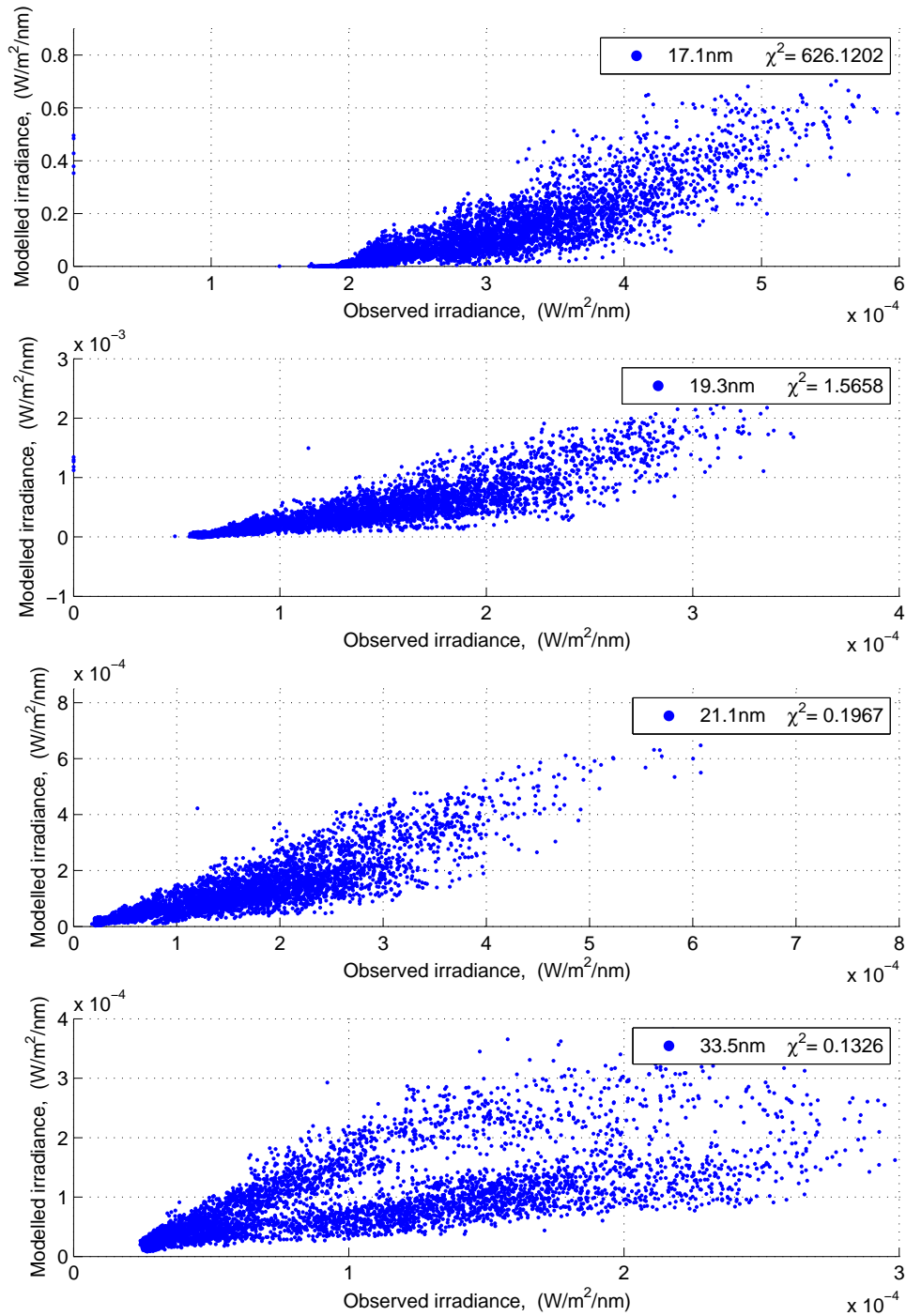


Figure 2.33 - Scatter plot using the parameters from 33.5nm model 2 and Chi-squared test ( $\chi^2$ ) in each case. Upper panel: scatter plot of 17.1nm, middle panels: scatter plot of 19.3nm and 21.1nm, lower panel: scatter plot of 33.5nm.



SOURCE: Author

Figure 2.34 - Solar Spectral Irradiance (SSI) using the parameters from 33.5nm model 2 (green line) and Solar Spectral Irradiance (SSI) from TIMED/SEE (blue line) from Jan. 01 (2010) to Dec. 01 (2010). Upper panel: SSI at 21.1nm, lower panel: SSI at 33.5nm.

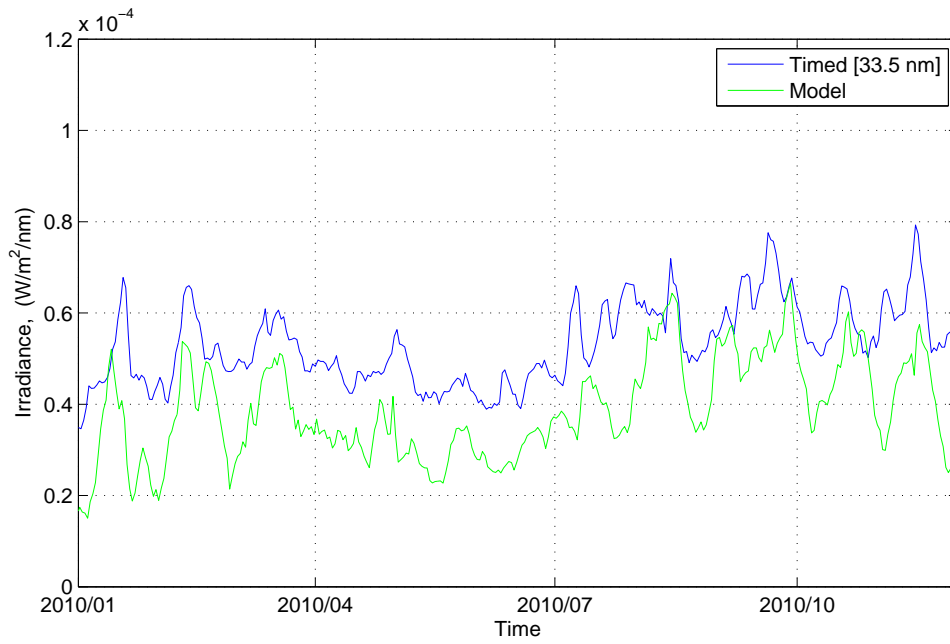
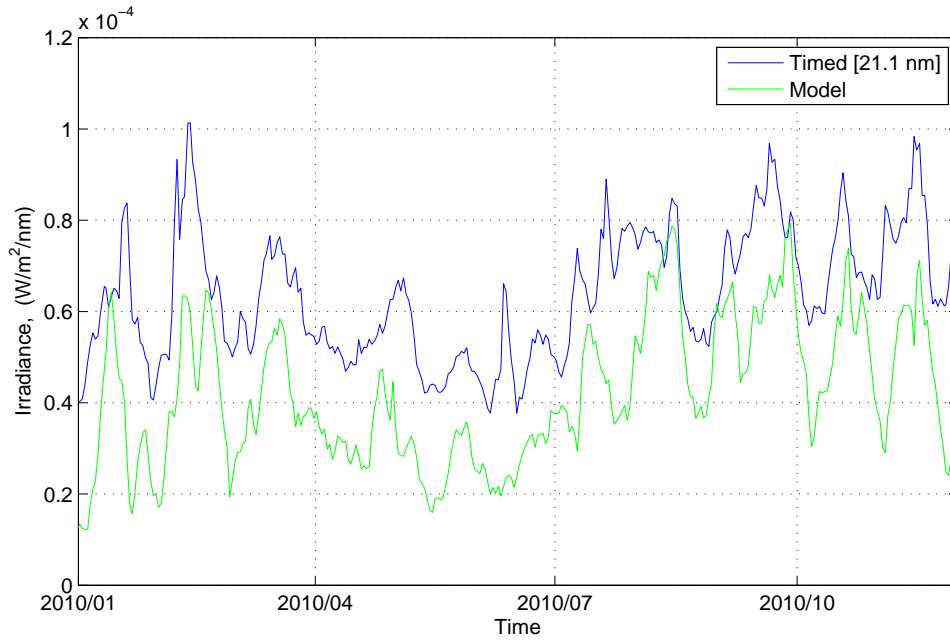
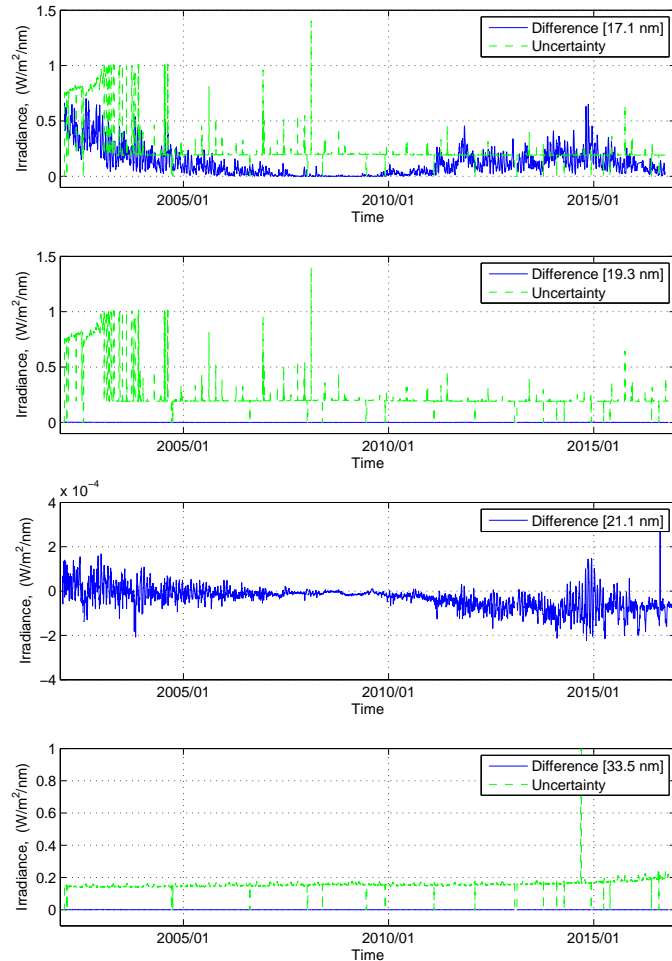


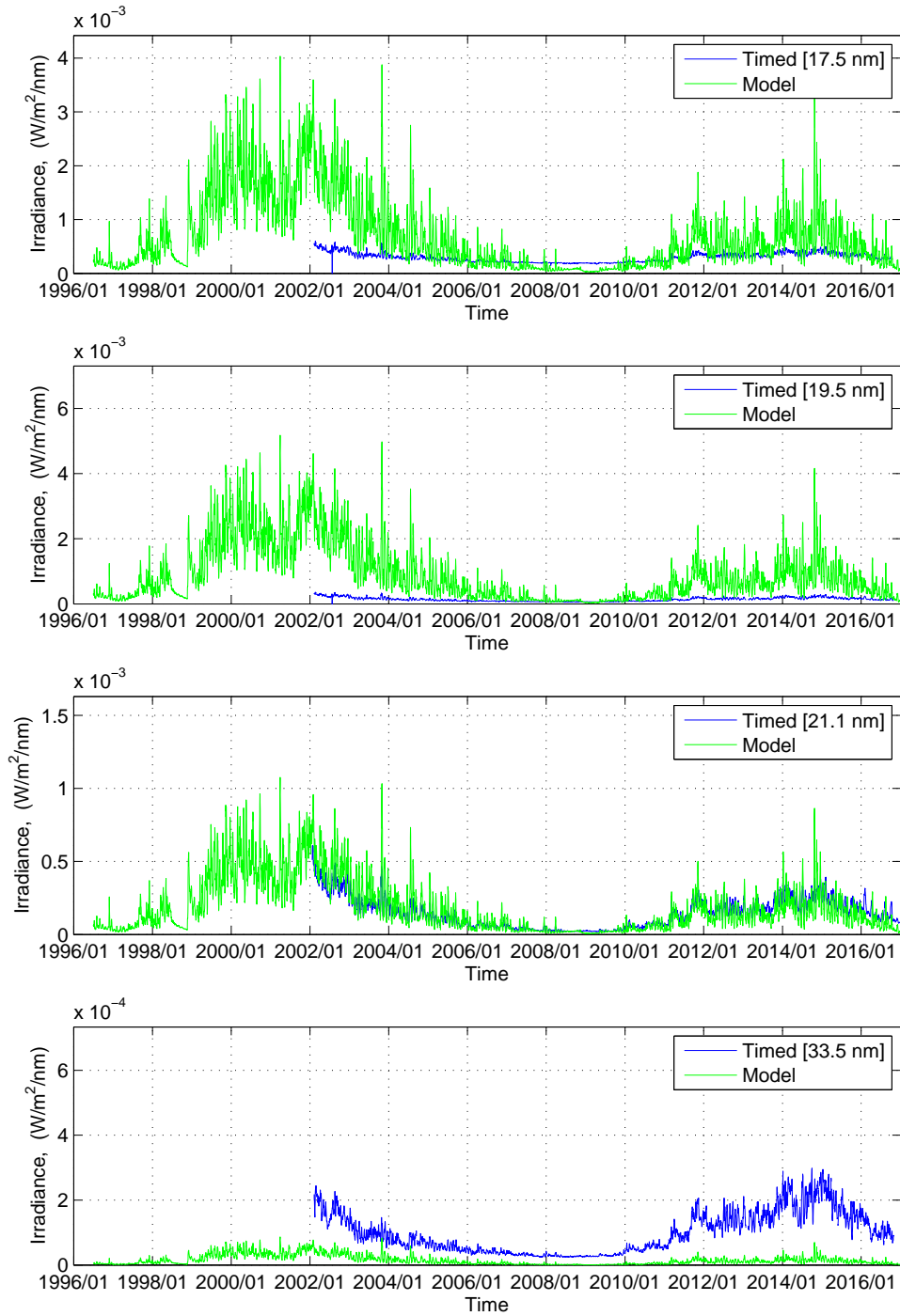
Figure 2.35 - Comparison between the observed uncertainty from TIMED/SEE (dotted green line) and difference between observational and modelled data using the parameters from 33.5nm model 2 (blue line). Upper panel: analysis at 17.1nm, middle panels: analysis at 19.3nm and difference between observed and modelled data at 21.1nm, lower panel: analysis at 33.5nm.



SOURCE: Author

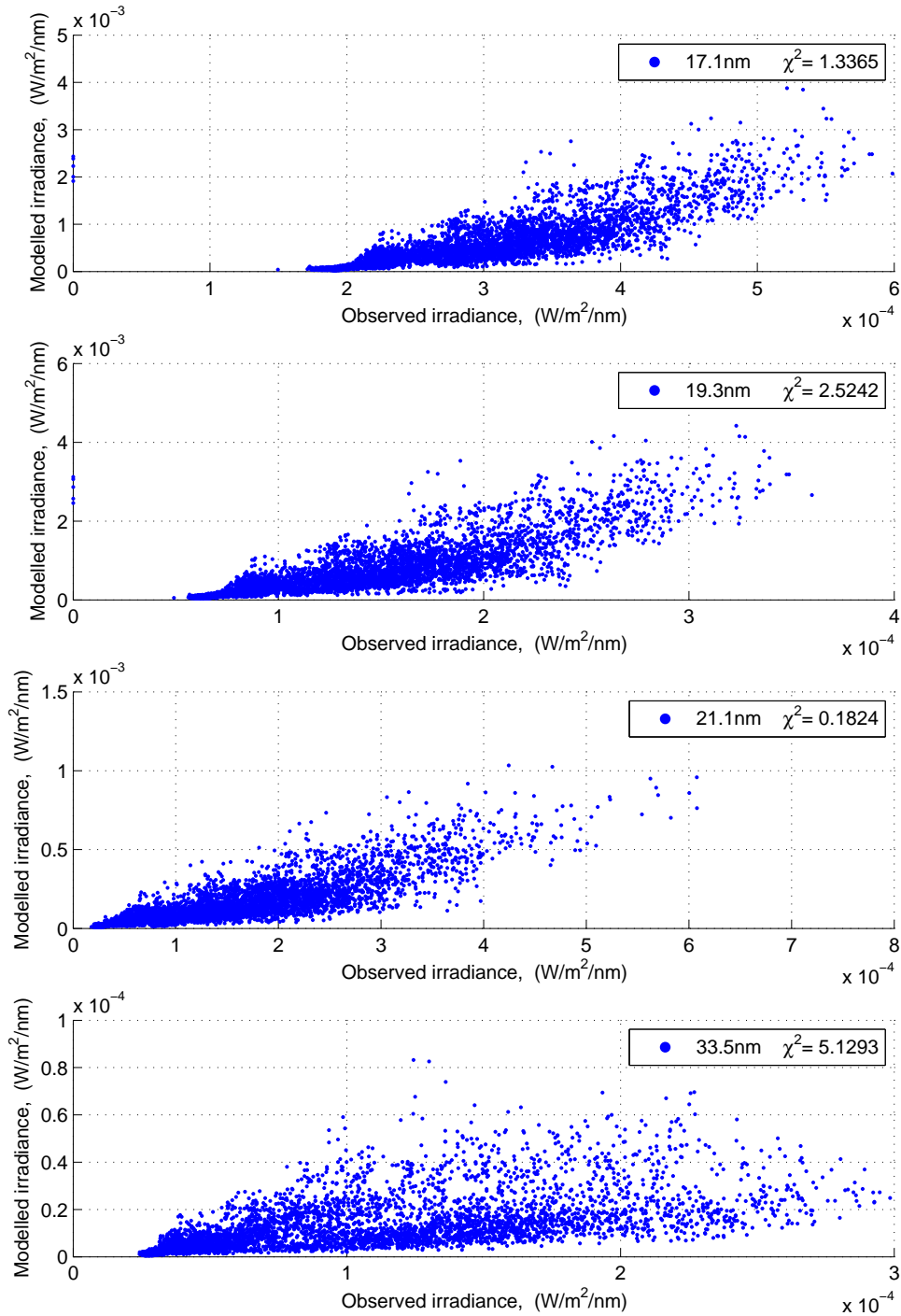
Furthermore, using 21.1nm model 1 it is possible to fit one wavelength 21.1nm (Figure 2.36). This behaviour is evident in the scatter plot (Figure 2.37) and the lower value of chi-squared test is present at 21.1nm. Also, using 21.1nm model 3 parameters it is not possible to follow none of them (Figure 2.40 and 2.41).

Figure 2.36 - Solar Spectral Irradiance (SSI) using the parameters from 21.1nm model 1 (green line) and Solar Spectral Irradiance (SSI) from TIMED/SEE (blue line) during the solar cycle 23 and 24. Upper panel: SSI at 17.1nm, middle panels: SSI at 19.3nm and 21.1nm, lower panel: SSI at 33.5nm.



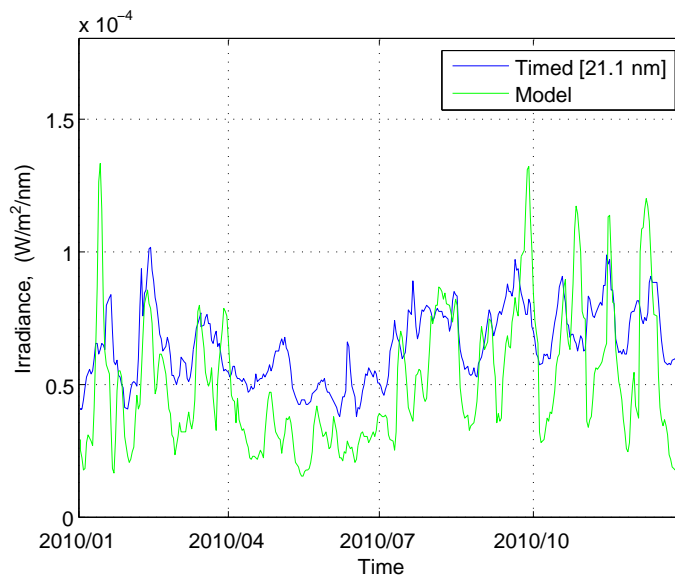
SOURCE: Author

Figure 2.37 - Scatter plot using the parameters from 21.1nm model 1 and Chi-squared test ( $\chi^2$ ) in each case. Upper panel: scatter plot of 17.1nm, middle panels: scatter plot of 19.3nm and 21.1nm, lower panel: scatter plot of 33.5nm.



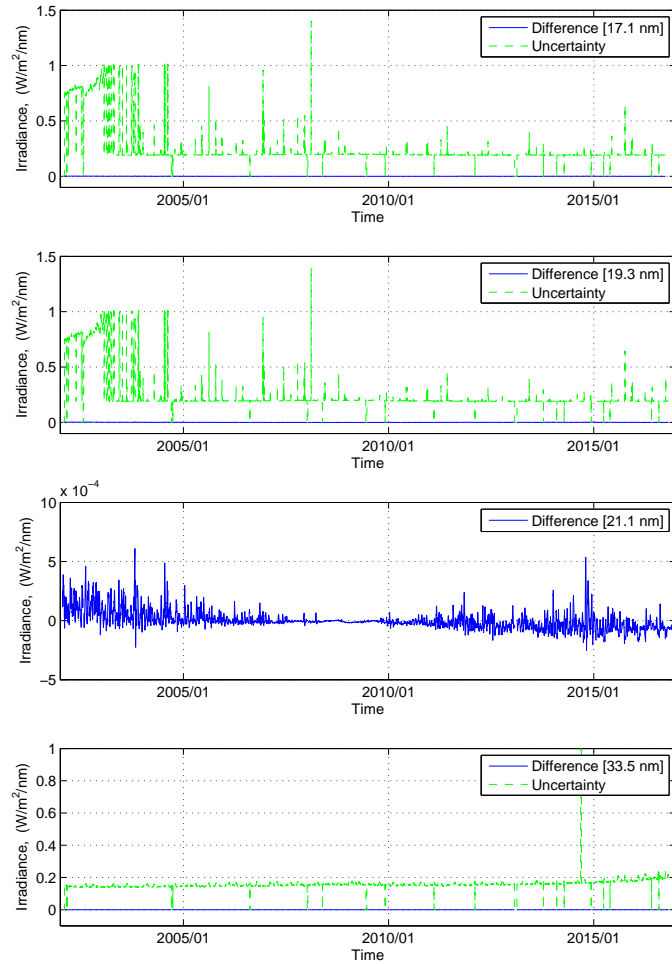
SOURCE: Author

Figure 2.38 - Solar Spectral Irradiance (SSI) using the parameters from 21.1nm model 1 (green line) and Solar Spectral Irradiance (SSI) from TIMED/SEE (blue line) from Jan. 01 (2010) to Dec. 31 (2010).



SOURCE: Author

Figure 2.39 - Comparison between the observed uncertainty from TIMED/SEE (dotted green line) and difference between observational and modelled data using the parameters from 21.1nm model 1 (blue line). Upper panel: analysis at 17.1nm, middle panels: analysis at 19.3nm and difference between observed and modelled data at 21.1nm, lower panel: analysis at 33.5nm.



SOURCE: Author

Figure 2.40 - Solar Spectral Irradiance (SSI) using the parameters from 21.1nm model 3 (green line) and Solar Spectral Irradiance (SSI) from TIMED/SEE (blue line) during the solar cycle 23 and 24. Upper panel: SSI at 17.1nm, middle panels: SSI at 19.3nm and 21.1nm, lower panel: SSI at 33.5nm.

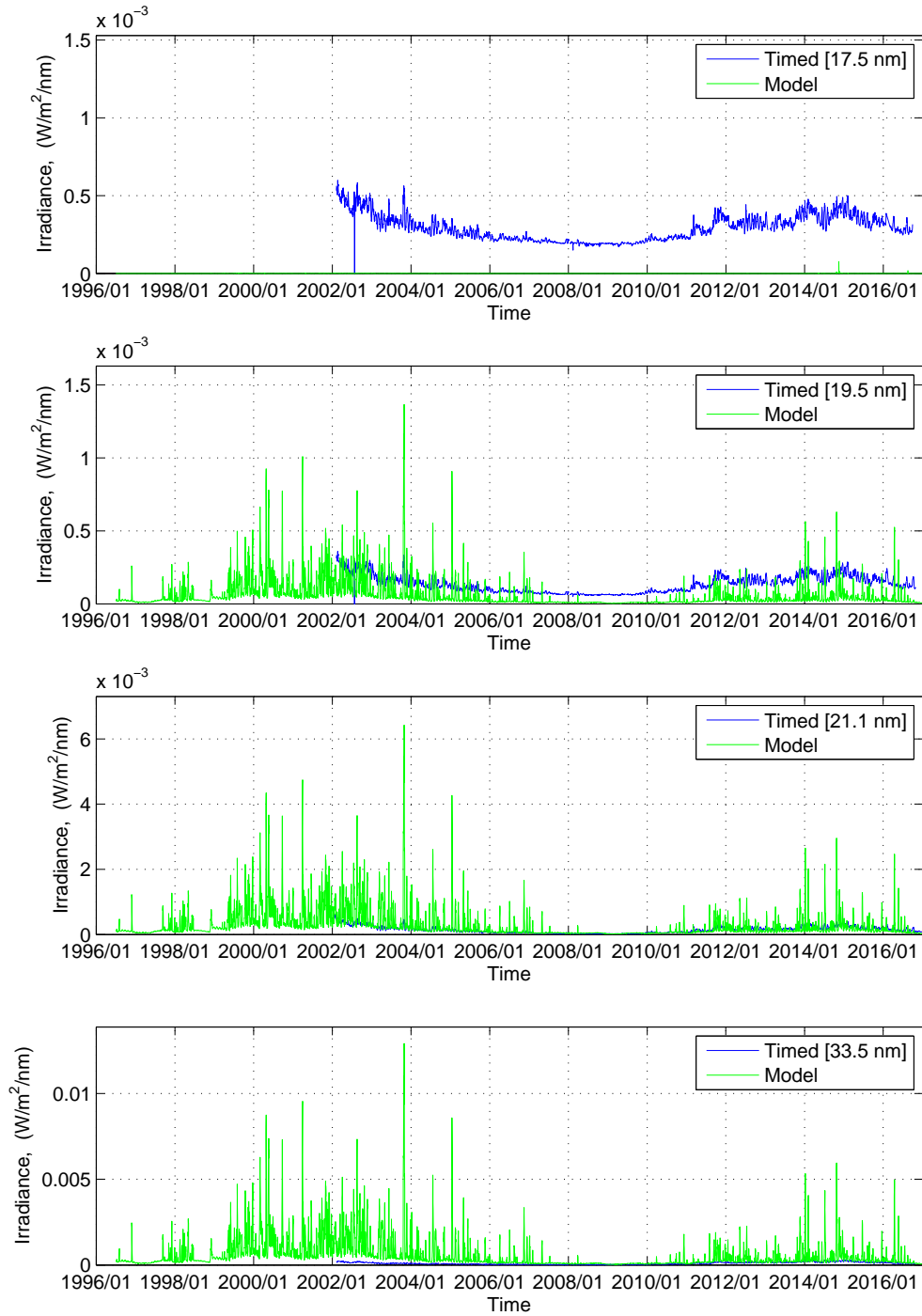
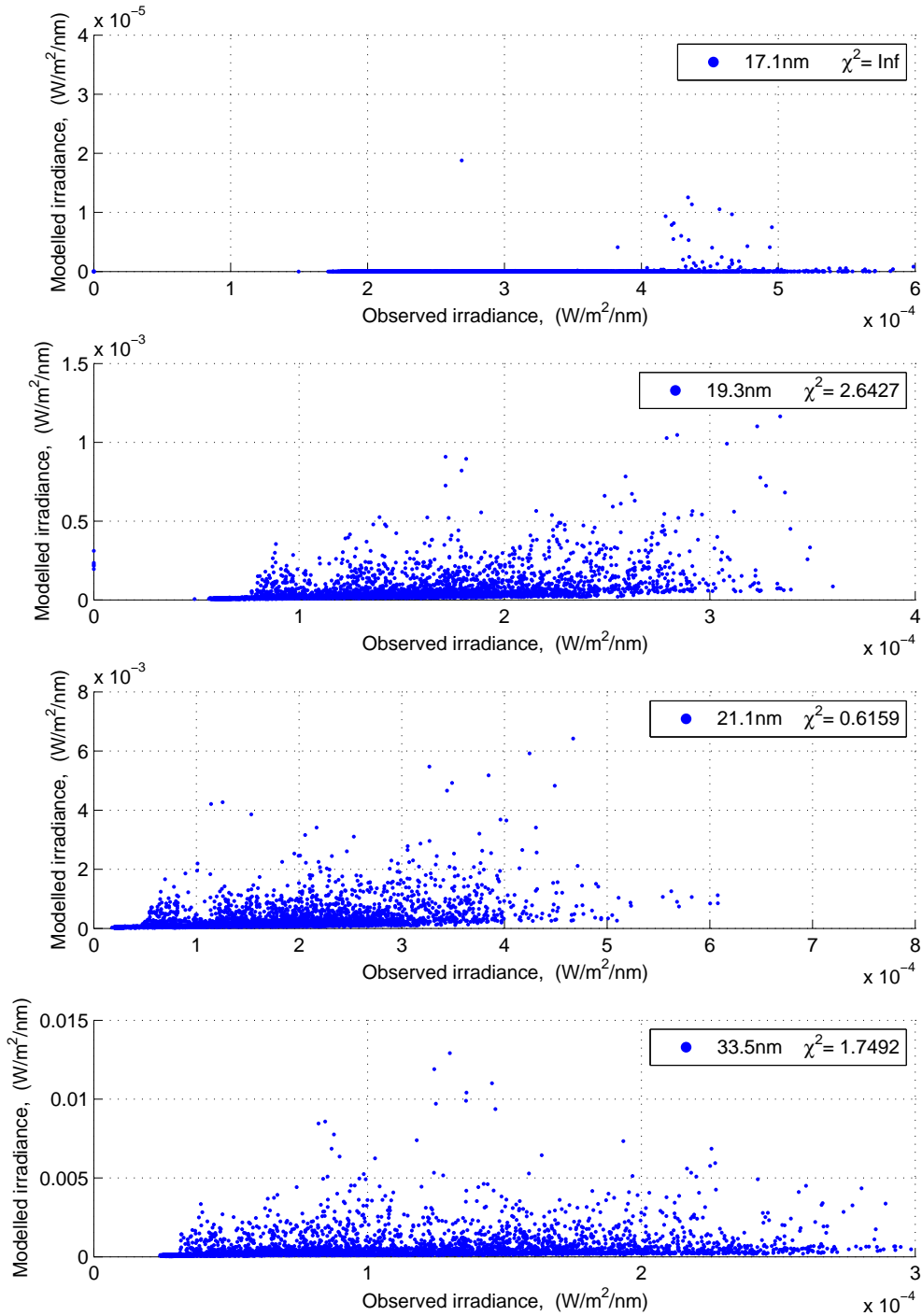
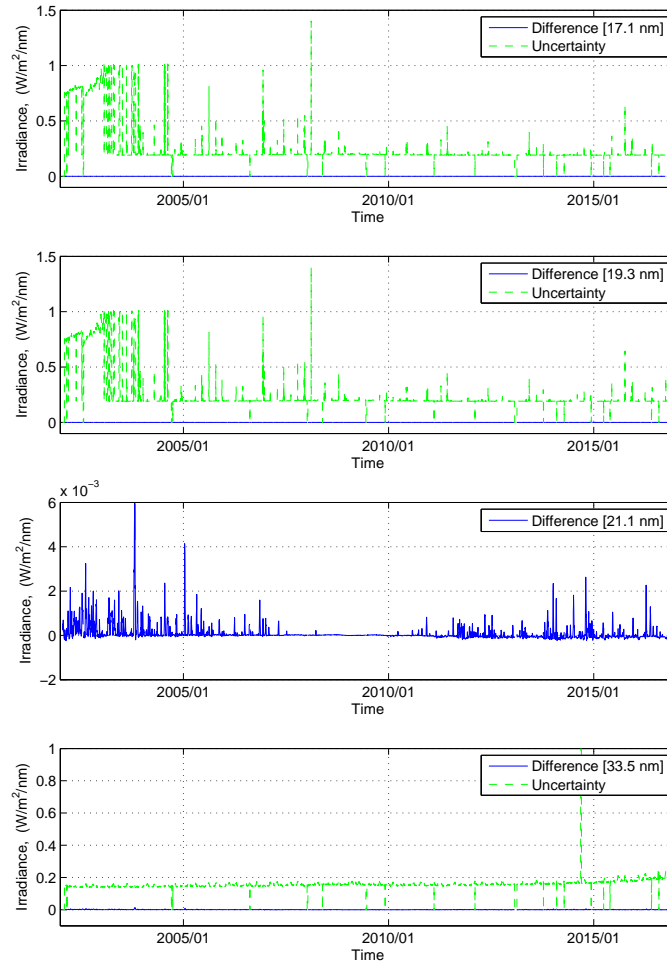


Figure 2.41 - Scatter plot using the parameters from 21.1nm model 3 and Chi-squared test ( $\chi^2$ ) in each case. Upper panel: scatter plot of 17.1nm, middle panels: scatter plot of 19.3nm and 21.1nm, lower panel: scatter plot of 33.5nm.



SOURCE: Author

Figure 2.42 - Comparison between the observed uncertainty from TIMED/SEE (dotted green line) and difference between observational and modelled data using the parameters from 21.1nm model 3 (blue line). Upper panel: analysis at 17.1nm, middle panels: analysis at 19.3nm and difference between observed and modelled data at 21.1nm, lower panel: analysis at 33.5nm.



SOURCE: Author

Besides, using 17.1nm, 19.3nm and 21.1nm model 2 one can follow four wavelengths 17.1, 19.3, 21.1 and 33.5nm (Figure 2.43). But values of chi-squared test show the lower fit to be 17.1nm (Figure 2.44). Using 17.1nm and 19.3nm model 2 it is possible to reproduce only two wavelengths 17.1 and 19.3nm (Figure 2.47). The values of chi-squared test and the scatter plot show the best fit with 19.3nm (Figure 2.48).

Figure 2.43 - Solar Spectral Irradiance (SSI) using the parameters from 17.1nm, 19.3nm and 21.1nm model 2 (green line) and Solar spectral Irradiance (SSI) from TIMED/SEE (blue line) during the solar cycle 23 and 24. Upper panel: SSI at 17.1nm, middle panels: SSI at 19.3nm and 21.1nm, lower panel: SSI at 33.5nm.

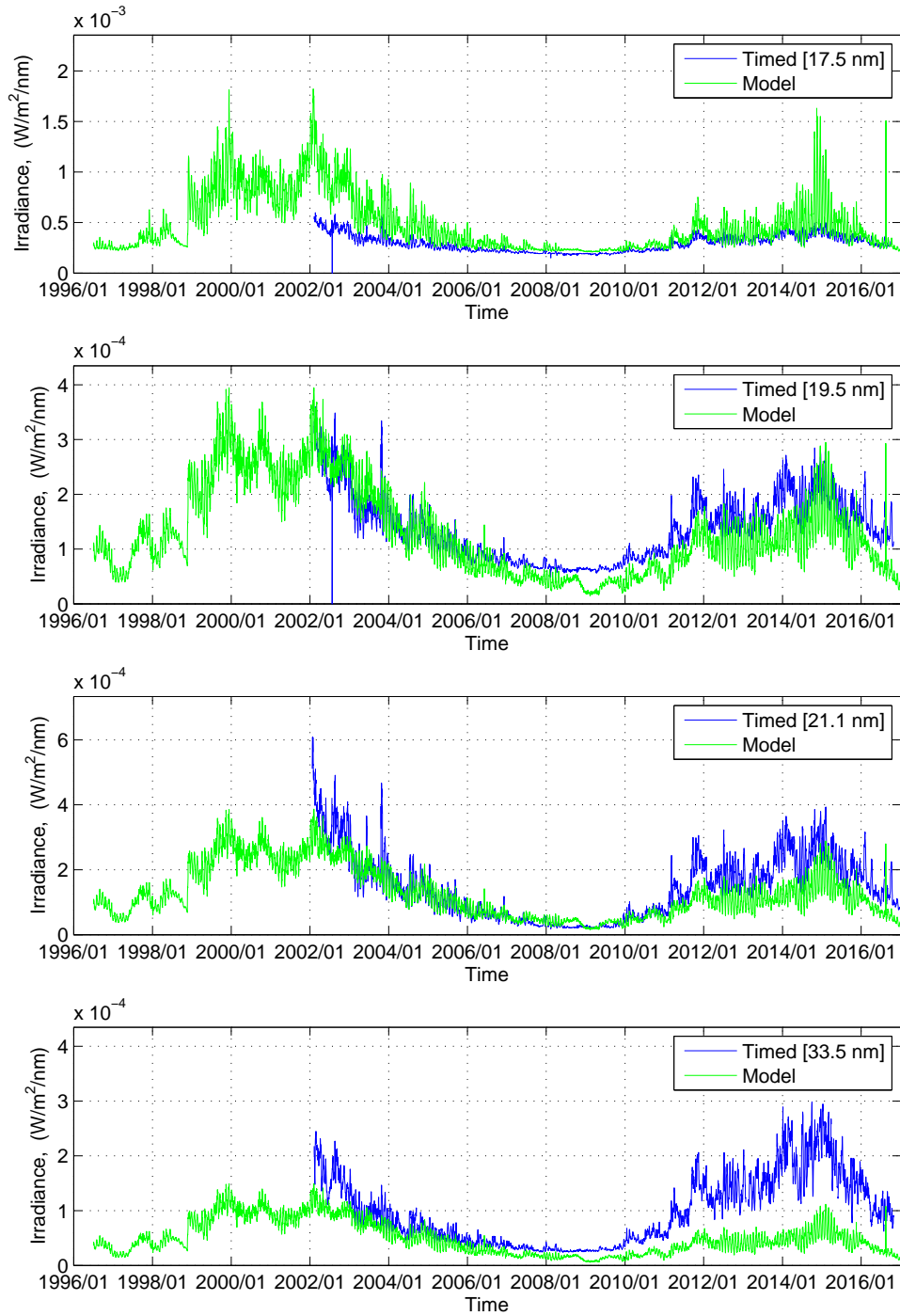
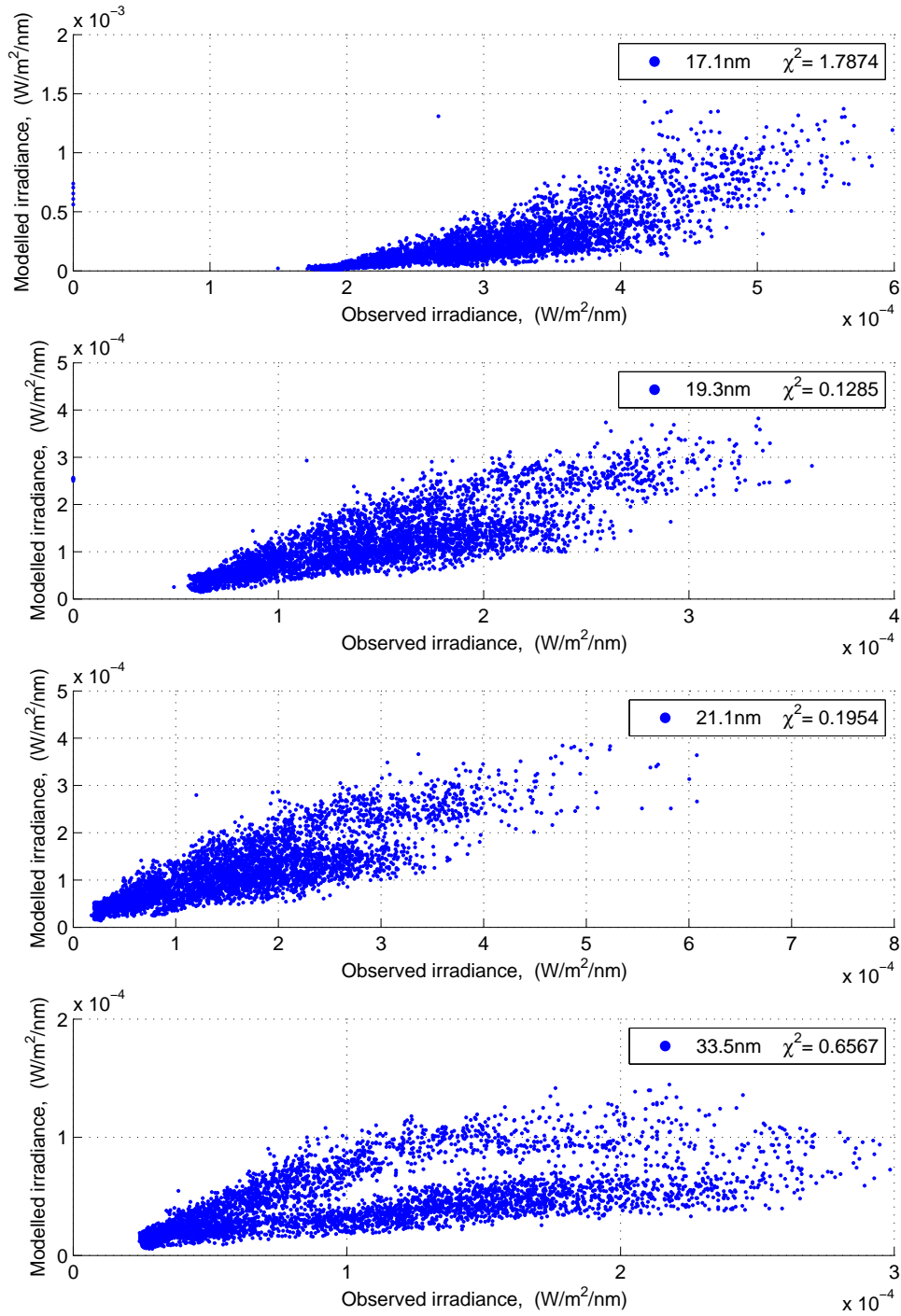


Figure 2.44 - Scatter plot using the parameters from 17.1nm, 19.3nm and 21.1nm model 2 and Chi-squared test ( $\chi^2$ ) in each case. Upper panel: scatter plot of 17.1nm, middle panels: scatter plot of 19.3nm and 21.1nm, lower panel: scatter plot of 33.5nm.



SOURCE: Author

Figure 2.45 - Solar Spectral Irradiance (SSI) using the parameters from 17.1nm, 19.3nm and 21.1nm model 2 (green line) and Solar spectral Irradiance (SSI) from TIMED/SEE (blue line) from Jan. 01 (2004) to Dec. 31 (2004). Upper panel: SSI at 17.1nm, middle panels: SSI at 19.3nm and 21.1nm, lower panel: SSI at 33.5nm.

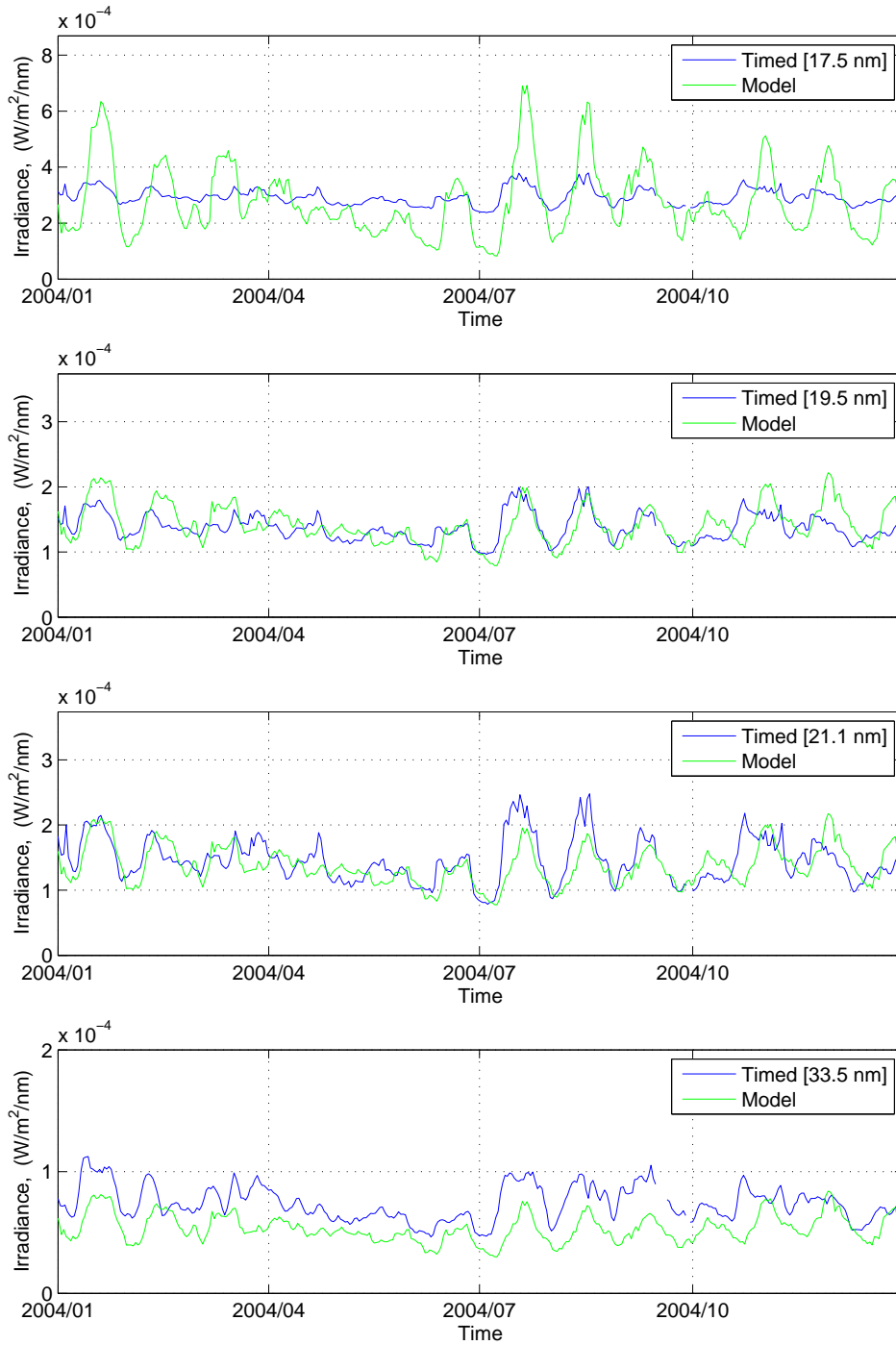
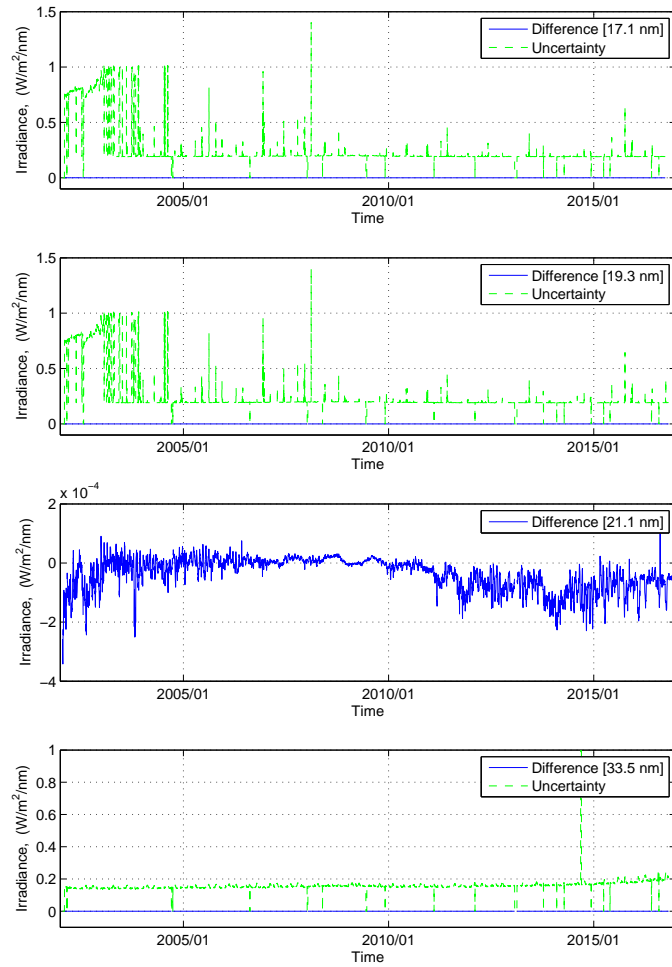


Figure 2.46 - Comparison between the observed uncertainty from TIMED/SEE (dotted green line) and difference between observational and modelled data using the parameters from 17.1nm, 19.3nm and 21.1nm model 2 (blue line). Upper panel: analysis at 17.1nm, middle panels: analysis at 19.3nm and difference between observed and modelled data at 21.1nm, lower panel: analysis at 33.5nm.



SOURCE: Author

Figure 2.47 - Solar Spectral Irradiance (SSI) using the parameters from 17.1nm and 19.3nm model 2 (green line) and Solar Spectral Irradiance (SSI) from TIMED/SEE (blue line) during the solar cycle 23 and 24. Upper panel: SSI at 17.1nm, middle panels: SSI at 19.3nm and 21.1nm, lower panel: SSI at 33.5nm.

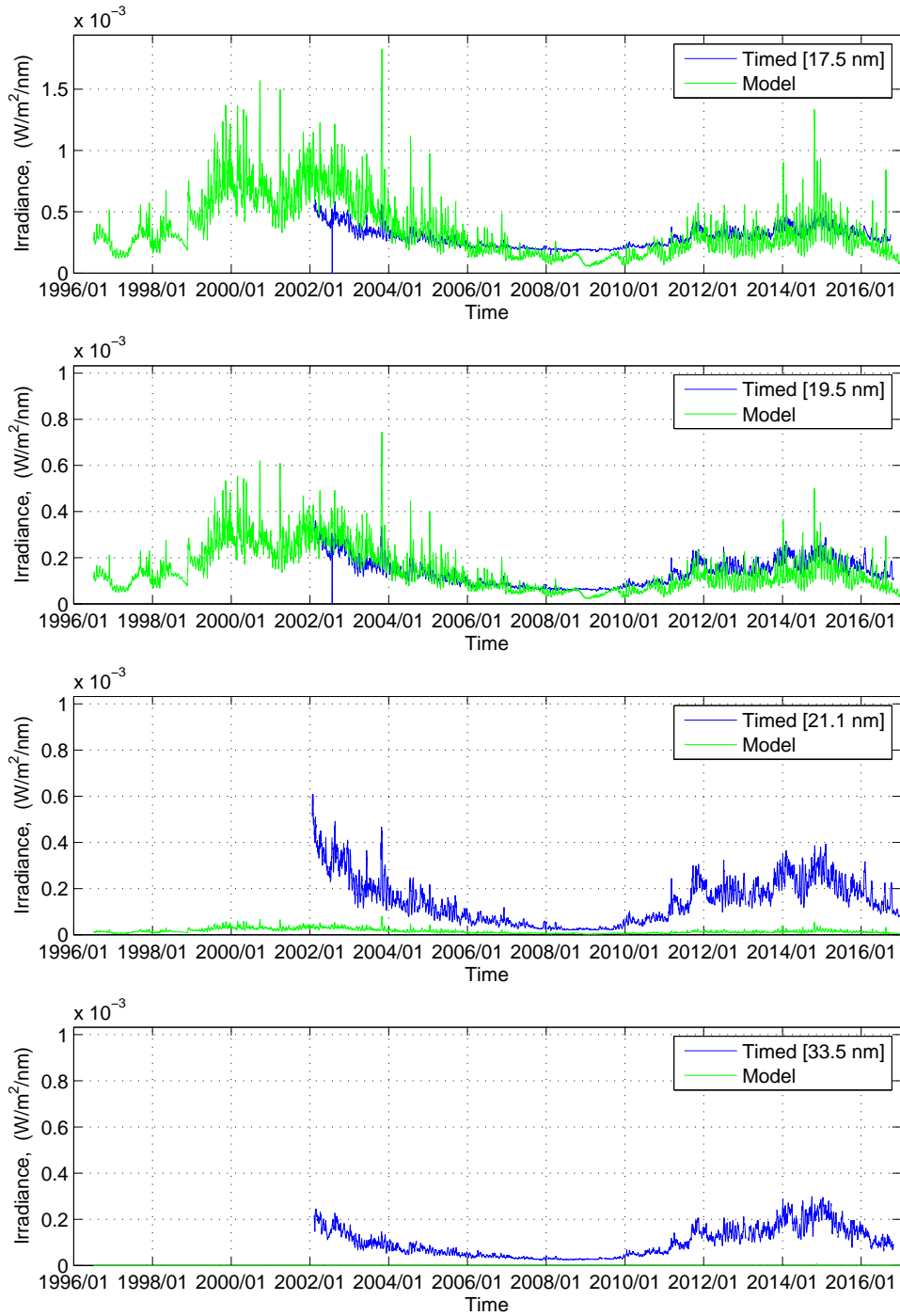
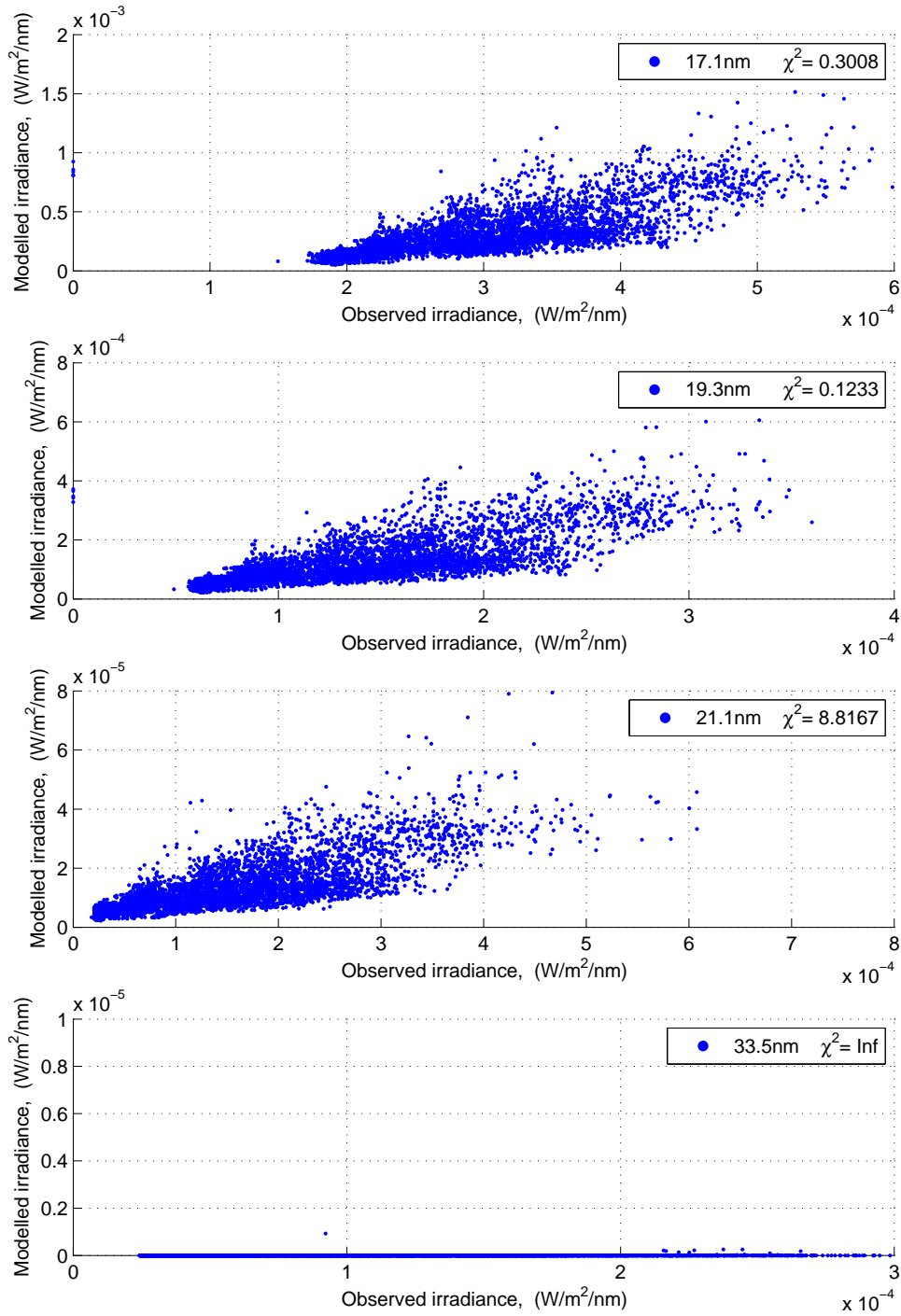
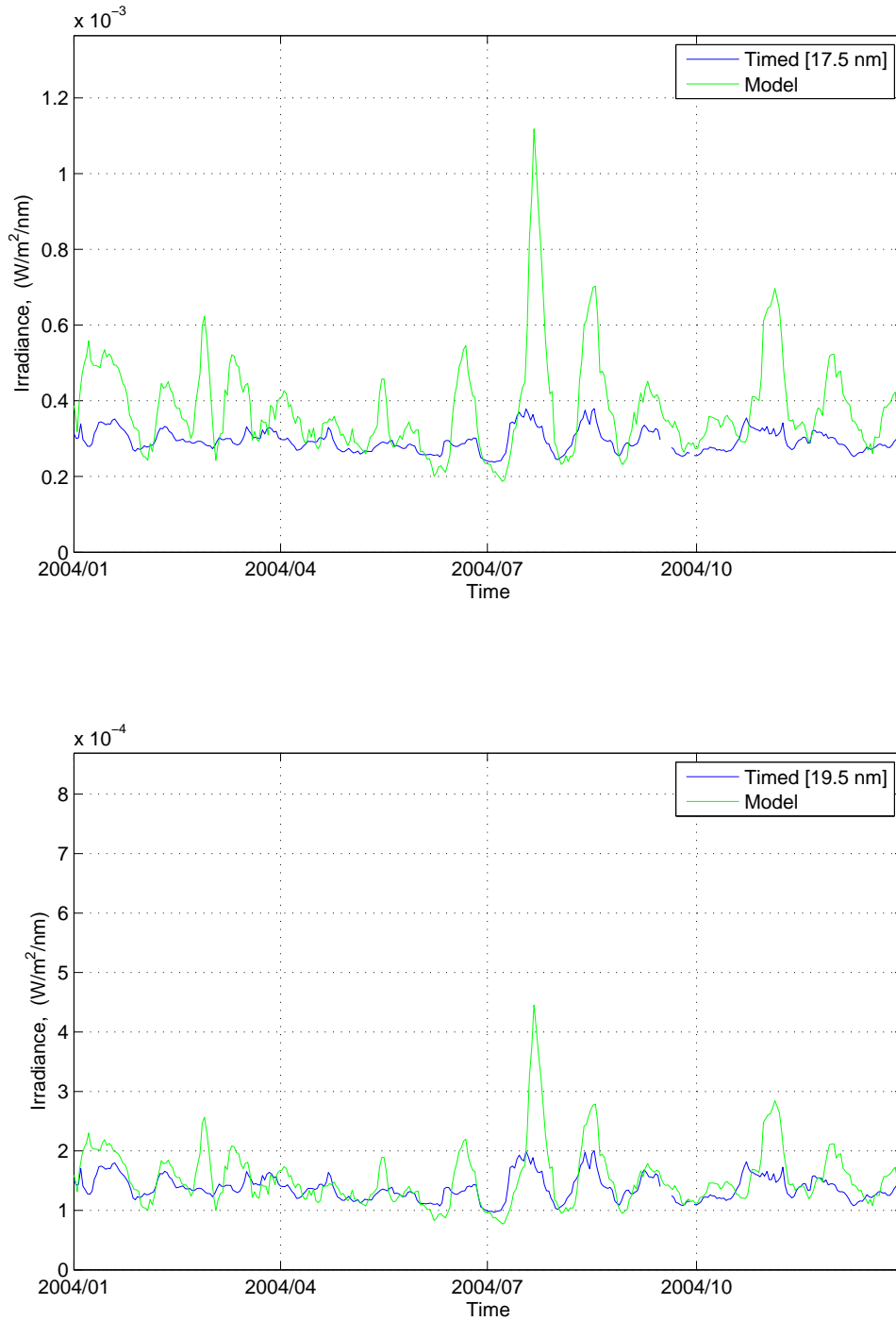


Figure 2.48 - Scatter plot using the parameters from 17.1nm and 19.3nm model 2 and Chi-squared test ( $\chi^2$ ) in each case. Upper panel: scatter plot of 17.1nm, middle panels: scatter plot of 19.3nm and 21.1nm, lower panel: scatter plot of 33.5nm.



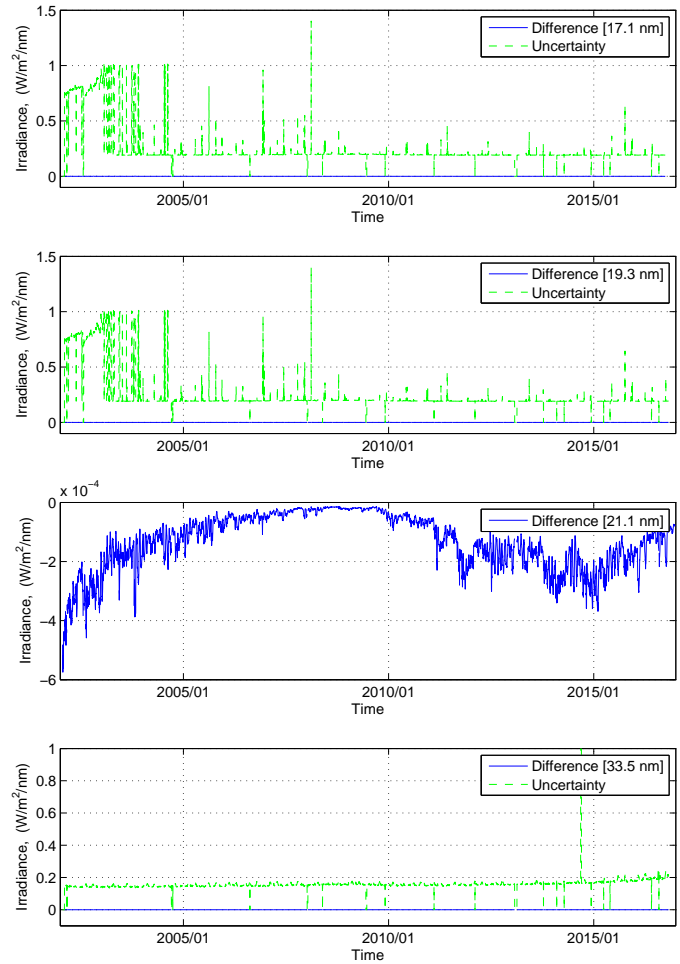
SOURCE: Author

Figure 2.49 - Solar Spectral Irradiance (SSI) using the parameters from 17.1nm and 19.3nm model 2 (green line) and Solar Spectral Irradiance (SSI) from TIMED/SEE (blue line) from Jan. 01 (2004) to Dec. 31 (2004). Upper panel: SSI at 17.1nm, lower panel: SSI at 19.3nm.



SOURCE: Author

Figure 2.50 - Comparison between the observed uncertainty from TIMED/SEE (dotted green line) and difference between observational and modelled data using the parameters from 17.1nm and 19.3nm model 2 (blue line). Upper panel: analysis at 17.1nm, middle panels: analysis at 19.3nm and difference between observed and modelled data at 21.1nm, lower panel: analysis at 33.5nm.



SOURCE: Author

Furthermore, using the 21.1nm and 33.5nm model 3 only it is possible to reproduce the Solar Spectral Irradiance of their (Figure 2.51 and 2.52).

Figure 2.51 - Solar Spectral Irradiance (SSI) using the parameters from 21.1nm and 33.5nm model 3 (green line) and Solar Spectral Irradiance (SSI) from TIMED/SEE (blue line) during the solar cycle 23 and 24. Upper panel: SSI at 17.1nm, middle panels: SSI at 19.3nm and 21.1nm, lower panel: SSI at 33.5nm.

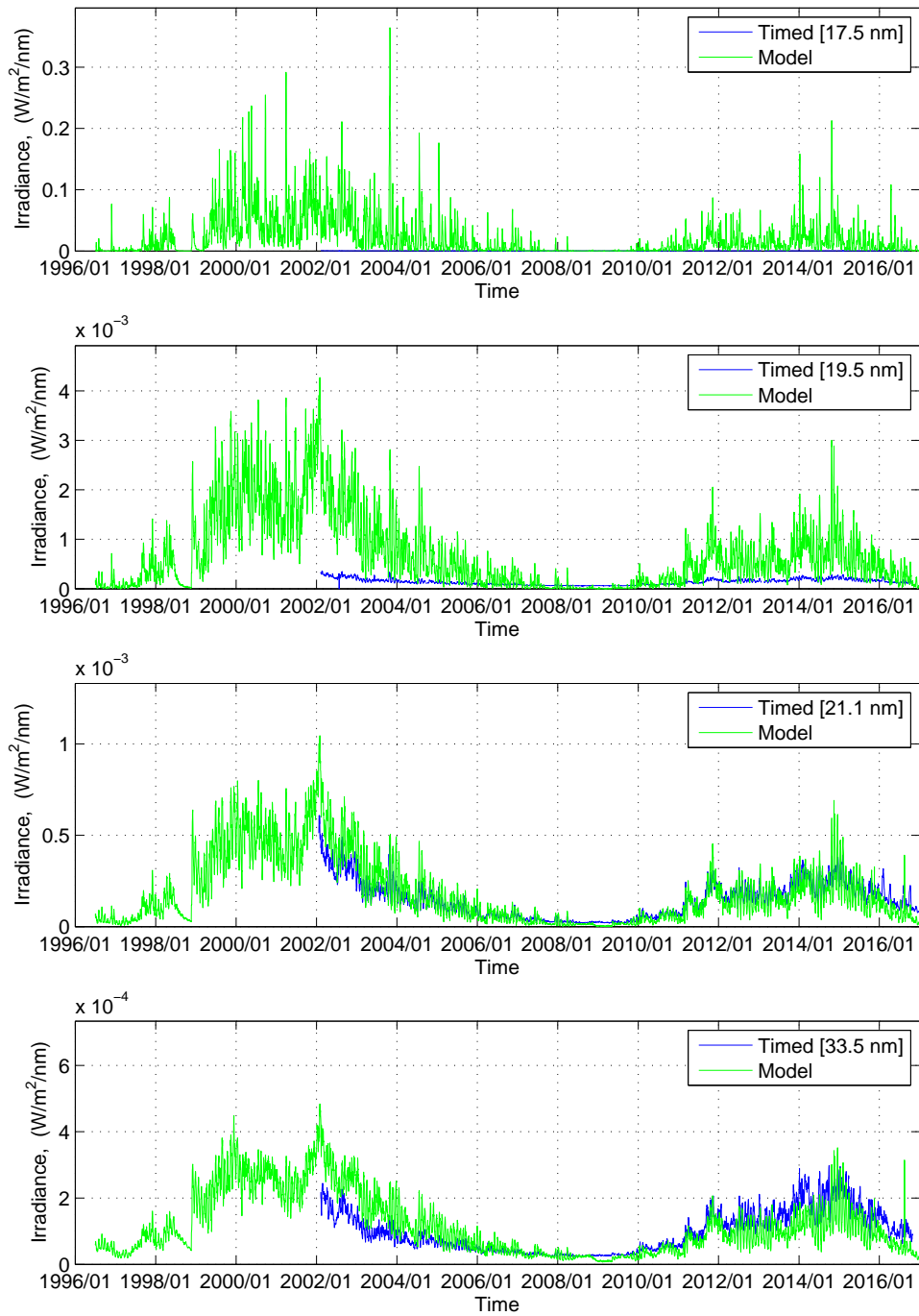
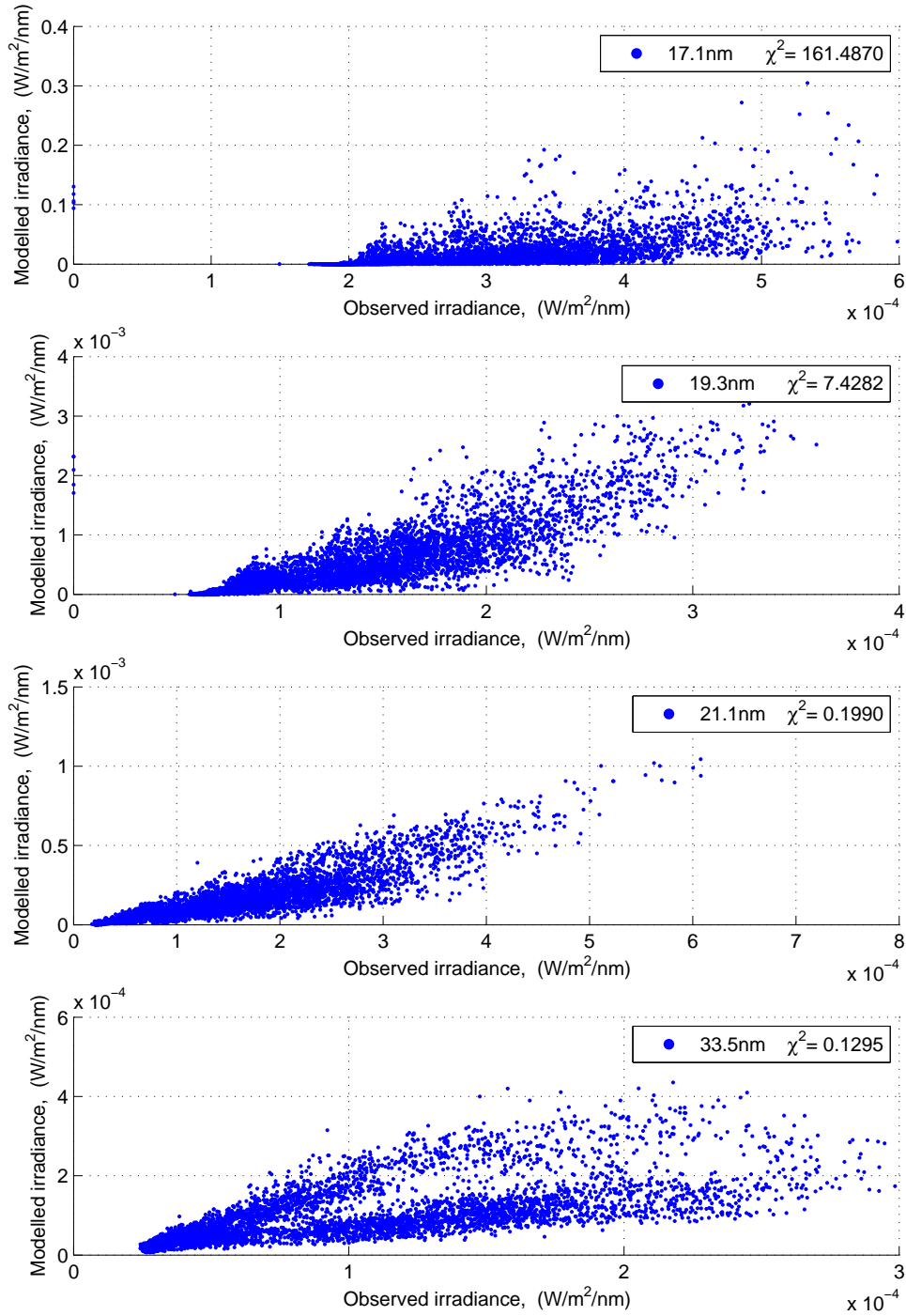


Figure 2.52 - Scatter plot using the parameters from 21.1nm and 33.5nm model 3 and Chi-squared test ( $\chi^2$ ) in each case. Upper panel: scatter plot of 17.1nm, middle panels: scatter plot of 19.3nm and 21.1nm, lower panel: scatter plot of 33.5nm.



SOURCE: Author

Figure 2.53 - Solar Spectral Irradiance (SSI) using the parameters from 21.1nm and 33.5nm model 3 (green line) and Solar Spectral Irradiance (SSI) from TIMED/SEE (blue line) from Jan. 01 to Dec. 31 (2010). Upper panel: SSI at 21.1nm, lower panel: SSI at 33.5nm.

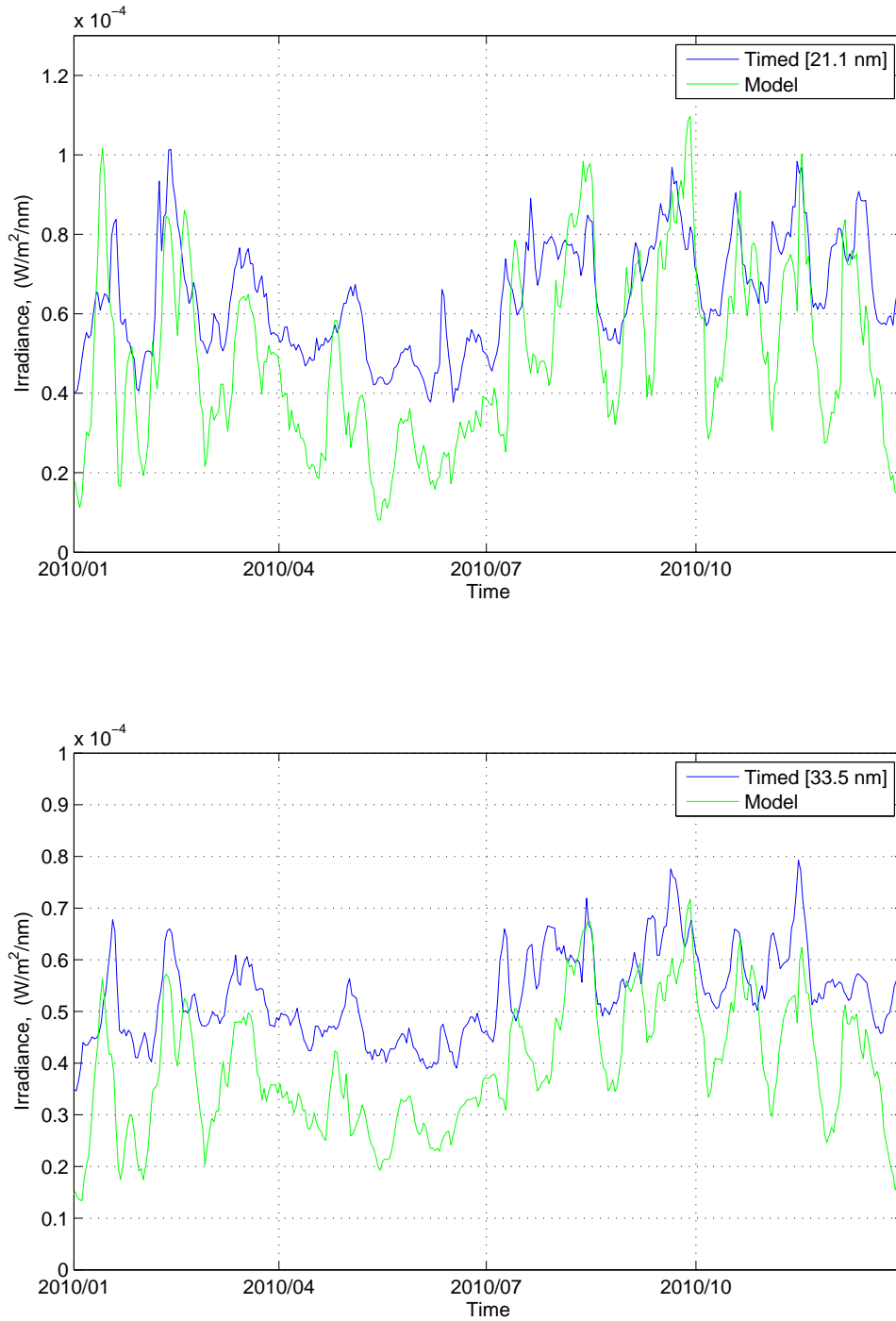
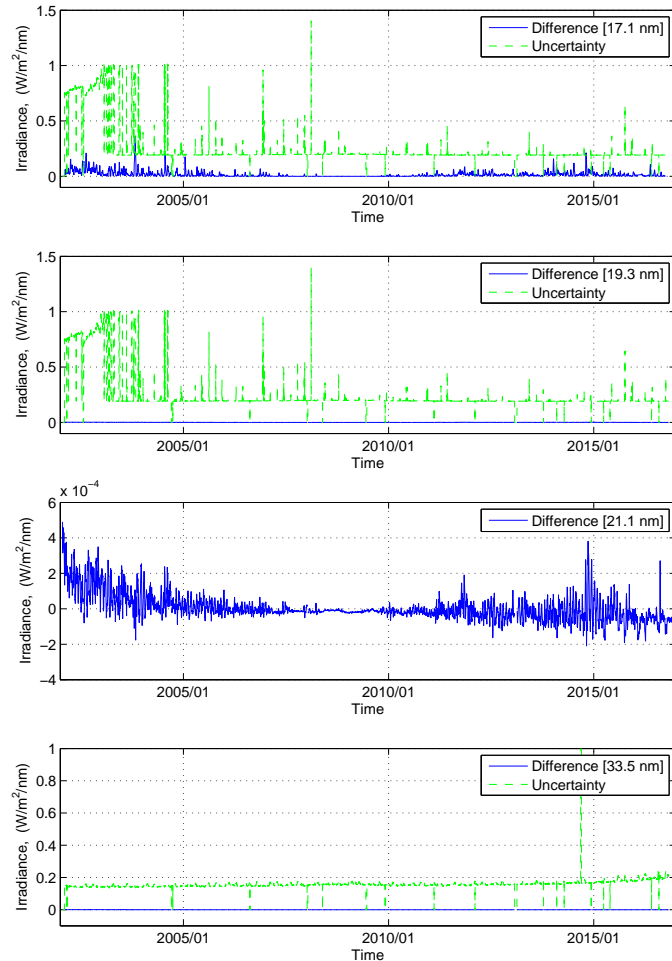


Figure 2.54 - Comparison between the observed uncertainty from TIMED/SEE (dotted green line) and difference between observational and modelled data using the parameters from 21.1nm and 33.5nm model 3 (blue line). Upper panel: analysis at 17.1nm, middle panels: analysis at 19.3nm and difference between observed and modelled data at 21.1nm, lower panel: analysis at 33.5nm.



SOURCE: Author

The 19.3nm and 21.1nm model 1 is not able to follow the wavelength 17.1nm. Also, during the solar cycle 24 it is not possible to fit 33.5nm adequately (figures 2.55 and 2.56).

Figure 2.55 - Solar Spectral Irradiance (SSI) using the parameters from 19.3nm and 21.1nm model 1 (green line) and Solar Spectral Irradiance (SSI) from TIMED/SEE (blue line) during the solar cycle 23 and 24. Upper panel: SSI at 17.1nm, middle panels: SSI at 19.3nm and 21.1nm, lower panel: SSI at 33.5nm.

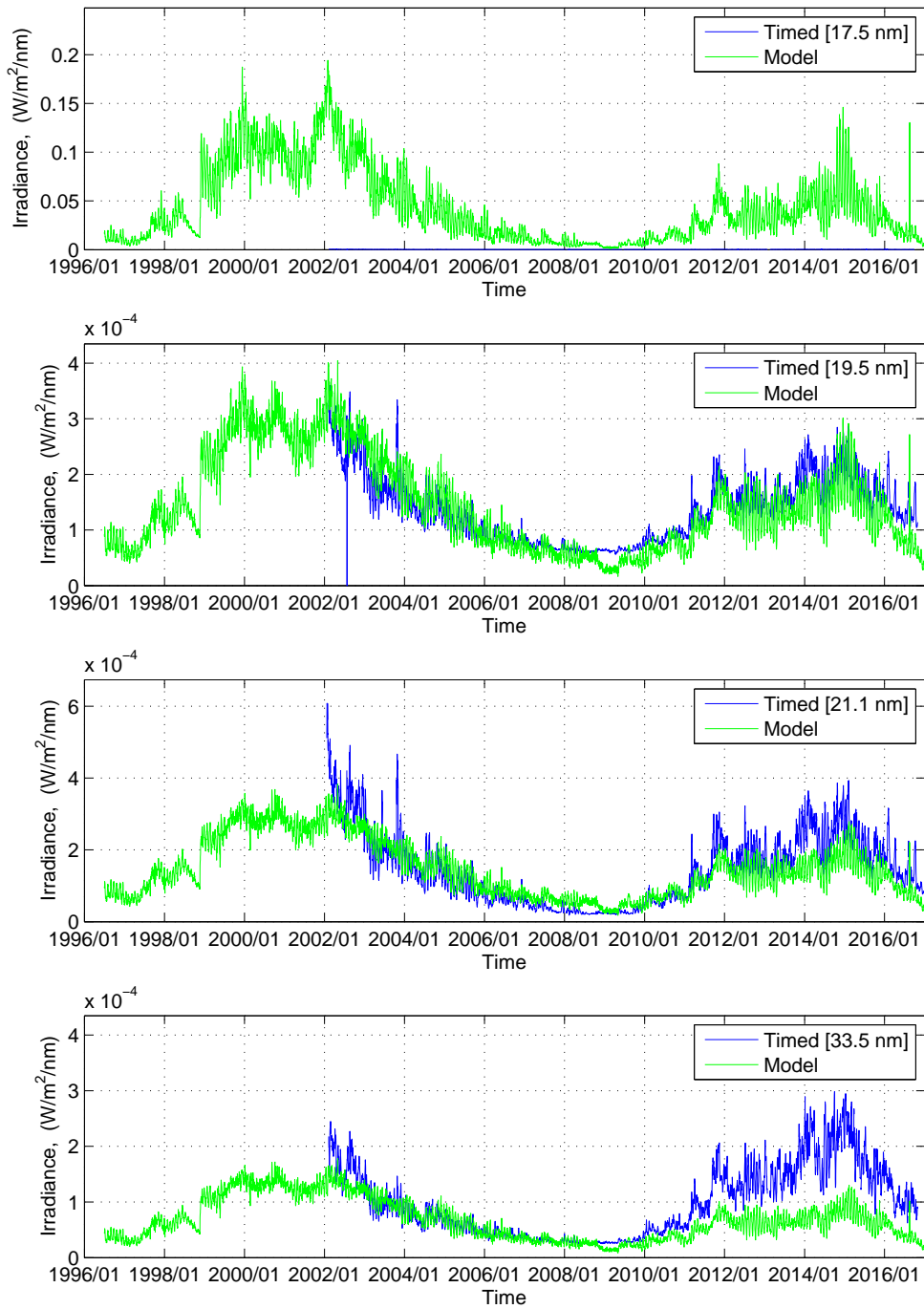
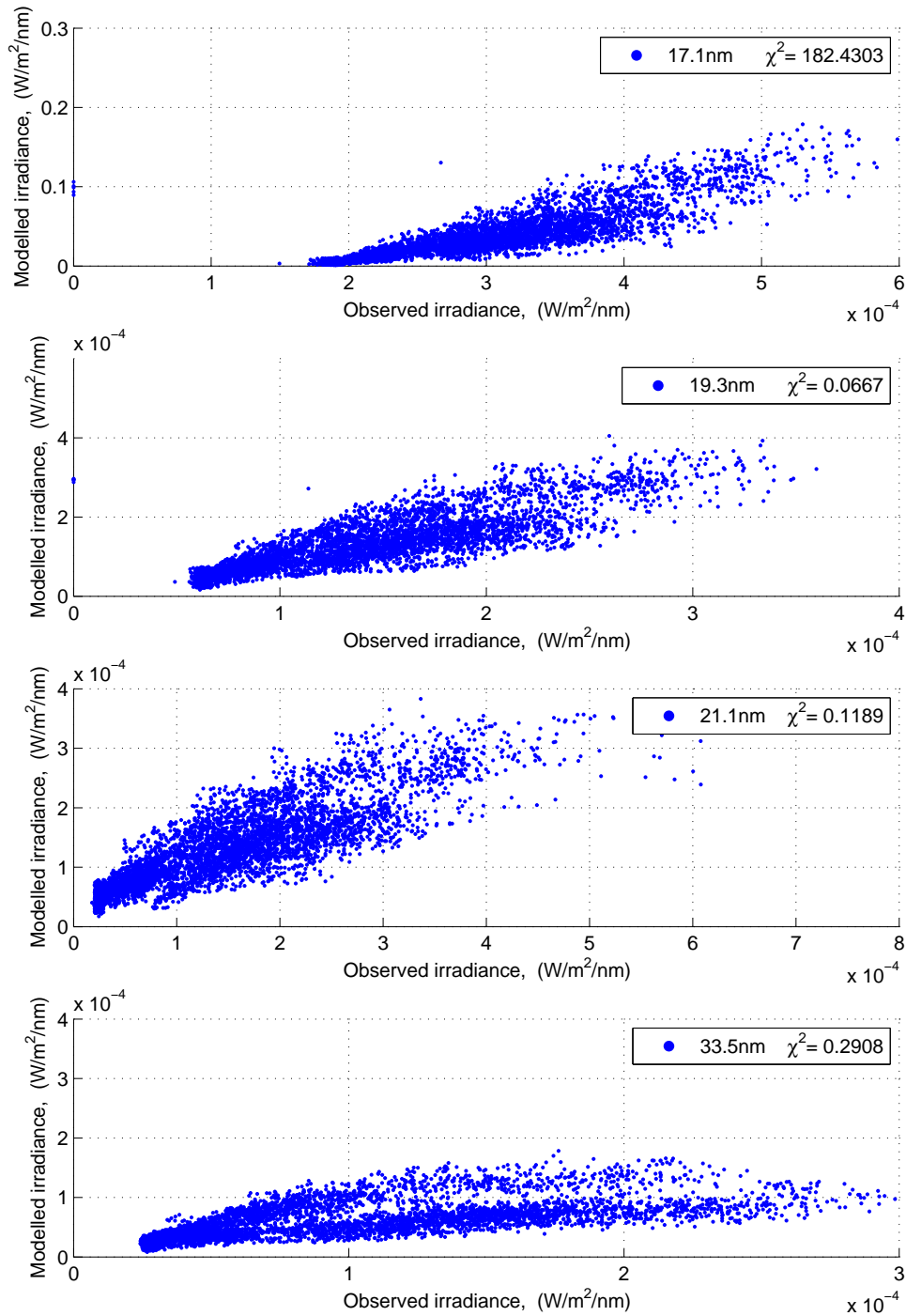


Figure 2.56 - Scatter plot using the parameters from 19.3nm and 21.1nm model 1 and Chi-squared test ( $\chi^2$ ) in each case. Upper panel: scatter plot of 17.1nm, middle panels: scatter plot of 19.3nm and 21.1nm, lower panel: scatter plot of 33.5nm.



SOURCE: Author

Figure 2.57 - Solar Spectral Irradiance (SSI) using the parameters from 19.3nm and 21.1nm model 1 (green line) and Solar Spectral Irradiance (SSI) from TIMED/SEE (blue line) from Jan. 01 to Dec. 31 (2007). Upper panel: SSI at 19.3nm, middle panels: SSI at 21.1nm, lower panel: SSI at 33.5nm.

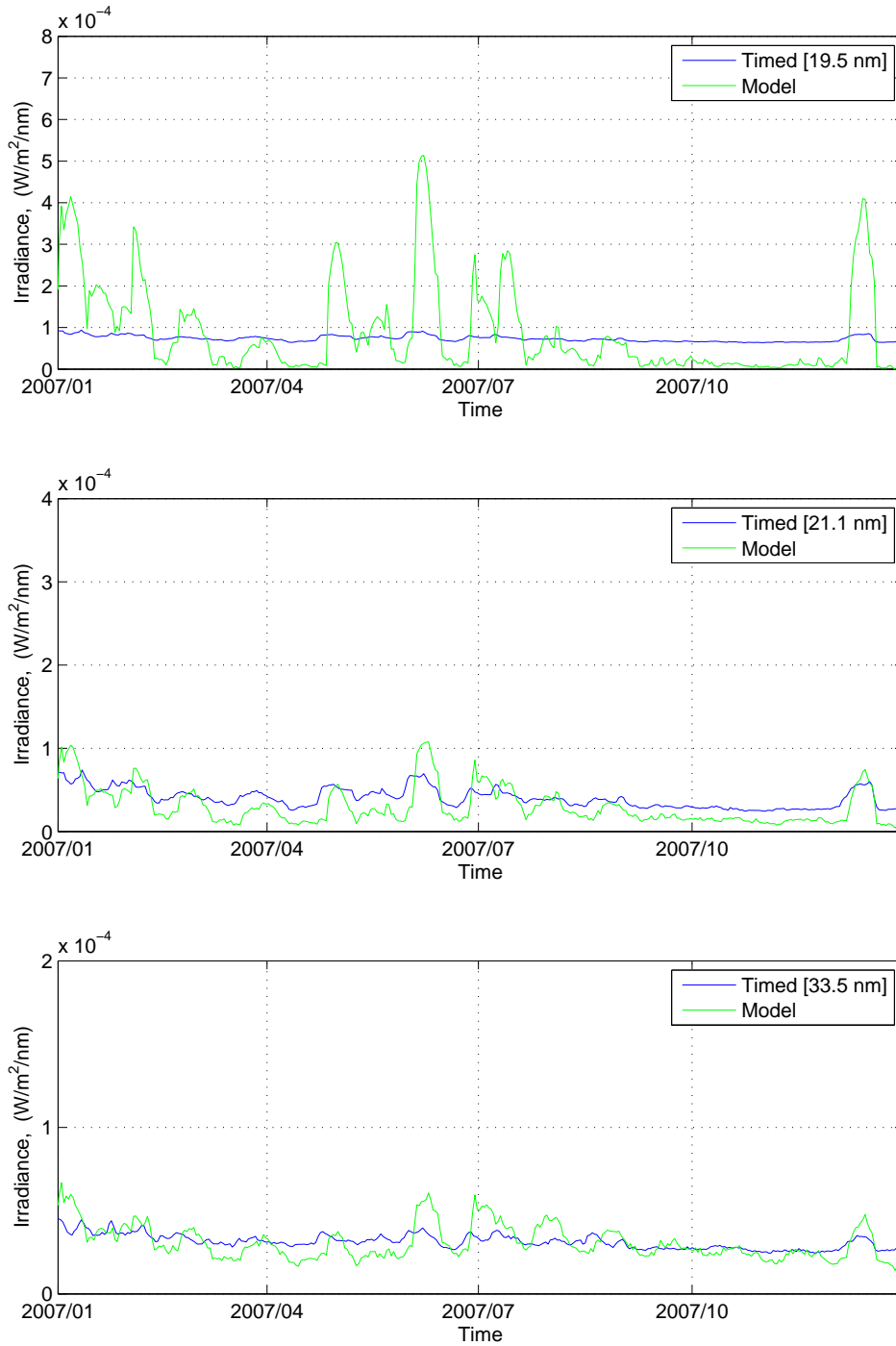
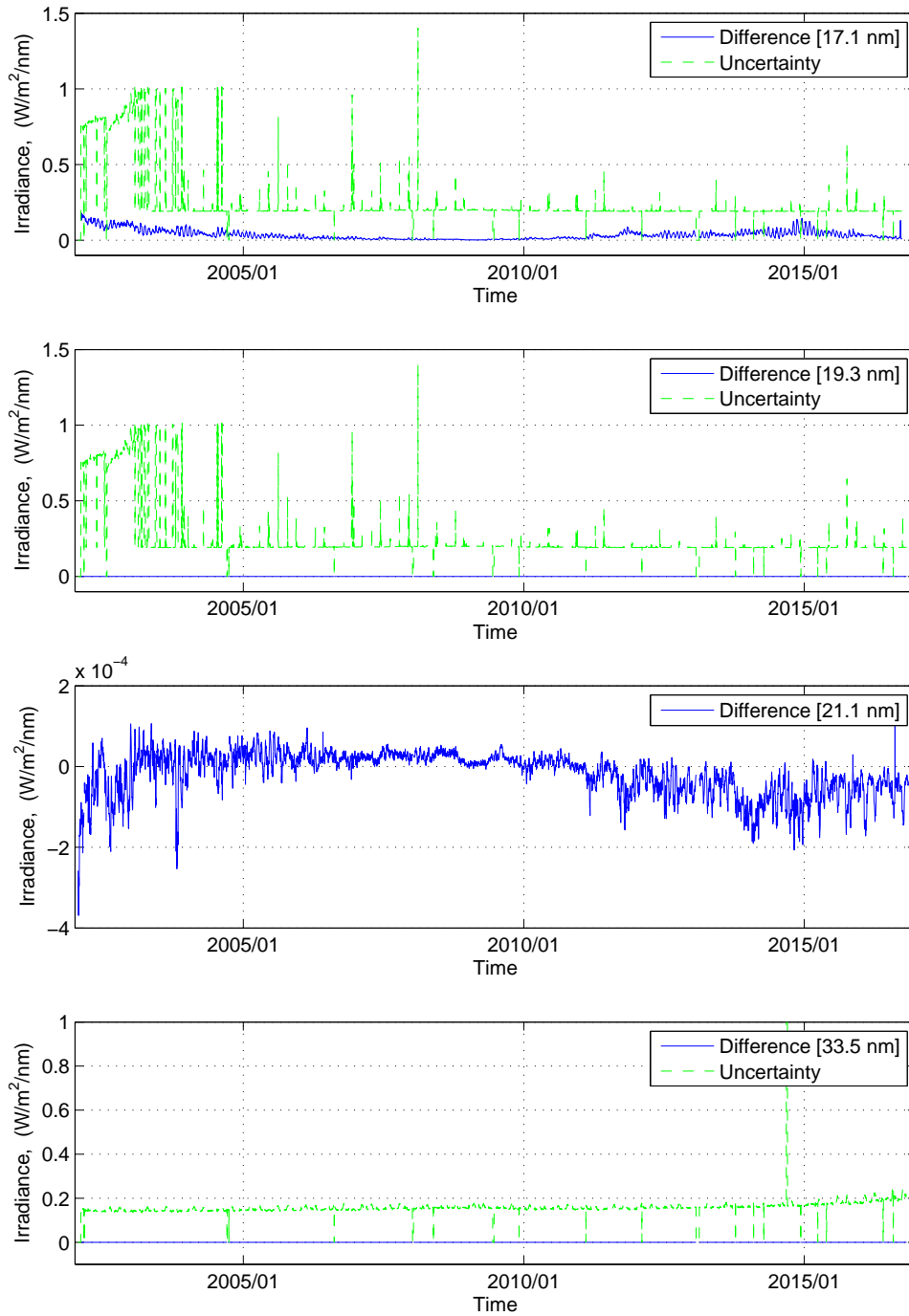


Figure 2.58 - Comparison between the observed uncertainty from TIMED/SEE (dotted green line) and difference between observational and modelled data using the parameters from 19.3nm and 21.1nm model 1 (blue line). Upper panel: analysis at 17.1nm, middle panels: analysis at 19.3nm and difference between observed and modelled data at 21.1nm, lower panel: analysis at 33.5nm.



The parameters from 17.1nm model 5 show that the variability is followed at 19.3nm in this specific case (Figure 2.26) from Jan. 01 (2012) to Jan. 01 (2014). The parameters of the 19.3nm model 5 display the variations at 21.1nm during the interval Jan. 01 (2012) to Jan. 01 (2014) and they are in a good agreement with the observational data. However, at 19.3nm and 33.5nm the variations are reasonably described (Figure 2.30). The 33.5nm model 2 exhibits the variations at 21.1nm and 33.5nm but the model values are below the observed values from TIMED (Figure 2.34) during the interval Jan. 01 (2010) and Dec. 31 (2010).

The parameters from 21.1nm model 1 represent large scale variations during the last solar cycles at 21.1nm, but during Jan. 01 (2010) to Dec. 31 (2010) the CODET model does not describe appropriately the variations of the Solar Spectral Irradiance in this specific wavelength (Figure 2.38). The 21.1nm model 3 parameters are not displaying the variations at any wavelengths.

The 17.1 – 19.3 – 21.1nm model 2 represent in a good agreement the variations of the Solar Spectral Irradiance at 19.3nm, 21.1nm and 33.5nm from Jan. 01 (2004) to Dec. 31 (2004)(Figure 2.45). The parameters of the model 17.1 – 19.3nm are following the Solar Spectral Irradiance trend in these specific wavelengths (Figure 2.49). The parameters from 21.1 – 33.5nm model show the variations of the Solar Spectral Irradiance, but the modelled irradiance is below the observational data during the period from Jan. 01 (2010) to Dec. 31 (2010)(Figure 2.53).

The 19.3nm and 21.1nm model 1 is able to describe adequately the variations of the 21.1nm and 33.5nm between Jan. 01 (2007) and Dec. 31 (2007) (Figure 2.57).

Also, the difference between observational and modelled data is within the limits of the observational uncertainty, shown in figures 2.27, 2.31, 2.35, 2.39, 2.42, 2.46, 2.50, 2.54, 2.58.

## 2.4 Summary

The CODET model was presented. The optimization algorithm was applied using four specific wavelengths 17.1nm, 19.3nm, 21.1nm and 33.5nm. Several experiments were performed. Some different population size and generation in each experiment were tried, but the best results were obtained using 25 generations and population size of 8. Also, it was chosen ten days over the last solar cycles and the goodness-of-fit was made using the observational data from TIMED/SEE. It is possible to follow the variability in Solar Spectral Irradiance over the last solar cycles.

The average temperature and density profiles in all layers (from  $R_{sun} = 1.0$  to  $R_{sun} = 2.5$ ) were obtained in each model. They were analyzed and evaluated from the profiles reported in the literature. Using the previous analysis, 9 models were selected. The parameters of these models were applied in each wavelength over the solar cycle 23 and 24 and it was compared to observational data. The scatter plot in each case was obtained. Also, the chi-squared test was calculated for each case. Small intervals (one year or two years) were analyzed using these 9 models. Three models shows the variability is recovered in short time scales. These models are 193nm model 5, 17.1 – 19.3 – 21.1nm model 2 and 19.3 – 21.1nm model 1.

The difference between the modelled and observational Solar Spectral Irradiance was calculated. These differences were compared with the observational uncertainty. They were within the limits of the observational uncertainty. Performed this analysis, three models were selected and discussed in the next chapter.

### 3 ELECTRON DENSITY AND TEMPERATURE PROFILES DURING THE SOLAR CYCLE 23 AND 24

#### Contents

---

3.1 Electron density and temperature profiles through the solar corona . . . . .	110
3.2 Temperature and Density maps . . . . .	118
3.3 Intensity maps . . . . .	124
3.4 Plasma $\beta$ parameter in solar corona . . . . .	132
3.5 Summary . . . . .	134

---

Determinations of coronal densities have been made since  $\sim 1950$  from Van de Hulst and Pottasch models from eclipse observations and empirical laws relating brightness with height (Chapter 1.4). Due to the problem with the direct measurements of the plasma parameters, profiles of electron density and temperature from the CODET model described in the section 2.1 will be presented in this thesis.

For this purpose, photospheric magnetic field (synoptic charts) from MDI/SOHO and HMI/SDO was used. This magnetic field is used as an input parameter of the surface flux transport model from SCHRIJVER (2001). The magnetic field is extrapolated through the solar corona using the PFSS package (section 2.1.2). This allows a description of the magnetic field and consequently of the parameters of plasma through the solar corona.

Using the extrapolated magnetic field it is possible to build the density and temperature profiles (equations 2.10 and 2.12), and then the emission is calculated (equation 2.14). The emission is a key quantity because it validates our model when it is compared with observational data.

In this chapter, discussion of the selected models from the analysis of the chapter 2 will be presented, as well as their importance to model the Solar Spectral Irradiance. The evolution of the electron density and temperature profiles through the solar corona in different layers ( $R_{\text{sun}}=1.000, 1.016, 1.032, 1.049, 1.067, 1.165, 1.282, 1.427, 1.608, 1.843$  solar radii) during the solar cycle 23 and 24, will be presented. Density and temperature maps in different layers ( $R_{\text{sun}}=1.000, 1.016, 1.032, 1.049, 1.067, 1.165$  solar radii) in the solar atmosphere will be shown. The plasma  $\beta$  parameter was calculated using the equation 2.5 and the parameters of the selected models.

The Solar Spectral Irradiance (SSI) was obtained using the best models described

in the previous chapter. The parameters in each model are shown in the Table 3 and compared with the observational data (TIMED/SEE) from the Figure 2.24 to the Figure 2.58.

Table 3.1 - New numbering of the models in this chapter and the corresponding model described in the previous chapter.

Model	Corresponding model from chapter 2
Model 1	19.3nm (model 5)
Model 2	17.1 – 19.3 – 21.1nm (model 2)
Model 3	19.3 – 21.1nm (model 1)

SOURCE: Author

Table 3.2 - Parameters ( $\gamma$ ,  $\alpha$ ,  $N_o$ ,  $T_o$  and  $B_{sat}$ ) for each selected model.

Parameter	Model 1	Model 2	Model 3
$\gamma$	0.6644	1.252	4.8864
$\alpha$	-5.0187	-1.4938	-1.7328
$N_o$	$0.99929 \times 10^8$	$2.95592 \times 10^8$	$2.42667 \times 10^8$
$T_o$	$1.76760 \times 10^6$	$1.66501 \times 10^6$	$1.694350 \times 10^6$
$B_{sat}$	1.3042	4.175	5.9766

SOURCE: Author

In the following section the parameters of the selected models will be used to describe the temperature and density profiles through the solar corona.

### 3.1 Electron density and temperature profiles through the solar corona

The electron density and temperature profiles were obtained using the equations 2.10 and 2.12 and the parameters shown in Table 3. The electron density and temperature average profiles were obtained from different layers through the solar atmosphere ( $R_{sun}=1.000, 1.016, 1.032, 1.049, 1.067, 1.165, 1.282$ ). Variations in temperature and density during the last solar cycles are displayed, in the figures 3.1, 3.3 and 3.5.

Table 3.3 lists the minimum temperature value in each layer in the solar cycle 23 and 24, using the selected models (Table 3).

Table 3.3 - Minimum temperature values (MK) in each layer (Rsun=1.000, 1.016, 1.032, 1.049, 1.067, 1.165, 1.282) during the solar cycle 23 and 24, using the selected models.

Model 1	Min T value (MK)	Min T value (MK)	Model 2	Min T value (MK)	Min T value (MK)	Model 3	Min T value (MK)	Min T value (MK)
Rsun	solar cycle 23	solar cycle 24	Rsun	solar cycle 23	solar cycle 24	Rsun	solar cycle 23	solar cycle 24
1.000	1.492	1.583	1.000	1.021	1.304	1.000	1.067	1.336
1.016	1.610	1.670	1.016	1.227	1.459	1.016	1.269	1.495
1.032	1.603	1.667	1.032	1.274	1.488	1.032	1.318	1.524
1.049	1.589	1.672	1.049	1.319	1.506	1.049	1.365	1.549
1.067	1.582	1.674	1.067	1.365	1.540	1.067	1.413	1.570
1.165	1.648	1.706	1.165	1.574	1.608	1.165	1.618	1.643
1.282	1.732	1.717	1.282	1.644	1.633	1.282	1.676	1.670

SOURCE: Author

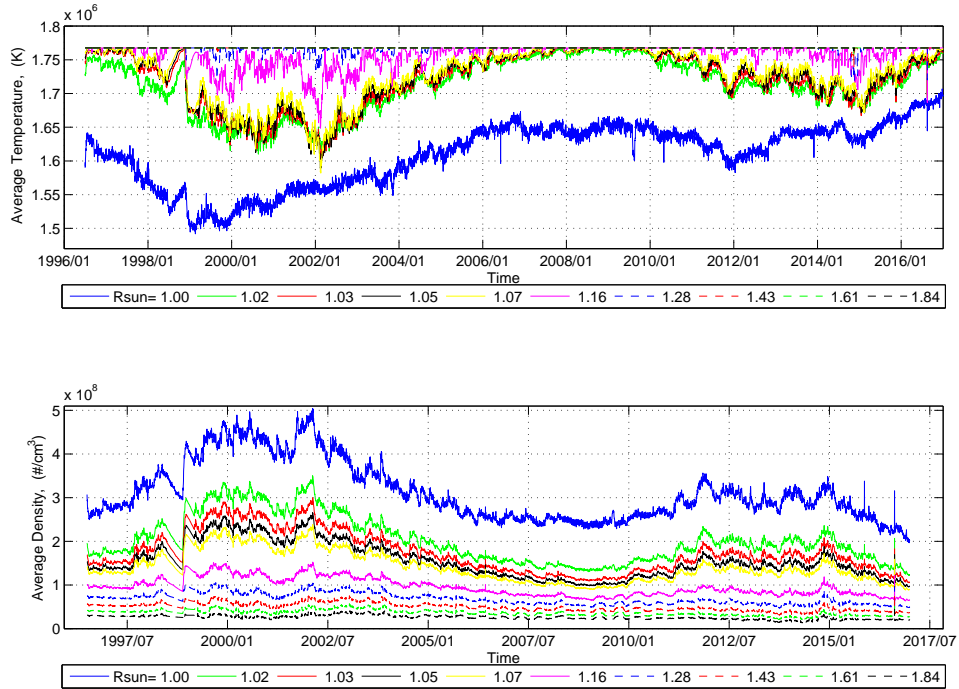
The maximum values of density profiles in different layers (Rsun=1.000, 1.016, 1.032, 1.049, 1.067, 1.165, 1.282) are present in the following Table:

Table 3.4 - Maximun density values ( $cm^{-3}$ ) in each layer (Rsun=1.000, 1.016, 1.032, 1.049, 1.067, 1.165, 1.282) during the solar cycle 23 and 24, using the selected models.

Model 1	Max N value ( $10^8 cm^{-3}$ )	Max N value ( $10^8 cm^{-3}$ )	Model 2	Max N value ( $10^8 cm^{-3}$ )	Max N value ( $10^8 cm^{-3}$ )	Model 3	Max N value ( $10^8 cm^{-3}$ )	Max N value ( $10^8 cm^{-3}$ )
Rsun	solar cycle 23	solar cycle 24	Rsun	solar cycle 23	solar cycle 24	Rsun	solar cycle 23	solar cycle 24
1.000	5.047	3.307	1.000	29.000	14.770	1.000	949690000	470900000
1.016	3.503	2.417	1.016	13.837	8.538	1.016	18700000	19114000
1.032	3.000	2.081	1.032	9.7286	6.068	1.032	1564000	2036500
1.049	2.656	1.881	1.049	7.3263	4.593	1.049	193700	333660
1.067	2.382	1.718	1.067	5.704	3.560	1.067	29290	69415
1.165	1.522	1.187	1.165	2.0897	1.502	1.165	59.900	138.670
1.282	1.047	0.886	1.282	0.9423	0.7714	1.282	0.682	1.850

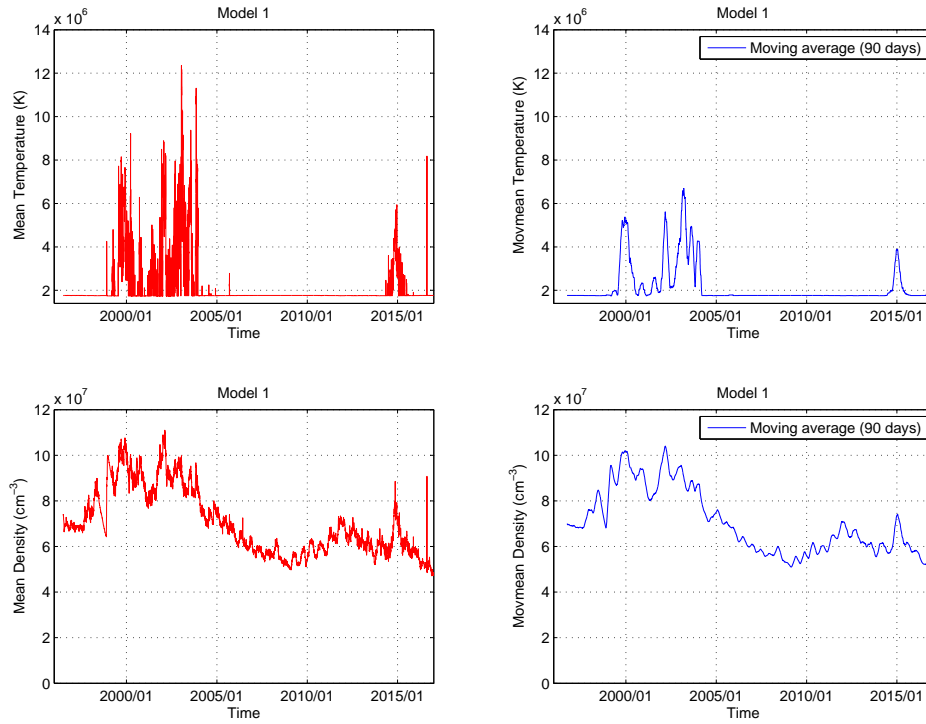
SOURCE: Author

Figure 3.1 - Average temperature (upper panel) and density (lower panel) profiles using the parameters from the model 1, through different layers ( $R_{\text{sun}}=1.000, 1.016, 1.032, 1.049, 1.067, 1.165, 1.282$ ), during the solar cycle 23 and 24.



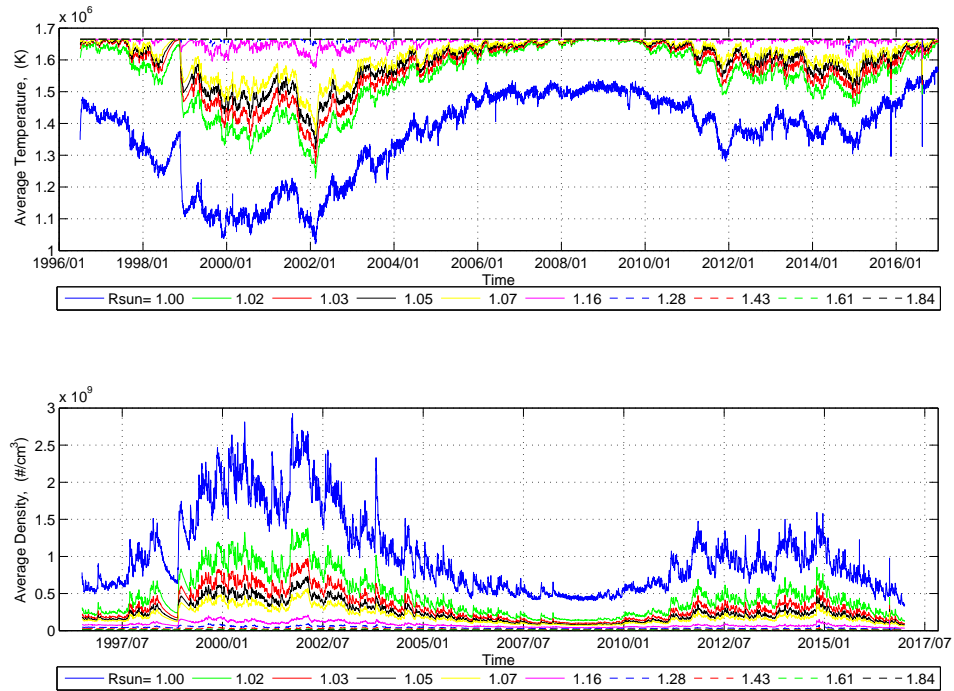
SOURCE: Author

Figure 3.2 - Evolution of plasma parameters during the solar cycle 23 and 24, using the model 1. Upper left panel: mean temperature per day (red line). Upper right panel: moving average temperature with time period of 90 days. Lower left panel: mean density per day (red line). Lower right panel: moving average density with the time period of 90 days.



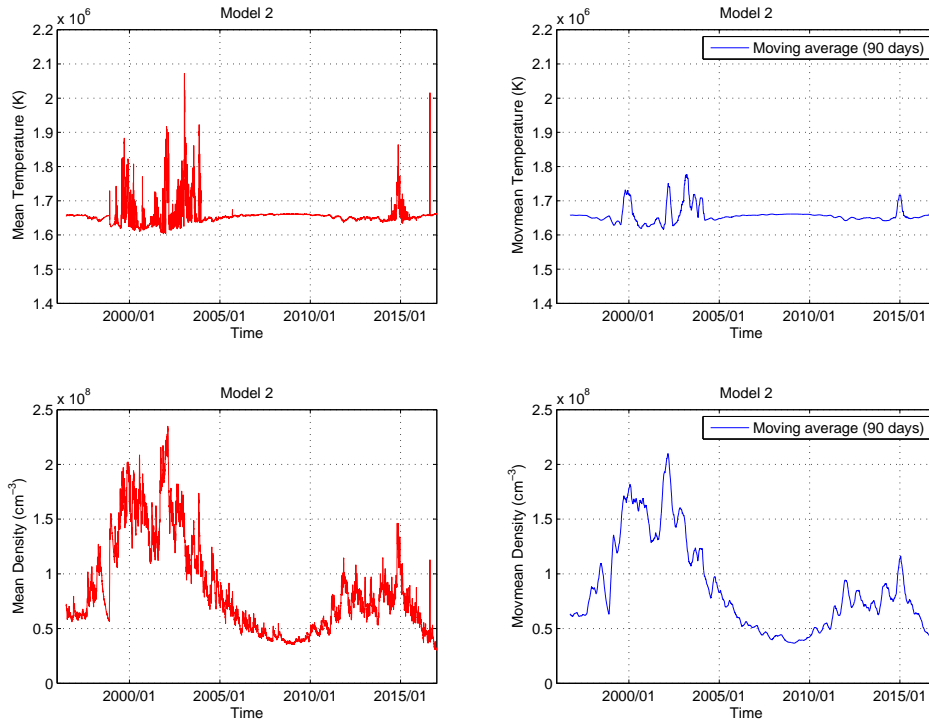
SOURCE: Author

Figure 3.3 - Average temperature (upper panel) and density (lower panel) profiles using the parameters from the model 2, in different layers ( $R_{\text{sun}}=1.000, 1.016, 1.032, 1.049, 1.067, 1.165, 1.282$ ), during the solar cycle 23 and 24.



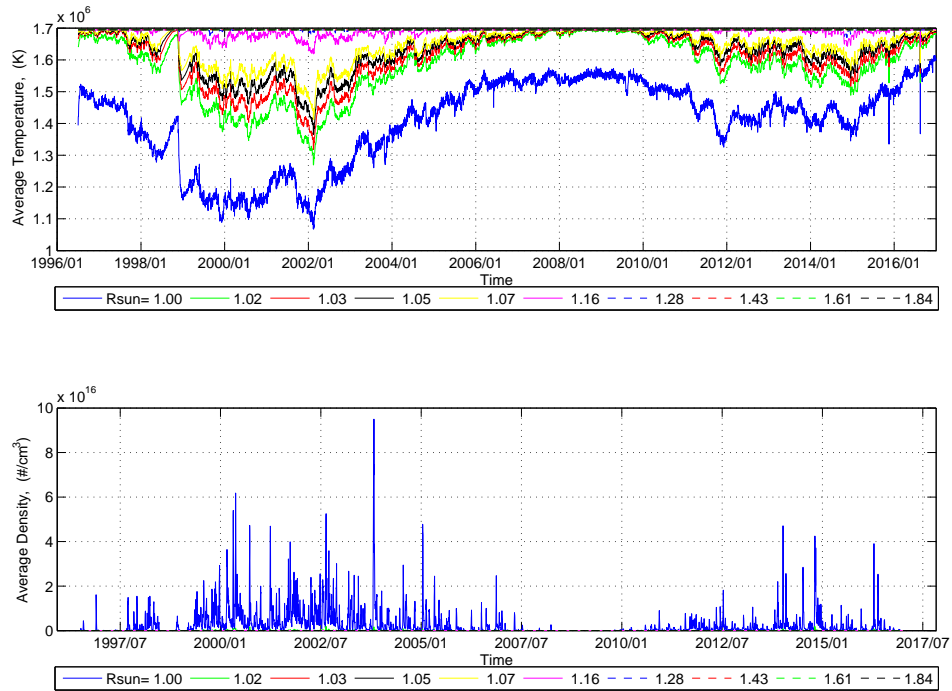
SOURCE: Author

Figure 3.4 - Evolution of plasma parameters during the solar cycle 23 and 24, using the model 2. Upper left panel: mean temperature per day (red line). Upper right panel: moving average temperature with time period of 90 days. Lower left panel: mean density per day (red line). Lower right panel: moving average density with the time period of 90 days.



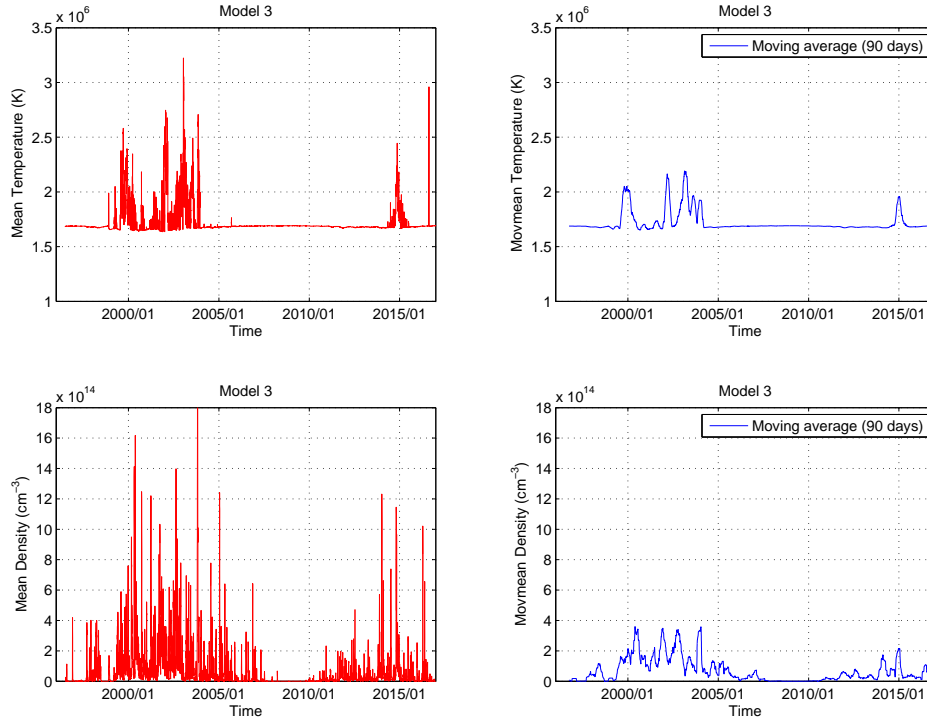
SOURCE: Author

Figure 3.5 - Average temperature (upper panel) and density (lower panel) profiles using the parameters from the model 3, in different layers ( $R_{\text{sun}}=1.000, 1.016, 1.032, 1.049, 1.067, 1.165, 1.282$ ), during the solar cycle 23 and 24.



SOURCE: Author

Figure 3.6 - Evolution of plasma parameters during the solar cycle 23 and 24, using the model 3. Upper left panel: mean temperature per day (red line). Upper right panel: moving average temperature with time period of 90 days. Lower left panel: mean density per day (red line). Lower right panel: moving average density with the time period of 90 days.



SOURCE: Author

Lower values in temperature are shown in the solar cycle 23, while in the solar cycle 24 the temperature increases (from figures 3.1 to 3.5 upper panels). Also, in the external layers the temperature is higher during the last solar cycles, using all models. The temperature is near to 1MK in the model 1, 2 and 3. The increase in temperature between  $R_{sun} = 1.000$  and  $R_{sun} = 1.282$  was calculated using the values reported in the Table 3.3. The model 1 shows an increase during the solar cycle 23 of 86.14% and the solar cycle 24 of 92.19%. On the other hand, model 2 shows 62.10% of increase during the solar cycle 23 and 79.85% in the solar cycle 24. The model 3 shows an increase of 63.66% during the solar cycle 23 and 80.0% in the solar cycle 24.

Using the selected models the daily average was calculated. Then, the evolution

of the temperature and density profiles were evaluated using the moving average during the solar cycle 23 and 24, using the selected models. The moving average was searching variations in a time period of 90 days. High values in temperature and density were present during the solar cycle 23 compared to the solar cycle 24 (figures 3.2, 3.4, 3.6).

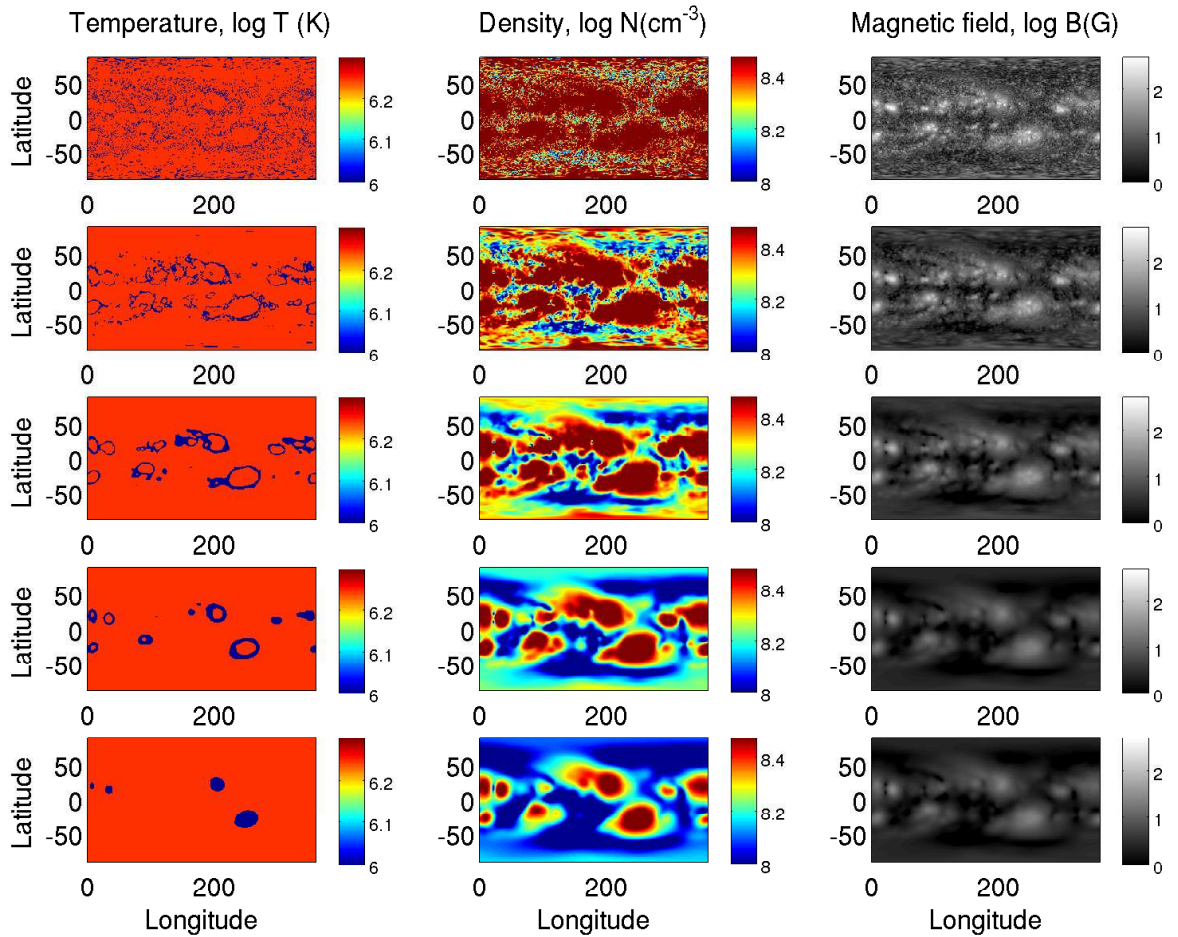
The maximum density values are higher in the solar cycle 23 and lower in the solar cycle 24. The external layers show lower values in average density than the layers near the photosphere (from figures 3.1 to 3.5 lower panels). The model 3 exhibits values near to  $470900000 \times 10^8 \text{cm}^{-3}$  and  $949690000 \times 10^8 \text{cm}^{-3}$ . These values are excessive compared to the expected values. The model 1 and 2 are in accordance to values reported in the literature (Table 3.4). Decrease in density between  $R_{sun} = 1.000$  and  $R_{sun} = 1.282$  was calculated using the reported values in the Table 3.4, only for the model 1 and model 2. The model 1 shows for the solar cycle 23 an increase of 20.7% and 26.79% in the solar cycle 24. In model 2 the decrease in the solar cycle 23 is 3.24% and in the solar cycle 24 is 0.05%. The behavior in the model 3 is related to atypical values present in this model.

### 3.2 Temperature and Density maps

The analysis of the temperature and density maps were obtained using the parameters corresponding to each model (Table 3), except for the model 3 because it does not agree with the reported values. The temperature, density and magnetic field maps were compared through different layers ( $R_{sun} = 1.00, 1.02, 1.05, 1.10, 1.16$ ).

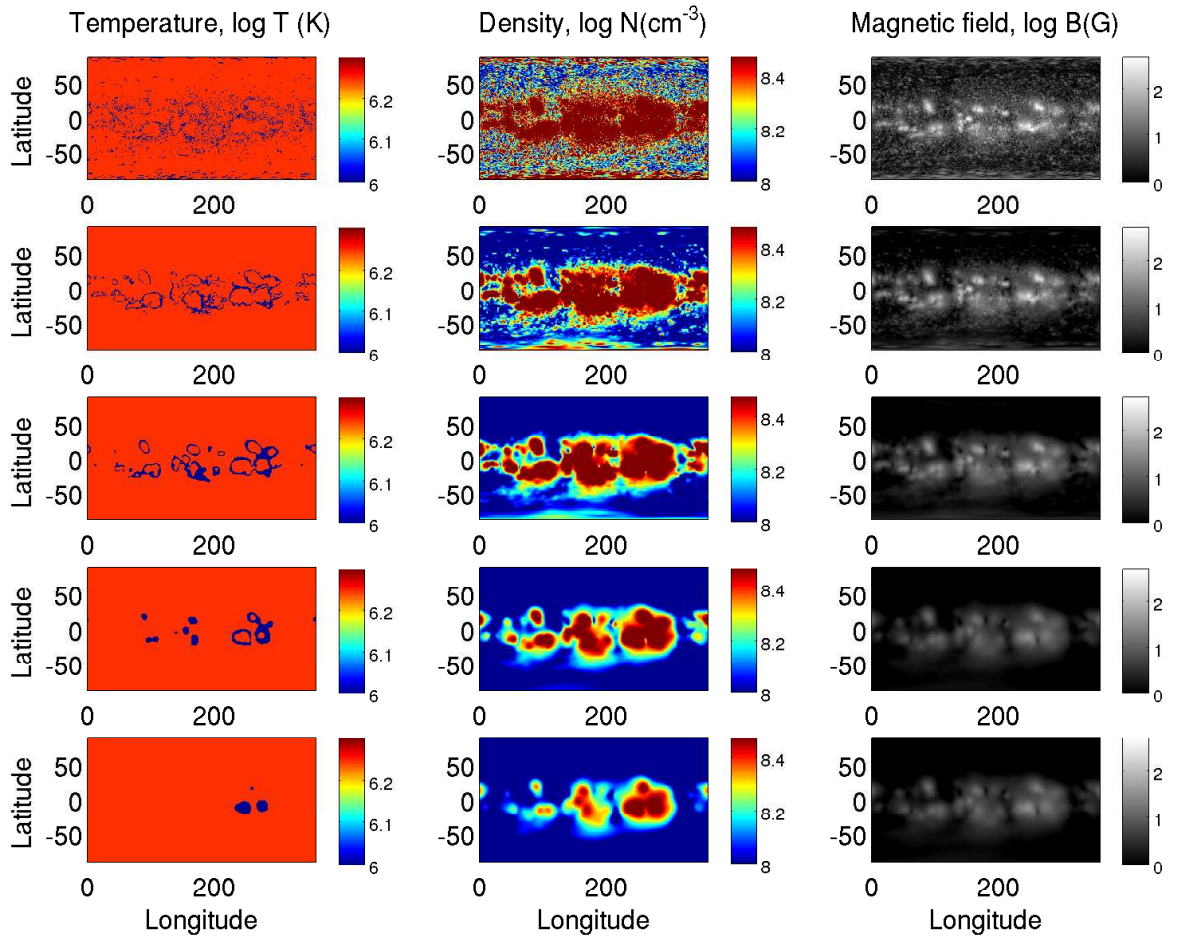
The magnitude of the magnetic field was obtained from PFSS model ( $B = \sqrt{(B_r^2 + B_\phi^2 + B_\theta^2)}$ ) in these specific layers. For these purposes three days were selected: Oct. 01 (1999), Oct. 01 (2014) and Oct. 01 (2016). From the model 1 (figures 3.7, 3.8 and 3.9), contour regions with lower values in temperature are related to regions with moderate magnetic field, higher values of density related to higher values of magnetic field in all layers. The model 2 (figures 3.10, 3.11 and 3.12) shows colder regions when the magnetic field is more intense, in the same way regions with higher values in density in regions with stronger magnetic field. Also in the last layers ( $R_{sun} = 1.10, 1.16$ ) the temperature is constant in Oct. 01 (2016).

Figure 3.7 - Comparison between temperature, density and magnitude of magnetic field in different layers first row  $R_{sun} = 1.00$ , second row  $R_{sun} = 1.02$ , third row  $R_{sun} = 1.05$ , fourth row  $R_{sun} = 1.10$  and the last row  $R_{sun} = 1.16$ , using the model 1, Oct. 01 (1999). First column: temperature maps (log temperature  $T(K)$ ), second column: density maps (log density  $N(cm^{-3})$ ) and last column: magnetic field maps (log magnetic field  $B(G)$ ).



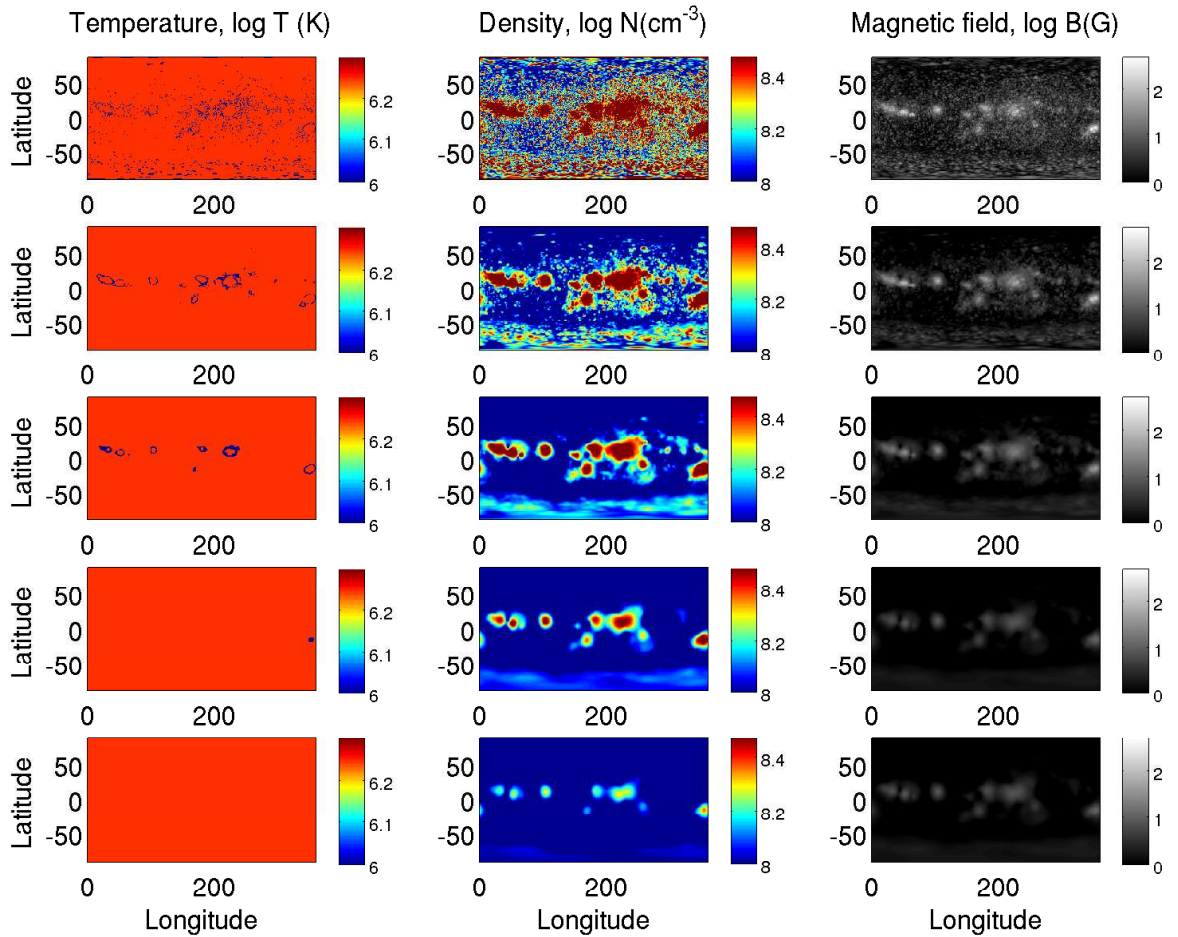
SOURCE: Author

Figure 3.8 - Comparison between temperature, density and magnitude of magnetic field in different layers first row  $R_{sun} = 1.00$ , second row  $R_{sun} = 1.02$ , third row  $R_{sun} = 1.05$ , fourth row  $R_{sun} = 1.10$  and the last row  $R_{sun} = 1.16$ , using the model 1, Oct. 01 (2014). First column: temperature maps (log temperature  $T(K)$ ), second column: density maps (log density  $N(cm^{-3})$ ) and last column: magnetic field maps (log magnetic field  $B(G)$ ).



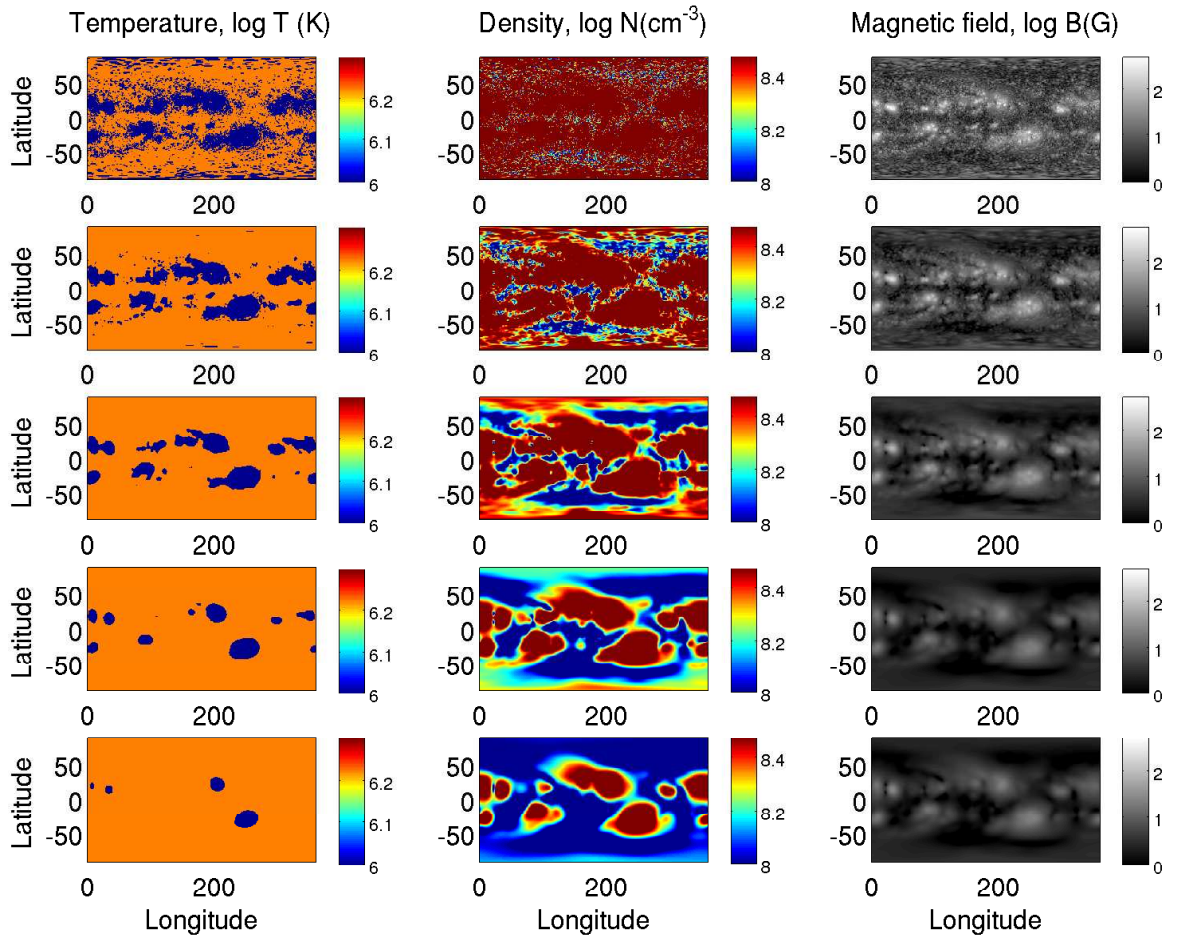
SOURCE: Author

Figure 3.9 - Comparison between temperature, density and magnitude of magnetic field in different layers first row  $R_{sun} = 1.00$ , second row  $R_{sun} = 1.02$ , third row  $R_{sun} = 1.05$ , fourth row  $R_{sun} = 1.10$  and the last row  $R_{sun} = 1.16$ , using the model 1, Oct. 01 (2016). First column: temperature maps (log temperature  $T(K)$ ), second column: density maps (log density  $N(cm^{-3})$ ) and last column: magnetic field maps (log magnetic field  $B(G)$ ).



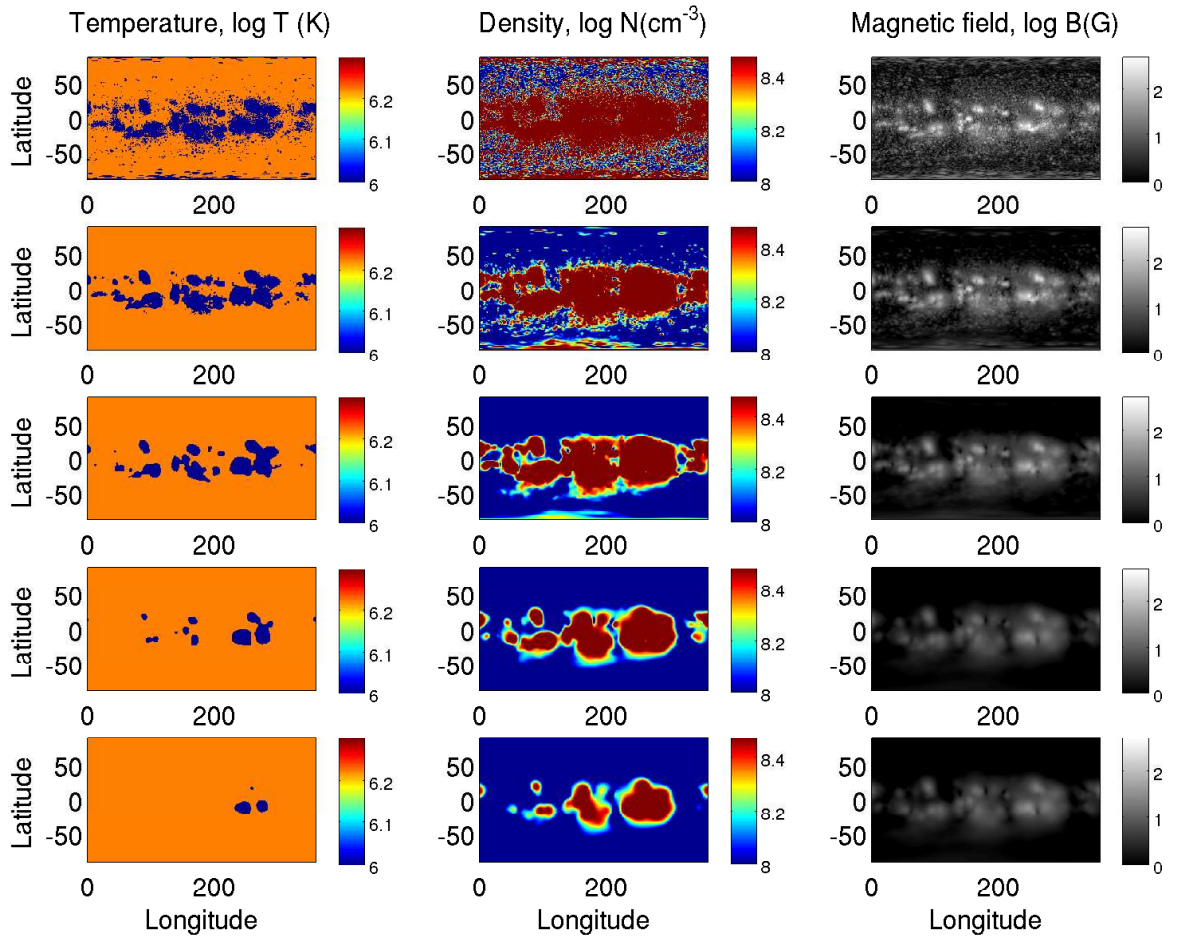
SOURCE: Author

Figure 3.10 - Comparison between temperature, density and magnitude of magnetic field in different layers first row  $R_{sun} = 1.00$ , second row  $R_{sun} = 1.02$ , third row  $R_{sun} = 1.05$ , fourth row  $R_{sun} = 1.10$  and the last row  $R_{sun} = 1.16$ , using the model 2, Oct. 01 (1999). First column: temperature maps (log temperature T(K)), second column: density maps (log density  $N(\text{cm}^{-3})$ ) and last column: magnetic field maps (log magnetic field B(G)).



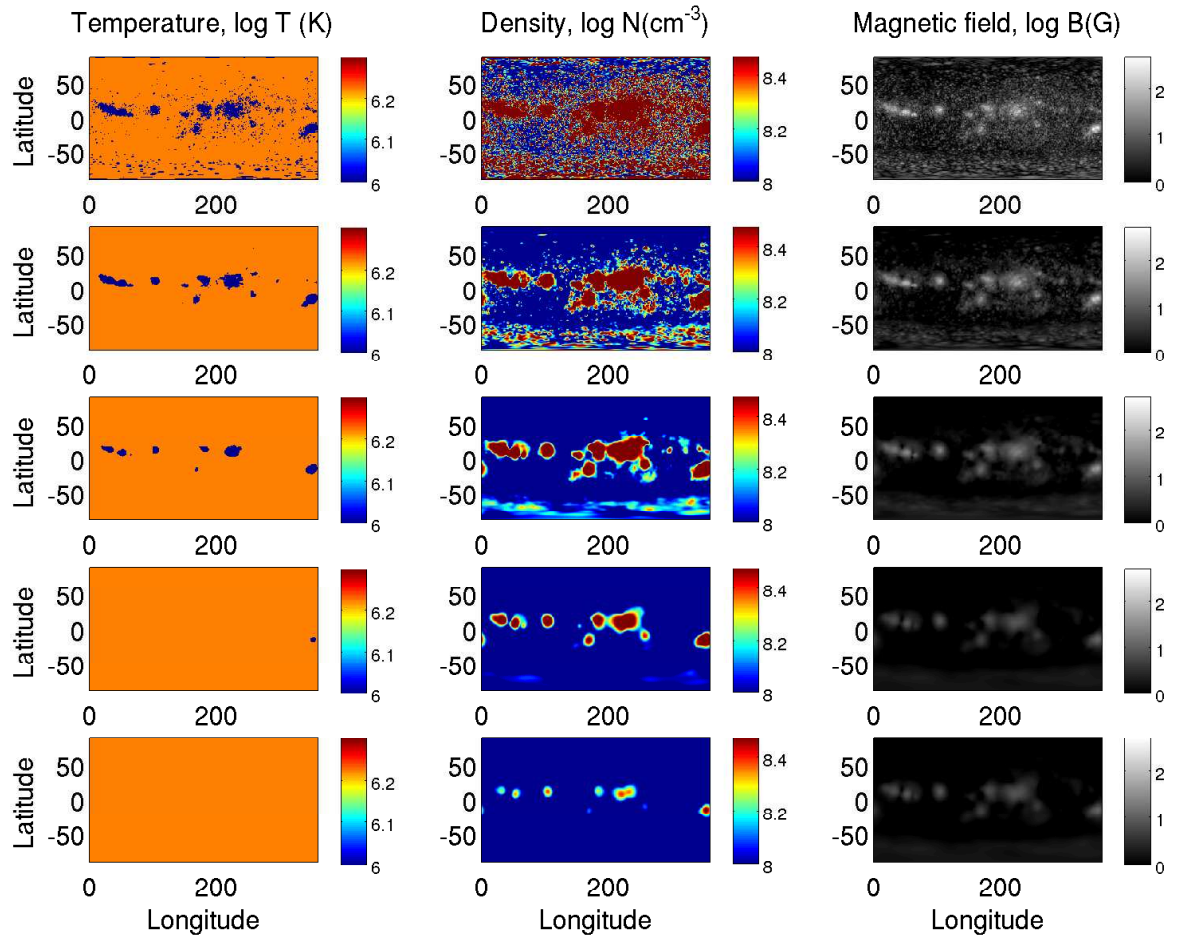
SOURCE: Author

Figure 3.11 - Comparison between temperature, density and magnitude of magnetic field in different layers first row  $R_{sun} = 1.00$ , second row  $R_{sun} = 1.02$ , third row  $R_{sun} = 1.05$ , fourth row  $R_{sun} = 1.10$  and the last row  $R_{sun} = 1.16$ , using the model 2, Oct. 01 (2014). First column: temperature maps (log temperature T(K)), second column: density maps (log density  $N(cm^{-3})$ ) and last column: magnetic field maps (log magnetic field B(G)).



SOURCE: Author

Figure 3.12 - Comparison between temperature, density and magnitude of magnetic field in different layers first row  $R_{sun} = 1.00$ , second row  $R_{sun} = 1.02$ , third row  $R_{sun} = 1.05$ , fourth row  $R_{sun} = 1.10$  and the last row  $R_{sun} = 1.16$ , using the model 2, Oct. 01 (2016). First column: temperature maps (log temperature T(K)), second column: density maps (log density  $N(cm^{-3})$ ) and last column: magnetic field maps (log magnetic field B(G)).



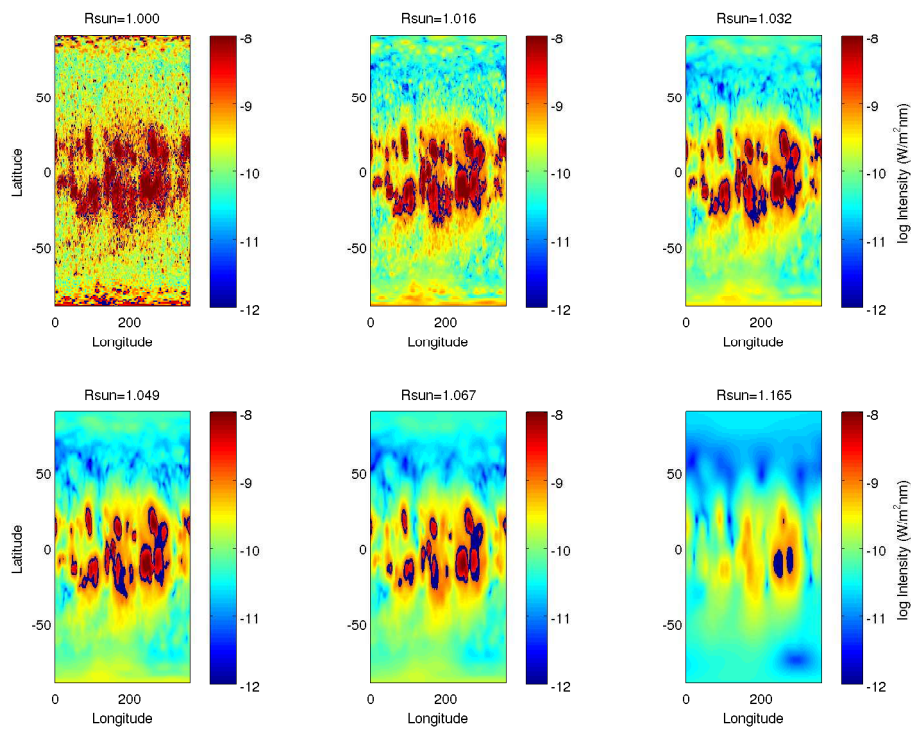
SOURCE: Author

### 3.3 Intensity maps

The intensity maps were obtained using the four wavelengths (17.1, 19.3, 21.1 and 33.5nm) in different layers of the solar atmosphere  $R_{sun}=1.000$ , 1.016, 1.032, 1.049, 1.067 and 1.165 solar radii. The behavior of the emission through different layers in a specific day (Oct. 01 (2014)) was explored. The model 1 at  $R_{sun} = 1.000$  shows that

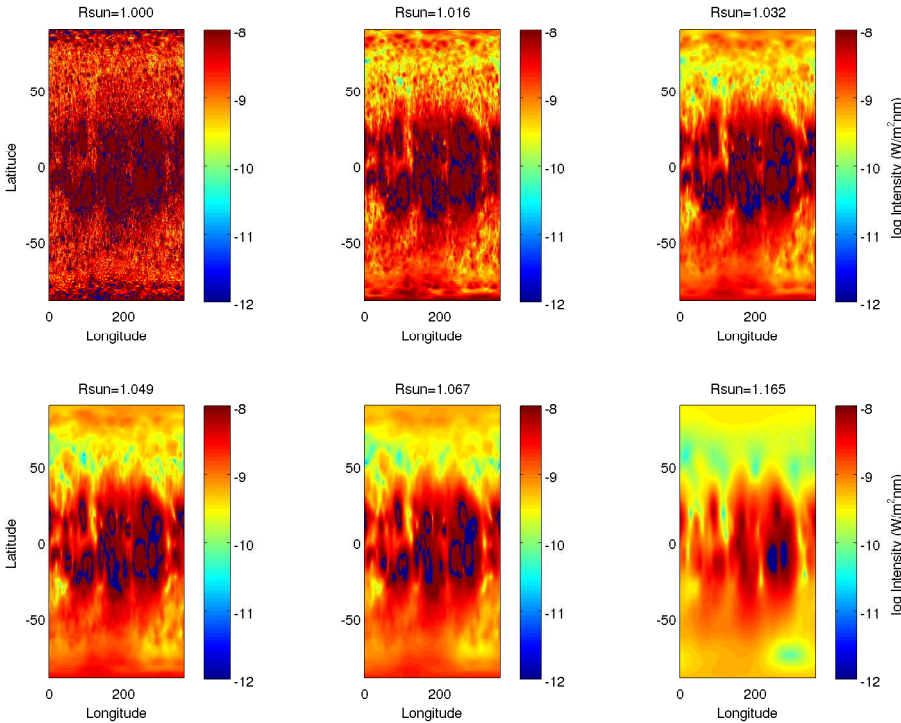
the edges of the sunspots are colder than the interior, in all wavelengths. However, in upper layers it is possible to see regions near the sunspots that show higher values in intensity (figures 3.13, 3.14, 3.15 and 3.16). The model 2 shows regions inside the sunspots are colder than their surroundings. The photospheric features show higher values of intensity in all layers and wavelengths (figures 3.17, 3.18, 3.19 and 3.20).

Figure 3.13 - Intensity map at  $17.1nm$  from model 1, Oct. 01 (2014)



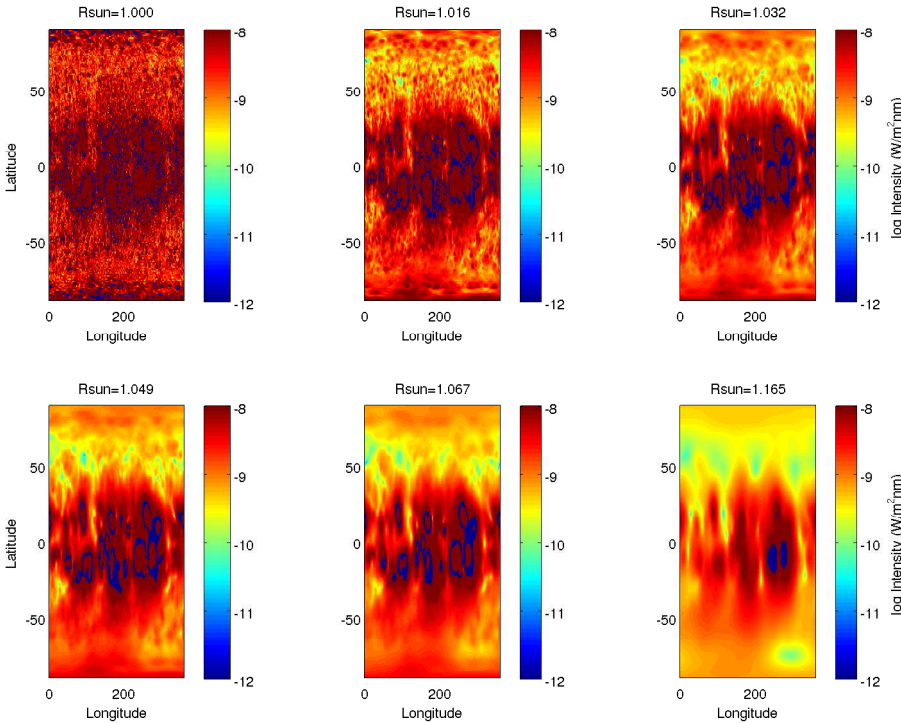
SOURCE: Author

Figure 3.14 - Intensity map at 19.3nm from model 1, Oct. 01 (2014)



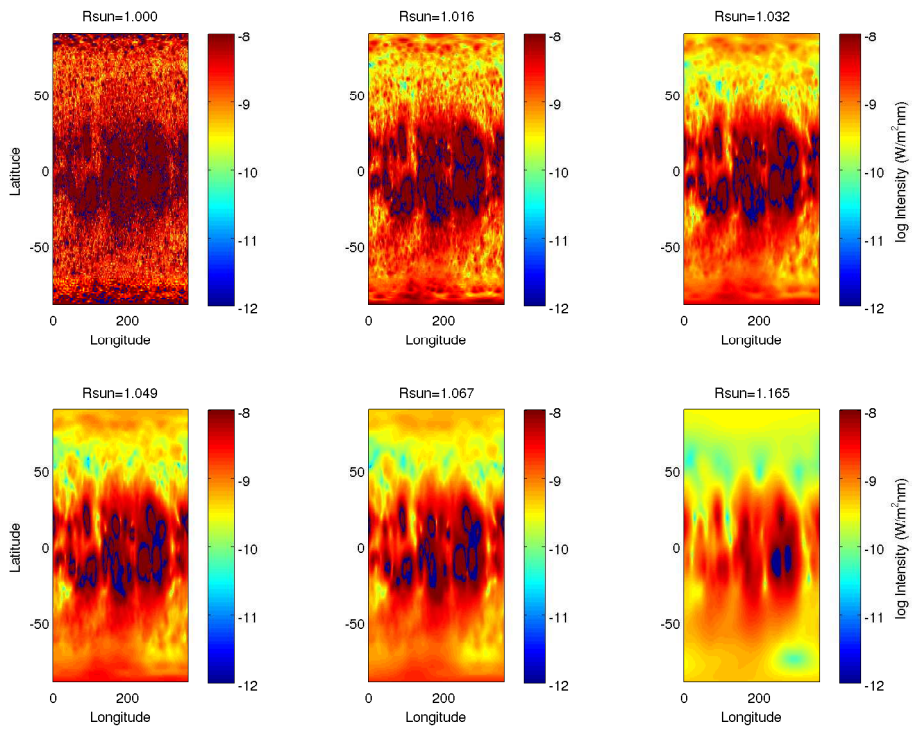
SOURCE: Author

Figure 3.15 - Intensity map at 21.1nm from model 1, Oct. 01 (2014)



SOURCE: Author

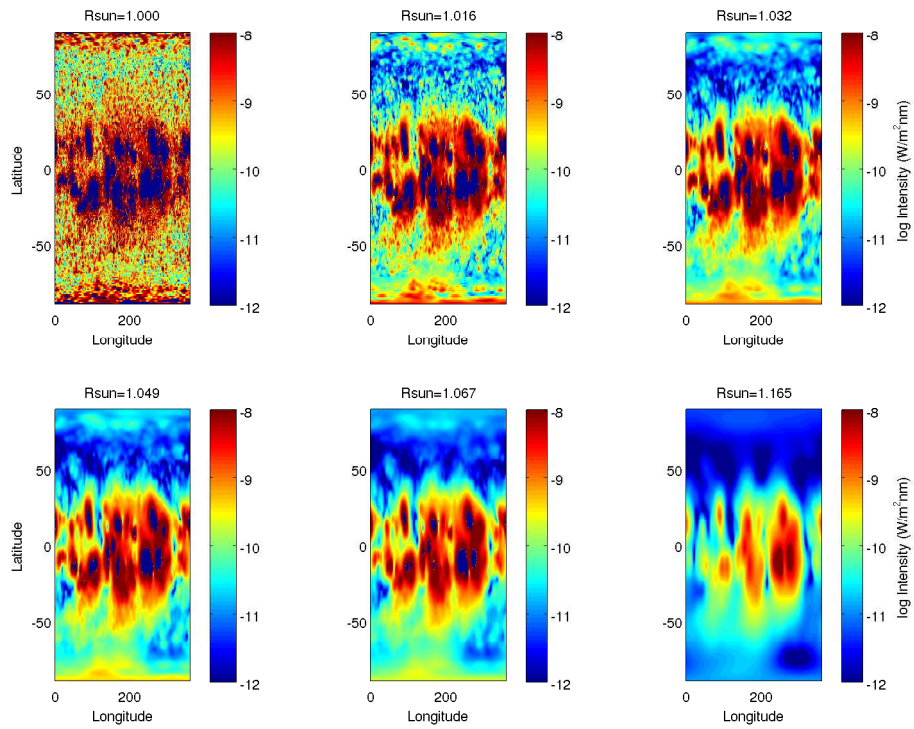
Figure 3.16 - Intensity map at  $33.5\text{nm}$  from model 1, Oct. 01 (2014)



SOURCE: Author

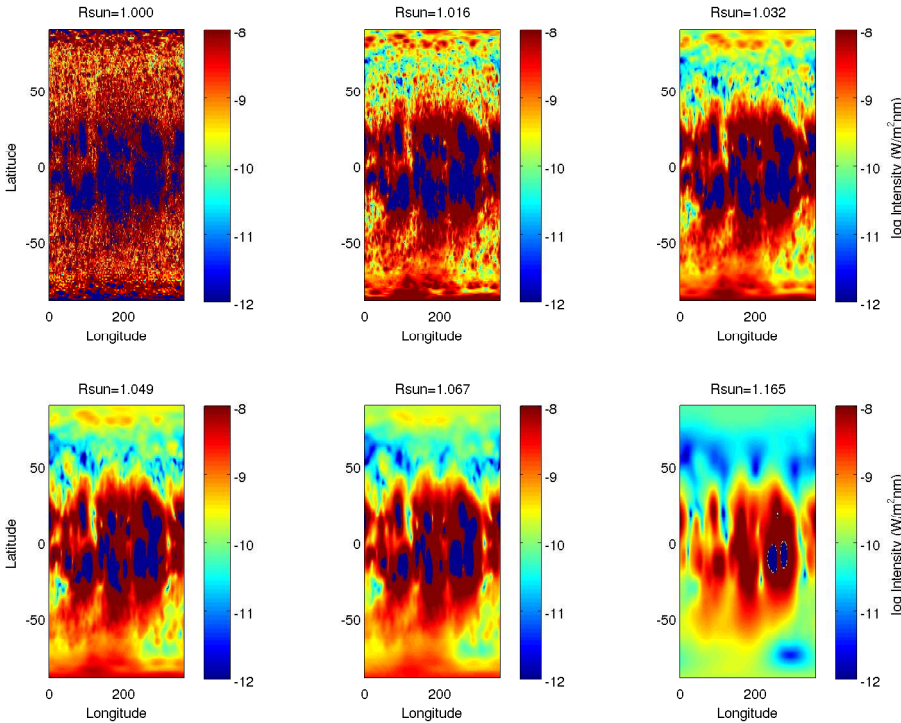
## Model 2

Figure 3.17 - Intensity map at  $17.1nm$  from model 2, Oct. 01 (2014)



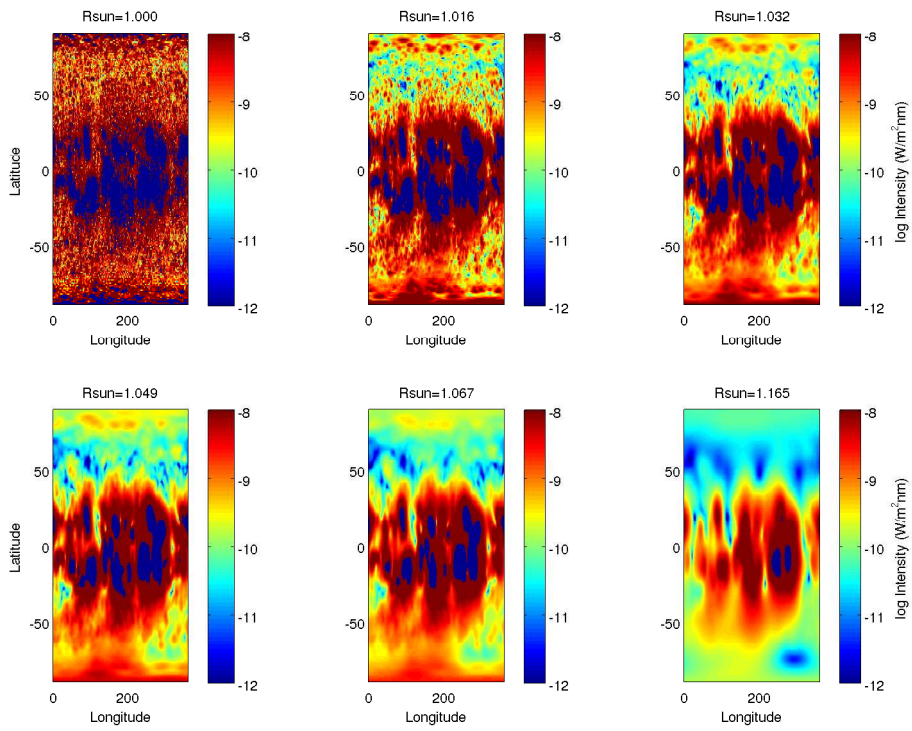
SOURCE: Author

Figure 3.18 - Intensity map at 19.3nm from model 2, Oct. 01 (2014)



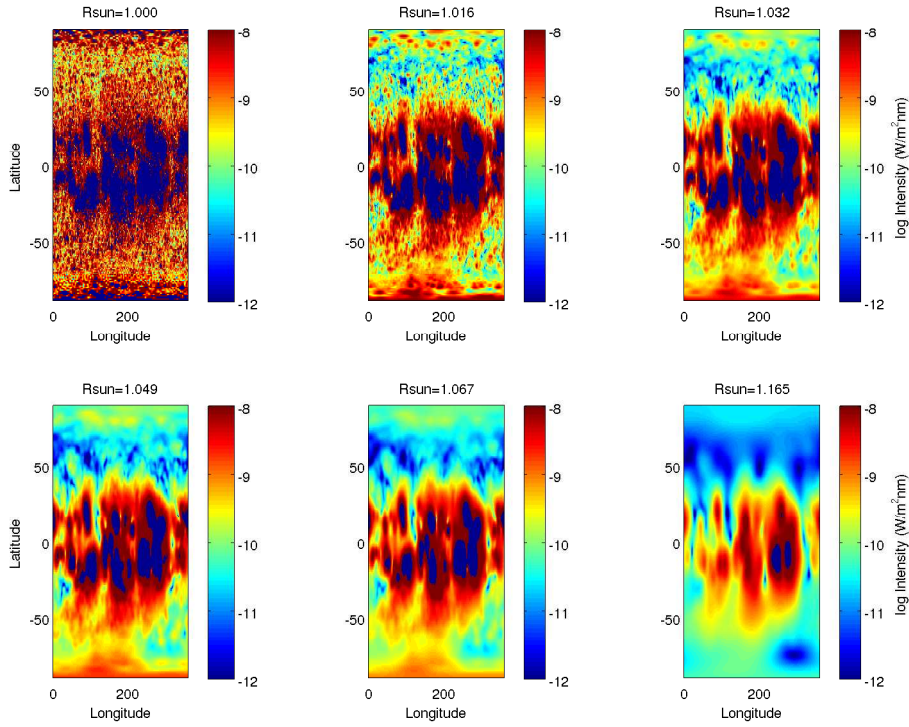
SOURCE: Author

Figure 3.19 - Intensity map at  $21.1nm$  from model 2, Oct. 01 (2014)



SOURCE: Author

Figure 3.20 - Intensity map at 33.5nm from model 2, Oct. 01 (2014)

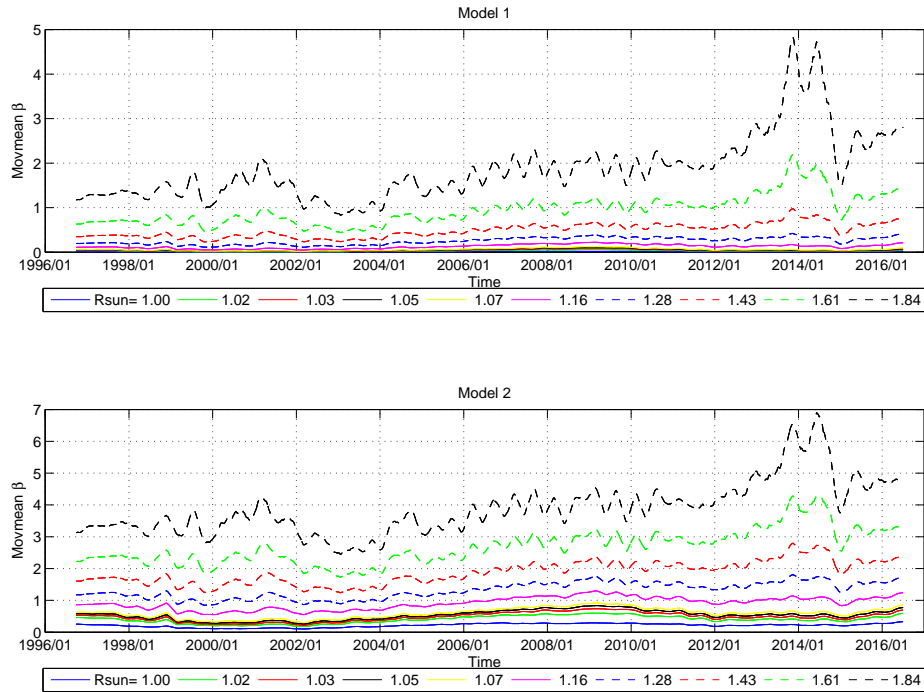


SOURCE: Author

### 3.4 Plasma $\beta$ parameter in solar corona

The structure of the solar atmosphere is complex, due to interchanging roles of plasma and magnetic pressure. This behavior is usually described by plasma  $\beta$ . The plasma  $\beta$  parameter was calculated using the photospheric magnetic field from 1996 to 2016. Also, using the density and temperature profiles from model 1 and 2, the average  $\beta$  value was calculated through all layers and the evolution of the parameter  $\beta$  over the last two solar cycles per day (Figure 3.21) was analyzed. The models show the  $\beta$  values  $< 1.0$  over this period, related to the behavior above the photosphere. The  $\beta$  values obtained from the models are higher than 1.0. The moving average using the two models shows an increase over the solar cycle 24 (Figure 3.21).

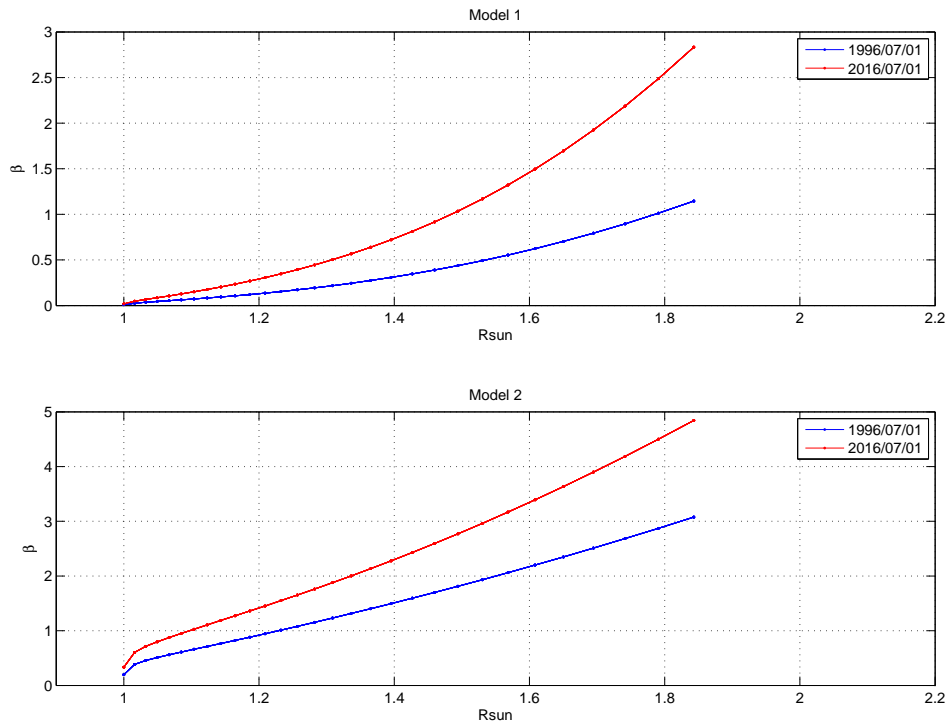
Figure 3.21 - Evolution of the plasma  $\beta$  parameter during the solar cycle 23 and 24. Using the moving average  $\beta$  values with the time period of 90 days. Upper panel: Model 1 parameters through all layers. Lower panel: Model 2 parameters through all layers.



SOURCE: Author

The variation in the height was evaluated using data of two days, the variations were explored from  $Rsun = 1.000$  to  $Rsun = 1.8431$ . For model 1 in Jul. 01 (1996) the  $\beta$  values are  $< 1.00$  for less higher values of  $Rsun = 1.800$ , but in  $Rsun = 1.8431$   $\beta$  value is older to 1.00. In Jul. 01 (2016) in  $Rsun > 1.5$  show values of  $\beta > 1$  (upper panel Figure 3.22). The model 2 describes a different behavior, on Jul. 01 (1996)  $\beta > 1.00$  at the height of 1.2089, in Jul. 01 (2016)  $\beta > 1.00$  occurs at the height of  $Rsun = 1.1$ .

Figure 3.22 - Plasma  $\beta$  variation with the height through the solar atmosphere. Two days were chosen Jul.01 (1996) (blue line) and Jul. 01 (2016) (red line).



SOURCE: Author

### 3.5 Summary

The modelled SSI is in agreement with the observational data and validates the model. The temperature profiles in different layers through the solar atmosphere show an interesting behavior: layers near to the photosphere are colder than the external layers. These decrease is lower in the solar cycle 24 compared with the solar cycle 23. However, the moving average temperature analysis shows an increase in temperature (expected behavior), when variations in intervals of 90 days were calculated. These variations in temperature follow the variations of the magnetic field through the solar cycle.

The electron density follows the sunspot trend during the solar cycle and it is related to the variations of the magnetic flux. Also, in the layers near to the photosphere the density lower values compared to external layers. The temperature profiles shows lower values in layers near the photosphere, in external layers the temperature are

constant. The behavior of the density and temperature profiles are in agreement to the relationship with the variation of magnetic field.

The emission in layers near the photosphere show that the edges of the sunspots are colder than the interior. But at upper layers it is possible to see regions near to the sunspots with higher values in intensity (model 1). However, model 2 shows that regions inside the sunspots are colder than their surroundings. In the selected models, the photospheric features show higher values of intensity in all layers and wavelengths.

The plasma  $\beta$  parameter was calculated in order to validate the physics of the model. The behavior obtained from the selected model shows that  $\beta$  changes between values lower than unit in the chromosphere and transition region and higher than unit at lower corona ( $\sim 1.8$  solar radii). But, values higher than unit were found in layers near the photosphere, probably due to the values of extrapolated magnetic field or uncertainty in the force free extrapolated codes (discussed in [GARY \(2001\)](#)).



## 4 EVOLUTION AND EMISSION OF THE ACTIVE REGION NOAA 11855

### Contents

---

4.1	Evolution of the Active region NOAA 11855 . . . . .	138
4.1.1	Emission . . . . .	138
4.2	Summary . . . . .	142

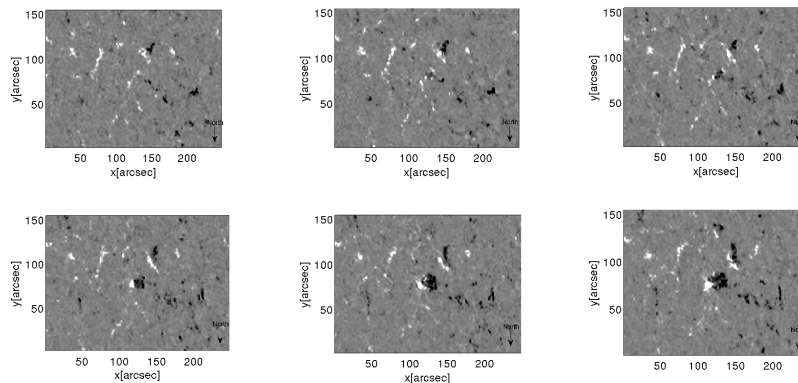
---

The problem of active region heating requires precise descriptions of physical plasma parameters such as density and temperature. In this way it is possible to understand the relationship between coronal structures and the photospheric magnetic field.

Some coronal features can be characterized using parameters such as the temperature and density, but the diagnosis of density and temperature is not trivial. The active regions exhibit the hottest temperatures because the heated plasma is trapped while in open-field regions seem to be cooler because the plasma transport is efficient (Table 1.2, 1.4 and 1.5).

The emergence flux region evolution from Sep. 29 2013 from 6:00UT to 18:00UT (Figure 4.1) is the starting point of this study. This evolution was studied using the magnetic field from HMI/SDO. The flux emergence patches appear at  $[x,y]=(140, 80)$  arcsec and  $[x,y]=(150, 110)$  arcsec. These patches will evolve to become Active Region NOAA11855.

Figure 4.1 - Evolution of the emergence flux region in HMI/SDO photospheric magnetic field. North is bottom.

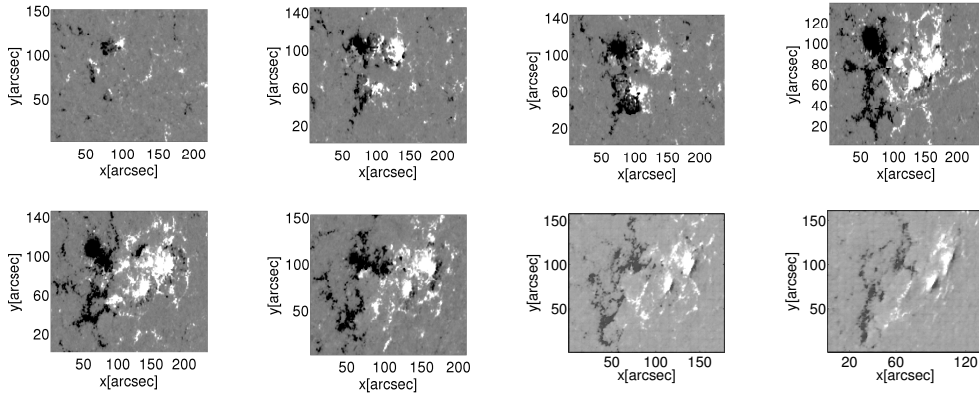


SOURCE: Author

## 4.1 Evolution of the Active region NOAA 11855

The evolution of the emergence flux region shows regions that evolve to the formation of the Active Region NOAA 11855 or HARPS 3244 from Sep. 29 18:00UT to Oct. 07 13:00UT. For this purpose it was used the vectorial magnetic field products (SHARPS) observed by HMI instrument aboard SDO spacecraft. These vectorial magnetic patches do not have the same size overall period of interest (Figure 4.2).

Figure 4.2 - Evolution of the Active Region NOAA11855 (SHARPS/HMI), from Sept. 29 to Oct. 06 (2013). First row: Sept. 29 18:00UT, Sept. 30 18:00UT, Oct. 01 00:00UT, Oct. 02 12:00UT. Second row: Oct. 03 12:00UT, Oct. 04 18:00UT, Oct. 05 18:00UT and Oct. 06 18:00UT. North is up.

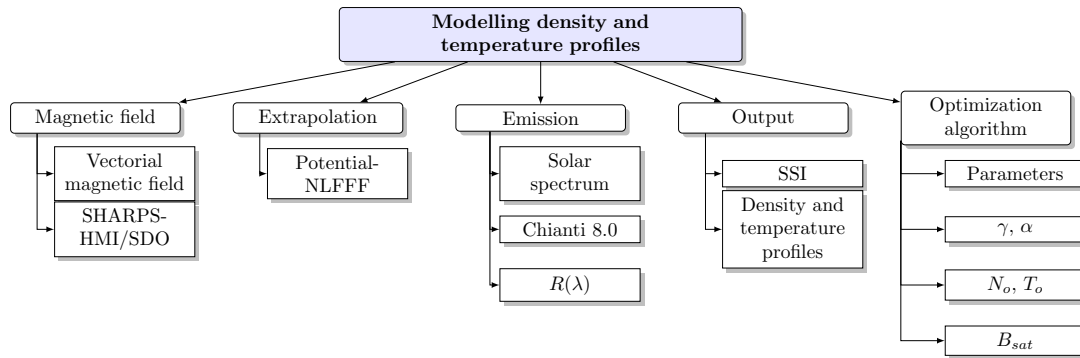


SOURCE: Author

### 4.1.1 Emission

The emission was obtained using the model described in the section 2.1. The model was modified (Figure 4.3), using patches from SHARPS/HMI over the solar photosphere and the potential coronal magnetic field was obtained from NLFFF/SWW from  $R_{sun} = 1.0$  to  $R_{sun} = 1.15$ . The emission was calculated using the CHIANTI atomic database 8.0 at the  $30.4nm$  and  $17.1nm$ . Also, the model parameters described in the chapter 3 (model 1 and model 2) were applied in this specific region.

Figure 4.3 - Schematic description of the density and temperature model in ARs.

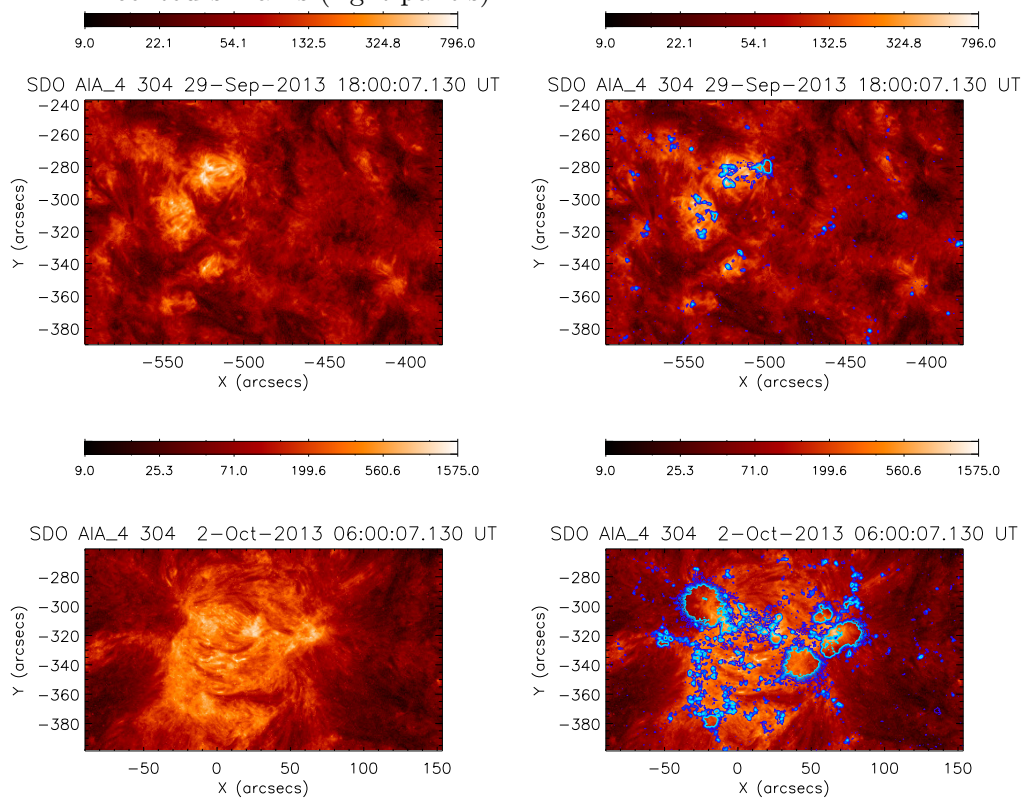


SOURCE: Author

In order to compare the emission in each selected region, the composite images were obtained using AIA images and vectorial magnetic field from SHARPS (Figure 4.4 and 4.5). These procedures allow selection of region of interest. In each of these regions of the AIA instrument, it was calculated the integrated emission. These emissions were compared with the emission obtain from the model (Figure 4.6).

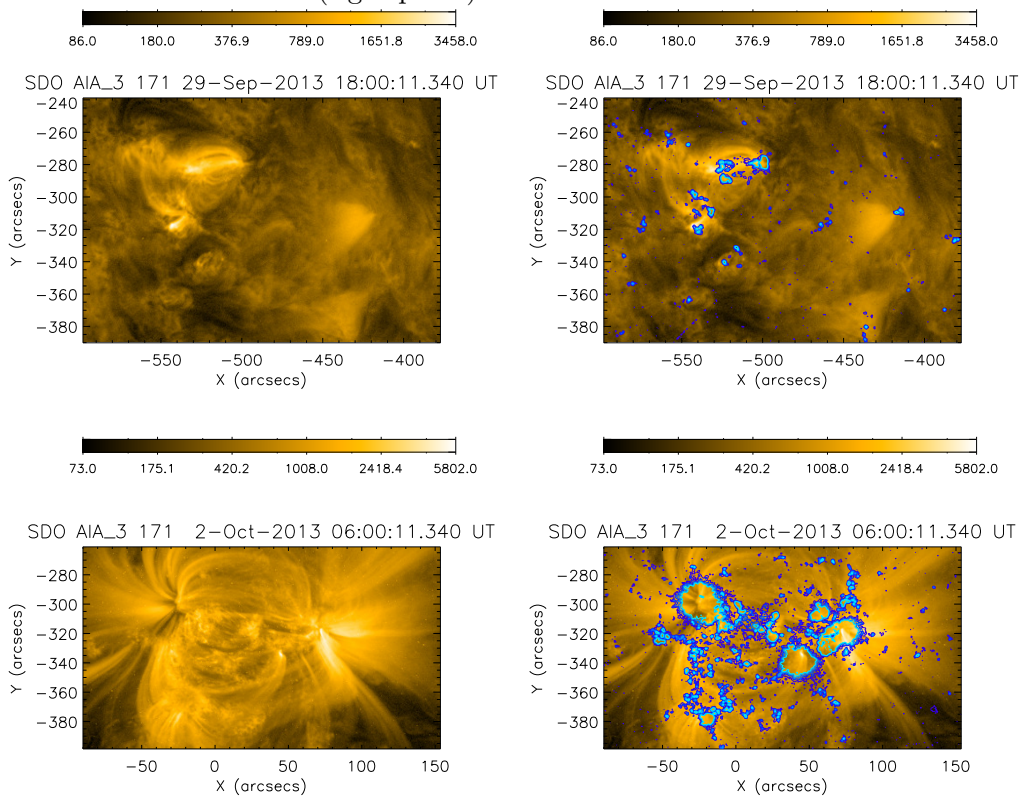
These wavelengths describe the emission from the hot loops in  $17.1nm$  and from the active region in the lower transition region in  $30.4nm$ . The emission is not linked to flares. The intensity increase is steeper in  $30.4nm$  than in  $17.1nm$  as we can see from the faster flux emergence in the upper chromosphere, as compared to the corona.

Figure 4.4 - Images at  $30.4nm$  from AIA/SDO (left panel) and composite images using photospheric magnetic field from HMI/SDO for the same region with blue contours marks (right panels).



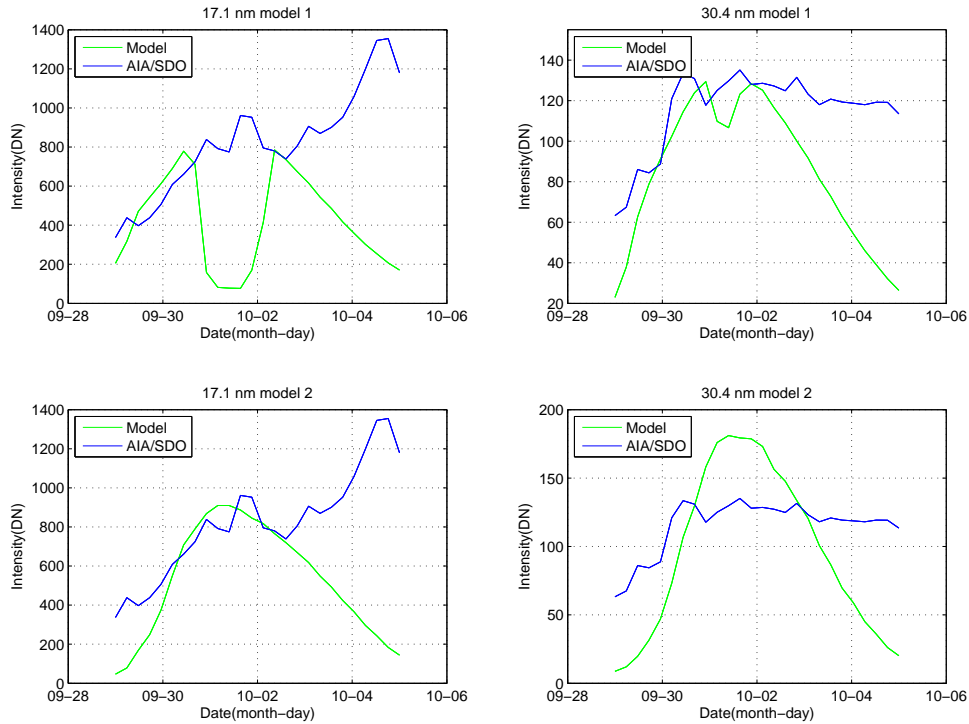
SOURCE: Author

Figure 4.5 - Images at  $17.1nm$  from AIA/SDO (left panel) and composite images using photospheric magnetic field from HMI/SDO for the same region with blue contours marks (right panel).



SOURCE: Author

Figure 4.6 - Emission in the NOAA 11855 using the parameters from selected models (chapter 3). Integrated intensity from the AIA/SDO (blue line), emission from the CODET model (green line). Upper panels: Emission at  $17.1nm$  and  $30.4nm$  using the parameters of the model 1. Lower panels: Emission at  $17.1nm$  and  $30.4nm$  using the parameters of the model 2.



SOURCE: Author

## 4.2 Summary

The evolution of the emergence flux region shows regions that evolve to the formation of the Active Region NOAA 11855.

Unfortunately, using the CODET model it is not possible to recover the emission from the Active Regions NOAA 11855, probably due to the magnetic field extrapolated with different tool (NLFFF) and the method to obtain the magnetic field is different.

## 5 CONCLUSIONS

The solar cycle related properties of the solar magnetic field are relevant to the dynamo theory (section 1.1). Some characteristics such as the level of activity are related to the sunspot number (with a period of 11 years) as sunspots evolve from appearing at high latitudes in the beginning of the solar cycle, gradually progressing toward the equator. Also, the pattern is repeated with all magnetic polarities reversed (22 years). All of these characteristics are related to the Babcock-Leighton model, which in turn describes the flux-transport mechanism at the solar photosphere, the main idea of the CODET model. In this way the density and temperature profiles mimic the solar cycle properties, and in general the dynamics of the solar atmosphere.

Variations of the coronal temperature and density are a function of latitude and phase of the solar cycle. They provide an important constraint, necessary to model the solar wind. These relations are necessary to evaluate the relationship with the heliosphere and the Earth's atmosphere.

The CODET model was built and successfully applied to obtain the Solar Spectral Irradiance (SSI), density and temperature profiles during the last solar cycles. The CODET model uses the synoptic magnetic field from MDI/SOHO and HMI/SDO, a flux transport model from SCHRIJVER (2001), magnetic field extrapolation from PFSS/SSW, an emission model using the CHIANTI atomic database 8.0 and the optimization algorithm Pikaia from BELUGA-MATLAB optimization package.

Let us now consider some more specific issues and results:

- The variation of the irradiance and the plasma parameters is due to the evolution of the solar magnetic field. This assumption was checked using the CODET model. Also, the performance of the model is comparable to that of the observational data from TIMED/SEE. It is possible to follow the Solar Spectral Irradiance (SSI) variation between solar activity maximum and minimum. The agreement with the data is gratifying considering that the CODET model do not have a MHD approach.
- Using the CODET model it is possible to reproduce the spectral solar irradiance (SSI) in four different wavelengths,  $17.1nm$ ,  $19.3nm$ ,  $21.1nm$  and  $33.5nm$  during the solar cycle 23 and 24. The model was able to fit simultaneously three wavelengths in the EUV band.

- The photosphere is homogeneous during the solar minimum. When the solar cycle is in rising phase the sunspots appear. In general the sunspots are regions with relatively lower temperature and inside of them the convection motion is blocked by the strong magnetic field. Also, the sunspots are cooler than the quiet photosphere. These dynamics are recovered using the CODET model, and evaluated in temperature and emission maps.
- The chromosphere shows a temperature profile increasing with height, due to chromospheric material, which is much less dense than the photospheric material and receives heat from below. The temperature in the transition region increases extremely rapid. This behavior is shown, in the temperature profiles obtained from the CODET model.
- The temperature profiles show lower values in temperature in internal layers during the solar cycle 23. However, in the solar cycle 24 the temperature increases in internal layers near the photosphere. Also, in the external layers the temperature is higher than in the internal layers during the two last solar cycles. Although, the average temperature in each solar cycle is higher in the solar corona as expected. The solar cycle 23 shows lower temperature values than the solar cycle 24.
- The density profiles shows lower values in the external layers and high values in layers near the photosphere. Higher values in the density profiles were present during the solar cycle 23 compared to the solar cycle 24. The electron density profiles follow the sunspot trend during the solar cycle and they are related to the variations of the magnetic flux.
- The relationship between magnetic field, density and temperature were evaluated using both selected models. The modelled temperature profile is inversely proportional to the magnetic field, in the same way higher values in density are related to a strong magnetic field through the solar atmosphere.
- Two models were selected. They are in agreement with the description in [SCHRIJVER \(2001\)](#), the upper atmosphere emission over sunspots being reduced compared to other regions. On the other hand, the photospheric features shown higher values of emission in all layers and wavelengths.
- The emission behavior is in agreement with temperature in the selected models. The complex dynamics of solar atmosphere influences the emission

variations at different temporal scales. In the periods from hours to days, the sunspots, faculae and the evolution of the active regions influence the emission. In long time scales, of the order of the solar cycle period, the redistribution of the surface magnetic field plays an important role. In the CODET model this dynamics can be recovered using the flux transport model from [SCHRIJVER \(2001\)](#). Also, observations suggest that faculae increase radiance considerably more than sunspots. These behaviors are recapturing through the CODET model when different layers through the solar atmosphere were observed.

- The  $\beta$  parameter behavior is recovered using our model and it has physical meaning. This parameter shows high values over the solar cycle 24 related to the gas pressure dominating over the magnetic pressure. Opposite case occurs during the solar cycle 23 where the magnetic pressure dominates over the gas pressure.

On the other hand, large pieces of evidence exist which suggest that  $\beta$  is  $> 1$  at relatively low coronal heights, as it actually happens in the obtained values from CODET model. These unexpected values can be related to the extrapolation magnetic field method. The physical consequence of the high- $\beta$  regions are associated to ejection event and reconnection.

- The CODET model is a powerful tool to describe variations in large time scales - two last solar cycles ( $\sim 22$ -years). However, one limitation of CODET is that it is not possible to reconstruct the emission from short time scales and small regions over the solar photosphere.
- The analysis of flux emergence regions shows that laminarity (intermittency) and entropy are present. They have shown an important relationship between the emergence flux regions, the Active Regions and the dynamics of the solar atmosphere.

Future work:

- The spectral coverage of the CODET model can be extended (ie. UV, since to this band influences the Earth's atmosphere and climate in large time scales).
- Development of the magnetic flux transport code to perform SSI forecast in near real time, as well as the density and temperature profiles and variation through the solar atmosphere.

- The photospheric solar data will be locally available in the coming years from The Brazilian Experimental Solar Telescope development at INPE.
- The model can be applied to study of solar like stars .

## REFERENCES

- AIRAPETIAN, V. S.; ALLRED, J. Forward modeling of synthetic EUV/SXR emission from solar coronal active regions: case of AR 11117. v. 18, 2015. 7
- ALLEN, C. W. Interpretation of electron densities from corona brightness. **Monthly Notices of the Royal Astronomical Society**, v. 107, p. 426, 1947. 27
- ASCHWANDEN, M. J. **Physics of the solar corona - an introduction with problems and solutions. 2. ed.** Berlin: Springer-Verlag Berlin Heidelberg, 2005. 4, 6, 25, 27, 29
- BASU, S.; ANTIA, H. M. Characteristics of solar meridional flows during solar cycle 23. **The Astrophysical Journal**, v. 717, p. 488–495, jul. 2010. 14
- BILLINGS, D. E. **A guide to the solar corona.** New York: Academic Press, 1966. 28, 30, 31
- CHARBONNEAU, P. Genetic algorithms in astronomy and astrophysics. **The Astrophysical Journal Supplement**, v. 101, p. 309, dec. 1995. 44
- \_\_\_\_\_. Dynamo models of the solar cycle. **Living Reviews in Solar Physics**, v. 7, p. 3, dec. 2010. 9
- DAVIS, L. **Handbook of genetic algorithms.** New York: Van Nostrand Reinhold, 1998. 44
- DEVORE, C. R.; BORIS, J. P.; SHEELEY JR., N. R. The concentration of the large-scale solar magnetic field by a meridional surface flow. **Solar Physics**, v. 92, p. 1–14, may 1984. 15
- DIKPATI, M.; CHARBONNEAU, P. A Babcock-Leighton flux transport dynamo with solar-like differential rotation. **The Astrophysical Journal**, v. 518, p. 508–520, jun. 1999. 9
- DIKPATI, M.; GILMAN, P. A. Flux-transport solar dynamos. **Space Science Review**, v. 144, p. 67–75, apr. 2009. 10
- DWIVEDI, B. N.; PARKER, F. b. E. N. **Dynamic sun.** United Kingdom: Cambridge University Press, 2003. 14

ERMOLLI, I.; MATTHES, K.; DUDOK de WIT, T.; KRIVOVA, N. A.; TOURPALI, K.; WEBER, M.; UNRUH, Y. C.; GRAY, L.; LANGEMATZ, U.; PILEWSKIE, P.; ROZANOV, E.; SCHMUTZ, W.; SHAPIRO, A.; SOLANKI, S. K.; WOODS, T. N. Recent variability of the solar spectral irradiance and its impact on climate modelling. **Atmospheric Chemistry & Physics**, v. 13, p. 3945–3977, apr. 2013. [34](#), [38](#)

FLIGGE, M.; SOLANKI, S. K.; UNRUH, Y. C. Modelling irradiance variations from the surface distribution of the solar magnetic field. **Astronomy and Astrophysics**, v. 353, p. 380–388, jan. 2000. [37](#)

FONTENLA, J. M.; AVRETT, E. H.; LOESER, R. Energy balance in the solar transition region. III - Helium emission in hydrostatic, constant-abundance models with diffusion. **The Astrophysical Journal**, v. 406, p. 319–345, mar. 1993. [5](#)

FONTENLA, J. M.; HARDER, J.; LIVINGSTON, W.; SNOW, M.; WOODS, T. High-resolution solar spectral irradiance from extreme ultraviolet to far infrared. **Journal of Geophysical Research (Atmospheres)**, v. 116, p. D20108, oct. 2011. [28](#), [31](#), [37](#)

FONTENLA, J. M.; LANDI, E.; SNOW, M.; WOODS, T. Far-and extreme-UV solar spectral irradiance and radiance from simplified atmospheric physical models. **Solar Physics**, v. 289, p. 515–544, feb. 2014. [31](#)

GARY, G. A. Plasma beta above a solar active region: rethinking the paradigm. **Solar Physics**, v. 203, p. 71–86, oct. 2001. [135](#)

GESTAL, M.; RIVERO, D.; J.R., R.; DORADO J. PAZOS, A. **Introducción a los algoritmos genéticos y la programación genética**. España: Universidade da Coruña, 2010. [44](#)

GIBSON, S. E.; CHARBONNEAU, P. Empirical modeling of the solar corona using genetic algorithms. **Journal of Geophysical Research**, v. 103, p. 14511–14522, jul. 1998. [45](#)

GOLUB, L.; PASACHOFF, J. M. **The solar corona**. New York: Cambridge University Press, 2009. [6](#), [21](#), [23](#), [30](#)

GUERRERO, G.; KÄPYLÄ, P. J. Dynamo action and magnetic buoyancy in convection simulations with vertical shear. **Astronomy and Astrophysics**, v. 533, p. A40, sep. 2011. [9](#)

GUERRERO, G.; SMOLARKIEWICZ, P. K.; KOSOVICHEV, A.; MANSOUR, N. Solar differential rotation: hints to reproduce a near-surface shear layer in global simulations. **IAU Symposium 294**, v. 294, p. 417–425, jul. 2013. [9](#)

GUHATHAKURTA, M.; ROOTTMAN, G.; FISHER, R.; ORRALL, F.; ALTROCK, R. Coronal density and temperature structure from coordinated observations associated with the total solar eclipse of 1988 March 18. **The Astrophysical Journal**, v. 388, p. 633–643, apr. 1992. [26](#), [28](#)

HABBAL, S. R.; DRUCKMÜLLER, M.; MORGAN, H.; DAW, A.; JOHNSON, J.; DING, A.; ARNDT, M.; ESSER, R.; RUŠIN, V.; SCHOLL, I. Mapping the distribution of electron temperature and Fe charge states in the corona with total solar eclipse observations. **The Astrophysical Journal**, v. 708, p. 1650–1662, jan. 2010. [26](#), [28](#)

HATHAWAY, D. H. Doppler measurements of the sun's meridional flow. **The Astrophysical Journal**, v. 460, p. 1027, apr. 1996. [14](#)

\_\_\_\_\_. The solar cycle. **Living Reviews in Solar Physics**, v. 12, p. 4, dec. 2015. [xiii](#), [8](#)

HAYES, A. P.; VOURLIDAS, A.; HOWARD, R. A. Deriving the electron density of the solar corona from the inversion of total brightness measurements. **The Astrophysical Journal**, v. 548, p. 1081–1086, feb. 2001. [26](#)

HOWARD, R.; LABONTE, B. J. The sun is observed to be a torsional oscillator with a period of 11 years. **The Astrophysical Journal**, v. 239, p. L33–L36, jul. 1980. [13](#)

JIANG, J.; HATHAWAY, D. H.; CAMERON, R. H.; SOLANKI, S. K.; GIZON, L.; UPTON, L. Magnetic flux transport at the solar surface. **Space Science Reviews**, v. 186, p. 491–523, dec. 2014. [15](#), [16](#)

KÄPYLÄ, P. J.; KORPI, M. J.; BRANDENBURG, A. Large-scale dynamos in turbulent convection with shear. **Astronomy and Astrophysics**, v. 491, p. 353–362, nov. 2008. [9](#)

KÄPYLÄ, P. J.; KORPI, M. J.; BRANDENBURG, A.; MITRA, D.; TAVAKOL, R. Convective dynamos in spherical wedge geometry. **Astronomische Nachrichten**, v. 331, p. 73, jan. 2010. [9](#)

- KÄPYLÄ, P. J.; KORPI, M. J.; TUOMINEN, I. Local models of stellar convection: Reynolds stresses and turbulent heat transport. **Astronomy and Astrophysics**, v. 422, p. 793–816, aug. 2004. 9
- KOMM, R. W.; HOWARD, R. F.; HARVEY, J. W. Rotation rates of small magnetic features from two- and one-dimensional cross-correlation analyses. **Solar Physics**, v. 145, p. 1–10, may 1993. 14
- KOUTCHMY, S.; ZIRKER, J. B.; STEINOLFSON, R. S.; ZHUGZHDA, I. D. **Coronal activity**. Tucson: University of Arizona Press, 1991. 26
- KRESTZSCHMAR, M.; LILENSTEN, J.; ABOUDARHAM, J. Variability of euv and quiet sun emission and reference spectrum using sumer. **Astronomy and Astrophysics**, v. 419, p. 345–356, 2004. 7
- KRIVOVA, N. A.; SOLANKI, S. K.; FLIGGE, M.; UNRUH, Y. C. Reconstruction of solar irradiance variations in cycle 23: is solar surface magnetism the cause? **Astronomy and Astrophysics**, v. 399, p. L1–L4, feb. 2003. 37
- KRIVOVA, N. A.; VIEIRA, L. E. A.; SOLANKI, S. K. Reconstruction of solar spectral irradiance since the Maunder minimum. **Journal of Geophysical Research (Space Physics)**, v. 115, p. A12112, dec. 2010. 45
- LAMING, J. M. The FIP and inverse FIP effects in solar and stellar coronae. **Living Reviews in Solar Physics**, v. 12, sep. 2015. 21
- LEIGHTON, R. B. Transport of magnetic fields on the sun. **The Astrophysical Journal**, v. 140, p. 1547, nov. 1964. 13
- LOCKWOOD, M. Reconstruction and prediction of variations in the open solar magnetic flux and interplanetary conditions. **Living Reviews in Solar Physics**, v. 10, p. 4, dec. 2013. 48
- MACKAY, D. H.; YEATES, A. R. The sun's global photospheric and coronal magnetic fields: observations and models. **Living Reviews in Solar Physics**, v. 9, p. 6, dec. 2012. 15
- MACRIS, C. **Physics of the solar corona**. Dordrecht: Springer Netherlands, Astrophysics and Space Science Library (series), 1971. 30
- MAZZOTTA, P.; MAZZITELLI, G.; COLAFRANCESCO, S.; VITTORIO, N. Ionization balance for optically thin plasmas: Rate coefficients for all atoms and

ions of the elements H to NI. **Astronomy and Astrophysics**, v. 133, p. 403–409, dec. 1998. [xiii](#), [22](#), [23](#), [24](#)

McCLOUGHAN, J.; DURRANT, C. J. A method of evolving synoptic maps of the solar magnetic field. **Solar Physics**, v. 211, p. 53–76, dec. 2002. [15](#)

MEIER, R. R. Ultraviolet spectroscopy and remote sensing of the upper atmosphere. **Space Science Reviews**, v. 58, p. 1–185, 1991. [7](#)

METCALFE, T. S.; CHARBONNEAU, P. Stellar structure modeling using a parallel genetic algorithm for objective global optimization. **Journal of Computational Physics**, v. 185, p. 176–193, feb. 2003. [45](#)

MEYER, J.-P. Solar-stellar outer atmospheres and energetic particles, and galactic cosmic rays. **The Astrophysical Journal Series**, v. 57, p. 173–204, jan. 1985. [xiii](#), [22](#), [23](#), [24](#)

MIESCH, M. S.; BRUN, A. S.; De ROSA, M. L.; TOOMRE, J. Structure and Evolution of Giant Cells in Global Models of Solar Convection. **The Astrophysical Journal**, v. 673, p. 557–575, jan. 2008. [13](#)

MITALAS, R.; SILLS, K. R. On the photon diffusion time scale for the sun. **The Astrophysical Journal**, v. 401, p. 759, dec. 1992. [4](#)

NASA. **The solar structure**. 2000. Available from:  
<<http://www-istp.gsfc.nasa.gov/istp/outreach/solarmax/pics.html>>.  
Access in: 30 October 2016. [3](#)

NEWKIRK JR., G. The solar corona in active regions and the thermal origin of the slowly varying component of solar radio radiation. **The Astrophysical Journal**, v. 133, p. 983, may 1961. [26](#)

NORDLUND, Å.; STEIN, R. F.; ASPLUND, M. Solar surface convection. **Living Reviews in Solar Physics**, v. 6, p. 2, dec. 2009. [12](#), [13](#)

NOVEMBER, L. J.; SIMON, G. W. Precise proper-motion measurement of solar granulation. **The Astrophysical Journal**, v. 333, p. 427–442, oct. 1988. [13](#)

NOVEMBER, L. J.; TOOMRE, J.; GEBBIE, K. B.; SIMON, G. W. The detection of mesogranulation on the sun. **The Astrophysical Journal letters**, v. 245, p. L123–L126, may 1981. [13](#)

- PESNELL, W. D.; THOMPSON, B. J.; CHAMBERLIN, P. C. The Solar Dynamics Observatory (SDO). **Solar physics**, v. 275, p. 3–15, jan. 2012. [32](#)
- PETER, H.; JUDGE, P. G. On the doppler shifts of solar ultraviolet emission lines. **The Astrophysical Journal**, v. 522, p. 1148–1166, sep. 1999. [45](#)
- PINTO, T. S. N. **Diagnóstico de explosões solares em microondas através da reconstrução da dinâmica de elétrons injetados em um campo magnético construído pela teoria de campos livres de força**. 110 p. PhD Thesis (PhD) — Instituto Nacional de Pesquisas Espaciais (INPE), São José dos Campos, 2015-02-23 2015. [45](#)
- RAFTERY, C. L. **EUV and X-ray Spectroscopy of the Active Sun**. PhD Thesis (PhD) — PhD Thesis, 2012, 2012. [43](#)
- REALE, F. Coronal loops: observations and modeling of confined plasma. **Living Reviews in Solar Physics**, v. 11, p. 4, dec. 2014. [29](#)
- RIEUTORD, M.; LUDWING, H.-G.; ROUDIER, T.; NORDLUND, .; STEIN, R. A simulation of solar convection at supergranulation scale. **Nuovo Cimento C Geophysics Space Physics C**, v. 25, p. 523, sep. 2002. [13](#)
- RIEUTORD, M.; RINCON, F. The sun’s supergranulation. **Living Reviews in Solar Physics**, v. 7, p. 2, dec. 2010. [13](#)
- SCHATTEN, K. H.; WILCOX, J. M.; NESS, N. F. A model of interplanetary and coronal magnetic fields. **Solar Physics**, v. 6, p. 442–455, mar. 1969. [47](#), [48](#)
- SCHERRER, P. H.; SCHOU, J.; BUSH, R. I.; KOSOVICHEV, A. G.; BOGART, R. S.; HOEKSEMA, J. T.; LIU, Y.; DUVAL, T. L.; ZHAO, J.; TITTLE, A. M.; SCHRIJVER, C. J.; TARBELL, T. D.; TOMCZYK, S. The Helioseismic and Magnetic Imager (HMI) investigation for the Solar Dynamics Observatory (SDO). **Solar Physics**, v. 275, p. 207–227, jan. 2012. [32](#), [33](#)
- SCHRIJVER, C. J. Simulations of the photospheric magnetic activity and outer atmospheric radiative losses of cool stars based on characteristics of the solar magnetic field. **The Astrophysical Journal**, v. 547, p. 475–490, jan. 2001. [16](#), [17](#), [18](#), [48](#), [109](#), [143](#), [144](#), [145](#)
- SCHRIJVER, C. J.; De ROSA, M. L. Photospheric and heliospheric magnetic fields. **Solar Physics**, v. 212, p. 165–200, jan. 2003. [47](#)

SINGH, J.; SAKURAI, T.; ICHIMOTO, K.; TAKEDA, A. Spectroscopic studies of the solar corona III. Density diagnostics using the infrared lines of Fe XIII. **Publications of the Astronomical Society of Japan**, v. 54, p. 807–816, oct. 2002. 26

SOHO - SOLAR AND HELIOSPHERIC OBSERVATORY. **Coronagraph images from LASCO**. 2017. Available from: <<https://sohowww.nascom.nasa.gov/data/realtime/c3/512/>>. Access in: 17 August 2016. 27

SOLANKI, S. K. Small-scale photospheric structure of the solar magnetic fields outside sunspots. **Astronomical Society of the Pacific Conference Series**, v. 248, p. 45, 2001. 4, 5

\_\_\_\_\_. Sunspots: an overview. **The Astronomy and Astrophysics Review**, v. 11, p. 153–286, 2003. 5

SOLANKI, S. K.; KRIVOVA, N. A.; HAIGH, J. D. Solar irradiance variability and climate. **Annual Review of Astronomy and Astrophysics**, v. 51, p. 311–351, aug. 2013. 7

SOLOMON, S. C.; WOODS, T. N.; DIDKOVSKY, L. V.; EMMERT, J. T.; QIAN, L. Anomalously low solar extreme-ultraviolet irradiance and thermospheric density during solar minimum. **Geophysical Research Letters**, v. 37, p. L16103, aug. 2010. 2

STEINER, O. **Chromosphere: magnetic canopy**. Bristol: Encyclopedia of Astronomy and Astrophysics, 2000. 5

STIX, M. **The sun : an introduction**. Berlin - Springer: Astronomy and astrophysics library, 2000. 4, 6

THE SOUTH FLORIDA AMATEUR ASTRONOMERS ASSOCIATION AND THE FOX OBSERVATORY AT MARKHAM PARK. **Temperatures in some specific wavelengths**. 2003–2017. Available from: <<http://www.sfaaa.com/index.php/the-sun-now>>. Access in: 5 June 2016. 29

TRIPATHI, D.; MASON, H. E.; YOUNG, P. R.; Del ZANNA, G. Density structure of an active region and associated moss using Hinode/EIS. **Astronomy and Astrophysics**, v. 481, p. L53–L56, apr. 2008. 29

UCAR. **The differential rotation**. 2017. Available from: <<https://www2.hao.ucar.edu/hao-science/solar-convecton-and-mean-flows-lsv>>. Access in: 30 October 2016. 14

UNRUH, Y. C.; SOLANKI, S. K.; FLIGGE, M. The spectral dependence of facular contrast and solar irradiance variations. **Astronomy and Astrophysics**, v. 345, p. 635–642, may 1999. 37

VERNAZZA, J. E.; AVRETT, E. H.; LOESER, R. Structure of the solar chromosphere. III - models of the EUV brightness components of the quiet-sun. **The Astrophysics Journal Series**, v. 45, p. 635–725, apr. 1981. 28, 42

VIEIRA, L. E. A.; SOLANKI, S. K. Evolution of the solar magnetic flux on time scales of years to millenia. **Astronomy and Astrophysics**, v. 509, p. A100, jan. 2010. 37, 45

VIEIRA, L. E. A.; SOLANKI, S. K.; KRIVOVA, N. A.; USOSKIN, I. Evolution of the solar irradiance during the Holocene. **Astronomy and Astrophysics**, v. 531, p. A6, jul. 2011. 37, 45

WARNECKE, J.; LOSADA, I. R.; BRANDENBURG, A.; KLEEORIN, N.; ROGACHEVSKII, I. Bipolar magnetic structures driven by stratified turbulence with a coronal envelope. **The Astrophysical Journal Letters**, v. 777, p. L37, nov. 2013. 9

WARREN, H. P. NRLEUV 2: A new model of solar EUV irradiance variability. **Advances in Space Research**, v. 37, p. 359–365, 2006. 42

WARREN, H. P.; MARISKA, J. T.; LEAN, J. A new reference spectrum for the EUV irradiance of the quiet Sun 1. Emission measure formulation. **Journal of Geophysical Research**, v. 103, p. 12077–12090, jun. 1998. 21, 42

WIEGELMANN, T.; THALMANN, J. K.; SOLANKI, S. K. The magnetic field in the solar atmosphere. **Astronomy and Astrophysics Review**, v. 22, p. 78, nov. 2014. 4, 5, 7, 29, 47

WOODS, T. N.; EPARVIER, F. G.; HOCK, R.; JONES, A. R.; WOODRASKA, D.; JUDGE, D.; DIDKOVSKY, L.; LEAN, J.; MARISKA, J.; WARREN, H.; McMULLIN, D.; CHAMBERLIN, P.; BERTHIAUME, G.; BAILEY, S.; FULLER-ROWELL, T.; SOJKA, J.; TOBISKA, W. K.; VIREECK, R. Extreme Ultraviolet Variability Experiment (EVE) on the Solar Dynamics Observatory

(SDO): Overview of science objectives, instrument design, data products, and model developments. **Solar physics**, v. 275, p. 115–143, jan. 2012. 32

WORDEN, J.; HARVEY, J. An evolving synoptic magnetic flux map and implications for the distribution of photospheric magnetic flux. **Solar Physics**, v. 195, p. 247–268, aug. 2000. 34

YEO, K. L. Analysis and modeling of solar irradiance variations. **ArXiv e-prints**, dec. 2014. 20

ZEEMAN, P.; WINAWER, B. The magnetic separation of absorption lines in connection with sun-spot spectra. **The Astrophysical Journal**, v. 32, p. 329, dec. 1910. 5

ZIRIN, H. **Astrophysics of the sun**. Cambridge and New York: Cambridge University Press, 1988. 4



## **PUBLICAÇÕES TÉCNICO-CIENTÍFICAS EDITADAS PELO INPE**

### **Teses e Dissertações (TDI)**

Teses e Dissertações apresentadas nos Cursos de Pós-Graduação do INPE.

### **Manuais Técnicos (MAN)**

São publicações de caráter técnico que incluem normas, procedimentos, instruções e orientações.

### **Notas Técnico-Científicas (NTC)**

Incluem resultados preliminares de pesquisa, descrição de equipamentos, descrição e ou documentação de programas de computador, descrição de sistemas e experimentos, apresentação de testes, dados, atlas, e documentação de projetos de engenharia.

### **Relatórios de Pesquisa (RPQ)**

Reportam resultados ou progressos de pesquisas tanto de natureza técnica quanto científica, cujo nível seja compatível com o de uma publicação em periódico nacional ou internacional.

### **Propostas e Relatórios de Projetos (PRP)**

São propostas de projetos técnico-científicos e relatórios de acompanhamento de projetos, atividades e convênios.

### **Publicações Didáticas (PUD)**

Incluem apostilas, notas de aula e manuais didáticos.

### **Publicações Seriadas**

São os seriados técnico-científicos: boletins, periódicos, anuários e anais de eventos (simpósios e congressos). Constam destas publicações o Internacional Standard Serial Number (ISSN), que é um código único e definitivo para identificação de títulos de seriados.

### **Programas de Computador (PDC)**

São a seqüência de instruções ou códigos, expressos em uma linguagem de programação compilada ou interpretada, a ser executada por um computador para alcançar um determinado objetivo. Aceitam-se tanto programas fonte quanto os executáveis.

### **Pré-publicações (PRE)**

Todos os artigos publicados em periódicos, anais e como capítulos de livros.

